

APPLICATION OF ATTOSECOND TECHNIQUES TO CONDENSED MATTER SYSTEMS

DISSERTATION

Presented in Partial Fulfillment of the Requirements for the Degree Doctor of
Philosophy in the Graduate School of The Ohio State University

By

Gregory J. Smith, B.Sc., M.Sc.
Graduate Program in Physics

The Ohio State University

2020

Dissertation Committee:

Louis F. DiMauro, Advisor

L. Robert Baker

Jay A. Gupta

Yuri V. Kovchegov

© Copyright by

Gregory J. Smith

2020

ABSTRACT

In this thesis, we lay the groundwork for performing attosecond transient absorption spectroscopy (ATAS) measurements in the condensed phase using mid-infrared (MIR) lasers. This was accomplished by designing, building and testing several pieces of home-built experimental equipment, including a MIR / extreme ultraviolet (XUV) Mach-Zehnder interferometer and a two-dimensional XUV spectrometer. A home-made bright XUV light source was designed and demonstrated to be nearly two orders of magnitude brighter than existing sources. Finally, the equipment was used to study ultrafast dynamics in germanium, a technologically important indirect bandgap semiconductor.

This thesis is organized as follows. Chapter 1 introduces the relevant background, including ultrafast dynamics and the tools required to observe them. Chapter 2 details the commercial laser system, the home-built *transient absorption beamline* (TABLE) and the XUV spectrometer. In Chapter 3, we design and optimize the XUV light source for high flux, which is a general requirement for ATAS measurements and especially needed at longer wavelengths with poor high harmonic generation (HHG) quantum efficiency. Also covered in Chapter 3 are basic diagnostics of the XUV & IR optics, as well as our XUV detector. In Chapter 4, we present the results of a MIR ATAS experiment in germanium, which is a technologically important indirect bandgap semiconductor. Chapter 5 concludes the dissertation with a roadmap for future condensed matter studies. An appendix provides instructions on how to operate some aspects of the home-built experimental apparatus.

Dedicated to my family.

ACKNOWLEDGMENTS

First and foremost, I would like to thank my advisors, Professors Louis F. DiMauro and Pierre Agostini for the opportunity to work on cutting edge research using world-class tools. They fostered a productive and collaborative environment from which I greatly benefited. Over the years, they gave invaluable feedback, asked probing questions, and drew upon their vast knowledge of physics to help me succeed.

I am also indebted to my colleagues and collaborators for their help throughout the years. Stephen Hageman designed major components of TABLE apparatus and assisted with nearly every single experiment; his insights regarding various experimental & instrumental considerations undoubtedly improved the quality of my research. Andrew Piper designed the OMRON vacuum control system and developed an the interferometric stabilization scheme for the TABLE. Dietrich Kiesewetter coded the computer-motor interface and the homemade laser pointing software; he also helped with the initial design of the TABLE, hunted down sources of interferometric instability and made subtle improvements to the apparatus. Kent Talbert wrote the entire LabVIEW software data collection suite from scratch and provided numerous last-minute bug fixes and feature improvements. Dr. Antoine Camper implemented the phase plate & phase grating, helped calibrate the photon spectrometer, and contributed to its early design. Sierra O'Bryan also worked on the initial optical design of the photon spectrometer. Dr. Yaguo Tang synthesized thin film germanium samples for ATAS experiments. Eric Moore automated the TABLE alignment system. Tim Gorman contributed to countless discussions about physics, experimental design and laser troubleshooting. And I would like to thank everyone else in the DiMauro group who has helped me throughout the years: Stephen Schoun, Dr. Tim Scarborough, Dr. Cosmin Blaga, Dr. Hyunwook Park, Dr. Junliang Xu, Urszula Szafruga, Kaikai Zhang, Kevin Guedenkauf, Zhou Wang, Yu Hang (Marco) Lai, Bryan Smith, Dr. Sha (Lisa) Li, Dr. Abraham Camacho, Daniel Tuthill, Dr. Vyacheslav (Slava) Leshchenko, and Dr. Li Fang.

Gratitude is also directed towards my collaborators. Jakub Husek, Dr. Anthony Cirri, Somnath Biswas & Prof. Robert Baker from the OSU Chemistry Department joined many useful discussions pertaining to data collection, experimental design and sample considerations. Dr. Drake Austin performed the Keldysh ionization simulations and helped me

understand some of the finer points of the Keldysh model; thanks go to Prof. Enam Chowdhury for arranging this collaboration. Dr. Christian Ott designed the original “cage and crank” vacuum flange manipulator which was adapted to work with our photon spectrometer. Michael Chilcote, Michael Newburger, Jinsong Xu & Yutichai Mueangnern from OSU, Prof. S.K. Sundaram from Alfred University, Dr. Grant Johnson, Dr. Venkateshkumar (Venky) Prabhakaran, Dr. Le Wang & Dr. Yingge Du from PNNL provided samples for ATAS measurements. Marieke Jager from the Leone group and Norman Niewrzella from the Semiconductor Manufacturing Technology Business Group at Carl Zeiss SMT GmbH helped with the design of the ellipsoidal mirror. Rich Pfisterer, Ryan Irvin and Donna Pfisterer from Photon Engineering provided a university gratis software license of FRED, and answered questions about using the software.

I could not have achieved a fraction of what I’ve accomplished without the OSU support staff. Pete Gosser and Michael Graham of the Physics Machine Shop manufactured countless parts (including our vacuum chambers) and provided consulting about general machining practices and mechanical design. Special thanks go to Jon Shover from the Astronomy Machine Shop for welding the vacuum chambers and the high pressure cell. Phil Davids and Mark Reed helped out with general facility issues and logistics. Kent Ludwig repaired and improved our rough vacuum system. Kris Dunlap, Mary Kay Jackson, Shirley McClung, Dameyon Shipley, Kyle Schechter & Jessica Middleton helped with administrative issues.

Last but not least, I’d like to recognize those who encouraged me to attend graduate school: Prof. Meigan Aronson, Dr. Jack Simonson, Dr. Jacob E. Grose, and Carlos Marques. In particular, I’d like to thank Prof. Aronson and Dr. Simonson for their mentorship during my time at Brookhaven National Laboratory. They set me down this path and I thank them for it.

VITA

2010	B.Sc. Physics & Mathematics. SUNY Stony Brook, Stony Brook, NY
2010 - 2012	Research Analyst. Correlated Electron Group, Condensed Matter Physics and Materials Science Division at Brookhaven National Laboratory, Upton, NY
2014	M.Sc. Physics. The Ohio State University, Columbus, OH
2014 - present	Graduate Research Associate. The Ohio State University, Columbus, OH

Publications

J. E. Bækhøj, D. Kiesewetter, A. J. Piper, S. Hageman, **G. Smith**, K. J. Schafer, P. Agostini and L. F. DiMauro. Strong Field Simulator: Quantum Path Analysis Using Attosecond Pulses. *Phys. Rev. X*, 2020 (submitted).

V. E. Leshchenko, B. K. Talbert, Y. H. Lai, S. Li, Y. Tang, S. J. Hageman, **G. Smith**, P. Agostini, L. F. DiMauro and C. I. Blaga. High-power few-cycle Cr:ZnSe mid-infrared source for attosecond soft x-ray physics. *Optica*, 7(8):981-988, 2020.

A. Camper, H. Park, S. J. Hageman, **G. Smith**, T. Auguste, P. Agostini and L. F. DiMauro. High relative-phase precision beam duplicator for mid-infrared femtosecond pulses. *Opt. Lett.*, 44(22):5465-5458, Nov. 2019.

L. Steinke, J. W. Simonson, W.-G. Yin, **G. J. Smith**, J. J. Kistner-Morris, S. Zellman, A. Puri, and M. C. Aronson. CaMn₂Al₁₀: Itinerant Mn magnetism on the verge of magnetic order. *Phys. Rev. B*, 92(2):020413, July 2015.

W. Miiller, J. M. Tomczak, J. W. Simonson, **G. Smith**, G. Kotliar, and M. C. Aronson. Protected Fe valence in quasi-two-dimensional α -FeSi₂. *J. Phys.: Condens. Matter*, 27(17):175601, May 2015.

Y.-H. Chiu, N. G. Minutillo, R. E. Williams, **G. J. Smith**, D. W. McComb, J. A. Carlin, E. Johnston-Halperin, and F. Yang. Photoluminescence evolution in GaAs/AlGaAs core/shell nanowires grown by MOCVD: Effects of core growth temperature and substrate orientation. *Journal of Crystal Growth*, 429:1, Nov. 2015.

G. J. Smith, J. W. Simonson, T. Orvis, C. Marques, J. E. Grose, J. J. Kistner-Morris, L. Wu, K. Cho, H. Kim, M. A. Tanatar, V. O. Garlea, R. Prozorov, Y. Zhu, and M. C. Aronson. Intrinsic nanostructure in $Zr_{2-x}Fe_4Si_{16-y}$ ($x = 0.81$, $y = 6.06$). *J. Phys.: Condens. Matter*, 26(37):376002, Sept. 2014.

J. W. Simonson, M. E. Pezzoli, V. O. Garlea, **G. J. Smith**, J. E. Grose, J. C. Misuraca, G. Kotliar, and M. C. Aronson. Local moments and suppression of antiferromagnetism in correlated $Zr_4Fe_4Si_7$. *Phys. Rev. B*, 88(8):081107, Aug. 2013.

J. W. Simonson, Z. P. Yin, M. Pezzoli, J. Guo, J. Liu, K. Post, A. E. Menko, N. Hollmann, Z. Hu, H.-J. Lin, C.-T. Chen, C. Marques, V. Leyva, **G. Smith**, J. W. Lynn, L. L. Sun, G. Kotliar, D. N. Basov, L. H. Tjeng, and M. C. Aronson. From antiferromagnetic insulator to correlated metal in pressurized and doped LaMnPO. *PNAS*, 109(27):E1815, July 2012.

J. W. Simonson, **G. J. Smith**, K. Post, M. Pezzoli, J. J. Kistner-Morris, D. E. McNally, J. E. Hassinger, C. S. Nelson, G. Kotliar, D. N. Basov, and M. C. Aronson. Magnetic and structural phase diagram of $CaMn_2Sb_2$. *Phys. Rev. B*, 86(18):184430, Nov. 2012.

J. W. Simonson, K. Post, C. Marques, **G. Smith**, O. Khatib, D. N. Basov, and M. C. Aronson. Gap states in insulating $LaMnPO_{1-x}F_x$ ($x = 0 - 0.3$). *Phys. Rev. B*, 84(16):165129, Oct. 2011.

Fields of Study

Major Field: Physics

Studies in Ultrafast Physics: Agostini-DiMauro Ultrafast Atomic Physics Research Group

Table of Contents

	Page
Abstract	ii
Dedication	iii
Acknowledgments	iv
Vita	vi
List of Figures	xi
List of Tables	xxiv

1	Introduction	1
1.1	Observing Ultrafast Dynamics	1
1.2	HHG: The Right Tool for the Job	4
1.3	High Harmonic Generation	5
1.3.1	Single Atom Response	7
1.3.2	Macroscopic Picture	12
1.4	Attosecond Transient Absorption Spectroscopy (ATAS)	18
1.4.1	Overview	18
1.4.2	Experimental Geometry: Real and Imaginary Parts of \tilde{n}	20
1.5	MIR Beam Shaping Using a Binary Phase Mask	23

Chapters

2	Experimental Apparatus	26
2.1	Introduction	26
2.2	Laser System	27
2.2.1	Spitfire and TOPAS	27
2.2.2	Active Pointing Correction Systems	32
2.2.3	Beam routing into the TABLE interferometer	36
2.3	Vacuum System	36
2.3.1	The Need for High Vacuum	36
2.3.2	Design Goals	38
2.3.3	Manufacturing Considerations	39
2.3.4	Vacuum System Details	40
2.4	XUV Optics	53
2.4.1	Design Goals	53
2.4.2	Fresnel Reflection from a Rough Surface	56
2.4.3	Aberration-Free Focusing	61

2.4.4	Metallic Filters	71
2.5	MIR Optics	71
2.5.1	The Generation Arm	73
2.5.2	The Pump Arm	74
2.5.3	Aligning into the TABLE Interferometer	77
2.6	XUV Photon Spectrometer	78
2.6.1	Optical Description	78
2.6.2	Spectral Calibration	78
2.7	Conclusion	88
3	XUV Light Source Design and Apparatus Performance	89
3.1	Introduction	89
3.2	HHG Gas Sources	89
3.2.1	Introduction	90
3.2.2	Free Expansion Nozzle	90
3.2.3	Low Pressure Cell	94
3.2.4	High Pressure Cell	102
3.2.5	Pulsed Amsterdam Piezo Valve	117
3.3	XUV Focal Spot Size	122
3.4	MCP response	127
3.5	Conclusion	129
4	ATAS Experiments in Germanium	130
4.1	Introduction	130
4.2	Experimental Considerations	131
4.2.1	Sample Requirements	131
4.2.2	Data Collection Sequence	134
4.2.3	The Supporting Nitride Membrane	137
4.2.4	Laser Damage	141
4.3	Finite Beam Size Considerations: Measuring ΔA	144
4.3.1	Relating Macroscopic and Microscopic Absorbance	144
4.3.2	XUV-MIR Misalignment	146
4.4	Nonlinear Excitation of Germanium	149
4.4.1	Description of the Nonlinear Model	151
4.4.2	Indirect Transitions	156
4.4.3	Spectral Content of the Laser Pulse	157
4.4.4	Keldysh Results	158
4.4.5	Thin Film Interference Calculations	163
4.4.6	Volume Averaging	169
4.4.7	Sample Heating	171
4.5	Experimental Results	176
4.5.1	Long-Lifetime Excited States in Ge	176
4.5.2	Frequency Filtering & Background Subtraction	181
4.5.3	Decomposition of Spectral Response	183
4.5.4	State Blocking Population Model	193
4.5.5	Discussion of Carrier Dynamics	197

4.5.6 Including Phonons	198
4.6 Summary	200
5 Conclusions	202
Appendix A Guidelines for using the TABLE	203
A.1 TABLE / OMRON Pump-down Procedure	203
A.2 TABLE / OMRON Venting Procedure	204
A.3 The High Pressure Cell (HPC)	205
A.3.1 Introduction	205
A.3.2 Initial Installation and Alignment	206
A.3.3 Alignment with the HPC Installed	212
A.3.4 Using the HPC	213
Bibliography	214

List of Figures

Figure	Page
1.1 Our ability to directly observe short events has rapidly improved over the past several decades (red line). The current record (not shown in this figure) for the world's shortest observed event is 247×10^{-21} s, corresponding to the time it takes for a photon to travel across a molecular hydrogen bond [1]. Figure adapted from [2].	2
1.2 Accessible ultrafast physical processes at different photon energies, time and length scales. Fundamental atomic, molecular & electronic processes are shown in blue; collective phenomena found in the condensed phase are shown in pink. Figure adapted from [3].	3
1.3 A comparison of HHG and XFEL light sources. Figure adapted from [4].	5
1.4 The three step model of HHG. Figure adapted from [5].	6
1.5 Ionization fraction at the peak of a 65 fs pulse ($t = 0$), calculated using the cycled-averaged OTB-corrected ADK rate.	9
1.6 ADK saturation intensity for a sech^2 pulse.	11
1.7 High harmonic cutoff energy for a 65 fs FWHM pulse at saturation intensity.	11
1.8 Time and frequency domain pictures of HHG. Figure adapted from [6].	12
(a)	12
(b)	12
1.9 The critical ionization fraction, η_c for argon (solid lines) and helium (dashed lines) at different fundamental wavelengths. Refractive index information from [7–9].	15
1.10 The optimal phase matching density, ρ_{opt} is inversely proportional to the refractive index mismatch, Δn (Eqs. (1.21) and (1.31)). As a result, higher interaction pressures are needed to properly phase match higher photon energies. The data shown is for a fundamental wavelength of 800 nm, but the same trend holds for $\lambda_1 = 0.4 – 2.0 \mu\text{m}$. Argon’s behavior above 250 eV is due to the $L_{2,3}$ absorption edge. Refractive index data from references [7–9].	16
1.11 1D absorption model from Eq. (1.33).	17

1.12	Cartoon illustrating ATAS in a semiconductor. The MIR pulse induces electron dynamics in conduction (CB) and valence bands (VB) near the Fermi energy (E_F), and the XUV pulse induces electron transitions between the core and VB/CB. Shown here are the orbitals $3d_{3/2}$ and $3d_{5/2}$, which serve as the initial states for M_4 - and M_5 -edge absorption, respectively.	18
1.13	Normal and non-normal incident geometries. a) Normal incidence geometry showing Fresnel coefficients R_F , T_F for interfaces and total transmission T and reflectance R for a slab of thickness L . Figure recreated from [10]. b) Non-normal geometry showing definitions of angles θ_i , θ_r and θ_t with respect to each interface.	20
1.14	Consequences of ignoring the real part of \tilde{n} when calculating the transmission T of germanium (left) and silicon (right). Top panels: complex refractive index. The Ge M -edge absorption feature is visible near 30-35 eV, and the Si L -edge is near 100 eV. Data from [7]. Bottom panels: relative error in T , as defined in Eq. (1.43), introduced by ignoring the contribution of $\text{Re}(\tilde{n})$. An infinite number of bounces (Eq. (1.41)) is assumed.	22
1.15	Calculated intensity pattern of the MIR beam at the focus after passing through a centered π -plate using two different methods. Left panel: numerical evaluation of the intensity (modulus squared of Eq. (1.48) using Eq. (1.49)) and a measured input laser beam profile. Middle panel: intensity profile of an equivalent TEM ₀₁ mode (Eq. (1.52)). Right panel: intensity lineouts at $x_p = 0$ comparing the numerical result to the TEM ₀₁ approximation.	24
2.1	Block diagram of part of the DiMauro lab complex showing the laser path from the laser bay to the southeast target room. Other experiments and laser systems are omitted for visual clarity. Optical tables are represented as gray boxes. SF: Spitfire laser system consisting of a MaiTai oscillator, two Empower pump lasers, internal stretcher, amplifier & internal compressor (bypassed for this experiment); EC: Spitfire external compressor; OPA: Light Conversion HE TOPAS Prime; TABLE: 4' \times 10' optical table for the transient absorption beamline.	28
2.2	FROG analysis of the TOPAS' signal output ($\lambda = 1400$ nm). The top row shows the measured (in red) intensity and reconstructed (in blue) phase information in both the temporal and spectral domains. The retrieved parameters are shown in the top right panel. The bottom row shows the measured and reconstructed spectrograms, as well as their difference.	30
2.3	Implementation of active stabilization systems between the amplifier in the laser bay and external compressor in the target room (not to scale). M0 & C0 are the motorized mirror and digital camera used for the single-point correction scheme. M1, M2, C1 & C2 are the motorized mirrors and cameras used for the two-point correction scheme. W is an uncoated CaF ₂ window used to reduce air currents between the laser bay and target rooms. PVC tubes that surround the beam path are omitted for visual clarity. Inset images show the attenuated beam as imaged by C1 & C2.	32

2.4	Typical passive pointing stability of the Spitfire’s amplifier as measured on cameras C1 & C2. Left panels: x and y coordinates of the centroid vs. time; right panels: 2D histogram of beam centroid positions for the same time period. The 2-point correction scheme was activated between 09:00 (9 am) and 17:00 (5 pm) on 07-30; this system is responsible for the stable performance in the middle in the plot. Long term thermal drift is apparent at all other times.	33
2.5	Single-point stabilization of the Spitfire’s amplifier as measured on cameras C1 & C2. This dataset contains about 10 correction events, which are visible as abrupt jumps in the time series. The skew of the centroid distributions highlights the limitations of the single-point correction scheme.	34
2.6	Two-point stabilization of the Spitfire’s amplifier as measured on cameras C1 & C2.	35
2.7	Estimation of XUV propagation losses through a vacuum level of 10^{-7} Torr and a distance of 4 meters. Transmission is well over 99.999% for this pressure-length product. Atomic scattering data obtained from references [7, 11], and the calculation follows Eqs. (2.9) to (2.11). Absorption features are present in most elements below 40 eV due to excitation of the valence electrons: M -edge in Ar, K -edges in H & He, L -edges in N ₂ & O ₂ . At higher energies we see the L -edge in argon at $\simeq 240$ eV and the K -edge in N ₂ at $\simeq 410$ eV.	37
2.8	Overhead rendering of the TABLE’s vacuum chambers. In-air optics are omitted for visual clarity. G: generation chamber; DP: differential pumping chamber; D: MIR diagnostic station; GV: gate valve, F: metal filter; M: mirror chamber; T: target chamber; S: XUV photon spectrometer. The generation through mirror vacuum chambers sit atop an optical table measuring 4’ \times 10’.	41
2.9	Angled rendering view of the TABLE’s vacuum chambers showing the two-level 4’ \times 10’ optical table. G: generation chamber; DP: differential pumping chamber; D: MIR diagnostic station; GV: gate valve, F: metal filter; M: mirror chamber; T: target chamber; S: XUV photon spectrometer.	42
2.10	Rendering of the metallic filter assembly in the spectral filter chamber. Metallic filters are shown with a false green color.	45
2.11	Photograph of the underside of the mirror chamber during installation showing the vibration-dampening bellows. Steel rods (not visible) connect the interior of the bellows feet to the interior breadboard. After installation, the flat metal disks were secured to the optical table using clamps.	46
2.12	Photograph of the ellipsoidal mirror in its motorization stack prior to being installed in the mirror chamber.	47
2.13	Rendering of the mirror chamber’s sealing surface showing detail of the differentially pumped double o-ring. O-rings are not shown in this figure. The two o-ring glands, the central pumping channel and the welded 1/4” stainless steel pumping tube are visible. Four through holes for the 5/16” sealing bolts are visible at the perimeter of the chamber’s sealing surface.	49

2.14	Block diagram of the TABLE's rough vacuum system showing rough and turbo pumps, control valves and pressure gauges. TC: thermocouple pressure gauge; P: UHV pressure gauge; \otimes : manual valve, \bowtie : rough vacuum solenoid or UHV pneumatic gate valve. UHV is indicated by blue shaded region. G: generation chamber, DP: differential pumping chamber, M: mirror chamber, T: target chamber, S: photon spectrometer chamber.	52
2.15	Schematic of the Transient Absorption BeamLine (TABLE). Blue shaded region represents vacuum. BS: beamsplitter, S: computer-controlled shutter, L: lens, I: iris, 2C: optics for two-color generation, HHG: high harmonic generation, F: metallic filter, EM: ellipsoidal mirror, HM: hole mirror, SH: sample holder, CF: long-pass color filter, WP: $\lambda/2$ waveplate, P: wire-grid polarizer, W: delay wedges, PD: photodiode and associated optics, DG: dispersive grating, MCP/P: micro-channel plate and phosphor.	54
2.16	Fresnel reflectance for s-polarized light on smooth metal mirrors at a grazing angle of 5 degrees. Refractive index data obtained from [7, 11]. Calculation follows Eqs. (2.16) and (2.19).	58
2.17	Extinction length in gold at various incident angles. Refractive index data obtained from [7, 11].	59
2.18	Fresnel reflectance for s-polarized light from a single smooth gold mirror as a function of incident angle. Calculation follows Eqs. (2.16) and (2.19).	60
2.19	Effect of surface roughness on reflectance. Calculation follows Eqs. (2.16) and (2.19).	61
2.20	Coordinate system used for the light path function F . Source point A is located a distance r from the center of the mirror at angle α and height z . Focus point B is located a distance r' away, with angle β and height z' . The impact point P of an individual ray is located on the mirror surface at point $(y, z) = (w, l)$. The curvature of the mirror is used to calculate the distance x between $P(w, l)$ and the yz plane. Figure adapted from [12].	62
2.21	Complex ray tracing simulation showing severe aberrations at the focus of a demagnifying toroidal mirror (TM). The entrance arm l_1 is 150 cm, the exit arm l_2 is 50 cm, and the grazing angle is 5 degrees. Top panel: overhead view of the simulation showing the source rays (red) and the focused rays (green). Bottom panel: intensity at the focal plane in arbitrary units. Calculations were performed using Photon Engineering's FRED software [13].	66
2.22	Fresnel reflectance for s-polarized light from two smooth gold mirrors as a function of incident angle. Calculation follows Eqs. (2.16) and (2.19).	67
2.23	Overhead view of the ellipsoidal mirror geometry used in our beamline. Mirror surface S is shown in blue; foci $f_{1,2}$ are represented by black dots. Rays that strike the center (red) and the edges (black) of the mirror are depicted as lines. Vertical scale is enlarged to show detail. Drawing is otherwise to scale to match the dimensions in Table 2.2.	69
2.24	The effect of curvature on the local grazing angle along the mirror's symmetry axis ($z = 0$). Light that strikes the edges of the mirror will experience a slightly different grazing angle than the design angle.	72

2.25 Height deviation of our ellipsoidal mirror from an ideal surface, as measured by a Carl Zeiss M400 precision tactile measurement device. Data provided by Carl Zeiss Laser Optics GmbH.	72
2.26 Calculated XUV transmission of various metallic filters. Data from [7].	73
2.27 Numerical propagation of the MIR ($N = 2^{13}$, $\lambda = 1450$ nm, $\tau_p = 44$ fs) beam through the pump arm for vacuum ($n = 1$). The beam path layout follows Fig. 2.15. From top left to bottom right, each panel shows the intensity profile of the beam as the beam propagates towards the focus. The top left panel shows the measured intensity and the remaining panels are calculations. The peak intensity at the focus is 3.68×10^{11} W/cm ² per 1 μ J input energy.	76
2.28 Counting scheme to determine the absolute harmonic order.	80
2.29 Two-source harmonic generation scheme. The pump beam is not used in this application. Extraneous XUV optics are omitted for visual clarity. Figure adapted from [14].	81
2.30 Two-source harmonic spectrum. Top panel: log scale 2D detector image. Middle panel: log scale of the power spectrum, computed by taking the FFT of the top panel along spatial dimension. Bottom panel: vertical integration of the top panel.	82
2.31 Integrated power spectrum (middle panel of Fig. 2.30) for selected harmonic orders and different diffraction orders. Harmonics with the matching spatial frequencies share the same line style and color. Note the poor visibility of the $m = 4$ peaks in the integrated power spectrum follows from the weak spatial interference pattern in the raw power spectrum.	84
2.32 Gaussian fit to the HHG yield in Fig. 2.30. Triangles indicate the harmonics used in the grating efficiency calculation; matching colors indicate matching harmonic orders across the different diffraction orders ($m = 1, 2, 3, 4$), following Fig. 2.31.	85
2.33 Fano resonances used for low energy spectral calibration. Left panel: XUV spectra with and without argon gas at the XUV focus. Middle panel: measured absorbance A of argon showing the absorption profile of the $n = 4$ and $n = 5$ $3s3p^6np$ resonances. Right panel: calibrated spectra showing the expected locations the higher resonances.	87
3.1 Rendering of the continuous free expansion nozzle. Gas flows from the base of the nozzle (bottom) and out of the 200 μ m aperture (top). The top surface is beveled so the nozzle can be brought closer to the MIR focus without clipping the beam.	92
3.2 On-axis Mach number M , mass density ρ and pressure P for a free expansion nozzle.	93
3.3 On-axis interaction pressure and absorption length for the free expansion nozzle. Left panel: On-axis pressure as a function of nozzle backing pressure for various on-axis distances x . Vertical dashed lines indicate pressures at which the vacuum system is overwhelmed (5 mTorr). Right panel: Required average interaction pressure as a function of absorption length L_{abs} for both gases at 30 and 100 eV.	94

3.4	Rendering of the low pressure cell (LPC). The interaction region is contained within the rectangular block. The circular disk is attached to the universal gas receiver (not shown) via the four through holes.	95
3.5	Conceptual gas flow schematic of the LPC. Arrows indicate direction of gas flow. Red shaded region indicates laser path.	96
3.6	Calculated on-axis density and pressure for the low pressure cell.	97
3.7	Effect of the laser hole diameter d on the LPC gas flow. Left panel: chamber pressure. Dashed horizontal line the indicates maximum sustainable operating pressure. Right panel: interaction pressure. Circles indicate the interaction pressure at the maximum sustainable backing pressure.	98
3.8	Interaction pressures and XUV absorption lengths for the low pressure cell (LPC). Left panel: interaction pressure of helium (blue) and argon (red) as a function of backing pressure. Bright lines correspond to $d = 400 \mu\text{m}$, faint lines are for $d = 200 \mu\text{m}$. Right panel: absorption length for the interaction pressures shown in the left panel.	99
3.9	Total harmonic yield of the LPC as a function of interaction pressure. To calculate the integrated yield, harmonic spectra are background subtracted, normalized for exposure time and integrated over the sensor area.	100
3.10	On-axis ionization fraction of helium (blue) and pulse envelope (red) at the focus of an 800 nm $\tau = 65 \text{ fs}$, $I_0 = 2.32 \times 10^{15} \text{ W/cm}^2$ pulse. Times on the rising edge of the pulse where the ionization fraction is below the critical ionization fraction η_c are shaded to indicate when harmonics are phase matched. The blue region denotes times when $\eta < \eta_c \simeq 0.55\%$ for photons with energies above 50 eV. The red region shows the additional times where lower energy ($< 50 \text{ eV}$) photons can be phased matched as their critical ionization fraction is slightly higher ($\eta_c \simeq 0.7\%$).	101
3.11	Cutaway view of the HPC interaction region. From bottom left to top right: welded gas feedthrough, concentric inner & outer pipes, connection to edge-welded bellows. The high pressure region is shaded blue. The green lines indicate the gas flow direction; the red line indicates the laser propagation direction.	102
3.12	Cutaway view of the HPC assembly showing the flexible bellows connection and connection to the chamber wall.	103
3.13	Photograph of the HPC's inner pipe showing the laser-drilled hole (bottom center of pipe).	104
3.14	Schematic used to calculate the pressures inside the HPC and generation chamber.	105
3.15	Schematic showing the geometry and pressure profile of the HPC's rough vacuum line.	107
3.16	Measured HPC pressure performance using the temporary spectroscopy station. P_H is measured from the gas source's inline pressure regulator; P_{baratron} is measured using a diaphragm gauge immediately outside the chamber wall; P_L is measured using a cold cathode gauge (PTR90) and corrected using values from the manufacturer's datasheet. Linear fits to P_{baratron} and P_L are performed for $P_H < 3000 \text{ Torr}$. Regulators were changed at $P_H \sim 3000$ and $\sim 8000 \text{ Torr}$, which account for the discontinuities.	107

3.17 Calculated on-axis pressure and density profiles for helium with $P_H = 760$ Torr, $P_M = 0.7$ Torr and $P_L = 3 \times 10^{-4}$ Torr.	109
3.18 Expected XUV reabsorption in the P_M region for different generating media. P_M calculated using $P_H = 760$ Torr via Eq. (3.15). Absorption data from [7].	110
3.19 HPC calculated performance as a function of interaction pressure, assuming $a_H = 100 \mu\text{m}$ and the fit from in Fig. 3.16. For both panels, blue (red) lines correspond to argon (helium), dashed (dotted) lines correspond to 30 (100) eV photons. Vertical dashed lines indicate the highest experimentally achieved pressures.	111
3.20 Total harmonic yield as function of interaction pressure in the HPC. To calculate the integrated yield, harmonic spectra are background subtracted, normalized for exposure time and integrated over the sensor area (divergence and energy).	113
3.21 Harmonics generated from helium as a function of interaction pressure for $\lambda_1 = 800$ nm, a peak intensity of $2.67 \times 10^{15} \text{ W/cm}^2$ and a $200 \mu\text{m}$ Zr filter. Note that different energy harmonics are phase matched at different pressures. To calculate the integrated yield, harmonic spectra are background subtracted, normalized for exposure time and integrated over the sensor area.	113
3.22 Comparison of the LPC and the HPC in helium at 800 nm. Generation conditions for each were optimized (LPC: 17 Torr interaction pressure, $2.32 \times 10^{15} \text{ W/cm}^2$; HPC: 650 Torr, $2.67 \times 10^{15} \text{ W/cm}^2$) in helium at 800 nm. The higher interaction pressure extends the phase matched region from ~ 110 eV to ~ 130 eV, and increased pressure-length product increases the XUV brightness by at least two orders of magnitude across the spectrum. Note that harmonics with energies less than half the cutoff are contaminated by 2 nd order diffraction from the XUV spectrometer's grating. Faint blue line removes the calculated absorption losses in the medium pressure (M) region. Normalized yield is calculated by background subtracting the 2D spectra, integrating the spatial dimension of the sensor, normalizing by exposure time and applying the Jacobian.	114
3.23 Relative performance of the HPC compared to the LPC in the energy range 75 - 150 eV. Faint blue line includes the calculated transmission factor in the M region. Datasets are the same as in Fig. 3.22.	115
3.24 Performance of the HPC using argon at 1450 nm. Normalized yield is calculated by background subtracting the 2D spectra, integrating the spatial dimension of the sensor, normalizing by exposure time and applying the Jacobian.	116
3.25 Spectral lineouts of Fig. 3.24 for pressures below the maximum in harmonic yield. Normalized yield is calculated by background subtracting the 2D spectra, integrating the spatial dimension of the sensor, normalizing by exposure time and applying the Jacobian.	117
3.26 Labeled picture of the Amsterdam Piezovalve showing dimensions (mm). The gas and electrical connections are located on the rear of the device; the nozzle aperture is located at the center of the front face (flat side).	118

3.27 Integrated yield as a function of off-axis nozzle distance used to determine the on-axis distance, x . A fit of Eq. (3.19) to the data yields an on-axis distance of $573 \mu\text{m}$.	119
3.28 Integrated harmonic yield from the piezo valve as a function of interaction pressure. The inset shows excellent quadratic behavior with respect to interaction pressure. Assumed on-axis distance is $x = 573 \mu\text{m}$. To calculate the integrated yield, harmonic spectra are background subtracted, normalized for exposure time and integrated over the sensor area. The total yield has been multiplied by 4 to account for the 250 Hz rep. rate to compare it to the 1 kHz datasets.	120
3.29 A selection of piezo valve spectra as a function of interaction pressure. Assumed on-axis distance is $x = 573 \mu\text{m}$. Normalized yield is calculated by background subtracting the 2D spectra, integrating the spatial dimension of the sensor, normalizing by exposure time and applying the Jacobian. Total yield is multiplied by 4 to account for the 250 Hz rep. rate.	121
3.30 A comparison of the HPC and piezo valve harmonic yield under typical operating conditions.	122
3.31 Schematic of XUV knife edge measurement. EM: ellipsoidal mirror, z_0 : XUV focal plane.	123
3.32 A typical XUV knife edge measurement near the focal plane. The total harmonic yield was used in this calculation.	124
3.33 Evolution of XUV beam waist as a function of propagation direction, z . The Rayleigh range z_R and beam waist w_0 are extracted from the fit to Eq. (3.21). The total harmonic yield was used in this calculation.	125
3.34 Energy-resolved fit parameters following a knife edge measurement of two-color harmonic spectrum generated in argon using 1430 nm / 715 nm light. The focal plane position (z_0), beam waist radius (w_0), Rayleigh range (z_R), and half-angle divergence (θ) are calculated for each harmonic. Error bars represent one standard deviation on the parameters.	126
3.35 Harmonic spectra as a function of MCP voltage. Harmonics were generated in argon gas with a 1250 nm fundamental. The aluminum L -edge is visible at 72.7 eV.	127
3.36 Integrated harmonic yield Y as a function of MCP voltage. GC1 was obtained by summing the spectra in Fig. 3.35, GC2 was taken under similar but slightly less efficient harmonic generation conditions. Approximate gain is calculated assuming $G = 10^7$ at 2400 VDC and using the fitting coefficient from GC1.	128
4.1 Calculated XUV transmission of various materials. Data from [7].	132

4.2 Spatially averaged ground state absorbance A of our 100 nm germanium sample. The ground state absorbance is defined by $A_{\text{g.s.}} = -\log_{10}(\bar{S}_{\text{Ge+SiN}}/\bar{S}_{\text{SiN}})$, where the overbar denotes a spatial average over the sample area (182 points for Ge+SiN, 196 points for SiN). The blue line is the average absorbance of the Ge, with the shaded region representing ± 1 std. The red line shows the result of frequency filtering to eliminate the oscillations, which originate from a measurement artifact of the harmonic comb (see Section 4.5.2 for details). The $M_{4,5}$ edge of Ge is visible around 30 eV.	133
4.3 Schematic of competing raster methods, shown in the sample's reference frame. The clear aperture of the sample is represented by the interior of the black square. The laser propagation direction is out of the page. The laser focal spots are shown as red circles, and the movement of the sample holder relative to the laser focus is indicated by arrows. A 200 μm border exists between the raster array and the perimeter of the sample's clear aperture. This diagram is to scale for a $1 \times 1 \text{ mm}^2$ clear aperture sample, a 60 μm diameter MIR focal spot and a 200 μm step size.	136
4.4 Cartoon showing the cross section of the free standing sample heterostructure. A 500 μm thick Si frame supports a freestanding 30 nm low stress silicon nitride membrane (Norcada QX7300X), upon which 100 nm of germanium has been deposited. The Si frame has a $3 \times 3 \text{ mm}^2$ square clear aperture and a $7.5 \times 7.5 \text{ mm}^2$ square external dimension. The taper of the Si frame thickness along the perimeter of the clear aperture forms a knife edge. In an ATAS experiment, the XUV and MIR pulses propagate from the top to bottom of the figure.	140
4.5 XUV transmission measurements of Al metallic filter and silicon nitride membrane. Left panel: normalized XUV counts for i) unfiltered HHG signal, ii) HHG going through a 200 nm Al filter and iii) HHG going through a 200 nm Al filter and 30 nm of silicon nitride. Counts are scaled by the Jacobian. Right panel: transmission curves obtained from the left panel's data. Also shown are literature values for 20 nm of silicon nitride (purple dots) and 200 nm of Al with two 4 nm oxide layers (red dashes) [7]. Multilayer interference is not taken into account. Oscillations in measured transmission are numerical artifacts originating from a finite detector noise floor and XUV brightness instabilities. The deviation between the measured and literature transmission for SiN below 40 eV, and for Al between 36 and 55 eV, is due to a measurement artifact as will be discussed in Section 4.5.2.	140
4.6 XUV transmission map of 30 nm silicon nitride freestanding membrane. Left panel: integrated XUV counts in the range 30 – 34 eV. Sample holder motor positions are indicated by x- and y-positions. Right panel: histogram of logarithmic deviation of counts from the average. Dashed line shows a normal distribution.	141

4.7	<i>In-situ</i> imaging of the samples within the target chamber. Left: optical setup for <i>in-situ</i> imaging of samples. C: Si CCD camera, HM: hole mirror, SH: sample holder, FM: translatable silver mirror, L: lens. Right: false color image showing the sample holder with a 3 x 3 grid of 5 mm diameter clear apertures. Samples are held in a clamshell design centered in the clear apertures and are backlit using a flashlight.	142
4.8	Laser damaged 200 nm silicon membrane samples. Left panel: XUV map of pristine Si before being exposed to MIR laser. Center panel: XUV map of damaged sample after being pumped with $\approx 65 \mu\text{J}$ of $\lambda = 1500 \text{ nm}$ at 1 kHz repetition rate in two locations. Right panel: microscope image of damaged sample (beige) showing large sections of missing material (white). Red circles in all three pictures indicate the two locations that were exposed to MIR laser light.	142
4.9	The effect of finite pump and probe sizes in measuring the change in absorbance in an ATAS experiment. Left panel shows the relative sensitivity of ΔA as a function of the relative sizes of the XUV and $\bar{\eta}_z$ spots. The red dot represents our experimental configuration ($a \simeq 5$), which yields $\simeq 96\%$ measuring efficiency. The right panel shows the expected ΔA amplitudes as a function of both a and $\alpha_{10} L \eta_0$. See Eq. (4.13) and surrounding text for details.	147
4.10	The effect of relative misalignment of the MIR and XUV spots. Linear excitation is assumed for this calculation.	147
4.11	Band structure of germanium. Transition energies are labeled in black; the X , Γ and L valleys are labeled in red. Figure adapted from [15].	149
4.12	Channel- and initial band-resolved effective bandgaps Δ_i (solid line, left axes) and Keldysh parameters γ_i (dashed lines, right axes) as a function of peak intensity. The shaded region under γ_i corresponds to intensities where $\gamma_i < 1$ for 1430 nm (blue) and 1450 nm (red).	154
4.13	Prefactor for indirect transition rates assuming a Poisson distribution. For germanium and a pulse duration of 60 fs, the indirect transition factor is about 0.7.	157
4.14	TOPAS spectral content at $\lambda = 1401 \text{ nm}$	158
4.15	Transition type and initial band resolved contributions to the final conduction band density. Inset text denotes the values of n_i at the peak intensity (for $\tau = 0 \text{ fs}$) as the minimum number of photons required to excite the electron across the gap increases by 1.	160
4.16	Total conduction band (CB) population as a function of laser pulse delay. Inset shows the pulse envelope.	161
4.17	Contributions of the initial bands to the final conduction band (CB) density at the end of the pulse ($\tau = \infty$). Dark lines are for $\lambda = 1430 \text{ nm}$, faint lines are for $\lambda = 1450 \text{ nm}$	161
4.18	Contributions by indirect and direct transitions to the final conduction band (CB) density at the end of the pulse ($\tau = \infty$). Dark lines are for $\lambda = 1430 \text{ nm}$, faint lines are for $\lambda = 1450 \text{ nm}$	162

4.19	Optical properties of the Ge/SiN heterostructure and a freestanding 100 nm Ge membrane as a function of wavelength. For the R , A and T panels, solid lines represent the coherent calculations, and dashed lines represent the incoherent calculations. TMM calculations assume monochromatic light.	164
4.20	Broadband TMM calculations for a 100 nm Ge film and 30 nm SiN membrane. The red region represents Ge; green is SiN; white is vacuum. Solid lines are TMM results, dashed lines are Eq. (4.36).	166
4.21	Broadband TMM calculations for a 100 nm freestanding Ge thin film. The red region represents Ge; white is vacuum. Solid lines are TMM results, dashed lines are Eq. (4.36).	167
4.22	Calculated intensity distributions in Ge/SiN heterostructures and Ge thin films. Dark colors follow broadband TMM calculations, light colors follow Eq. (4.36).	169
4.23	Cross sectional slice of the MIR intensity profile, XUV intensity profile and total excited state fraction at the rear of the Ge sample in a Ge/SiN heterostructure and the center of the MIR pulse ($\tau = 0$ fs). The MIR intensity profile follows from a broadband TMM calculation for a 100 nm Ge / 30 nm SiN heterostructure and an input pulse energy of $2.85 \mu\text{J}$ of $\lambda = 1430 \text{ nm}$	170
4.24	Calculated volume averaged final ΔA (Eq. (4.13)) as a function of input pulse energy. These curves were calculated using $\alpha_{10}(32 \text{ eV})$ and assuming different interference terms $I_p(z)$ (see Eq. (4.37)).	172
4.25	Calculated volume averaged ΔA (Eq. (4.13)) as a function of pulse delay time, τ . These curves were calculated using $\alpha_{10}(32 \text{ eV})$ and assuming different interference terms $I_p(z)$ (see Eq. (4.37)).	173
4.26	Calculated absorbed energy from a single $\tau_p = 60 \text{ fs}$ pulse at $\lambda = 1430 \text{ nm}$ (dark lines) and $\lambda = 1450 \text{ nm}$ (faint lines).	174
4.27	Thermal data for a 100 nm Ge/ 30 nm SiN heterostructure extracted from the literature [16].	175
4.28	A delay-independent feature at 30 eV (red horizontal stripe) is observed in germanium for a repetition rate of 1 kHz, $\lambda = 1450 \text{ nm}$ and $1.75 \mu\text{J}$ pulse energy. The harmonic spectrum used for this measurement is shown in the left panel.	177
4.29	Evidence of a long-lifetime state in germanium. The left panel shows the $\Delta A(\tau = -\infty)$ lineouts for three pulse energies. A broad feature centered near 30 eV appears to scale with increasing pulse energy. The right panel plots the magnitude of the feature as a function of pulse energy, suggesting a linear scaling of the feature $\tau = -\infty$ feature.	177
4.30	Estimating the lifetime of the negative time delay feature. The maximum sample response at $\tau = -\infty$ is normalized to the pulse energy (PE) and plotted as a function of the inverse laser repetition rate (RR). The data is fit to an exponential decay with $\tau_p = 1.7 \text{ ms}$	178

4.31 Low repetition rate ATAS measurements reveal ultrafast dynamics in germanium. Left panel: an average of 6 measurements at 125 Hz. Right panel: an average of 2 measurements at 250 Hz. Consistent with Fig. 4.30, a slight $\tau = -\infty$ contribution is present in both measurements between 30 and 31 eV, visible as a positive ΔA at negative time delays.	179
(a)	179
(b)	179
4.32 Integrated lineouts of Fig. 4.31a. Dark lines are the average of 6 measurements, faint lines show the individual measurements.	180
4.33 Details of the low pass filter (LPF) used for the measured ground and excited states of germanium. Black lines are interpolated data, red lines are filtered data. The same LPF (cut-off $f_L = 0.507 \text{ eV}^{-1}$, bandwidth $b_L = 0.5 \text{ eV}^{-1}$) has been applied to both datasets.	181
4.34 Preparing the spectrogram data ($RR = 125 \text{ Hz}$, $\lambda = 1430 \text{ nm}$, $PE = 2.88 \pm 0.41 \mu\text{J}$) for spectral decomposition analysis. Left panel: averaged spectrogram from $N = 6$ measurements. Middle panel: spectrogram after subtracting the average ΔA signal for $\tau < -50 \text{ fs}$. Right panel: spectrogram after applying a low pass filter (LPF) along the energy axis. A common colorscale is used for all figures.	183
4.35 Single-intensity state blocking signal for a peak intensity of 640 GW/cm^2 ($\lambda = 1430 \text{ nm}$), from Eq. (4.47).	186
4.36 Volume-averaged state blocking signal for a pulse energy of $2.85 \mu\text{J}$ ($\lambda = 1430 \text{ nm}$) from Eq. (4.48).	187
4.37 Illustrating the effects of numerically shifting and broadening the ground state absorption spectrum using Eqs. (4.51) and (4.53). Left panels: a band shift of 50 meV yields a ΔA_{shift} profile peaked at about 15×10^{-3} . Right panels: A Gaussian (Lorentzian) broadening of 0.5 eV (2.7 eV) yields a ΔA_{broad} profile with a magnitude of about 7×10^{-3}	188
4.38 Spectral decomposition of the filtered data using a Gaussian broadening function. The contributions of broadening, band shifting, state blocking are compared to the filtered measured dataset.	189
4.39 Time dependence of the spectral decomposition results. The black lines in the broadening and shifting plots are guides for the eye.	190
4.40 Spectral decomposition of the filtered data without broadening ($\sigma = 0$). The contributions of band shifting and state blocking are compared to the filtered measured dataset.	191
4.41 Delay-dependent parameters from the $\sigma = 0$ decomposition result in Fig. 4.40. The black line in the top panel is a guide for the eye.	192
4.42 Initial state- and channel-resolved Keldysh excitation rate. The rate has been normalized for each intensity to showcase the intensity dependence of the excitation duration. Brighter colors correspond to a higher excitation rate.	194
4.43 Initial band- and channel-resolved Keldysh excitation rate for $\lambda=1430 \text{ nm}$. Solid (dashed) lines are direct (indirect) transitions. The total excitation rate includes all bands and transitions.	195

4.44 State $b(\tau)$ of Eq. (4.58) (solid black line) is fit to the integrated state blocking signal $\Delta A_{\text{SB}}(\tau)$ for holes (red) and electrons (blue). The dashed line shows state $a(\tau)$, and the magenta dashdot line shows the total excited population $a(\tau) + b(\tau)$. Lifetimes τ_a and τ_b are extracted from the fit.	196
4.45 Comparison of the extracted band shift ΔE from Fig. 4.41 (blue) to the predicted acoustic phonon population density $PA(t)$ of Eq. (4.59). The black curve is $PA(t)$ when a_e , a_h and b_e are included as source terms in Eq. (4.59); the red curve is $PA(t)$ when b_e is the only source term. $PA(t)$ is plotted in arbitrary units.	199
A.1 Exterior view of the generation chamber with the HPC installed showing the ancillary vacuum hardware. Red arrow indicates input laser path; green arrow points towards the HPC's RV pump.	206
A.2 The HPC with bracket installed on the XYZ translation stage, configured for the generation chamber. The hose clamp and gas supply tube are omitted from this drawing for clarity.	208
A.3 Laser filament in the aligned outer pipe of the HPC. The inner pipe is not yet installed. Alignment of the outer pipe is done at very low intensities; after alignment the power was increased to create a filament for illustrative purposes only. This picture was taken in the target chamber during the initial testing of the HPC. The geometry of this chamber requires that the orientation of the mounting bracket is reversed compared to what is shown in Fig. A.2.	210
A.4 Laser drilling the inner pipe. A card blocks the laser after exiting the HPC. The HPC was pressurized with Ar gas to enhance the filament for illustrative purposes.	211

List of Tables

Table	Page
1.1 ADK parameters [17].	8
2.1 Values of $E_{ij0}(\alpha, r, 0)$ up to 4 th order, used in the calculation of the light path function F . Terms in excess of 4 th order are indicated by *. See text for definitions of S and T . Table adapted from [12].	63
2.2 Specifications of the ellipsoidal mirror. Data provided by Carl Zeiss Laser Optics GmbH.	70
2.3 Experimentally measured Fano parameters for the $3s3p^6np$ resonance series in argon [18].	87
3.1 Gas parameters used in Eq. (3.4). Table recreated from Ref [19].	91
4.1 Material parameters used in the Keldysh simulation for germanium. Abbreviations used are as follows: CB: conduction band; VB: valence band; HH: heavy hole band; LH: light hole band; SO: split-off band.	150
4.2 Values for the intensity-scaling factor $m_i^R \Delta^{\text{eff}}$, calculated using Eq. (4.21) and Table 4.1.	155
4.3 TMM calculated internal intensity ranges for a 100 nm Ge / 30 nm SiN heterostructure and a freestanding 100 nm Ge film.	168

Chapter 1

INTRODUCTION

1.1 Observing Ultrafast Dynamics

In June 1878, Eadweard Muybridge recorded what would become the world’s first motion picture. Using strings to trigger the shutters of multiple cameras, photographs were taken once every twenty-fifth of a second as a horse galloped by. In a now-famous series of images, it was shown that there were periods of time during which all four of the horse’s hooves were lifted from the ground. The project was financed by Amasa Leland Stanford, who later co-founded Stanford University with his wife, Jane.

Much like one needs a camera with a fast shutter to photograph the rapid motion of a hummingbird’s wings, researchers need ultrafast light sources to “see” the dynamics of particles within atoms, molecules and solids. Our understanding of the physical world is only as good as our ability to observe it, and fortunately movie-making technology has come a long way since the days of the robber baron¹. Figure 1.1 shows the astonishing progress of ultrafast technology over the past several decades, starting with the invention of the laser in 1960. The timescale of the shortest observed process has gone from nanoseconds ($1 \text{ ns} = 10^{-9} \text{ s}$) in the 1960s [2], femtoseconds ($1 \text{ fs} = 10^{-15} \text{ s}$) in the 1970s & 80s, to attoseconds ($1 \text{ as} = 10^{-18} \text{ s}$) in the early 2000s [20, 21], and zeptoseconds ($1 \text{ zs} = 10^{-21} \text{ s}$) in recent years [1, 22]. The rate of progress in this field has been nothing short of astounding, and it was driven entirely by the development of “faster” light sources and detection techniques [23].

¹Stanford was a prominent American industrialist and politician. Born in 1824 and raised outside of Albany, NY, he moved to Wisconsin in 1845 to open a law practice, but these efforts ended in flames when his office and library burned down. In 1852, he migrated to California where his luck quickly turned. Starting as a grocer benefiting from increased business associated with the Gold Rush, he quickly made political connections that he leveraged into fantastic business opportunities. Within a few short years, he had co-founded the California Republican Party and befriended President Lincoln. In 1861, he invested in the Central Pacific Railroad Company and was elected Governor of California. In 1862, the CPRR was fortuitously authorized by Congress to build part of the first transcontinental railroad. His business enjoyed federal loans, land grants and a legal monopoly on the economic & industrial lifeline connecting the West Coast to rest of the country. He engaged in the worst business practices of the time, including stock watering, kickbacks, rebates and bribes. Stanford was later elected to the US Senate where he served until his death, upon which his estate was frozen by the government due to outstanding railroad loans.

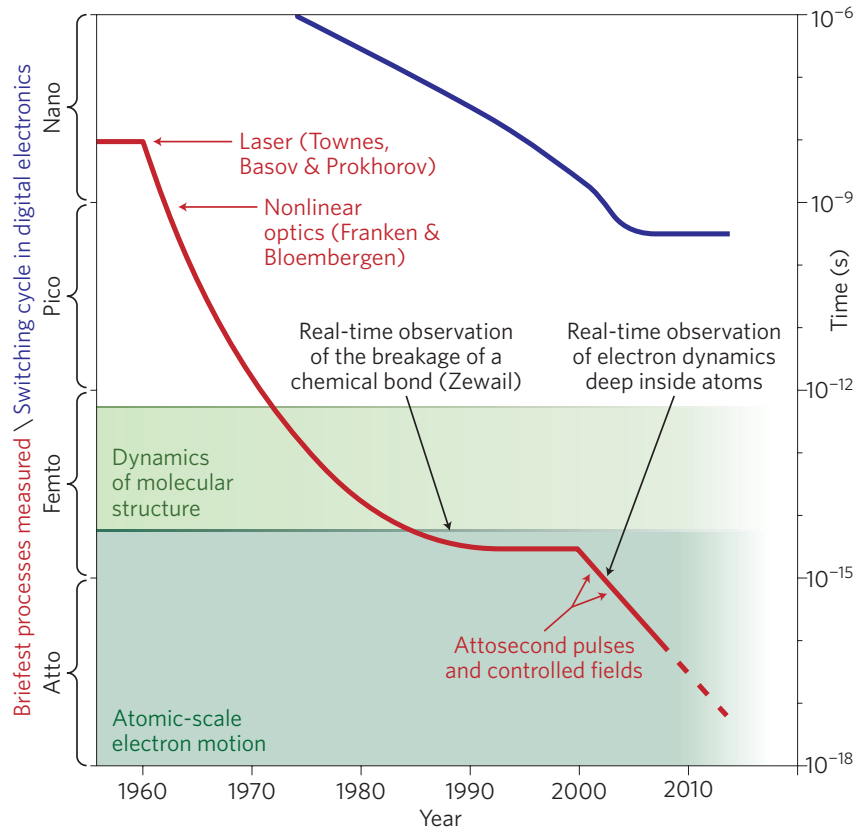


Figure 1.1: Our ability to directly observe short events has rapidly improved over the past several decades (red line). The current record (not shown in this figure) for the world's shortest observed event is 247×10^{-21} s, corresponding to the time it takes for a photon to travel across a molecular hydrogen bond [1]. Figure adapted from [2].

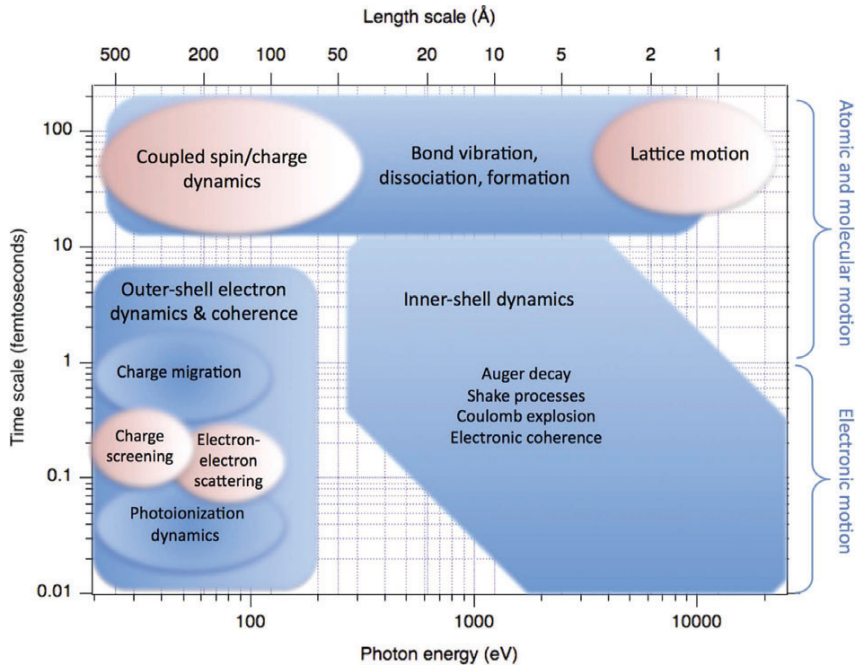


Figure 1.2: Accessible ultrafast physical processes at different photon energies, time and length scales. Fundamental atomic, molecular & electronic processes are shown in blue; collective phenomena found in the condensed phase are shown in pink. Figure adapted from [3].

The natural timescale of the electron is measured in attoseconds, with the Bohr model predicting an electron period about the hydrogen atom to be $T = 4m_e(\pi a_0)^2/hn = 152$ as [24]. Thus, to make a “movie” of an electron moving about a hydrogen atom, you would need to take a picture about once every 10 as. Figure 1.2 shows an overview of the time, length and energy scales of various observable ultrafast processes. We can see that there is a variety of fundamental (blue) and many-body (pink) processes that can be observed if one has a sufficiently fast camera. If we were to extend the vertical axis of this plot to picosecond ($1 \text{ ps} = 10^{-12} \text{ s}$) timescales, we would see slower condensed matter dynamics such as electron-phonon and phonon-phonon scattering, which are responsible for inter- & intravalley electron population transfer [16]. The horizontal axis of this plot corresponds to the photon energy needed to access these dynamics. A light source capable of producing sub-fs bursts of 20 – 100 eV photons can therefore capture a significant fraction of the naturally occurring physical processes in atoms, molecules, liquids and condensed matter [25].

One of the biggest developments in the past couple of decades has been an understanding of *high harmonic generation* (HHG), the process responsible for the worlds shortest light pulse at 53 attoseconds [26]. In the next section, we will compare the viability of HHG for studying condensed matter dynamics to that of another ultrafast light source, the *x-ray free electron laser* (XFEL).

1.2 HHG: The Right Tool for the Job

According to Fig. 1.2, if we want to observe ultrafast condensed matter dynamics we need a light source capable of producing ≤ 1 fs bursts of photons with energies around $\sim 20 - 300$ eV. This energy range is commonly referred to as the extreme ultraviolet (XUV, or alternatively EUV) regime. Synchrotrons can produce extremely bright XUV light with a ~ 30 ps duration, and advanced slicing techniques can reduce the pulse duration to ~ 100 fs, but with a concurrent reduction in brightness by a factor of $\sim 10^8$ [27]. However, this time resolution is insufficient for our needs. That leaves for our consideration two other light sources, HHG and XFEL.

Figure 1.3 compares the performance of x-ray free electron lasers (XFEL) to tabletop high harmonic generation (HHG) sources. XFELs can produce photons in excess of 10 keV, pulse durations measured in femtoseconds, and can be more than 1 million times brighter than HHG sources. Advanced XFEL techniques can produce sub-fs pulses [28]. However, XFELs are incredibly complex and expensive machines. For example, SLAC’s LCLS facility is 3.2 kilometers long, and the European XFEL has an estimated construction and commissioning cost in excess of €1 billion. Consequently, they require large teams of beamline scientists to operate, and users must apply for experiment time via a proposal system. At

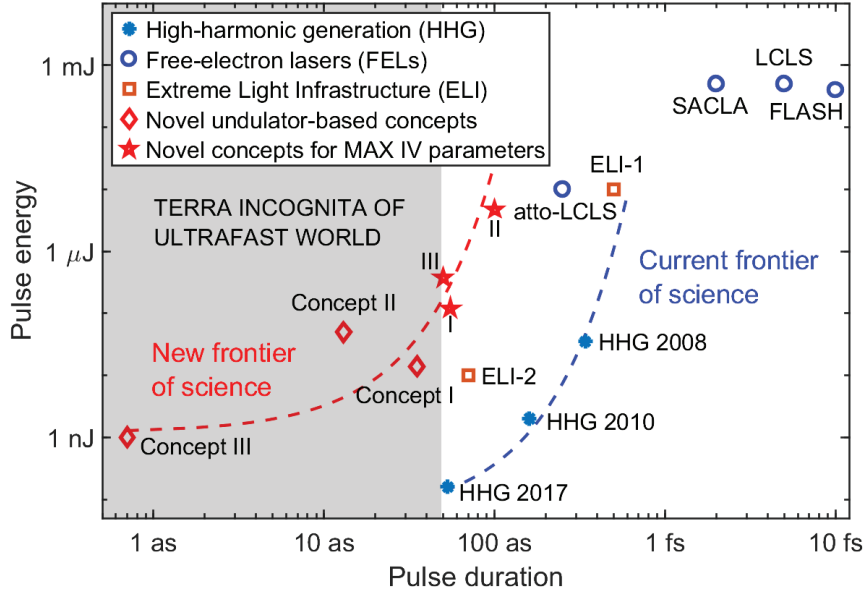


Figure 1.3: A comparison of HHG and XFEL light sources. Figure adapted from [4].

the LCLS, only a single experiment can be performed at a time. While XFELs are engineering marvels that permit the study of exotic physical processes, their low experimental throughput represents a huge bottleneck for many researchers.

On the contrary, high harmonic generation is a much simpler process and it is therefore more accessible to university researchers. The total cost of a HHG light source is on the order of a few hundred thousand dollars, with the bulk of that cost attributable to a commercially available ultrafast laser system and some standard high vacuum hardware. Depending on operating conditions, an HHG source can produce light from tens of eV to several hundred eV. Once operational, an HHG light source can be run by a single graduate student - although a team of 2–3 researchers is preferable. Additionally, experiments can in principle be run continuously for weeks or months at a time – something that is not feasible at national user facilities where research teams compete for limited experimental time.

The obvious downside to HHG compared to XFEL is the limited photon energy and reduced flux. But HHG light sources are still useful for many types of experiments, including *attosecond transient absorption spectroscopy* (ATAS). In Section 1.3, we will discuss the physics of HHG, and in Section 1.4 we will provide an overview of ATAS.

1.3 High Harmonic Generation

High harmonic generation (HHG) is the extremely nonlinear process in which a strong infrared field produces light with frequencies that are integer multiples of the fundamental

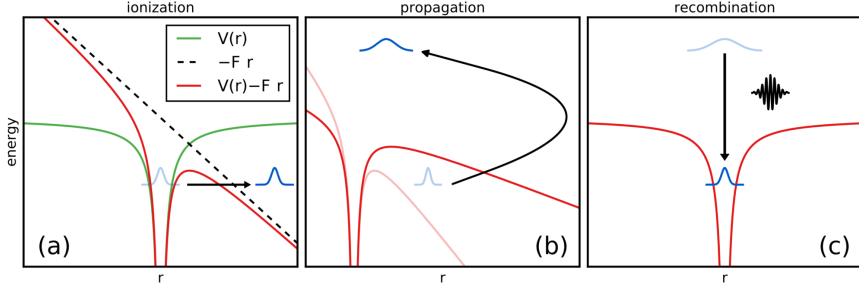


Figure 1.4: The three step model of HHG. Figure adapted from [5].

field after interacting with a medium. Rather than providing a first principles discussion of HHG, the main objective of this section is to understand how we can produce bright attosecond XUV light pulses with a sufficient spectral coverage for use in an ATAS experiment.

We consider the case of an atom in strong laser field, where the electric field of the laser is comparable to the Coulomb field of the parent atom. Under these conditions, there is an appreciable chance of ionization. To determine which physical process is responsible for the ionization, we must consider two energy scales: the ionization potential of the atom I_p and the *ponderomotive energy* of a free electron in a field U_p :

$$U_p = \frac{q_e^2 F_0^2}{4m_e \omega^2} \propto I_0 \lambda^2 \quad (1.1)$$

where m_e is the electron mass, q_e is the electron charge, ω is the frequency, F_0 is the electric field strength, I_0 is the intensity, and λ is the wavelength of the laser. A more convenient form of Eq. (1.1) is given below:

$$U_p [\text{eV}] = (9.33738 \times 10^{-5}) \times I_0 [\text{GW/cm}^2] \times (\lambda [\mu\text{m}])^2 \quad (1.2)$$

The Keldysh parameter γ compares the magnitudes of these two energy scales [29]:

$$\gamma = \sqrt{\frac{I_p}{2U_p}} \quad (1.3)$$

The value of γ determines the physical mechanism responsible for ionization. When $\gamma \gg 1$, we are in the multi-photon ionization (MPI) regime; $\gamma \leq 1/2$ corresponds to tunnel ionization, and $\gamma \ll 1$ corresponds to over the barrier (OTB) ionization. For the moment we will restrict our discussion to the tunneling regime, the regime in which HHG occurs.

1.3.1 Single Atom Response

We start with a microscopic picture of harmonic generation, focusing on the interaction between a single atom and the laser field. In the early 1990s, a semi-classical model was developed to describe the process of HHG [30, 31]. Figure 1.4 shows the three steps: tunnel ionization, classical propagation in the vacuum, and recombination of the electron and the parent ion. At recombination, the excess energy gained during the laser-driven propagation step is released as a high-energy photon. This very simple model is capable of reproducing the essential behavior of HHG and has the benefit of being readily interpretable. In the following subsections, we will present relevant details about this model.

Strong Field Ionization

In the three step model, the laser's electric field strength is on the order of the atomic potential that binds the electron to its parent atom. Consequently, the valence electron's wavepacket evolves subject to the sum of the shielded Coulomb field and the spatially varying laser field. In this configuration, the electron can tunnel out of the distorted Coulomb field, as shown in the left panel of Fig. 1.4. This step is most likely to occur at the peak of the field, which occurs every half-cycle of the laser period.

The DC-ionization rate from the ground state in the tunneling regime is best described by an analytical formula first derived by Ammosov, Delone & Krainov in 1986 [24, 32, 33]. Their formula is the limit $\omega \rightarrow 0$ of a more general expression for ionization in an alternating field developed by Perelelmov, Popov & Terent'ev (PPT) [34], and is therefore frequency (wavelength) independent. The resulting equation bears their names (ADK):

$$(\text{atomic u.}) \quad w_{ADK}(F) = c_{n^*l^*}^2 f(l, m) I_p \left(\frac{2F_0}{F} \right)^{2n^*-|m|-1} \exp \left(-\frac{2F_0}{3F} \right) \quad (1.4)$$

with²

$$c_{n^*l^*}^2 = \frac{2^{2n^*}}{n^* \Gamma(n^* + l^* + 1) \Gamma(n^* - l^*)}, \quad (1.5)$$

$$f(l, m) = \frac{(2l+1)(l+|m|)!}{2^{|m|}(|m|)! (l-|m|)!}, \quad (1.6)$$

$$F_0 = \sqrt{2I_p}, \quad (1.7)$$

$$n^* = \frac{1}{\sqrt{2I_p}}, \quad (1.8)$$

$$l^* = n^* - 1. \quad (1.9)$$

In the above equations, Γ is the Gamma function; F is the field amplitude; I_p is the

²Some authors use the notation G_{lm} in lieu of $f(l, m)$.

atom	I_p [eV]	I_p [at. u.]	l	m	F_0 [at. u.]	F_b [at. u.]	$c_{n^*l^*}^2$	$f(l, m)$
He	24.5874	0.90357	0	0	2.42946	0.20412	4.25575	1
Ne	21.5645	0.792481	1	0	1.99547	0.15702	4.24355	3
Ar	15.7596	0.579155	1	0	1.24665	0.08386	4.11564	3
Kr	13.9996	0.514476	1	0	1.04375	0.06617	4.02548	3
Xe	12.1298	0.445762	1	0	0.84187	0.04968	3.88241	3

Table 1.1: ADK parameters [17].

ionization potential; l and m are the orbital and magnetic quantum numbers of the valence electron, respectively; n^* is the effective quantum number and l^* is the effective orbital quantum number. Note that the above expressions are given in atomic units and are valid when $\gamma < 0.5$. The ADK parameters for atoms commonly used for HHG are listed in Table 1.1.

If the laser field is strong enough, the Coulomb field will be suppressed below the initial state and the electron can classically ionize without tunneling. This ionization channel is called *over the barrier* or *barrier suppression* ionization. At this point the ADK formula breaks down. The field strength at which the laser field is equal to the Coulomb field is:

$$F_b = \frac{I_p^2}{4} \quad (1.10)$$

Tong and Lin introduced an empirical correction to the ADK formula to model the barrier suppression regime [35]:

$$w_{OTB}(F) = w_{ADK}(F) \exp\left(-\frac{2\alpha Z_c^2}{\sqrt{F_0}} F\right) \quad (1.11)$$

where α is an experimentally derived correction factor and $Z_c = 1$ for neutral atoms. The cycle averaged ADK rate is:

$$\bar{w}_{ADK}(F) = \sqrt{\frac{2}{\pi}} \sqrt{\frac{3F}{2(2I_p)^{3/2}}} w_{ADK}(F) \quad (1.12)$$

In the above equations, the ionization rate is expressed as a rate per atomic unit of time. Conversions to experimentally convenient units are given below:

$$F \text{ [at. u.]} = \sqrt{\frac{I \text{ [W/cm}^2\text{]}}{3.55 \times 10^{16}}} \quad (1.13)$$

$$w_{ADK} \text{ [at. u.]} = \frac{w_{ADK} \text{ [1/s]}}{41.341 \times 10^{15}} \quad (1.14)$$

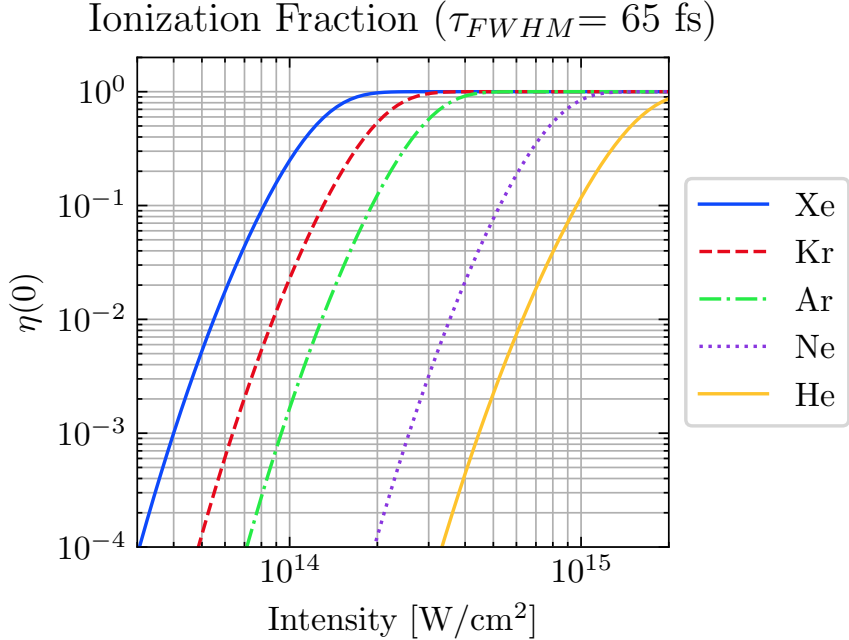


Figure 1.5: Ionization fraction at the peak of a 65 fs pulse ($t = 0$), calculated using the cycled-averaged OTB-corrected ADK rate.

The fraction of atoms ionized by time t is found by integrating the rate of ionization:

$$\eta(t) = 1 - \exp \left[- \int_{-\infty}^t w(t') dt' \right] \quad (1.15)$$

The ionization fraction for a 65 fs pulse using Eqs. (1.11) and (1.15) is shown in Fig. 1.5 for various generating media.

Propagation and Recombination

The recently liberated electron is assumed to be born with zero initial kinetic energy. It accelerates in the oscillating laser field, gaining kinetic energy along the way, as shown in the central panel of Fig. 1.4. Its kinetic energy is proportional to the cycle-averaged quiver energy U_p .

The birth phase of the electron (relative to the laser period) determines its classical trajectory. Some electrons will be driven away from the parent ion, never to return; some will be driven back to the birth location, where they can scatter off of, miss, or recombine with the parent ion. We will only concern ourselves with those electrons that recombine (right panel of Fig. 1.4). Upon recombination, the electron will emit a photon of energy $I_p + KE$, where I_p is the ionization potential of the atom and KE is the kinetic energy acquired during the propagation step. A classical analysis of the electron propagation

reveals that the maximum kinetic energy such an electron can gain is $3.17U_p$, and therefore the maximum photon energy is:

$$E_{\text{cutoff}} = \hbar\omega_{\text{cutoff}} = I_p + 3.17U_p \quad (1.16)$$

This quantity is often called the cutoff energy, and it is proportional to $I_0\lambda^2$. Thus, we can extend the maximum photon energy of the harmonics by increasing either the intensity or the fundamental wavelength of the incident laser pulse.

When increasing the intensity, we will eventually reach an intensity at which the gas is fully ionized by the leading edge of the pulse. The *saturation intensity*, I_s , is defined as the intensity at which the gas medium is 98% ionized at the peak of the pulse ($t = 0$). In this case, only 2% of the gas remains in the ground state for the falling edge of the pulse, which can be neglected for the purposes of HHG. If we assume a sech² pulse and integrate the ADK rate numerically, we can obtain the following expression for I_s [24]:

$$I_s = \frac{1.7I_p^{3.5}}{\left[\ln \frac{0.86c_{n*l*}^2 f(l,m) I_p 3^{2n^* - |m| - 1} \tau_p}{-\ln(1-p_s)} \right]^2} \times 10^{12} \text{ W/cm}^2 \quad (1.17)$$

In Eq. (1.17), I_p is the ionization potential in eV, τ_p is the FWHM pulse duration of a sech² pulse in fs, λ is the fundamental wavelength in μm , and p_s is the ionization probability at the peak of the pulse that defines the saturation of the ionization of the ground state population. We can calculate the corresponding cutoff energy by inserting Eq. (1.17) into Eqs. (1.2) and (1.16):

$$\hbar\omega_c [\text{eV}] = I_p + \frac{0.5I_p^{3.5}\lambda^2}{\left[\ln \frac{0.86c_{n*l*}^2 f(l,m) I_p 3^{2n^* - |m| - 1} \tau_p}{-\ln(1-p_s)} \right]^2} \quad (1.18)$$

We plot the saturation intensity in cutoff energy in Figs. 1.6 and 1.7 for $p_s = 0.98$. In Fig. 1.6, we can see that a shorter pulse allows us to use a significantly higher laser intensity before depleting the ground state, which makes intuitive sense. As will be discussed in Section 2.2, we generate harmonics using a 65 fs pulse, which gives us a saturation intensity of about $2 \times 10^{15} \text{ W/cm}^2$ for helium, $1 \times 10^{15} \text{ W/cm}^2$ for neon, $3.3 \times 10^{14} \text{ W/cm}^2$ for argon, $2.2 \times 10^{14} \text{ W/cm}^2$ for krypton and $1.3 \times 10^{14} \text{ W/cm}^2$ for xenon. These intensities are readily achieved with our Spittfire laser system. In Fig. 1.7, we show the quadratic cutoff energy scaling with respect to wavelength assuming a 65 fs FWHM pulse duration operating at saturation intensity. Furthermore, we see that atoms with higher ionization potentials support a higher cutoff energy, owing mainly to the higher saturation intensity.

Having discussed the limits of intensity scaling, we turn to the complications of wavelength scaling. Unfortunately, the brightness of an individual harmonic order will decrease strongly with increasing wavelength, with the single atom response scaling between λ^{-5} and

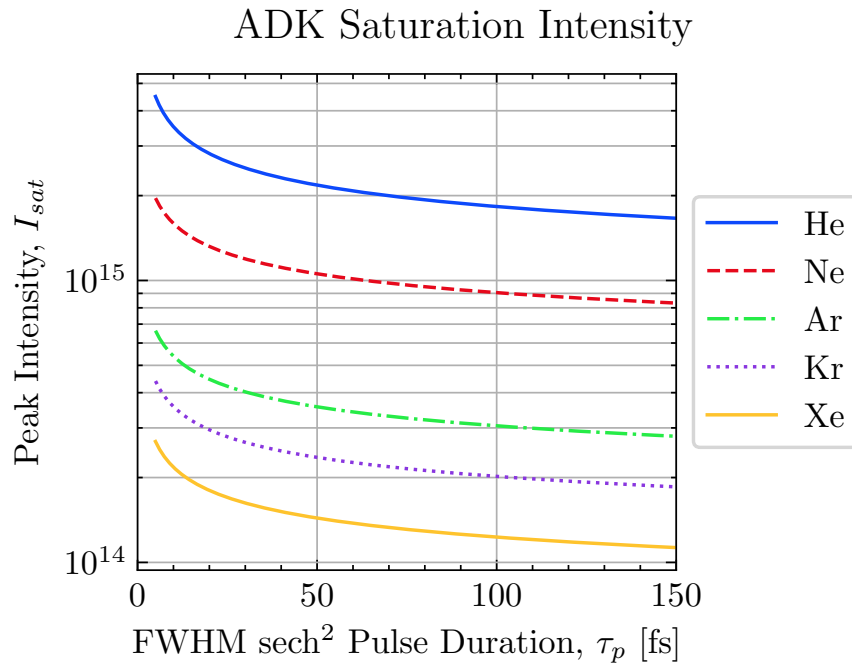


Figure 1.6: ADK saturation intensity for a sech² pulse.

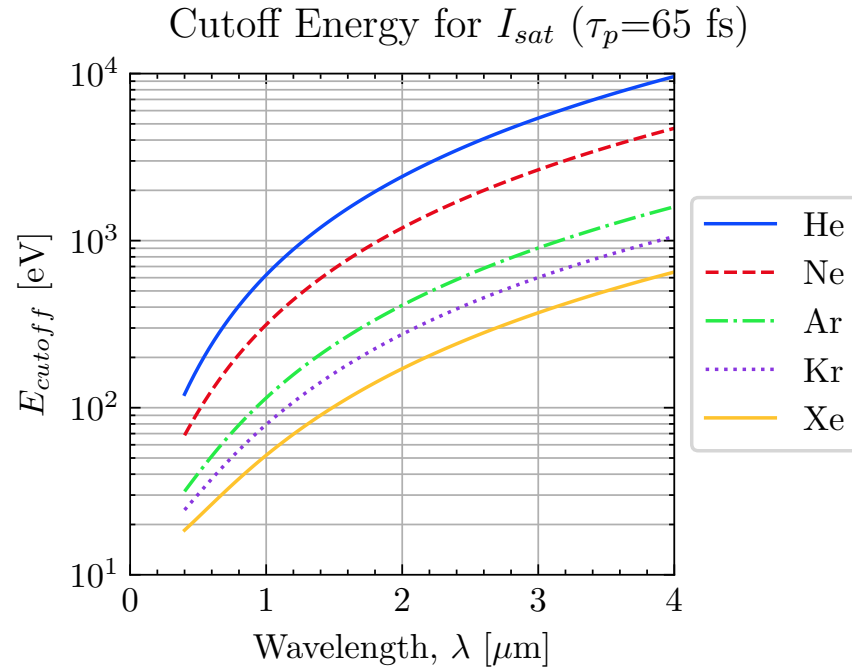


Figure 1.7: High harmonic cutoff energy for a 65 fs FWHM pulse at saturation intensity.

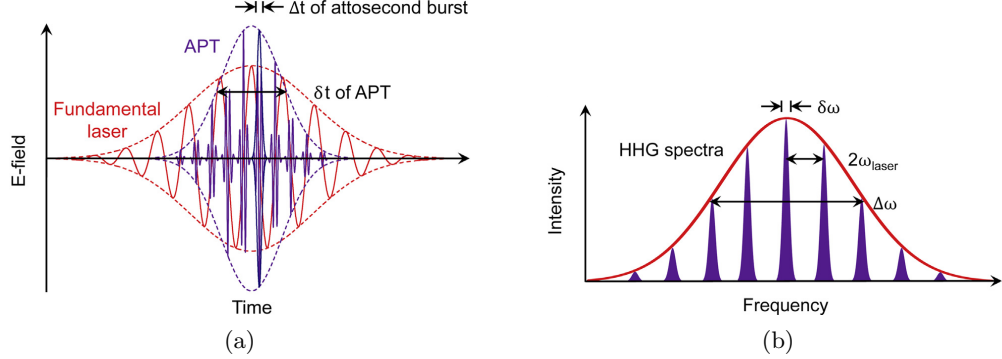


Figure 1.8: Time and frequency domain pictures of HHG. Figure adapted from [6].

λ^{-6} [36–38]. The precise nature of this scaling is beyond the scope of this work and involves the relative contribution of direct and rescattered quantum paths associated with harmonic production. Nevertheless, the reduced quantum efficiency of HHG at longer wavelengths presents a serious technical challenge when performing experiments that require a relatively high XUV flux.

So far, it appears that XUV spectrum is continuous in energy ranging from I_p to $\hbar\omega_{\text{cutoff}}$. This is because we have only been considering the effects of a single-cycle laser pulse. In a multi-cycle pulse, the ionization-propagation-recombination steps will happen twice per pulse (every $T_0/2$ seconds), and each event results in a brief burst of light, as shown in Fig. 1.8a. If we Fourier transform this comb of attosecond pulses, we will get a comb in the frequency domain with separation $2\omega_0$, as shown in Fig. 1.8b. This comb structure can be understood as the result of destructive interference between XUV light emitted every half laser cycle. Thus, we expect to see only odd harmonics of the laser frequency ω_0 .

If we break the symmetry of the generating field, say by introducing a weak second laser wavelength (of frequency 2ω), then this will eliminate half of the interference and allow the production of both even and odd harmonics. This technique is useful when a quasi-continuous spectrum is desired. On the other hand, if could suppress tunnel ionization (or recombination) for all but one burst, we would regain XUV continuum predicted by our single-pulse analysis. This would yield a single *isolated attosecond pulse* (IAP), providing increased temporal resolution. As an added benefit, the continuous spectrum would effectively increase the spectral resolution of our experiment.

1.3.2 Macroscopic Picture

We now zoom out to the macroscopic picture, which encompasses the entire gas-laser interaction volume. In the far field, the radiation from individual atoms will be coherently summed to form an bright XUV light source. The overall efficiency of the HHG process

depends on the phase mismatch Δk of the individual dipoles across the interaction volume. We will see how the phase matching determines optimal interaction pressures for a given driving wavelength. Additionally, we will see the effect of XUV reabsorption by the gas on the overall XUV brightness.

Phase Matching

HHG will be an efficient process if the wave vector mismatch Δk of the independent dipoles is zero. The phase mismatch term can be expressed as four separate factors, each arising from distinct physical phenomena [39]:

$$\begin{aligned}\Delta k &\equiv qk_\omega - k_{q\omega} \\ &= \Delta k_{\text{neutral}} + \Delta k_{\text{plasma}} + \Delta k_{\text{Gouy}} + \Delta k_{\text{dipole}}\end{aligned}\quad (1.19)$$

The first two terms represent the dispersion from the generating neutral atoms and the electron plasma. In the discussion that follows below, we will use the refractive index n at STP (pressure P_0 , number density ρ_0 , temperature T_0), where literature values are readily available. We assume that the index scales linearly with the interaction pressure (density). That is, we assume $n(\rho) = (1 - \eta)(\rho/\rho_0)n(\rho_0)$, where ρ is the interaction density before any atoms are ionized and η is the ionization fraction of the gas medium. For brevity, we will write the index of refraction at standard temperature and pressure (STP) as $n = n(\rho_0)$. Using this notation, the neutral dispersion mismatch term for an interaction density ρ is:

$$\begin{aligned}\Delta k_{\text{neutral}} &= qk_{\text{neutral}}(\lambda_1) - k_{\text{neutral}}(\lambda_q) \\ &= \frac{2\pi q}{\lambda_1}(1 - \eta)\frac{\rho}{\rho_0}\Delta n\end{aligned}\quad (1.20)$$

where we have used $k(\lambda) = \omega n/c = n/(2\pi\lambda)$ and defined Δn as:

$$\Delta n \equiv n_{\text{neutral}}(\lambda_1) - n_{\text{neutral}}(\lambda_q) \quad (1.21)$$

using the notation $\lambda_q \equiv \lambda_1/q$ for the wavelength of the q^{th} harmonic with frequency $\omega_q \equiv q\omega$ and λ_1 (ω_1) for the laser wavelength (frequency). To compute the plasma mismatch term, we start with the refractive index of a plasma:

$$n_{\text{plasma}}(\omega) = \sqrt{1 - \frac{\omega_p^2}{\omega^2}} \approx 1 - \frac{\omega_p^2}{2\omega^2} \quad (1.22)$$

$$\omega_p = \sqrt{\frac{e^2 \rho_e}{\epsilon_0 m_e}} \quad (1.23)$$

where ω_p is the plasma frequency and $\rho_e = \eta\rho$ is the plasma density. Then, the phase mismatch of the plasma is:

$$\begin{aligned}
\Delta k_{\text{plasma}} &= qk_{\omega_1} - k_{q\omega_1} \\
&= \frac{q}{2\pi\lambda_1}(n_{\text{plasma}}(\omega_1) - n_{\text{plasma}}(\omega_q)) \\
&= -\frac{1}{4\pi\lambda_1}\frac{q^2-1}{q}\frac{\omega_p^2}{\omega_1^2} \\
&\approx -\frac{q}{4\pi\lambda_1}\frac{\omega_p^2}{\omega_1^2} \quad (\text{for large } q) \\
&= -q\eta\rho r_e \lambda_1
\end{aligned} \tag{1.24}$$

Where r_e is the classical electron radius:

$$r_e = \frac{1}{4\pi\epsilon_0} \frac{e^2}{m_e c^2} \tag{1.25}$$

Note that since $\Delta n > 0$ for the wavelengths of interest, we have $\Delta k_{\text{plasma}} \leq 0$. Adding the two dispersive terms together, we get an expression for the dispersive phase mismatch terms:

$$\Delta k_{\text{neutral}} + \Delta k_{\text{plasma}} = \frac{2\pi q}{\lambda_1}(1-\eta)\frac{\rho}{\rho_0}\Delta n - q\eta\rho r_e \lambda_1 \tag{1.26}$$

Inspection of Eq. (1.26) reveals that there exists a *critical ionization fraction* η_c for which the dispersive phase terms sum to zero:

$$\eta_c \equiv \left(1 + \frac{\rho_0 r_e \lambda_1^2}{2\pi \Delta n}\right)^{-1} \tag{1.27}$$

We can rewrite Eq. (1.26) using η_c :

$$\Delta k_{\text{neutral}} + \Delta k_{\text{plasma}} = \frac{2\pi q \Delta n}{\lambda_1} \frac{\rho}{\rho_0} \left(1 - \frac{\eta}{\eta_c}\right) \tag{1.28}$$

The critical ionization fraction for helium and argon is shown in Fig. 1.9. Note that for $\eta < \eta_c$, the dispersive mismatch term is positive. We will see below that at the MIR focus, phase matching ($\Delta k = 0$) is impossible for $\eta > \eta_c$.

The third term of Eq. (1.19) is the geometrical phase mismatch caused by focusing:

$$\begin{aligned}
\Delta k_{\text{Gouy}} &= \frac{\partial}{\partial z} \left[q \arctan \left(\frac{2z}{b_1} \right) - \arctan \left(\frac{2z}{b_q} \right) \right] \\
&= q \frac{2b_1}{b_1^2 + 4z^2} - \frac{2b_q}{b_q^2 + 4z^2} \\
&\approx -(q-1) \frac{2b_1}{b_1^2 + 4z^2}
\end{aligned} \tag{1.29}$$

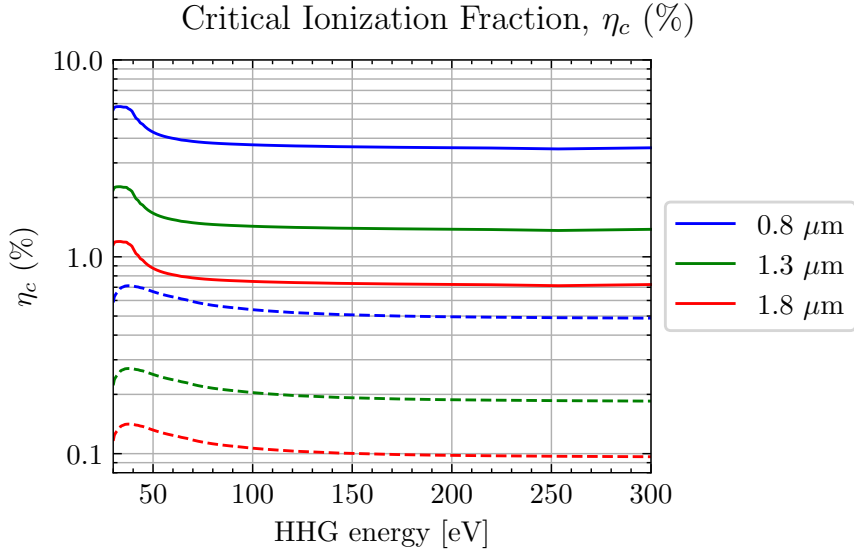


Figure 1.9: The critical ionization fraction, η_c for argon (solid lines) and helium (dashed lines) at different fundamental wavelengths. Refractive index information from [7–9].

where $b_1 = 2z_R$ is the confocal parameter and z_R is the Rayleigh range. For the q^{th} harmonic, we assume the nonlinear process obeys a power law p and $b_q = b_1 p/q$ [5]. Note that Δk_{Gouy} is negative for all values of z .

The fourth term arises from the intensity-dependent dipole phase acquired during the electron excursion [40–42]:

$$\Delta k_{\text{dipole}} = -\alpha_q \frac{\partial I}{\partial z} \quad (1.30)$$

The value of α_q depends on the quantum trajectory the electron takes during its excursion. For short trajectories, $\alpha_q = 2 \times 10^{-14} \text{ cm}^2/\text{W}$ and for long trajectories, $\alpha_q = 22 \times 10^{-14} \text{ cm}^2/\text{W}$ [43, 44]. The sign of Δk_{dipole} is positive (negative) if the gas source is located upstream (downstream) of the focus.

Experimentally, the phase matching can be adjusted by tuning the laser parameters (wavelength λ , intensity I , pulse duration, focal spot size w_0), the gas species (I_p , n and k) and interaction pressure p , and the gas location relative to the laser focus (z). Additionally, a variable aperture (iris) located just before the generation lens effectively tunes multiple laser parameters simultaneously, and is known colloquially as “the magic iris trick” [45]. Because Δk is dependent on the harmonic order q , it is impossible to perfectly phase match the entire harmonic spectrum simultaneously. As a result, we adjust the phase matching parameters to optimize the useful part of the harmonic spectrum, usually at the expense of the rest of the spectrum.

Also note that the dispersive terms phase can be controlled by tuning the interaction

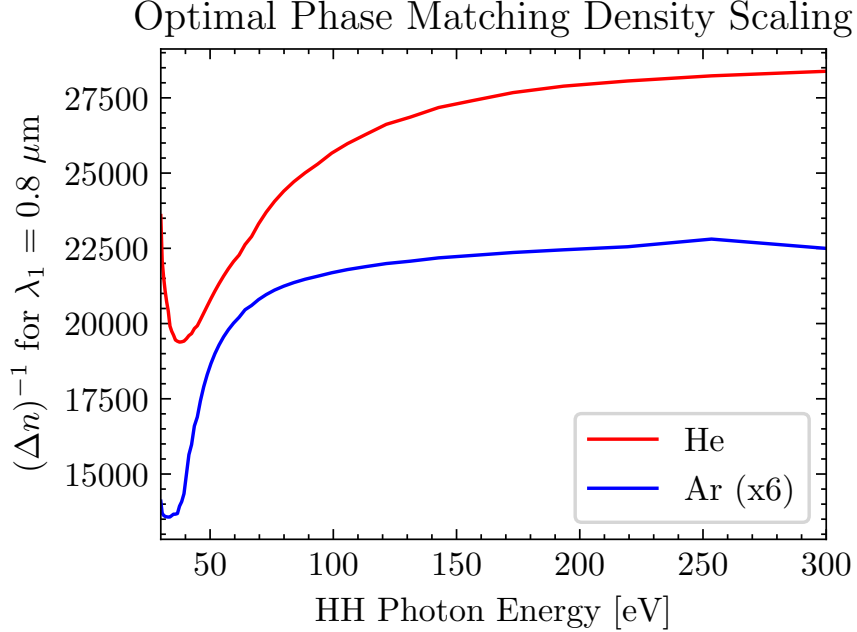


Figure 1.10: The optimal phase matching density, ρ_{opt} is inversely proportional to the refractive index mismatch, Δn (Eqs. (1.21) and (1.31)). As a result, higher interaction pressures are needed to properly phase match higher photon energies. The data shown is for a fundamental wavelength of 800 nm, but the same trend holds for $\lambda_1 = 0.4 - 2.0 \mu\text{m}$. Argon's behavior above 250 eV is due to the $L_{2,3}$ absorption edge. Refractive index data from references [7–9].

pressure p , while the other terms are (to first order) pressure independent. If we place the gas medium at the focus, $\Delta k_{\text{dipole}} = 0$, and $\Delta k_{\text{Gouy}} = -(q - 1)\lambda/(\pi w_0^2)$. In this case, the condition $\Delta k = 0$ can be met by setting to the density to the *optimal phase matching density* ρ_{opt} [39, 46]:

$$\frac{\rho_{opt}}{\rho_0} = \left(\frac{q-1}{q} \right) \frac{2\lambda^2}{\Delta n w_0^2 \left(1 - \frac{\eta}{\eta_c} \right)} \quad (1.31)$$

We therefore arrive at the conclusion that the optimal phase matching density scales with the square of the fundamental wavelength. Furthermore, tighter focusing ($w_0 \rightarrow 0$) and higher ionization fractions ($\eta \rightarrow \eta_c$) require higher densities to achieve good phase matching. Finally, the optimal phase matching density is inversely proportional to the refractive index mismatch, Δn . This quantity is shown in Fig. 1.10 for helium and argon at $\lambda_1 = 800 \text{ nm}$. From this figure, we can see that higher photon energies require higher interaction pressures. Therefore, creating bright harmonics at high photon energies from a long wavelength, relatively weak pulse requires significantly higher interaction pressures than low energy harmonics generated with a loosely focused 800 nm pulse. This is the

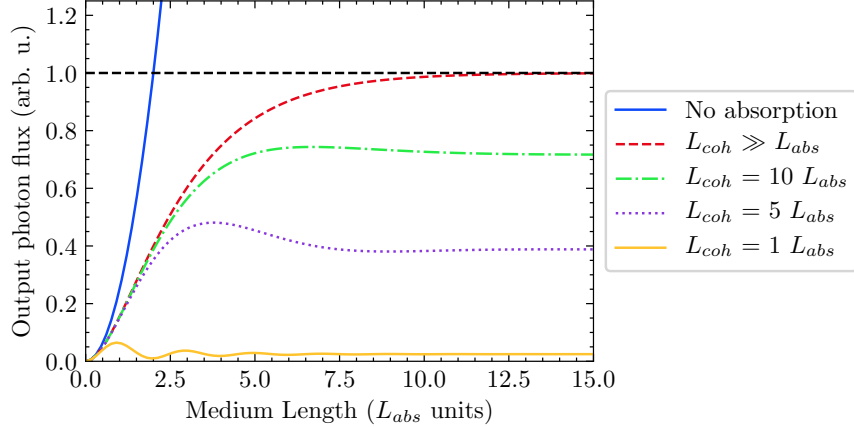


Figure 1.11: 1D absorption model from Eq. (1.33).

primary motivation for designing a vacuum system and gas source that can deliver high interaction pressures (see Section 3.2).

XUV Reabsorption

We now consider the effects of XUV absorption on the phase matching process using the 1-dimensional model introduced by Constant et. al. [47]. In doing so, we restrict ourselves to the on-axis emission of the q^{th} harmonic. That is, we consider only harmonics with a wave vector k_q that is collinear to the fundamental (k_0). In this case, the number of photons emitted per unit time and area is:

$$N_{\text{out}} = \frac{\omega_q}{4c\epsilon_0\hbar} \left| \left[\int_0^{L_{\text{med}}} dz \rho(z) A_q(z) \exp\left(-\frac{L_{\text{med}} - z}{2L_{\text{abs}}}\right) \exp(i\varphi_q(z)) \right] \right|^2 \quad (1.32)$$

Here, $\rho(z)$ is the gas medium density, $A_q(z)$ is the amplitude of the harmonic response at frequency ω_q and φ_q is its phase at the exit of the medium, which has length L_{med} . If we are using a loose focusing geometry, then the gas density and harmonic response amplitude are constant along the interaction volume: $\rho(z) = \rho$ and $A_q(z) = A_q$. With this restriction, Eq. (1.32) evaluates to:

$$N_{\text{out}} = \rho^2 A_q^2 \frac{4L_{\text{abs}}^2}{1 + 4\pi^2(L_{\text{abs}}^2/L_{\text{coh}}^2)} \left[1 + \exp\left(-\frac{L_{\text{med}}}{L_{\text{abs}}}\right) - 2 \exp\left(\frac{\pi L_{\text{med}}}{L_{\text{coh}}}\right) \exp\left(-\frac{L_{\text{med}}}{2L_{\text{abs}}}\right) \right] \quad (1.33)$$

Here, we use the notation $L_{\text{coh}} = \pi/\Delta k$ for the coherence length ($\Delta k = k_q - qk_0$) and $L_{\text{abs}} = 1/\sigma\rho$ for the absorption length.

Equation (1.33) is plotted in Fig. 1.11. In the limit of good phase matching ($L_{\text{coh}} \gg$

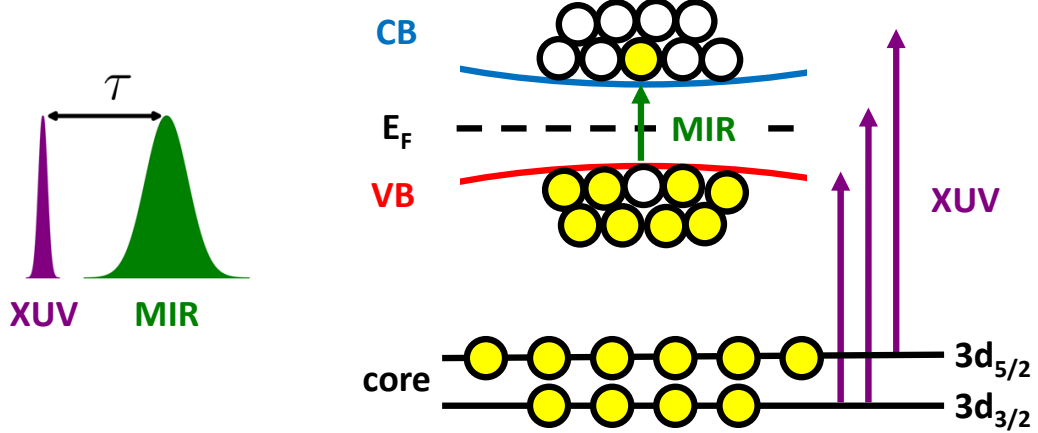


Figure 1.12: Cartoon illustrating ATAS in a semiconductor. The MIR pulse induces electron dynamics in conduction (CB) and valence bands (VB) near the Fermi energy (E_F), and the XUV pulse induces electron transitions between the core and VB/CB. Shown here are the orbitals $3d_{3/2}$ and $3d_{5/2}$, which serve as the initial states for M_4 - and M_5 -edge absorption, respectively.

L_{abs}), short interaction length ($L_{\text{coh}} \gg L_{\text{med}}$) and low absorption ($L_{\text{med}} \gg L_{\text{abs}}$) the harmonic yield is proportional to [48]:

$$N_{\text{out}} \sim A_q^2 z_0 (\rho L_{\text{med}})^2 \sim S_{\text{spot}} (PL_{\text{med}})^2 \quad (1.34)$$

where $z_0 = \pi w_0^2 / \lambda_1$ is the Rayleigh length and $S_{\text{spot}} = \pi w_0^2$ is the spot area at the focus. In this limit, the photon yield is proportional to the square of the pressure-length product. Otherwise, the optimized conditions are $L_{\text{med}} > 3L_{\text{abs}}$ and $L_{\text{coh}} > 5L_{\text{abs}}$.

Experimentally, L_{med} is fixed by the geometry of the gas source, L_{abs} is directly controlled by adjusting the backing pressure, and L_{coh} is indirectly controlled by other parameters (gas source position relative to focus, focusing conditions, iris diameter, etc.). Therefore, if we can increase the pressure-length product while maintaining favorable coherence lengths, we should be able to increase the harmonic yield to partially compensate for the quantum losses of longer fundamental wavelength. In Section 3.2, we will apply this simple model to the gas sources available in our lab to maximize our HHG yield.

1.4 Attosecond Transient Absorption Spectroscopy (ATAS)

1.4.1 Overview

Attosecond transient absorption spectroscopy (ATAS) is a pump-probe technique that measures the spectral response of a sample following interaction with an attosecond XUV pulse and a femtosecond visible / near-infrared / mid-infrared pulse. Experimentally, this means

placing a sample at the combined XUV-MIR focus in a transmission (normal) geometry. An XUV photon spectrometer is placed behind the sample and the transmitted XUV spectrum S is measured as a function of XUV-MIR delay τ (the MIR light is not measured). In the present work, we use the convention that $\tau > 0$ when the MIR pulse precedes the XUV pulse, which means the MIR field is the pump and the XUV is the probe. Typically, the XUV pulse is very weak and we only consider linear (first order) interactions; the VIS/MIR pulse can induce a linear or nonlinear response.

Unlike a gas phase sample, condensed phase samples do not have sharp atomic resonances with long dephasing times [49]. Therefore, the measured response is zero when the XUV pulse precedes the MIR pulse ($\tau < 0$). When $\tau > 0$, the pulse sequence interrogates the population dynamics of the system in response to an MIR-induced excitation. This process is shown schematically Fig. 1.12 for a semiconductor. Here, the MIR field (green arrow) excites electrons across the bandgap³ from valence band (VB) to the conduction band (CB). This leaves behind a transient hole in the VB (empty circle) and a transient electron in the CB (filled circle).

The experiment is engineered so that part of the XUV spectrum is resonant with transitions between core shell states and the valence/conduction bands. These transitions correspond to photon energies between 20 and a few hundred electron volts, depending on the material and the initial state. Due to electron screening, the core states are effectively shielded from the external MIR field. Since the XUV field is weak, we only need to consider linear absorption, which is due to the imaginary part⁴ of the linear dielectric function, ϵ [50]:

$$\text{Im} [\epsilon(\omega)] = 8 \left(\frac{\pi e}{m\omega} \right)^2 \sum_{i,f} |P_{f,i}|^2 J_{f,i}(\omega_{f,i}). \quad (1.35)$$

Here, e is the electron charge, m is the electron mass, $P_{f,i}$ is the transition matrix dipole element between the initial and final states, $J_{f,i}$ is the joint density of states, $\hbar\omega_{f,i}$ is the energy between the initial and final states, f runs over all unoccupied states near the Fermi energy, and i runs over all core states. We can see that the XUV transmission is sensitive to both state blocking (via the joint density of states) and renormalization of the inner core hole potential (via both the transition matrix element and the joint density of states). This observation justifies the decomposition of the measured signal into two constituent parts, as will be discussed in Section 4.5.3.

The energy required to transition between a core and valence state depends on the underlying atomic structure. Since each element has a unique spectral signature, ATAS provides elemental specificity. This can be exploited to track the movement of electrons between bonds or across simple heterostructures [51, 52].

³Note the MIR excitation can correspond to linear or nonlinear absorption, as well as direct or indirect transitions.

⁴Neglecting the real part of ϵ is justified in Section 1.4.2.

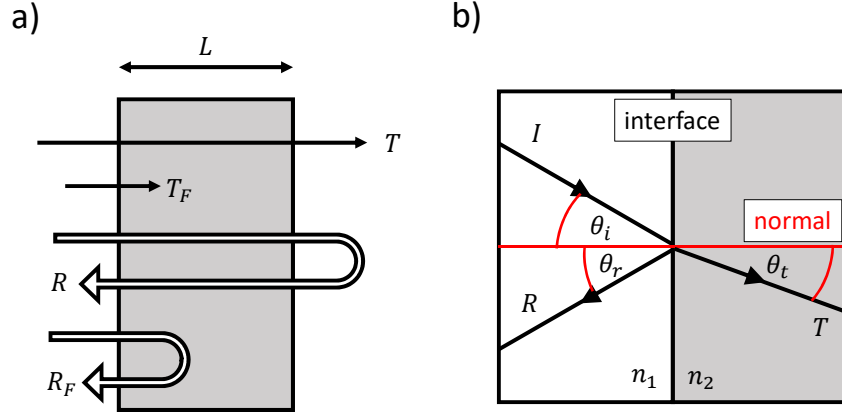


Figure 1.13: Normal and non-normal incident geometries. a) Normal incidence geometry showing Fresnel coefficients R_F , T_F for interfaces and total transmission T and reflectance R for a slab of thickness L . Figure recreated from [10]. b) Non-normal geometry showing definitions of angles θ_i , θ_r and θ_t with respect to each interface.

1.4.2 Experimental Geometry: Real and Imaginary Parts of \tilde{n}

In this section we will show why an ATAS experiment in normal geometry measures only the imaginary part of the refractive index, which was implicitly assumed in Eq. (1.35). To do so, we compare the relative contributions of the real and imaginary parts of \tilde{n} to the absorption losses in two thin film materials, germanium and silicon. In contrast, when the experiment is performed in a reflection geometry the signal will be sensitive to both parts of the complex index; this technique is called *attosecond transient reflection-absorption spectroscopy* (ATRAS). Recent examples of this technique can be found in the literature [50, 53].

In a transient absorption experiment, we measure the transmission T of a sample in response to excitation by an external field. Generally speaking, T depends on both parts of the complex refractive index: $\tilde{n} = n + ik$. However, in a normal transmission geometry it turns out that the contribution of $\text{Im}(\tilde{n})$ dominates the measured signal, and to a good approximation the role of $\text{Re}(\tilde{n})$ can be ignored. Note that in a non-normal reflection geometry, both parts of \tilde{n} make significant contributions to the measured signal. In the following discussion we will analyze the Fresnel equations to see why this is the case. This section will draw from arguments made in Reference [10].

First, we consider the normal geometry shown in the left panel of Fig. 1.13. We write the complex index of refraction in the following form:

$$\begin{aligned}\tilde{n} &= n - ik \\ &= (1 - \delta) - i\beta\end{aligned}\tag{1.36}$$

The Fresnel coefficients R_F and T_F describe the interface reflectance and transmittance and depend on both parts of the complex index \tilde{n} . For normal incidence, they are:

$$R_F = \left| \frac{n - ik - 1}{n - ik + 1} \right|^2$$

$$T_F = \frac{4n}{|n - ik + 1|^2}$$
(1.37)

Absorption in the bulk is described via the absorption length α :

$$\alpha = 4\pi k/\lambda$$
(1.38)

Ignoring interface effects, the transmission through the bulk is:

$$T_{\text{bulk}} = \exp(-\alpha L)$$
(1.39)

Note that α and T_{bulk} only depend on k .

The total reflectance R and transmission T are the result of interface effects plus bulk effects. We must consider the case where the detected light is the result of multiple reflections within the sample. Neglecting interference, we consider the case of $2N$ bounces where the laser's coherence length is less than the thickness of the bulk. In this case, the sum is incoherent with the expressions for T and R given by:

$$R = R_F + R_F T_F^2 T_{\text{bulk}}^2 \sum_{m=0}^N [R_F T_{\text{bulk}}]^{2m}$$

$$T = T_F^2 T_{\text{bulk}} \sum_{m=0}^N [R_F T_{\text{bulk}}]^{2m}$$
(1.40)

For the case of an infinite number of bounces, Eq. (1.40) simplifies to:

$$R = R_F + \frac{R_F T_F^2 T_{\text{bulk}}^2}{1 - R_F^2 T_{\text{bulk}}^2}$$

$$T = \frac{T_F^2 T_{\text{bulk}}}{1 - R_F^2 T_{\text{bulk}}^2},$$
(1.41)

whereas if only a single bounce occurs, Eq. (1.40) reduces to:

$$R = R_F + R_F T_F^2 T_{\text{bulk}}^2$$

$$T = T_F^2 T_{\text{bulk}}$$
(1.42)

We now consider the fractional error introduced by ignoring the interface effects described by T_F and R_F . That is, what would happen if we assume that the interfaces have no effect on the transmitted intensity? We introduce the relative error ϵ made by ignoring

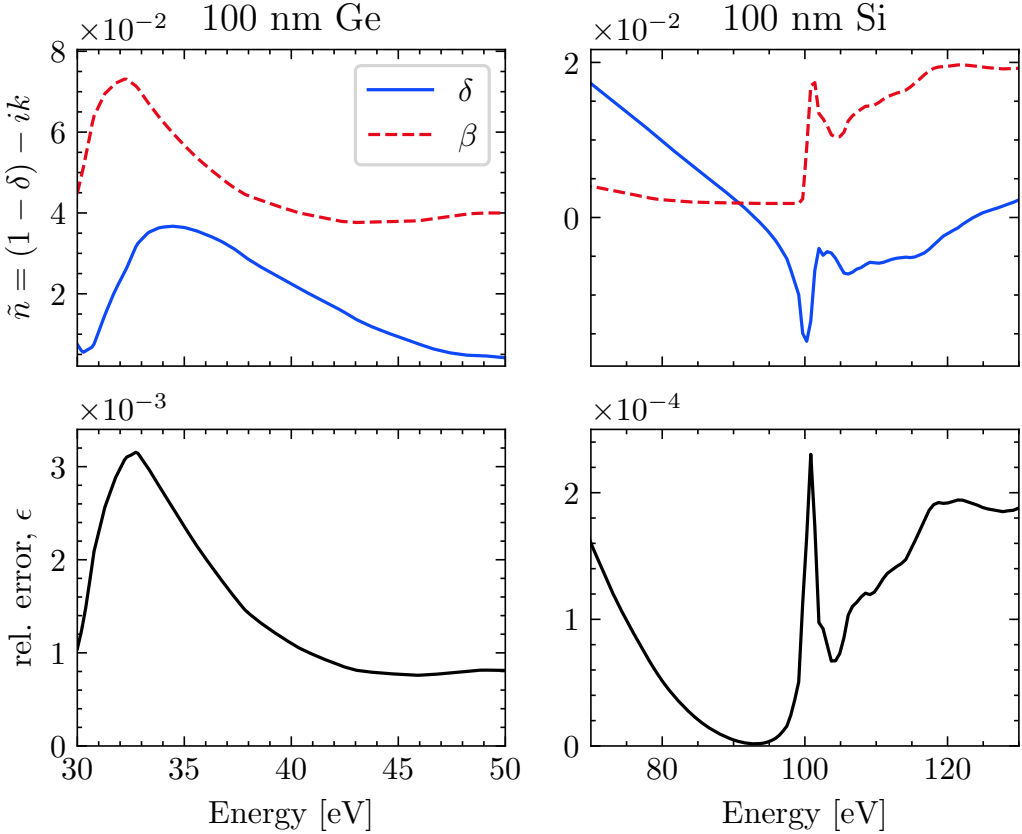


Figure 1.14: Consequences of ignoring the real part of \tilde{n} when calculating the transmission T of germanium (left) and silicon (right). Top panels: complex refractive index. The Ge M -edge absorption feature is visible near 30–35 eV, and the Si L -edge is near 100 eV. Data from [7]. Bottom panels: relative error in T , as defined in Eq. (1.43), introduced by ignoring the contribution of $\text{Re}(\tilde{n})$. An infinite number of bounces (Eq. (1.41)) is assumed.

the Fresnel coefficients of Eq. (1.41):

$$\epsilon \equiv \frac{T_{\text{bulk}}}{T} - 1 \quad (1.43)$$

As an example, consider a 100 nm thick Ge sample measured in transmission near the Ge M -edge (about 30 eV), as shown in Fig. 1.14. The relative error is in the range of a few parts in 10^3 , well below our experimental detection limit. Silicon was chosen due to its data availability above and below the absorption edge, but this behavior should hold for all materials in normal transmission.

The real part of the complex index becomes important when the sample isn't normal to the beam, as shown in the right panel of Fig. 1.13. In this case, the Fresnel equations are

a bit messier:

$$\begin{aligned} R_s &= \left| \frac{\tilde{n}_1 \cos \theta_i - \tilde{n}_2 \cos \theta_t}{\tilde{n}_1 \cos \theta_i + \tilde{n}_2 \cos \theta_t} \right|^2 \\ R_p &= \left| \frac{\tilde{n}_1 \cos \theta_t - \tilde{n}_2 \cos \theta_i}{\tilde{n}_1 \cos \theta_t + \tilde{n}_2 \cos \theta_i} \right|^2 \\ T_s &= 1 - R_s \\ T_p &= 1 - R_p \end{aligned} \tag{1.44}$$

Here, the subscripts s and p denote the polarization relative to the surface normal. For a sample in vacuum, $\tilde{n}_1 = 1$ and \tilde{n}_2 is the index of the sample. We can extract the relevant physics without any additional manipulation of Eq. (1.44). Right away, we can see that unlike Eq. (1.37), Eq. (1.44) is symmetric in the real and imaginary parts of the sample's complex index, \tilde{n}_2 . In the limit of a thick slab, ($L \gg \alpha$), the light is attenuated before it can reflect off the back surface and we have $T \rightarrow 0$ and $R \rightarrow R_{s,p}$. That is, the only contributions to the reflected intensity are from the interface and possibly the sample volume within $z \approx 1/\alpha$ of the interface. As a result, both parts of \tilde{n}_2 will make significant contributions to the reflected intensity. This geometry is common in transient reflection-absorption experiments [50, 53].

1.5 MIR Beam Shaping Using a Binary Phase Mask

In some experiments, we use a phase mask to shape the MIR beam profile at the focus. We have used two types of phase masks: a binary phase mask and a phase grating. In this document, we will restrict our discussion to the binary phase mask; see Stephen Hageman's dissertation [54] and Reference [55] for details about the phase grating. As will be shown below, a binary phase mask converts a TEM_{00} mode into a TEM_{01} -like mode at the focus [14, 54–57]. The two MIR spots are phase-locked to each other with a phase difference of π (the phase difference is tunable if using a phase grating). If the beam is focused onto a gas plume, each intensity lobe will locally drive HHG, and the harmonics will spatially interfere in the far-field. Below, we will show how a binary phase plate can produce a TEM_{01} -like mode at the focus.

The binary phase plate is a planar transmissive optic with a thickness step of size h at its center. Light passing through the thicker half of the plate experiences a phase shift of ϕ relative to the light transmitted through the thinner half of the plate:

$$\phi = 2\pi h(n - 1)/\lambda \tag{1.45}$$

where n is the refractive index of the glass. Ignoring Fresnel losses and material absorption,

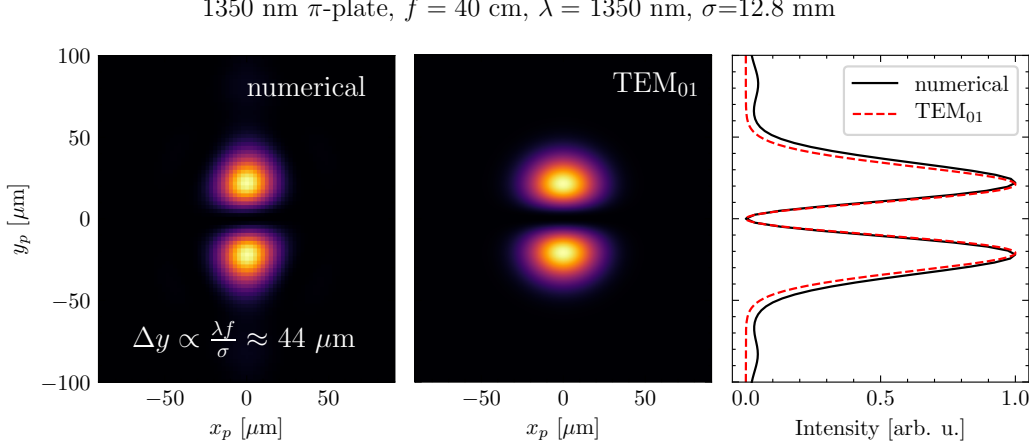


Figure 1.15: Calculated intensity pattern of the MIR beam at the focus after passing through a centered π -plate using two different methods. Left panel: numerical evaluation of the intensity (modulus squared of Eq. (1.48) using Eq. (1.49)) and a measured input laser beam profile. Middle panel: intensity profile of an equivalent TEM_{01} mode (Eq. (1.52)). Right panel: intensity lineouts at $x_p = 0$ comparing the numerical result to the TEM_{01} approximation.

the phase plate has a complex transmittance, τ_{pp} :

$$\tau_{pp}(x, y) = \begin{cases} 1, & \text{for } y > y_0, \\ \exp(-i\phi), & \text{for } y \leq y_0. \end{cases} \quad (1.46)$$

The parameter y_0 denotes the position of the phase step relative to the optical axis. We use a plate that has been manufactured with $\phi = \pi$ for $\lambda = 1350$ nm. Immediately after the phase plate, we place a lens of focal length f , which imparts an approximately quadratic phase onto the beam. The complex transmittance of the lens is given by τ_L [58]:

$$\tau_L = \exp\left(-\frac{k}{2f}(x^2 + y^2)\right) \quad (1.47)$$

We will use scalar diffraction theory to evaluate the electric field at a point $P = (x_p, y_p, z_p)$ located downstream of the phase plate [59]:

$$E(x_p, y_p, z_p) = \frac{i}{\lambda} \int_{+\infty}^{-\infty} \int_{+\infty}^{-\infty} \tau_L(x, y) \tau_{pp}(x, y) E_{in}(x, y) \frac{e^{-ikr}}{r} dx dy \quad (1.48)$$

where $E_{in}(x, y)$ is the input electric field at the phase plate and r is the radial coordinate:

$$r = \sqrt{(x_p - x)^2 + (y_p - y)^2 + z_p^2}$$

We apply the Fresnel and the paraxial approximations,

$$\frac{e^{-ikr}}{r} \approx \frac{1}{z_p} \exp \left[-ik \left(z_p + \frac{(x_p - x)^2 + (y_p - y)^2}{2z_p} \right) \right] \quad (1.49)$$

which is valid if P is close to the optical axis. Using this approximation, Eq. (1.48) was numerically integrated and evaluated at the focus [60]. E_{in} was calculated by imaging the TOPAS signal beam using a thermal camera and scaling it by the magnification factor of the generation arm's telescope ($M = 5/3$). The resulting intensity at the focal plane is shown in Fig. 1.15. We can see that there are two intensity lobes at the focus. The profile is quasi-Gaussian along the x_p -direction, and there are maxima located at:

$$y_p \approx \pm \frac{\lambda f}{2\sigma} \quad (1.50)$$

Where σ is the beam size of an equivalent Gaussian input beam:

$$E_{in}(x, y) = \exp \left[- \left(\frac{x^2 + y^2}{\sigma^2} \right) \right] \quad (1.51)$$

We therefore see that a TEM₀₀ beam sent through a centered π -plate and a lens will have two intensity lobes at the focus. It can be shown that the peak intensity of each lobe is roughly 37% of the intensity of a TEM₀₀ mode under identical focusing conditions (ignoring Fresnel losses from the phase plate). This beam profile is very similar to the intensity profile of a TEM₀₁ mode with an appropriate choice of the beam waist w_0 :

$$I_{01}(x_p, y_p, f) \propto \frac{8y_p^2}{w_0^2} \exp \left[-\frac{2(x_p^2 + y_p^2)}{w_0^2} \right] \quad (1.52)$$

$$\text{with } w_0 \approx \frac{\sqrt{2}}{2} \left(\frac{\lambda f}{\sigma} \right)$$

For this reason, it is often said that the π -plate converts a TEM₀₀ beam into a TEM₀₁ mode at the focus. The comparison between the numerical and the TEM₀₁ approximation for a centered π -plate are shown in Fig. 1.15.

Chapter 2

EXPERIMENTAL APPARATUS

2.1 Introduction

The research described in this thesis utilized several major experimental components: the laser system, the vacuum system, the XUV-MIR optics & interferometer, the target chamber and the XUV detector. Many of these subsystems were designed as improvements upon previously available equipment in the DiMauro lab, so comparisons will be made when applicable.

The laser system is the linchpin of our experiment. Its short, mid-infrared pulse allows us to generate XUV light via an extremely nonlinear process, photoexcite the sample and ultimately probe ultrafast dynamics in the samples. The laser's pointing, power, and pulse duration stability enables us to perform these sensitive experiments over extended periods of time. Details of the laser system and the general laboratory layout are discussed in Section 2.2.

Due to absorption, XUV light cannot propagate in air. Therefore, much of the experiment is performed under high vacuum using a home-built vacuum apparatus. Details of the vacuum system are discussed in Section 2.3.

After high harmonic generation, the XUV light needs to be spatially and spectrally manipulated before it can be used in our experiment. Most materials absorb strongly in this energy range, so special XUV optics are used for this purpose. Details of the XUV optics, along with a description of the XUV-MIR interferometer, are discussed in Section 2.4.

The XUV light is focused on our sample in a target chamber, and the transmitted light is detected by a home-built XUV photon spectrometer. A brief overview of these systems can be found in Section 2.6. A detailed description of these subsystems can be found in Stephen Hageman's dissertation [54].

2.2 Laser System

2.2.1 Spitfire and TOPAS

We use a commercial NIR laser system (Spectra Physics Spitfire ACE), which delivers 12 mJ of 800 nm light at a variable 100 – 1,000 Hz repetition rate with a 60 fs FWHM pulse duration. This system utilizes the chirped pulse amplification (CPA) technique to amplify the pulse energy from a weak seed pulse. In this scheme, a low energy femtosecond seed pulse is stretched in time, amplified and compressed [61]. As such, the Spitfire consists of an oscillator, a grating stretcher, a regenerative amplifier, a single-pass amplifier and a grating compressor.

The laboratory layout is shown in Fig. 2.1. All of the lasers in the DiMauro research group are located in a centralized laser bay, where foot traffic is kept to a minimum and air quality is nominally higher than the surrounding laboratory areas. This minimizes air disturbances around the laser systems and reduces the accumulation of dirt and debris on their optics. Experiments are performed in the adjacent target rooms which contain the vacuum systems and other experimental equipment. The Spitfire shares the laser bay with two home-built ultrafast laser systems (the “2 micron system” and the “4 micron system”, not shown in Fig. 2.1), as well as some laser development. The Spitfire is positioned so that its light can be directed to either the East, South or Southeast Target Rooms, depending on the needs of the researchers. To reduce air currents, welding curtains surround each optical table in the laser bay. When propagating the beam to target rooms, the beam path is enclosed in PVC tubing to reduce air currents and to increase user safety. A CaF₂ window is used to block air currents between the laser bay and the target rooms.

Referring to Fig. 2.1, the transient absorption beamline (TABLE) is located in the south-east target room. Laser light from the amplifier must be propagated uncompressed to the target room to avoid nonlinear propagation effects. To understand why we can compute the B integral, which provides a measure of the nonlinear phase accumulated during propagation:

$$B = \frac{2\pi}{\lambda} \int n_2 I(z) dz, \quad (2.1)$$

where n_2 is the nonlinear index of the material, defined via the refractive index $n = n_0 + n_2 I$.

The distance between the amplifier and the south target room is approximately 13 meters. For a propagation distance of 13 meters, a beam radius of 0.8 cm, a pulse energy of 12 mJ, a FWHM pulse duration of 60 fs, and a nonlinear index $n_2 = 8.0 \times 10^{20} \text{ cm}^2/\text{W}$ [62], $B = 1.53$, which indicates that nonlinear propagation effects are significant. On the other hand, the uncompressed pulse has slightly higher pulse energy (15 mJ, owing to the 20% transmission losses of the compressor), but a significantly longer pulse duration ($\sim 10^3$

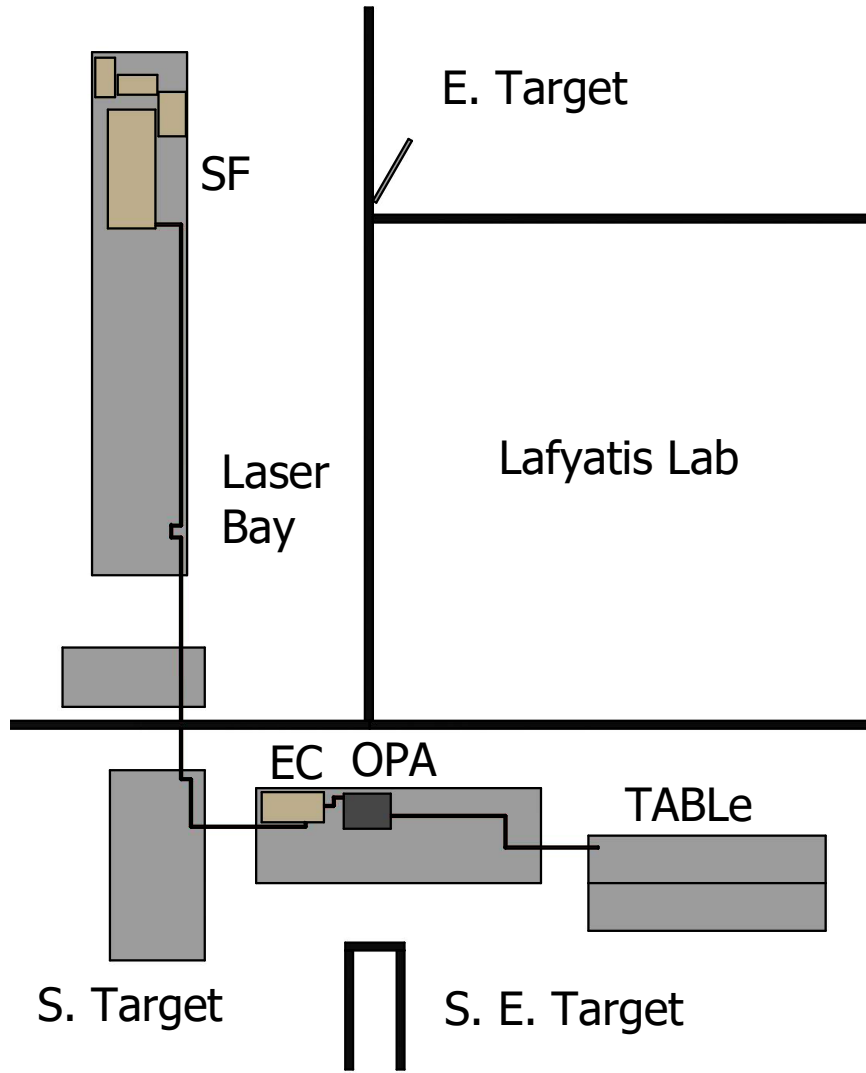


Figure 2.1: Block diagram of part of the DiMauro lab complex showing the laser path from the laser bay to the southeast target room. Other experiments and laser systems are omitted for visual clarity. Optical tables are represented as gray boxes. SF: Spitfire laser system consisting of a MaiTai oscillator, two Empower pump lasers, internal stretcher, amplifier & internal compressor (bypassed for this experiment); EC: Spitfire external compressor; OPA: Light Conversion HE TOPAS Prime; TABLE: 4' × 10' optical table for the transient absorption beamline.

longer), resulting in a negligible B value. For this reason, we use an external compressor centrally located between the south and south east target rooms, as shown in Fig. 2.1. This positioning allows the Spitfire to be used for either the TABLE in the southeast target room or the RABBITT apparatus [63–65] in the south target room (not shown in Fig. 2.1). The external compressor has an efficiency of 80%, giving us 12 mJ of 800 nm light with a FWHM pulse duration of 60 fs at the entrance of the OPA.

The output of the external compressor is sent into a commercial optical parametric amplifier (Light Conversion HE TOPAS Prime), which converts the 800 nm light to longer wavelengths ranging from 1.2 to 2.2 μm while roughly maintaining pulse duration. To minimize nonlinear propagation effects, the TOPAS is located immediately after the external compressor with only two steering mirrors between the external compressor and the TOPAS. Details of the TOPAS operation, alignment and optimization can be found in the user manual. Briefly, it utilizes a nonlinear process called optical parametric amplification (OPA), where the 800 nm pump (p) is converted into two longer wavelength photons (the signal s and the idler i) that obey the following energy conservation relation:

$$\frac{1}{\lambda_p} = \frac{1}{\lambda_s} + \frac{1}{\lambda_i} \quad (2.2)$$

Inside the TOPAS, a white light generation process creates a broadband seed pulse, followed by three stages of amplification in BBO crystals. The signal λ_s and idler λ_i wavelengths are determined by phase matching conditions inside the nonlinear crystals, which is controlled by setting the crystal angle relative to the incident laser light. The BBO crystals are mounted on encoded motorized stages, and the entire system is computer controlled and calibrated so the crystal angles change when the user specifies the desired wavelength. The conversion efficiency of the TOPAS ranges from 40 to 50 % (combined signal + idler pulse energy of 5 - 6 mJ), depending on the degree of optical alignment into the TOPAS and the desired wavelength. During the amplification process, all three beams are collinear. After the final amplification stage, a dichroic mirror inside the TOPAS separates the depleted 800 nm pump from the signal + idler, and a wavelength separator immediately outside the TOPAS splits the signal from the idler.

We use the *frequency resolved optical gating* (FROG) technique [66] to measure the pulse duration of the TOPAS on the optical table immediately after the output of the device. The result is shown in Fig. 2.2. At 1400 nm, we measure a pulse width (defined via the intensity FWHM) of $\tau_p = 43.8$ fs and a pulse bandwidth (defined as the spectral intensity FWHM) of $\Delta\omega = 58.5$ nm. This measurement was taken on the optical table immediately after the TOPAS, but as we will explain below, the interaction pulse duration used in experiments is slightly longer than this measured quantity due to the presence of several chromatic optical elements. We can calculate the interaction pulse duration, but first we need to introduce

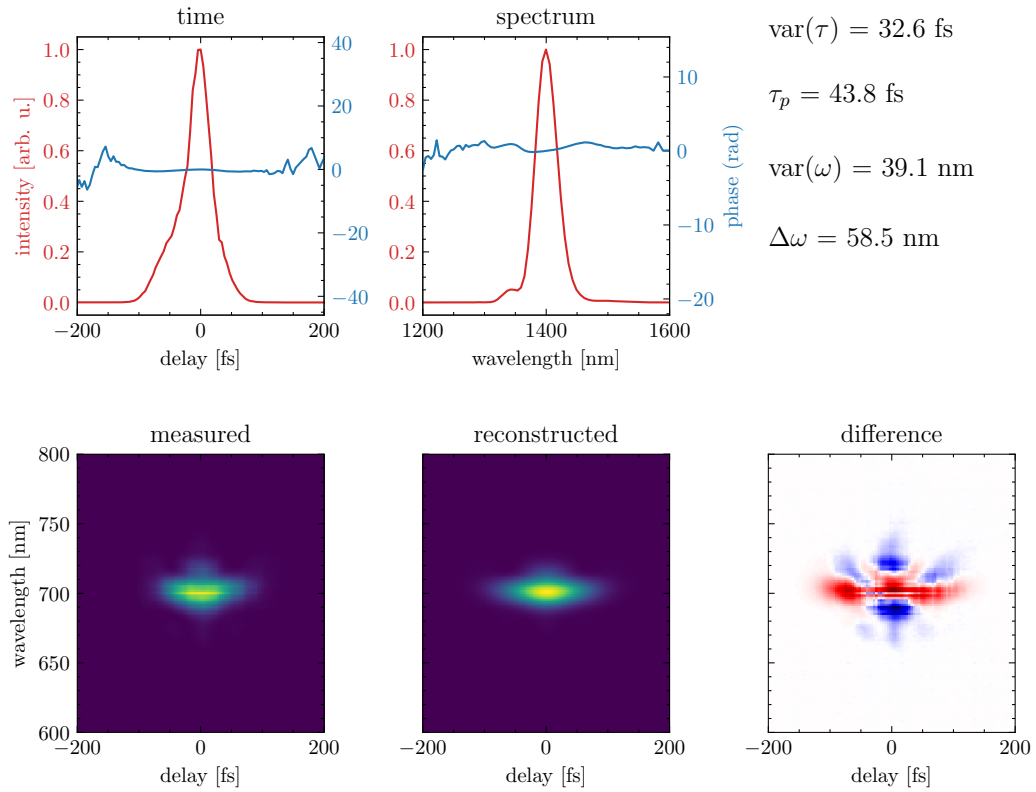


Figure 2.2: FROG analysis of the TOPAS' signal output ($\lambda = 1400 \text{ nm}$). The top row shows the measured (in red) intensity and reconstructed (in blue) phase information in both the temporal and spectral domains. The retrieved parameters are shown in the top right panel. The bottom row shows the measured and reconstructed spectrograms, as well as their difference.

some core concepts.

A broadband laser pulse is a coherent sum of many frequency components, and we will have a short pulse if and only if these frequency components destructively interfere at most times except at $t = 0$. This means that the relative phase between the frequency components is a critical parameter for a short pulse, and a short pulse will be stretched out in time if the phase is distorted from its optimal value. To quantify this effect in our optics, we can write the complex electric field $\tilde{E}(t, z)$ of an ultrashort laser pulse as [67]:

$$\tilde{E}(t, z) = \frac{1}{2} \tilde{\mathcal{E}}(t, z) e^{i(\omega_l t - k_l z)}, \quad (2.3)$$

where $\tilde{\mathcal{E}}(t, z)$ is the envelope varying slowly in space and time, defined as the Fourier transform of spectral weights at $z = 0$:

$$\tilde{\mathcal{E}}(t, z) = \frac{1}{\pi} \int_{-\infty}^{\infty} d\Omega \tilde{E}(\Omega, 0) e^{i\delta k_z} e^{i(\Omega - \omega_l)t}, \quad (2.4)$$

and δk is defined as the deviation of $k(\Omega) = \Omega n(\Omega)/c$ away from its value at the central frequency ω_l :

$$\begin{aligned} k(\Omega) &= k(\omega_l) + \delta k \\ &= k(\omega_l) + \left. \frac{\partial k}{\partial \Omega} \right|_{\omega_l} (\Omega - \omega_l) + \frac{1}{2} \left. \frac{\partial^2 k}{\partial \Omega^2} \right|_{\omega_l} (\Omega - \omega_l)^2 + \frac{1}{6} \left. \frac{\partial^3 k}{\partial \Omega^3} \right|_{\omega_l} (\Omega - \omega_l)^3 + \dots \end{aligned} \quad (2.5)$$

The *group velocity dispersion* GVD represents the frequency dependence of the group delay of the material. It is defined via the above expansion:

$$\text{GVD} \equiv \left. \frac{\partial^2 k}{\partial \Omega^2} \right|_{\omega_l} = \frac{2}{c} \frac{\partial n}{\partial \Omega} + \frac{\Omega}{c} \frac{\partial^2 n}{\partial \Omega^2} = \left(\frac{\lambda}{2\pi c} \right) \frac{1}{c} \left(\lambda^2 \frac{\partial^2 n}{\partial \lambda^2} \right). \quad (2.6)$$

A material with a finite GVD will have a characteristic dispersion length, L_d :

$$L_d = \frac{\tau_{G0}^2}{2|\text{GVD}|}, \quad (2.7)$$

over which an bandwidth-limited input pulse will have its duration increased by a factor of $\sqrt{2}$. It can be shown that the pulse duration after propagating through a length L of dispersive material is:

$$\tau_G(L) = \tau_{G0} \sqrt{1 + \left(\frac{L}{L_d} \right)^2}, \quad (2.8)$$

where we work with the Gaussian pulse duration τ_G , defined via $I(t) \propto \exp[-2(t/\tau_G)^2]$ and related to the FWHM duration τ_p via $\tau_p = 1.177\tau_G$.

In the generation arm, there are 3 lenses and a CaF₂ window. In the pump arm, the pulse travels through the delay wedges (approximately 2 mm of fused silica [68]), two BK-7

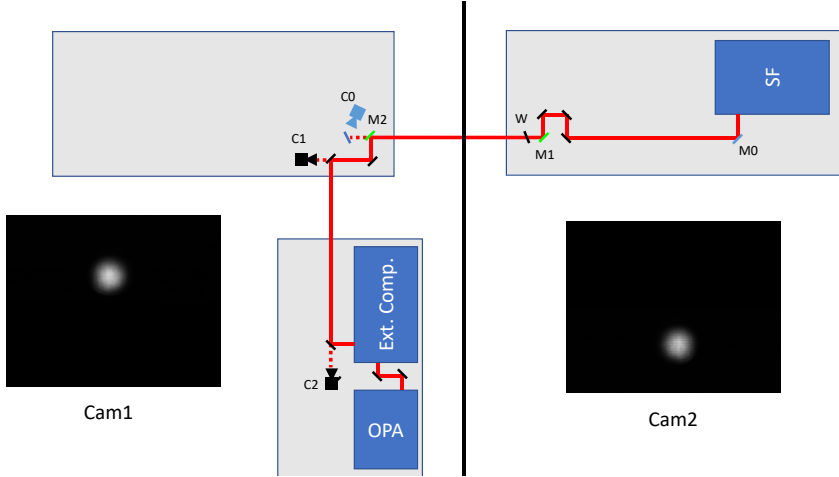


Figure 2.3: Implementation of active stabilization systems between the amplifier in the laser bay and external compressor in the target room (not to scale). M0 & C0 are the motorized mirror and digital camera used for the single-point correction scheme. M1, M2, C1 & C2 are the motorized mirrors and cameras used for the two-point correction scheme. W is an uncoated CaF_2 window used to reduce air currents between the laser bay and target rooms. PVC tubes that surround the beam path are omitted for visual clarity. Inset images show the attenuated beam as imaged by C1 & C2.

lenses (7 mm total thickness), and a 3 mm thick CaF_2 vacuum window [69]. These optics were chosen for their low dispersion at our commonly used wavelengths, and as a result hardly any pulse broadening occurs with our pulse durations. For the pump arm, Eq. (2.8) evaluates to $\tau_p = 44.0$ fs for an initial pulse duration of $\tau_{p0} = 43.8$ fs. The pulse duration of the generation interaction region is similar.

2.2.2 Active Pointing Correction Systems

As a nonlinear device, the performance of the TOPAS is extremely sensitive to input pointing, laser pulse parameters and laboratory environmental conditions. The large optical path length (≈ 15.5 m) between the amplifier and the TOPAS puts stringent requirements on the angular tolerances of the amplifier's output pointing. According to the specification sheet, the rms beam pointing stability of the amplifier at constant temperature is $< 5 \mu\text{rad}$ ($\approx 75 \mu\text{m}$ at 15.5 m, which is negligible compared to our 0.8 cm beam radius) at constant temperature, which is sufficient for our purposes. Unfortunately, the temperature in the laser bay varies significantly throughout the day – sometimes by several degrees – as a function of the occupancy of the Physics Research Building, building-wide energy conservation measures, and activity within the laser bay. Under these conditions, the amplifier's pointing changes by up to $20 \mu\text{rad}/^\circ\text{C}$ ($= 310 \mu\text{m}/^\circ\text{C}$ at 15.5 m).

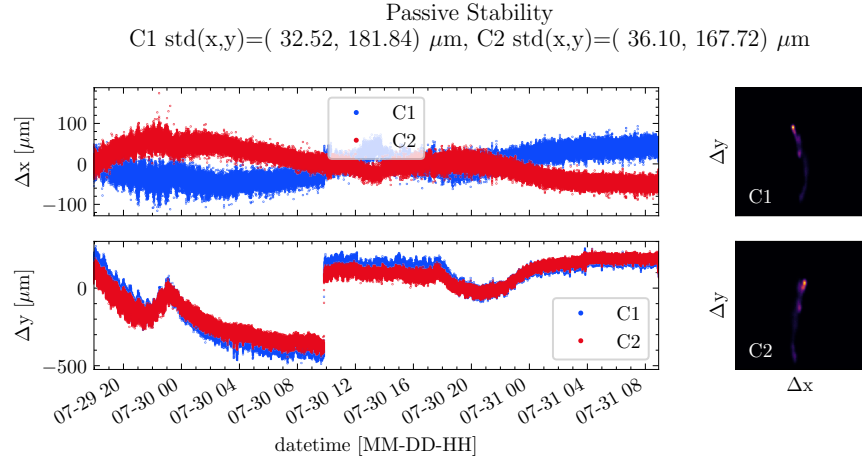


Figure 2.4: Typical passive pointing stability of the Spitfire’s amplifier as measured on cameras C1 & C2. Left panels: x and y coordinates of the centroid vs. time; right panels: 2D histogram of beam centroid positions for the same time period. The 2-point correction scheme was activated between 09:00 (9 am) and 17:00 (5 pm) on 07-30; this system is responsible for the stable performance in the middle in the plot. Long term thermal drift is apparent at all other times.

To combat this slow pointing drift, we actively stabilize the beam pointing between the amplifier and the external compressor as shown in Fig. 2.3. Note that there is not enough space to implement a pointing solution between the external compressor and the TOPAS. Over the years, we have used both a home-built single-point correction scheme and a commercial two-point correction scheme.

Figure 2.4 shows the passive pointing stability of the amplifier as measured by cameras C1 & C2 over the course of 28 hours. The left panel shows the x and y coordinates of the centroid (expressed as a deviation from the average position) sampled at 2 Hz. Note that the sign of Δx is reversed between C1 and C2; this is an artifact of the camera geometry; otherwise the data from the two cameras is self-consistent. The thermal drift is most apparent in the vertical direction; from midnight to 9 am the beam drifts vertically nearly 500 μm . Between 9 am and 5 pm we activated the two-point stabilization system (described below), which accounts for the good performance during this time period. At 5 pm, the stabilization system was turned off and the slow drift resumes. The right panels show 2D histograms of the centroid position, calculated from the time series data. From these plots, it is apparent that the laser drifts in a large arc pattern, with the primary deviation occurring in the vertical direction.

The single-point correction system was programmed and implemented by Dietrich Kiesewetter, who was a graduate student at the time [65]. In this scheme, a digital camera (C0 in Fig. 2.3) located approximately 7.8 m after the amplifier monitors the

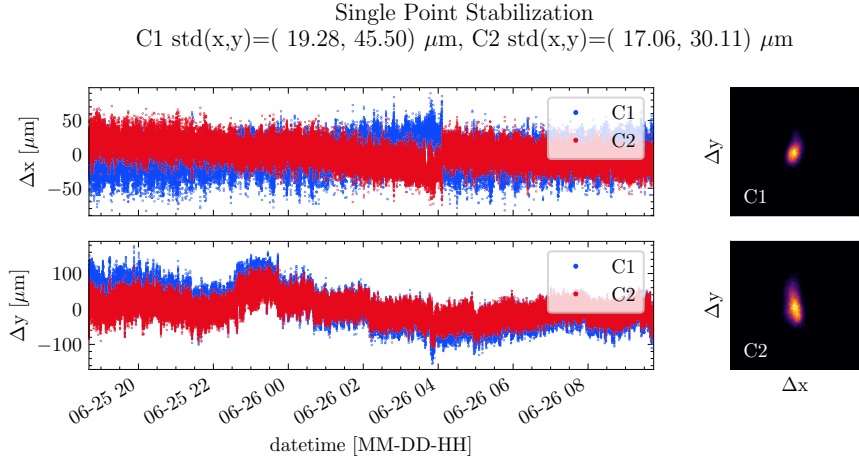


Figure 2.5: Single-point stabilization of the Spitfire’s amplifier as measured on cameras C1 & C2. This dataset contains about 10 correction events, which are visible as abrupt jumps in the time series. The skew of the centroid distributions highlights the limitations of the single-point correction scheme.

transmitted light of a high reflective mirror incident on a card. The position of the centroid is calculated on a rolling average basis and compared to a saved set point. When the centroid position deviates from the set point by more than a minimum correction size, a correction signal is sent to a motorized mirror (M0, located 33 cm after the amplifier). The minimum correction size is set by the user to avoid frequent small corrections to the beam, which results in high-frequency pointing jitter. The correction time interval is also user-adjustable, with typical values of 1 - 60 seconds. If the correction signal requires too large of a step, or if the integrated intensity of the beam falls below a set value, then the locking algorithm assumes that something is wrong and breaks the correction loop without taking corrective action. This prevents the system from taking corrective action in the event the beam is partially blocked by a third party.

The performance of the single-point stabilization system as reported by cameras C1 & C2 is shown in Fig. 2.5. Here, we can see the limitations of a single-point correction scheme. The system is very good at maintaining the position of the beam at C0, but it has no control over the pointing of the beam. As a result, the beam centroid continues to drift on downstream optics, albeit with reduced magnitude compared to the uncorrected case. This effect is apparent in the skewed 2D histograms in Fig. 2.5. The single-point stabilization system works well over short periods of time, but its geometry necessitates weekly realignment of the external compressor and all other downstream optics. Given the technical demands of our experiments and the sensitivity of the TOPAS to input pointing, this can be a prohibitively time consuming process. Unlike a single-point correction system,

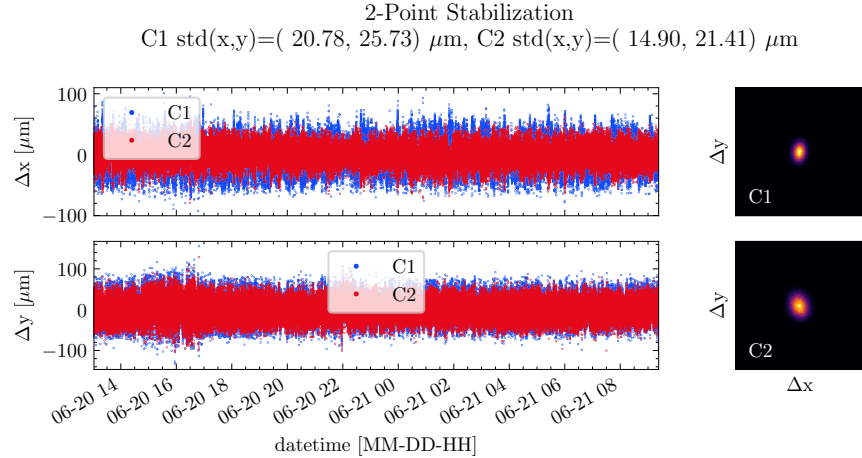


Figure 2.6: Two-point stabilization of the Spitfire’s amplifier as measured on cameras C1 & C2.

a two-point system only needs to be set once.

For the two-point stabilization system, a commercial system was chosen over a home-built solution to reduce the development and implementation time. We use a Newport GuideStar II, which utilizes two cameras (C1 & C2 in Fig. 2.3) and two motorized mirrors (M1 & M2) to monitor the beam centroid and make corrections. A patented correction algorithm running on purpose-built computational hardware is applied to the output of the cameras to solve for the necessary correction signals up to 3 times per second [70]. Beam pointing is usually recovered with a single corrective action, and even especially large pointing drifts are corrected well within 1 second. For numerical stability and increased sensitivity, the distance between M1 and M2 is made as large as possible (3.1 meters); the distance between C1 and C2 (1.75 meters) is also maximized and made similar to the M1-M2 distance; the distance between C1 and M2 is made as small as possible (75 cm).

The passive and actively-controlled pointing stability of the amplifier is shown in Fig. 2.6. Owing to the high correction frequency, individual corrections are small and not visible in the time series. The two-point system maintains both the centroid position and propagation direction, so there is minimal correlation between the reported centroid positions on C1 & C2. As a result, the pointing into the TOPAS rarely needs to be optimized under normal operation, saving valuable time and making experiments more repeatable.

The GuideStar II performs extremely well, but its software lacks the safety features of our home-built system. Specifically, there is no maximum allowable correction size, intensity or beam mode quality monitoring to prevent run-away corrections. For example, it is common to insert a paper card into the beam path to inspect the beam mode just before the external compressor. As a result, camera C2 will briefly see a partially clipped beam

with a centroid displaced by approximately the beam radius, and the GuideStar will take *immediate corrective actions* to adjust the pointing. These actions may result in a 15 mJ beam pointing in an unsafe direction. **Users are cautioned to keep clear of the beam path between the amplifier and the GuideStar cameras when the GuideStar locking algorithm is enabled.** To mitigate this issue, the GuideStar cameras are kept in a plastic enclosure and colleagues are made aware of the limitations of the GuideStar system.

2.2.3 Beam routing into the TABLE interferometer

After selecting the wavelength (signal, idler or depleted pump), the output of the TOPAS is sent approximately 3 meters downstream to the transient absorption optical table. Two motorized mirrors on the TOPAS optical table are used to align the laser into the TABLE interferometer. Unless otherwise noted, protected silver mirrors are used to propagate the TOPAS light for their broadband reflectivity, low absorption losses and high corrosion resistance.

2.3 Vacuum System

2.3.1 The Need for High Vacuum

The XUV light generated by the high harmonic process is absorbed strongly by air, as most gases have at least one electronic transition in the XUV regime. The magnitude of absorption can be estimated using the atomic scattering factors $f = f_1 + if_2$, which were taken from [11]. The photoabsorption cross section σ_a , the transmission ratio T , and the complex index of refraction \hat{n} of a gas can be calculated from these factors:

$$\sigma_a = 2r_0\lambda f_2 \quad (2.9)$$

$$T = \exp(-N\sigma_a d) \quad (2.10)$$

$$\hat{n} = 1 - \frac{1}{2\pi}Nr_0\lambda^2(f_1 + if_2) \quad (2.11)$$

In the above, λ is the wavelength, N is the number of atoms per unit volume, d is the optical path length and $r_0 = 2.8179403227(19) \times 10^{-6}$ nm is the classical electron radius. Since XUV light is ionizing radiation, propagating in air at ambient pressure will cause the light to be effectively attenuated to zero in a few hundred microns. For this reason, any aspect of the experiment involving XUV light must be kept under high vacuum.

For reference, the XUV portion of the transient absorption beamline is about 4 meters long. Figure 2.7 shows the expected XUV transmission losses for XUV propagation through a partial vacuum of common gases: argon and helium are often used for generation, while nitrogen, hydrogen and oxygen are common UHV system contaminants. From this figure,

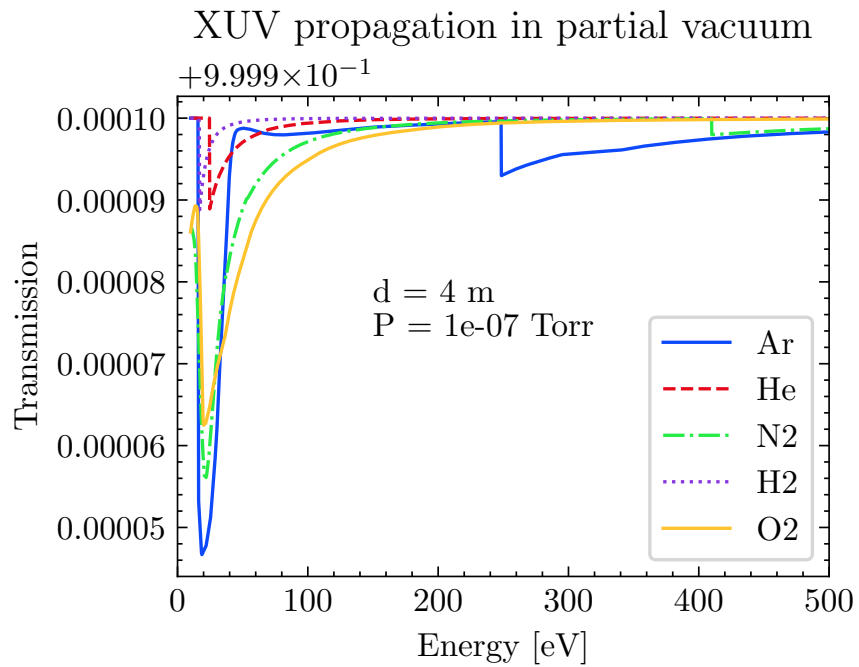


Figure 2.7: Estimation of XUV propagation losses through a vacuum level of 10^{-7} Torr and a distance of 4 meters. Transmission is well over 99.999% for this pressure-length product. Atomic scattering data obtained from references [7, 11], and the calculation follows Eqs. (2.9) to (2.11). Absorption features are present in most elements below 40 eV due to excitation of the valence electrons: *M*-edge in Ar, *K*-edges in H & He, *L*-edges in N₂ & O₂. At higher energies we see the *L*-edge in argon at $\simeq 240$ eV and the *K*-edge in N₂ at $\simeq 410$ eV.

we can see that the XUV transmission exceeds 99.99% for an average pressure of 10^{-7} Torr. Note that this calculation does not include reflection losses from the ellipsoidal mirror, transmission losses from the metallic filter or the sample, or geometric losses from clipping. This simple analysis tells us that the XUV portion of the beamline must be kept under relatively high vacuum to avoid needlessly reducing the XUV flux.

The microchannel plate (MCP) assembly in the photon spectrometer (see Section 2.6) puts additional constraints on the vacuum level. Contaminants in the spectrometer chamber (originating from a finite chamber pressure) lower the effective electrical resistance between the highly charged plates, resulting in a somewhat periodic current surge between the plates. This effect manifests itself in the data as a bright point source at a random location on the detector. In addition to reducing the fidelity of the data, each current surge counts towards the lifetime charge transfer limit of the MCP assembly, reducing its lifetime [71].

The low pressure condition required to minimize XUV absorption and instrumentation malfunction is in direct conflict with the requirements for high harmonic generation (HHG) and gas-phase attosecond transient absorption spectroscopy (ATAS) experiments. HHG requires a gas source to be placed near the MIR focus in the generation chamber, and a gas-phase ATAS experiment requires a similar gas source to be placed near the XUV-MIR focus in the target chamber. The gas from these sources will diffuse into neighboring chambers, raising the pressure of the entire beamline. In addition to the complications described above, higher pressures can overwhelm and damage the turbomolecular vacuum pumps used to keep the system at high vacuum. The vacuum apparatus was designed to localize the gas density at the interaction regions while allowing a range of optical configurations to be used.

2.3.2 Design Goals

The vacuum system was designed to be as modular as possible. In this sense, the TABLE apparatus can be thought of a permanently installed XUV light source and XUV-MIR interferometer that has the ability to accept modular end stations. This design principle has already allowed the study of electron rescattering in strong infrared fields by another graduate student [65]; going forward, new target chambers can be designed to meet the needs of future experiments while maintaining the integrity of the XUV light source and interferometer.

We employ magnetically levitated turbomolecular pumps which were prohibitively expensive at the time of the RABBITT apparatus' construction. These pumps are designed so that the vacuum side of the blade assembly does not make mechanical contact with the drive shaft and housing, which dramatically reduces vibrations during operation. Mag-lev turbopumps have a noise power spectrum an order of magnitude smaller than that of traditional turbopumps. This ultra-quiet operation allows us to mount the vacuum hardware

directly on the interferometer’s optical table. Likewise, we keep our rough vacuum system in an adjacent pump room to minimize acoustics, vibrations and oil contamination in the target rooms.

Large vacuum chambers have the benefit of being able to accommodate a seemingly limitless amount of optics and internal hardware, but they are very uncomfortable and difficult to work around. For this reason, we tried to keep the physical size of the chambers as small as possible while still allowing sufficient internal space for our current and reasonable future equipment needs (*in vacuo* motorized stages, optics, gas and electric feedthroughs, etc.). Additionally, it is difficult to physically move *in vacuo* optics during an experiment, making it difficult to optimize experimental conditions. Vacuum compatible optic mounts exist, but they are expensive, cumbersome to work with and generally considered specialty items that need to be custom ordered. Adjusting a non-motorized optic requires a venting / pumping cycle, which can take several hours. Early on in the design process, we made the decision to keep as many optics as possible outside of the vacuum system, greatly reducing the overall size of the vacuum system. Excluding the modular endstations, our vacuum chambers have a footprint that is approximately one third that of the RABBITT apparatus, which leaves more than half of our 4’ × 10’ optical table unoccupied.

2.3.3 Manufacturing Considerations

When we started this project, the DiMauro lab already had a working attosecond beamline: the RABBITT apparatus, located in the south target room [63]. We considered modifying this apparatus for our needs, but ultimately decided to build a second beamline. The RABBITT apparatus was being frequently used by more senior students working on projects with experimental requirements that were in conflict with those of a transient absorption experiment [64, 65]. At the minimum, we needed to build an XUV photon spectrometer and a condensed matter sample holder. We could have removed the electron spectrometer from the RABBITT apparatus and installed a condensed matter target chamber and photon spectrometer, but this would have been extremely disruptive to the rest of the group. Furthermore, the south target room was already crowded with the cluster apparatus [72], and our equipment would not fit in the room without significant modification to the existing laboratory environment. Also around the start of this project, the DiMauro lab complex was expanded by half a standard laboratory unit (one half of PRB 4115). A partial wall (about 12 feet high) was constructed in 4115, separating the Lafyatis lab from what would now be called the south east target room. Next, the wall separating the south and our half of 4115 was knocked down. The current lab layout can be seen in Fig. 2.1.

Modular aluminum vacuum chambers were not yet available on the commercial market [73], so we went with a welded design for our custom chambers. We considered both aluminum and stainless steel (SS) for the chamber material. Aluminum was preferred for

our application, as it is lighter and therefore easier to mount to an optical table. Due to the presence of a natural oxide layer, aluminum chambers have difficulty reaching UHV vacuum; fortunately our experimental requirement of 10^{-7} Torr is well within reach of an aluminum chamber. The biggest concern of an all-aluminum chamber was the softness of an aluminum knife edge. Recalling the geometry of a conflat flange, the “knife edge” is used to form a semi-permanent metal-metal sealing surface between the conflat and a metal gasket. Any imperfections in the knife edge will result in a sub-optimal sealing surface and will leak. The concern was that an aluminum knife edge could be easily damaged while working in and around the chamber. The solution to this problem is to use SS conflates with an Al chamber body. However, Al and SS cannot be welded together using traditional welding techniques; they must be joined using a difficult technique called *explosive welding*. Few companies are able to explosively weld UHV chambers, and those that do charge a premium for their manufacturing services. A mixed-metal chamber would have been prohibitively expensive, so we decided to use an all stainless steel design.

We decided to have our custom chambers manufactured by the Physics and Astronomy Machine Shops. This allowed us to consult with the machinists frequently during the design phase, which allowed us to converge on a design that met our experimental requirements while minimized machining operations and cost. To this end, we used off-the-shelf vacuum hardware (standard vacuum crosses, full nipples, etc.) whenever possible. The physical size of the ellipsoidal mirror and the XUV spectrometer necessitated a custom chamber design. To minimize engineering and machining complexity, we designed these chambers as simple “boxes”, i.e., using plate geometry.

2.3.4 Vacuum System Details

In this section, we will provide a brief overview of each vacuum chamber in the TABLE vacuum system. Renders of the final vacuum design are shown in Figs. 2.8 and 2.9. A cartoon of the beam path showing the beam path relative to the vacuum system is shown in Fig. 2.15.

The first half of the vacuum system (generation, differential pumping, diagnostic station, 1st metallic filter and mirror chambers) sits atop a custom split-level 4' × 10' optical table (TMC Vibration Control). The lower deck of the table is 24" wide and 12" thick and the upper deck is 20" thick. With this design, we are able to place the vacuum chambers directly on the lower deck while keeping the beam height of the in-air components at a standard height above the upper deck of the table. Like all other optical tables in the DiMauro lab, this table is not pneumatically floated; it sits directly on a steel leg assembly. This maintains the relative position between the optical tables and allows us to put the weight of the chambers on top of the table.

The second half of the vacuum system (target, differential pumping, 2nd metallic filter

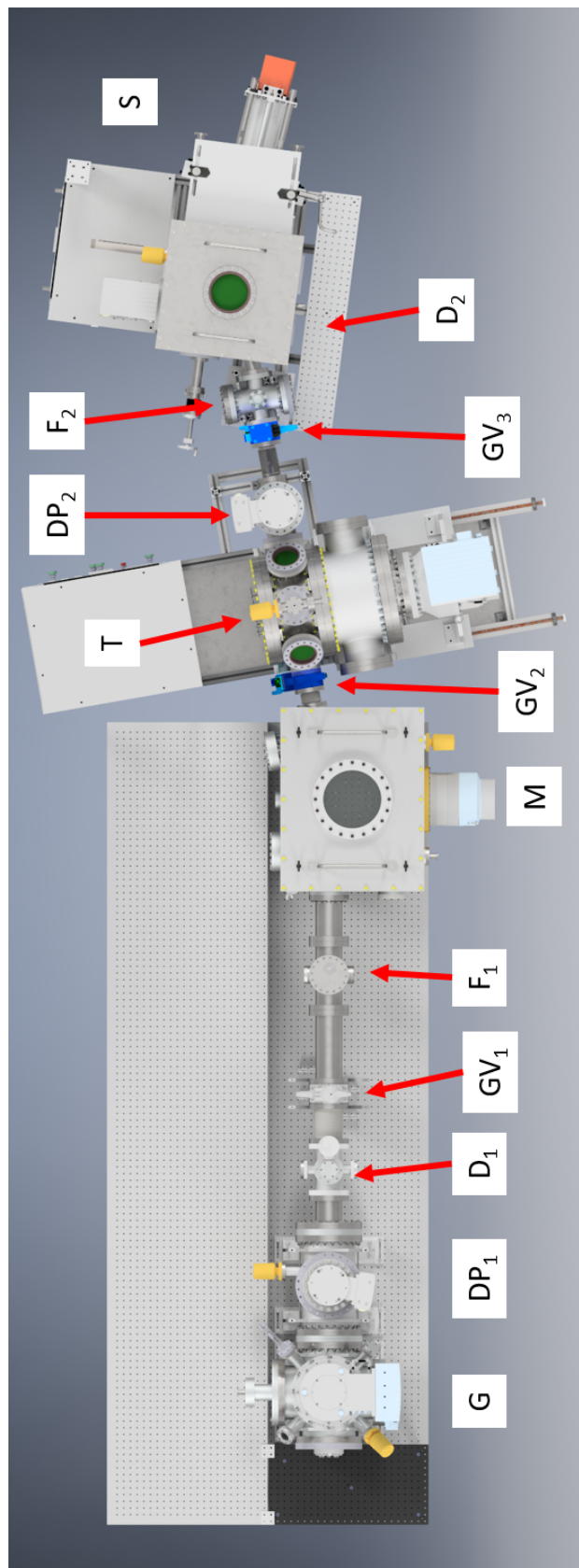


Figure 2.8: Overhead rendering of the TABLE's vacuum chambers. In-air optics are omitted for visual clarity. G: generation chamber; DP: differential pumping chamber; D: MIR diagnostic station; GV: gate valve; F: metal filter; M: metal filter; T: target chamber; S: XUV photon spectrometer. The generation through mirror vacuum chambers sit atop an optical table measuring $4' \times 10'$

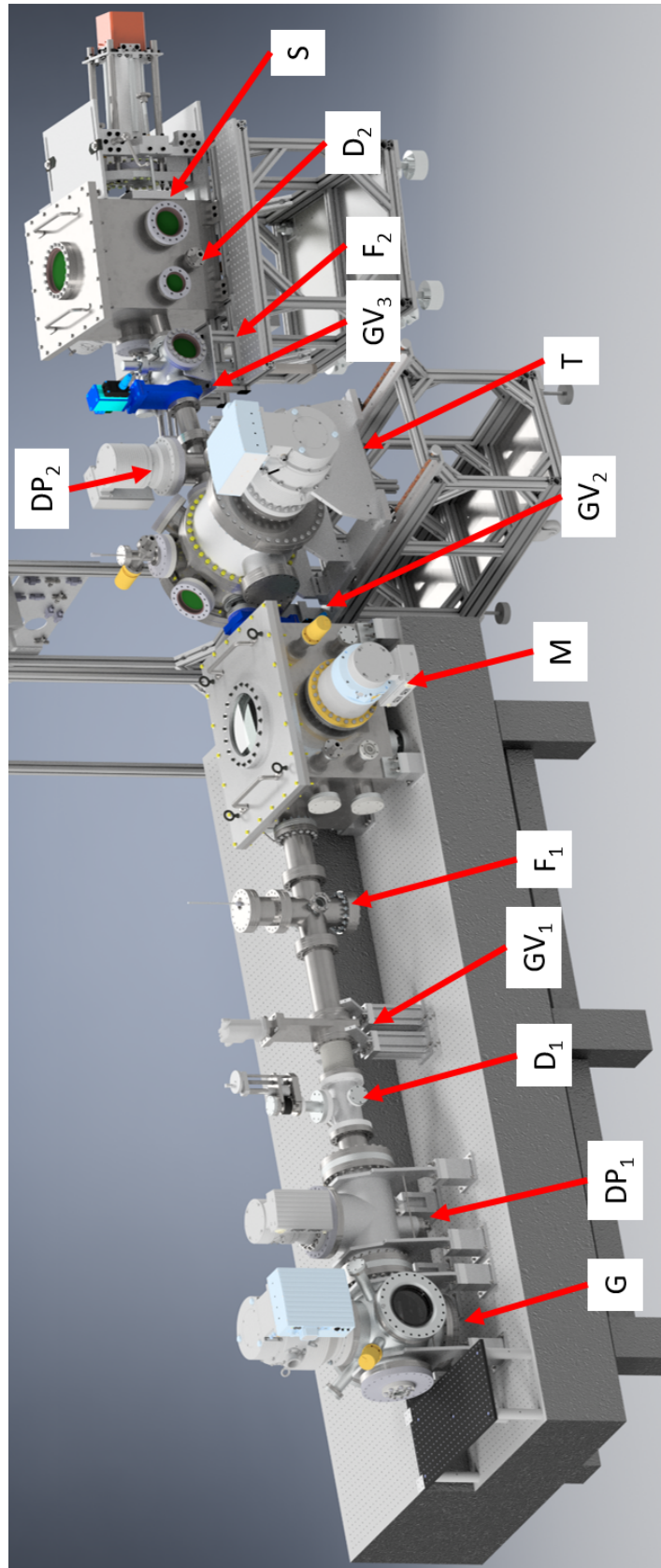


Figure 2.9: Angled rendering view of the TABLE's vacuum chambers showing the two-level 4' × 10' optical table. G: generation chamber; DP: differential pumping chamber; D: MIR diagnostic station; GV: gate valve, F: metal filter; M: mirror chamber; T: target chamber; S: XUV photon spectrometer.

and spectrometer chambers) is not directly connected to the optical table, but instead sits on floor-mounted extruded aluminum frames. This modularity allows us to swap the endstations as dictated by experimental requirements. Although this makes these chambers less mechanically stable, this is an acceptable compromise as they are not part of the interferometer.

We use three gate valves (GV) to create four different vacuum regions in the beamline. This allows us to vent or pump down these sections independently, which is useful when trying to preserve air-sensitive components (MCP, metal filters, samples) or to minimize downtime when performing a “quick fix” that necessitates venting a single section. All three gate valves are electro-pneumatically powered so that they can be controlled via the OMRON safety system⁵. GV₁ is positioned between the MIR diagnostic station and the metal filter, upstream of the ellipsoidal mirror. GV₂ is located between the mirror and target chambers. GV₃ is located between the target chamber’s differential pump and the spectrometer’s filter chamber. The four vacuum sections are colloquially referred to as the generation chamber, the mirror chamber, the target chamber and the spectrometer. Vacuum bellows are installed between the sections to facilitate chamber alignment.

Pressures in each chamber are monitored using a combination Pirani / cold cathode pressure gauge (Leybold PTR90) that can read pressures from 750 Torr to 7.5×10^{-9} Torr. Each vacuum section has a CF-to-KF adapter fitted with a blank KF flange, which is loosened while venting to prevent overpressurization of each vacuum section. The pressure in each turbo pump foreline is monitored by a thermocouple pressure gauge (Lesker KJL-6000) and analog controller.

Generation and Differential Pump Chambers

The first chamber in the vacuum system is the *generation chamber* (G), where the XUV light is produced via HHG. Attached to this chamber and separated by a vacuum aperture is the *differential pumping chamber* (DP₁). The geometry of these two chambers localizes the high gas pressures required for HHG within the generation chamber.

The generation chamber is designed to house the HHG gas nozzle or cell, and short focal length optics. It is here that the XUV light is created for the ATAS experiments. As such, it must be large enough to house an XYZ translation stage, as well as the necessary electric and gas line feedthroughs. The turbo pump must be large enough to maintain milliTorr or lower pressures while being subjected to large gas throughputs for the duration of an experiment. The geometry of the chamber must accommodate a range of focal lengths and optical layouts. To facilitate MIR/gas nozzle alignment, there must be a clear line of sight from outside the chamber to the MIR’s focal spot (roughly, the center of the generation chamber).

⁵Step-by-step instructions for the OMRON are provided in Appendices A.1 and A.2.

The generation chamber is a standard 6-way 10" ConFlat (CF) cross that has been modified by the Physics Machine Shop to have four additional 2.5" CF ports. These so-called radial ports are positioned at the corners of the top flange and are directed towards the center of the generation chamber. The 10" CF flanges are populated as follows. A large turbo pump (Oerlikon Leybold Turbovac Mag W 1300 iP, 1300 Liter/sec) is mounted on the top 10" CF flange. The bottom flange has a 50-pin electric feedthrough and tapped holes for mounting an internal aluminum breadboard, which holds the motorized XYZ manipulation stage, gas nozzle / cell, and any focusing optics. The front flange has zero length adapter with a custom o-ring sealed optical window mount (2" diameter, 1.5" clear aperture, 3 mm thick CaF₂), which allows the laser light to be routed into the chamber. A large 8" diameter viewport is mounted on the right flange, and a CF-to-KF adapting flange for the HPC (see Section 3.2.4) is mounted on the left flange. The rear flange holds the vacuum aperture assembly and a double-sided 10" CF flange, which connects to the front flange of the differential pump chamber. The 2.75" radial flanges hold a Leybold pressure gauge, a 2" diameter viewport and a 4-pipe 1/8" Swagelok gas feedthrough flange (Lesker).

The vacuum aperture assembly is modular, as it allows different sized apertures to be installed as necessary. Currently, we use a 10 mm diameter aperture which was chosen to maximize the XUV transmission downstream. This setup yields a pressure drop of about 2 orders of magnitude across the aperture.

The differential pumping chamber is a standard 3-way 10" CF tee with two additional 2.75" CF flanges pointing towards the optical axis. The front 10" CF flange is connected to the generation chamber; the top CF 10" flange holds a small turbo pump (Oerlikon Leybold Turbovac Mag W 400 iP, 400 L/s) and the rear 10" CF flange connects to the MIR diagnostic station. A KF blow-off assembly and a pressure gauge are mounted to the 2.75" CF flanges.

Typical operating pressures using a 200 μm diameter free expansion nozzle (Argon gas, $P_0 = -5 \text{ psig} \simeq 500 \text{ Torr}$ backing pressure, 2.75 Torr-liter/second throughput) are about 3 mTorr in the generation chamber and $5 \times 10^{-5} \text{ Torr}$ in the differential pump chamber.

MIR Diagnostic Station

An *MIR diagnostic station* (D₁) is located after the differential pumping chamber. The diagnostic station houses a silver mirror mounted to a linear shift mechanism. When retracted, the mirror is out of the optical axis; when inserted the MIR beam is diverted outside of the vacuum system through a window onto the upper deck of the split level optical table. This diagnostic station is used to measure the transmitted power of the generation arm when aligning the high pressure cell (HPC, see Section 3.2.4).



Figure 2.10: Rendering of the metallic filter assembly in the spectral filter chamber. Metallic filters are shown with a false green color.

Filter Chamber

The generation arm's MIR light is blocked at the first spectral *filter chamber* F_1 , which is located after the diagnostic station and before the XUV mirror. This chamber houses a o-ring sealed insertable rod upon which a clamshell assembly is mounted, as shown in Fig. 2.10. This assembly was designed to hold standard metallic filters made by Luxel or Lebow, or achromatic transmission gratings constructed from a microchannel plate (MCP) [74]. By changing the insertion of the rod into the chamber, the user can select which of the three filters is on the optical axis. A calibrated indicator located outside the chamber (not shown) has markings to indicate the approximate rod position for each filter. The precise height of the filter can be fine tuned while observing the spatial profile of the XUV beam, as reported by the XUV spectrometer. Note that using a mesh-supported filter will imprint a grid-like pattern into the XUV beam, which will be apparent in the spectrometer's readings. Retracting the rod fully allows the XUV-MIR beam to continue down the beamline unattenuated. Users should be cautioned that unattenuated MIR light from the generation arm will destroy condensed matter samples in the target chamber; as little as $3 \mu\text{J}$ of 1430 nm light will destroy a Ge/SiN heterostructure. For a more detailed discussion on the laser-sample considerations, see Chapter 4.



Figure 2.11: Photograph of the underside of the mirror chamber during installation showing the vibration-dampening bellows. Steel rods (not visible) connect the interior of the bellows feet to the interior breadboard. After installation, the flat metal disks were secured to the optical table using clamps.

Mirror Chamber

The *mirror chamber* (M) is located after the filter chamber at the end of the $4' \times 10'$ optical table. This chamber houses the ellipsoidal and hole mirrors (discussed in Section 2.4). The ellipsoidal mirror (EM) reimages the XUV source onto the target, while the hole mirror (HM) collinearly combines the generation arm's XUV with the pump arm's MIR, closing the interferometer. The two pulses leave the chamber through the exit flange, which is angled 10 degrees to the left to account for the 85 degree incident angle of the EM.

This chamber has windowed ports (2 inch diameter, 3 mm thickness CaF₂) that allow for positioning of the hole mirror before or after the ellipsoidal mirror, depending on experimental requirements. If the EM precedes the HM, then the MIR pump arm focal parameters can be tuned arbitrarily, but this flexibility comes at the cost of having an additional optic in the interferometer. If the HM precedes the EM, then both the XUV and the MIR pump share a common focusing optic which is outside the interferometer, which can improve interferometric stability.

An internal reinforced aluminum breadboard supports the optomechanical components within the chamber. This breadboard is mechanically coupled directly to the $4' \times 10'$ optical table using four stainless steel columns that run through openings on the underside of the mirror chamber, as shown in Fig. 2.11. Each port has a soft bellows housing that isolates chamber vibrations (originating from the pumping system) from the interferometrically stable optics within the chamber.

It is important to have remote *in vacuo* control of both the EM and the HM, as the final

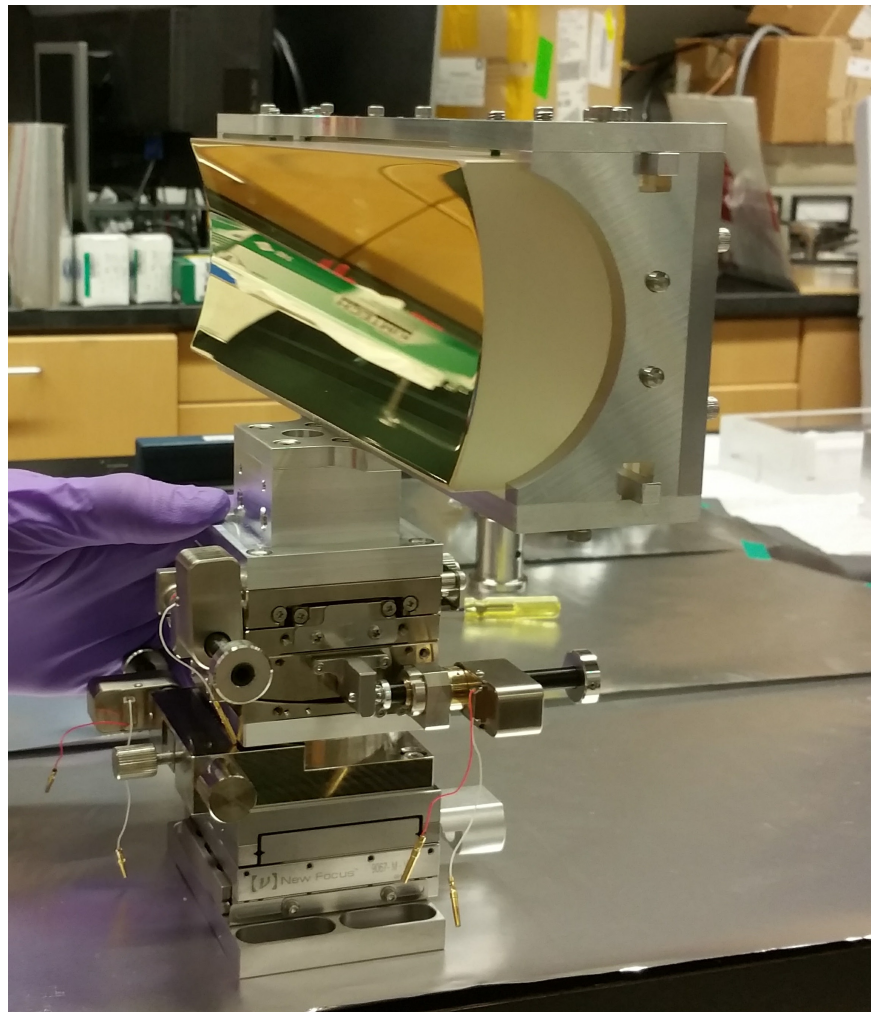


Figure 2.12: Photograph of the ellipsoidal mirror in its motorization stack prior to being installed in the mirror chamber.

alignment must be done with the XUV light. The optomechanical support of the ellipsoidal mirror was designed to avoid the cantilevering present in the XUV mirror of the RABBITT apparatus, which eliminates a source of mechanical instability. This required the use of custom vacuum compatible stages and spacers. To this end, the ellipsoidal mirror is placed atop a 5-axis vacuum compatible motorized stack, as shown in Fig. 2.12. Starting from the breadboard, we have an XY crossed-roller bearing stage assembly (Newport) actuated by encoded stepper motors (Thorlabs). Next, a rotation stage (OptoSigma KSPS-606M-EN-N-2) controls the yaw. A matched pair of custom goniometers (OptoSigma, 85 & 105 mm radii) with a center of rotation corresponding to the optical center of the ellipsoidal mirror, control the roll and pitch of the EM. All three rotations are actuated by Picomotors (Newport 8301-UHV). An aluminum bracket, constructed of 7075 aluminum and manufactured by the Physics Machine Shop, surrounds the optically inactive sides of the ellipsoidal mirror and secures it to the top of the optomechanical stack. The height of the ellipsoidal mirror is fixed by the combined height of the breadboard, optomechanical stack and aluminum bracket.

The hole mirror is mounted in a 2 inch diameter gimballed beamsplitter holder (OptoSigma BHAN-50M-8-32UNC), modified to work with a pair of Picomotors (Newport 8301-UHV) and to be vacuum compatible. This mount was chosen as it has a large clear aperture in both transmission and reflection at 45 degrees. This capability allows for the future implementation of an active interferometric control arm using a visible wavelength. The mirror chamber has two extra 4.5" CF ports for a future implementation of this control system.

The interior of the mirror chamber is accessed by removing the top panel, which was constructed from aluminum to reduce the weight. Nevertheless, the lid assembly weighs about 66 lbs (30 kg), so a manual winch was installed above the chamber so that any members of the group could remove the lid if necessary. When installed, the lid is sealed to the chamber body by use of a differentially pumped double o-ring face seal, as shown in Fig. 2.13. Three grooves are milled into the stainless steel face of the chamber for this purpose; the outer and innermost channels each hold a large o-ring, while the middle channel is continuously pumped via the beamline's rough vacuum system. The rough vacuum line splits before this turbo and provides pumping speed to both the turbo (Oerlikon Leybold Turbovac Mag W 700 iP) as well as the mirror chamber's differential groove. Note that a differentially pumped o-ring groove provides superior vacuum performance, as it reduces the pressure differential across a single o-ring; this approach is also robust against small scratches to the sealing surface that may arise due to frequent handling of the aluminum lid.

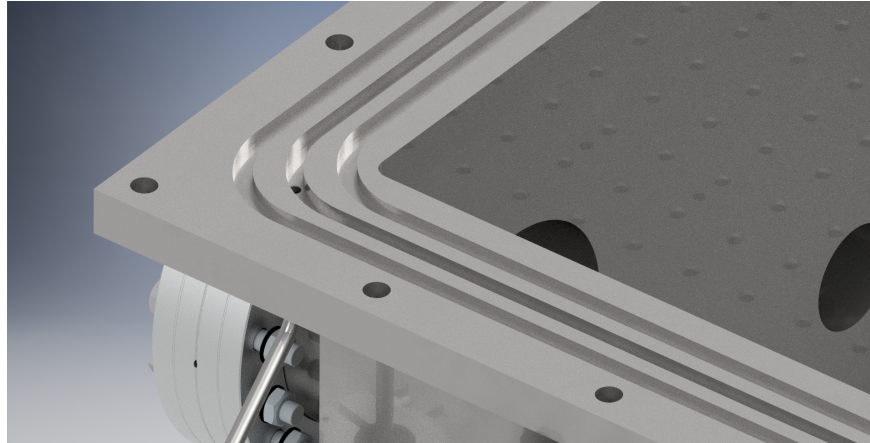


Figure 2.13: Rendering of the mirror chamber’s sealing surface showing detail of the differentially pumped double o-ring. O-rings are not shown in this figure. The two o-ring glands, the central pumping channel and the welded 1/4” stainless steel pumping tube are visible. Four through holes for the 5/16” sealing bolts are visible at the perimeter of the chamber’s sealing surface.

Target and 2nd Differential Pump Chambers

The *target chamber* (T) is located immediately after the mirror chamber, with the center of the chamber roughly corresponding to the XUV focal spot (750 mm from the ellipsoidal mirror). The chamber is an assembly of two 16” CF feedthrough collars populated with smaller radial flanges. The assembly is turned on its side so that the light enters and exits the chamber through the radial flanges.

The left collar has eight 6” CF radial flanges and serves as the interaction region. The interaction collar is mounted directly to the extruded aluminum frame (80/20 Inc.). The bottom radial flange supports an internal aluminum breadboard. The breadboard supports a motorized XYZ stage (Newport), upon which a sample holder can be attached. Encoded stepper motors (Thorlabs) are used for repeatable sample movement relative to the XUV-MIR focus. The top radial port has a 6”-to-2.75” zero length reducer and a 2.75” CF tee which holds a KF blow off valve, a pressure gauge, and a gas line feedthrough for gas phase measurements. Viewports are installed on the two top diagonal radial ports. A 50-pin electrical feedthrough (Accuglass) is mounted on one of the bottom diagonal ports. The horizontal radial flanges serve as the entrance and exit ports for the light. A vacuum aperture (5 mm diameter) is mounted on the external side of the horizontal exit port to limit gas flow into the spectrometer chamber when gas phase experiments are performed. The left 16” CF flange holds a 16”-to-8” zero length adapter. Currently, this 8” port is used as an access port, but it was originally designed to accommodate an electron spectrometer to record simultaneous photon and electron measurements (not implemented).

The right collar has two 8" CF radial flanges which are used as access ports. A large turbo pump (Oerlikon Leybold Turbovac Mag W 1300 iP) is mounted via a 16"-to-10" reducing flange. The assembly was designed to be opened in the middle by breaking the 16" CF connection between the two collars. To facilitate this motion, the right collar and turbo pump are mounted to a rail system using sets of single and dual track roller bearings (Thomson).

The second differential pumping chamber (DP_2) is a 4.5"/6" reducing cross located immediately after the target chamber. A modified 6"-to-4.5" zero length reducing flange holds a 5 mm diameter vacuum aperture and connects the target and differential pumping chambers. This aperture size significantly reduces the MIR flux and lowers the operating pressure in the photon spectrometer during gas phase measurements. An 8"-to-6" zero length reduces is used to connect a hybrid bearing turbo pump (Oerlikon Leybold Turbovac T450i) to the top of the DP_2 chamber.

An aluminum breadboard is mounted to the bottom radial flange at the center of the target chamber. A motorized crossed roller bearing XYZ stage (1" travel, Newport) sits atop the breadboard near the XUV-MIR focal plane. A custom modular bracket is mounted to the stage and accepts a 3x3 condensed matter sample holder (3x3 grid of 5 mm circular clear apertures in a clamshell geometry) and / or a gas nozzle.

For additional details on the target and differential chambers, see Stephen Hageman's dissertation [54].

2nd Filter and XUV Photon Spectrometer Chambers

A second filter chamber (F_2), is located after the target differential pumping chamber. Designed to filter out the residual MIR light from the pump arm, it is very similar to the first filter chamber (F_1). The main difference is that we use an UHV-rated linear actuator (Lesker LBD35-150-H) to control the filter's position in the beam, rather than an o-ring seal, which allows the ultimate pressure of the spectrometer chamber to reach UHV. The target chamber's vacuum aperture and the spatial mode from the hole mirror largely make this filter unnecessary, as most of the energy is blocked before it reaches the filter chamber.

The photon spectrometer's optics and chamber were custom built to meet our experimental needs. Stephen Hageman's dissertation [54] and Sierra O'Bryan's thesis [75] contain detailed discussions on these subsystems. Below, we provide a brief overview of the vacuum chamber and the optomechanics. For a brief overview of the photon spectrometer's optical design, see Section 2.6.

This chamber is a custom box design, with a removable lid sealed by a differential pumping groove similar to the mirror chamber. We have six-axis control over the positioning of the spectrometer's gratings. The gratings are mounted atop a 5-axis motion stack of linear, rotation and goniometric stages (Newport). The motion stack is mounted atop a

linear insertion mount (Lesker LSM38-25-H), mounted on the floor of the chamber, which provides vertical translation via a manual, external control wheel.

A small turbo pump (Oerlikon Leybold Turbovac Mag W 400 iP) is mounted to the chamber wall in a horizontal configuration. An internal aluminum breadboard mounted to the floor and walls of the chamber provides support for ancillary optics, including diverting optics for external MIR diagnostics. A linear actuator on the entrance wall pushes on a gearbox assembly to insert a 2" silver mirror into the beam path before the grating stack. When fully inserted, the beam is diverted out of the chamber through a viewport. An external breadboard, mounted to the chamber's extruded aluminum frame (8020 Inc.), holds MIR diagnostic optics used for finding temporal overlap.

A third linear actuator mounted on the turbo pump wall inserts baffles between the grating and the XUV detector to block zero-order diffracted light. An 8" CF custom edge-welded bellows connects the exit chamber wall and the XUV detector flange assembly. A custom mechanical assembly (the "cage and crank" system) provides three-axis control over the detector flange (horizontal translation, separation, and angle). This system allows us to optimize the grating-detector geometry, depending on which part of the XUV spectrum we want to resolve.

Caution: The bellows have a limited range of motion that is smaller than the cage and crank's range. It is possible to tear the bellows by moving the system outside its safe operation range. Even with the OMRON safety system armed, a tear in the bellows while the system is under vacuum would lead to the sudden and catastrophic venting of the entire beamline. Refer to [54] and the bellows calculator for additional details before using this system.

Rough Vacuum Details and OMRON Safety System

The turbo pumps are backed by a pair of rough vacuum systems that are located in an adjacent pump room. A schematic of the system is shown in Fig. 2.14. The generation and differential pumping chambers share a high throughput system, and the remaining chambers (mirror, target, target differential pumping, spectrometer) share a smaller system.

The large rough pump system consists of a rotary vane (RV, Leybold D65B, 65 m³/hr) and roots blower (Leybold WSU 501, 500 m³/hr) pump stack. This rough vacuum system is connected to the beamline via a large diameter copper and PVC tube. The pressure at the inlet flange of the roots blower is remotely monitored using a thermocouple gauge (Agilent Type 0531 TC), an electronic gauge controller (Lesker KJL615TC-E), a wireless networking router, and a touchscreen-enabled Raspberry Pi running a web applet (Kurt J. Lesker).

The smaller system uses the same model RV pump, but a smaller roots blower (Leybold WA 251, 250 m³/hr). Although it has half the pumping speed as the generation pump

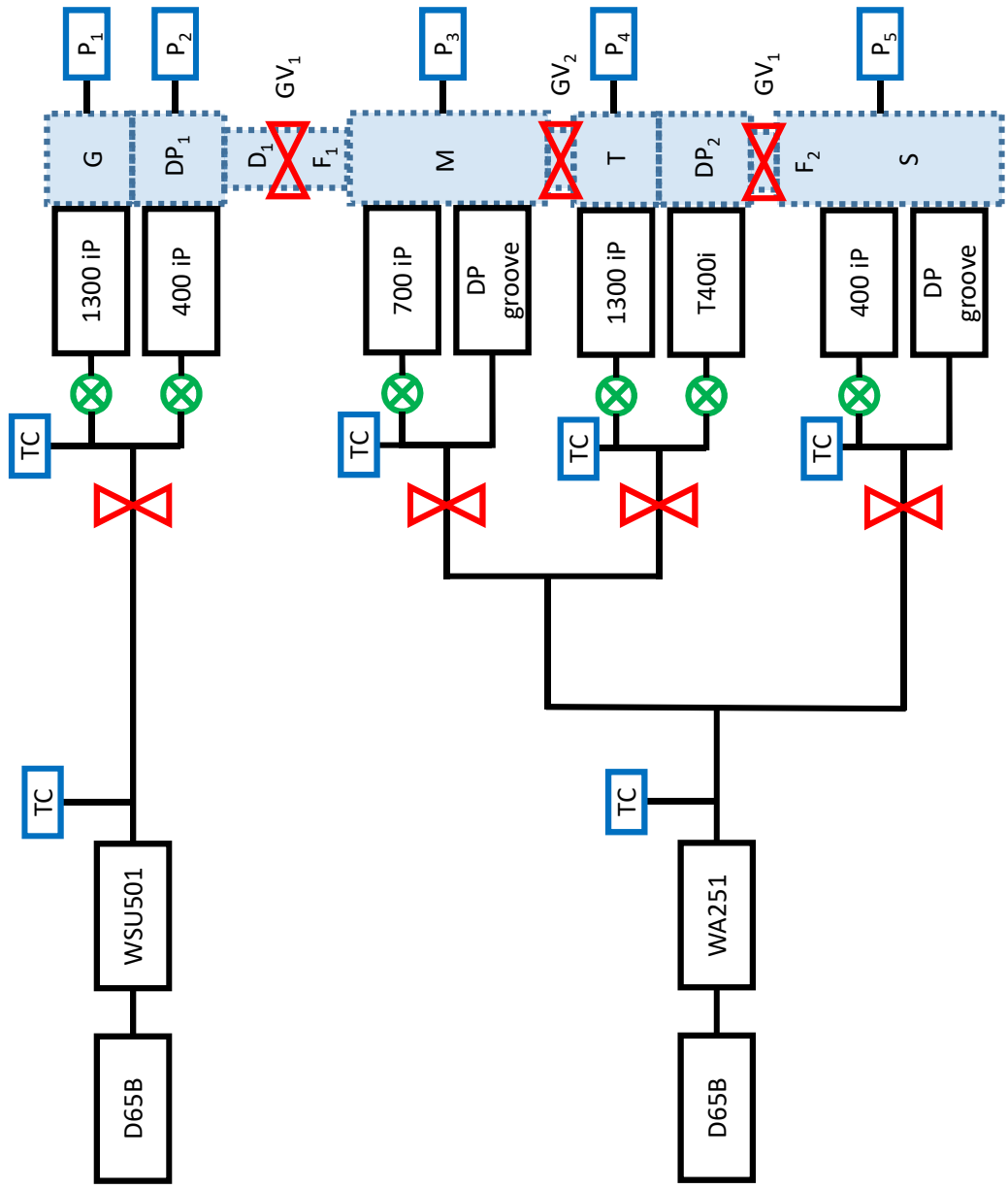


Figure 2.14: Block diagram of the TABLe's rough vacuum system showing rough and turbo pumps, control valves and pressure gauges. TC: thermocouple pressure gauge; P: UHV pressure gauge; \otimes : manual valve, \bowtie : rough vacuum solenoid or UHV pneumatic gate valve. UHV is indicated by blue shaded region. G: generation region. M: mirror chamber, DP: differential pumping chamber, T: target chamber, S: photon spectrometer chamber.

stack, the gas load for these chambers is minimal compared to the generation chamber. The pressure at the inlet flange of the roots blower is remotely monitored using a copy of the system that monitors the generation roots blower pressure.

Owing to the complexity of the vacuum system, we decided to implement a “safety system”, i.e., a programmable logic controller that controls the major components of the vacuum apparatus. The heart of this system is an OMRON PLC. Its design follows that of the RABBITT apparatus [63], although the new system controls significantly more equipment than its predecessor. Special thanks go to Andrew Piper [73], who programmed and implemented this system on our beamline. A full user manual is available on the group drive, and a quick start guide is available in Appendix A.1. In short, the OMRON safety system monitors the setpoints of the 5 UHV pressure gauges and controls the 6 turbo pumps, the 4 rough vacuum solenoid gate valves, the 3 UHV pneumatic gate valves and the 5 turbo pump solenoid vent valves according to a simple set of logic rules. This automation enables three main features. First, the user can pump down or vent individual sections (or the entire beamline) with a few button presses. With the exception of actuating the manual valves and the KF blow off flanges, this process is almost entirely automated which greatly reduces the complexity of using the vacuum system. Second, the OMRON verifies that there is no pressure differential across the UHV gate valves before they are opened. If the pressure on either side of the gate valve is above a setpoint, the OMRON will prevent it from opening. Finally, when the OMRON is armed, it will monitor the pressure in each chamber and perform an emergency shutdown/vent procedure if any pressure gauge reports pressures above a setpoint. In the event of a pump failure, the armed OMRON system will safely vent the beamline without any user intervention.

2.4 XUV Optics

In this section, we will discuss the XUV optical design of the TABLE system. We start with a statement of the design goals, followed by a general discussion of XUV focusing optics to motivate our choice of the Zeiss gold coated ellipsoidal mirror.

2.4.1 Design Goals

We started with several design requirements. First, we wanted to be able to deliver XUV light onto the sample with photon energies as high as 300 eV, which would enable us to study carbon containing materials such as graphene. However, we also wanted to preserve the lower energy portion of the harmonic spectrum, allowing the study of semiconductor and transition metal compounds. This broadband requirement restricts us to metal-coated reflective optics.

Condensed matter ATAS experiments have significantly higher XUV flux requirements

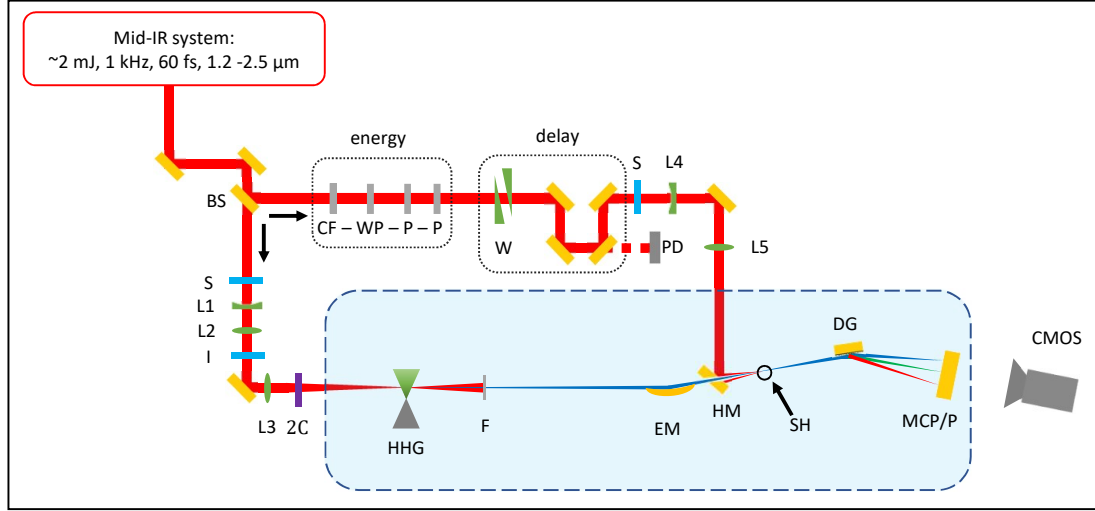


Figure 2.15: Schematic of the Transient Absorption BeamLine (TABLE). Blue shaded region represents vacuum. BS: beamsplitter, S: computer-controlled shutter, L: lens, I: iris, 2C: optics for two-color generation, HHG: high harmonic generation, F: metallic filter, EM: ellipsoidal mirror, HM: hole mirror, SH: sample holder, CF: long-pass color filter, WP: $\lambda/2$ waveplate, P: wire-grid polarizer, W: delay wedges, PD: photodiode and associated optics, DG: dispersive grating, MCP/P: micro-channel plate and phosphor.

compared to RABBITT experiments. This meant that our XUV focusing solution needed to have the highest reflectivity possible, and we needed to minimize any XUV losses elsewhere in the beamline. This restricts us to single optic solutions, and puts stringent requirements on the smoothness of the optic.

The MIR intensity profile at the focus is an important parameter for every experiment. In a transient absorption experiment, the pertinent experimental signal originates from the spatial overlap of the sample, the XUV and the MIR light in the interaction region. Ideally, neither pulse would have any spatial structure at the interaction plane. In the real world, we design the optics to minimize the intensity variation of the MIR over the spatial extent of the XUV spot. For finite beam sizes, this is accomplished by focusing the XUV tighter than the MIR while minimizing aberrations.

Although the primary scientific goal for this work was to perform transient absorption experiments in condensed matter, we designed the apparatus with other experiments in mind. Aside from general modularity, we wanted the beamline to be able to study strong field physics in helium [65]. Note that these two experiments have vastly different MIR intensity requirements: a condensed matter transient absorption experiment will need no more than 10^{12} W/cm^2 , whereas an $e-2e$ He experiment requires $\simeq 10^{14} \text{ W/cm}^2$. Achieving 10^{14} W/cm^2 in the interaction region while meeting the other experimental requirements requires a very tight MIR focusing geometry that the lab's previous attosecond beamline [63]

could not achieve. Therefore, special consideration was taken when designing the TABLE’s optics to ensure we could reach the required intensity. One important metric is the relative size of the XUV and MIR focal spots; both experiments require the XUV to be a fraction of the size of the MIR. This means that an experiment that requires tightly focused MIR light also requires a tightly focused XUV light. Ultimately, we chose to demagnify the XUV spot size by a factor of three, which reduces the XUV spot area by a factor of nine. This allows us to more strongly focus the MIR pump pulse, resulting in a nine-fold increase of interaction intensity without changing the relative spot sizes of the XUV and the MIR. The final design allowed us to reach our goal of 10^{14} W/cm² for the doubly ionized helium gas for $e - 2e$ experiments [65].

As we will discuss below, we are restricted to a reflective focusing geometry. As such, one relevant parameter is the ratio of the entrance and exit arms of the XUV optic. A desire to have modular endstations put a lower limit on the XUV optic’s exit arm; too short and the mirror chamber would have to merge with the target chamber. Likewise, the footprint of the beamline had to fit within the south east target room, which put constraints on the length of the entrance arm.

Reflective Optics

The XUV light is divergent after its generation and needs to be focused onto a sample for the experiment. The relatively short wavelength of the XUV puts stringent requirements on the surface quality of the focusing optic, raising the cost and manufacturing time significantly. Alignment of the optic is frustrated by the need for in-vacuum propagation and the invisible nature of XUV light. These factors lead us to pursue a “one size fits all” broadband optic rather than a series of interchangeable narrow bandwidth optics tailored for individual experiments.

The presence of strong absorption edges over the bandwidth of the XUV pulse precludes the use of transmissive optics for most applications. Narrow bandwidth transmissive optics have been designed to exploit the dispersion near an absorption edge [76]. However, these techniques cannot be extended to support the entire bandwidth of our XUV pulses. Reflective dielectric coatings have been designed for the XUV but they have a bandwidth of only 10 – 20 eV [65]. These considerations leave reflective optics as the only good choice for broadband XUV light.

XUV and x-ray reflective optics consist of highly polished curved substrates with a thin (typically 40 nm) metal coating applied to the polished surface. As a reflective optic, the precise shape of the surface (discussed below) determines the focusing properties, and the coating influences the spectral reflectivity and overall performance. The high tolerances and custom nature of these optics makes them very expensive (tens of thousands of dollars) with a long manufacturing lead time (12 months), so it was important to make an informed

decision about this purchase. In the following sections we will briefly introduce the physics relevant to XUV optics, namely Fresnel reflection from a rough surface. We will use these results to motivate the selection of our XUV optic.

2.4.2 Fresnel Reflection from a Rough Surface

We use the familiar Fresnel equations to model reflection from the surface of a conductive surface [77]. In the equations that follow, the vacuum is denoted by $j = 1$ and the conductive material is $j = 2$. The incident electric field is E_I and the reflected component is E_R . We use the standard convention to denote the polarization⁶: p -polarized light has an incident electric field parallel to the plane of incidence; s -polarized has an incident electric field perpendicular to the plane [78]. The complex reflection amplitudes $\hat{r}_{s,p}$ are written in terms of the complex impedance $\hat{Z}_j = \mu_j c / \hat{n}_j$ and the angle measured from the normal in each medium θ_j :

$$\hat{r}_s \equiv \left[\frac{E_R}{E_I} \right]_s = \frac{\hat{Z}_2 \cos \theta_1 - \hat{Z}_1 \cos \theta_2}{\hat{Z}_2 \cos \theta_1 + \hat{Z}_1 \cos \theta_2} \quad (2.12)$$

$$\hat{r}_p \equiv \left[\frac{E_R}{E_I} \right]_p = \frac{\hat{Z}_1 \cos \theta_1 - \hat{Z}_2 \cos \theta_2}{\hat{Z}_1 \cos \theta_1 + \hat{Z}_2 \cos \theta_2} \quad (2.13)$$

Next, we assume non-magnetic media ($\mu_1 = \mu_2 = \mu_0$) and that the initial medium is vacuum ($\hat{n}_1 = 1$). We can express the reflection amplitudes using the complex index of refraction $\hat{n}_2 = n_2 + ik_2$:

$$\hat{r}_s = \frac{\cos \theta_1 - \hat{n}_2 \cos \theta_2}{\cos \theta_1 + \hat{n}_2 \cos \theta_2} \quad (2.14)$$

$$\hat{r}_p = \frac{\cos \theta_2 - \hat{n}_2 \cos \theta_1}{\cos \theta_2 + \hat{n}_2 \cos \theta_1} \quad (2.15)$$

The reflectance R is the modulus squared of the reflection amplitudes:

$$R_s = \left| \frac{\cos \theta_i - \hat{n}_2 \cos \theta_t}{\cos \theta_i + \hat{n}_2 \cos \theta_t} \right|^2 \quad (2.16)$$

$$R_p = \left| \frac{\cos \theta_t - \hat{n}_2 \cos \theta_i}{\cos \theta_t + \hat{n}_2 \cos \theta_i} \right|^2 \quad (2.17)$$

We introduce the *glancing angle* $\phi \equiv \pi/2 - \theta$, which is the complement to θ . Total external reflection, where the incident rays do not penetrate the medium but rather propagate along the interface at angle $\phi_2 = 0$, occurs at incident glancing angles below the *critical incident angle* ϕ_c :

$$\cos \phi_c = 1 - \delta \quad (2.18)$$

⁶The designations s and p follow from the German words for perpendicular (*senkrecht*) and parallel (*parallel*).

where δ is defined via $\tilde{n} = (1 - \delta) - i\beta$. The x-ray optics literature often makes approximations to the above reflectance equations using either the small angle approximation ($\delta \ll 1$ and $\cos \phi_c \sim 1$, or $\phi_1 \ll 1$), or the assumption that we are operating near the critical angle ($\phi_1 \sim \phi_c$) [78]. Note these assumptions are not necessarily true for our geometry, especially at photon energies below 200 eV, where the critical angle for gold exceeds 10 degrees.

The above is valid for a perfectly smooth interface, but real optics have finite roughness. The effect of surface roughness on the reflection amplitude \hat{r} is commonly treated by either the *Debye-Waller* or *Néerot-Croce* factors. The relative sizes of the extinction length ($1/k_2$) and the in-plane characteristic length scale (δr) of the surface roughness determine which formalism is appropriate [79, 80]. For XUV light at a grazing angle on a gold surface, the extinction length is on the order of 10 nm, which is much smaller than the length scale of the surface roughness of highly polished materials (micron or mm scale). In this case, δr is large enough for the incident and reflected fields have a precise phase relationship and the Debye-Waller formalism is appropriate [81]. Thus, the reflectance of our mirror can be modeled as:

$$\hat{r}^{\text{rough}} = \hat{r}^{\text{smooth}} \exp(-2k_{1,z}^2 \langle z^2 \rangle) \quad (2.19)$$

where $\langle z^2 \rangle$ is the variance of the interface height and $k_{1,z} = 2\pi \cos \theta_i / \lambda$ is the normal component of the wave vector in medium 1 (in our case, vacuum). To get a sense of scale, a high quality off-the-shelf optic will have a surface roughness of $\langle z^2 \rangle = \lambda/10 = 63.2$ nm, which is 5 times larger than the wavelength of a 100 eV photon. It is clear that we need to take advantage of specialized manufacturing techniques while working in the XUV. Below, we apply this basic framework to guide the selection of the basic materials and geometric properties of our XUV focusing optic.

The Metallic Coating

Figure 2.16 shows the Fresnel reflectance for various materials at a fixed 5 degree grazing angle (85 degree incident angle). From this figure, we can see that the materials properties strongly influence mirror performance at these energies. Aluminum (Al) has a sharp absorption feature at 72 eV which is undesirable for a reflective optic; tungsten (W) and iridium (Ir) have extended spectral features between 35 and 50 eV. Silver (Ag) has the best reflectance below 250 eV. Copper (Cu) has the flattest performance out to 400 eV, with very few spectral features. Gold (Au) has good performance below 200 eV and a relatively flat spectral response outside the 150 - 200 eV region.

Gold, silver and copper are good candidates for our desired spectral range. However, silver and copper can tarnish when exposed to atmosphere, which would change their reflectivity over time. Although the optic will be stored under vacuum, it will inevitably be exposed to air during transport, installation and whenever the beamline is vented. Due to

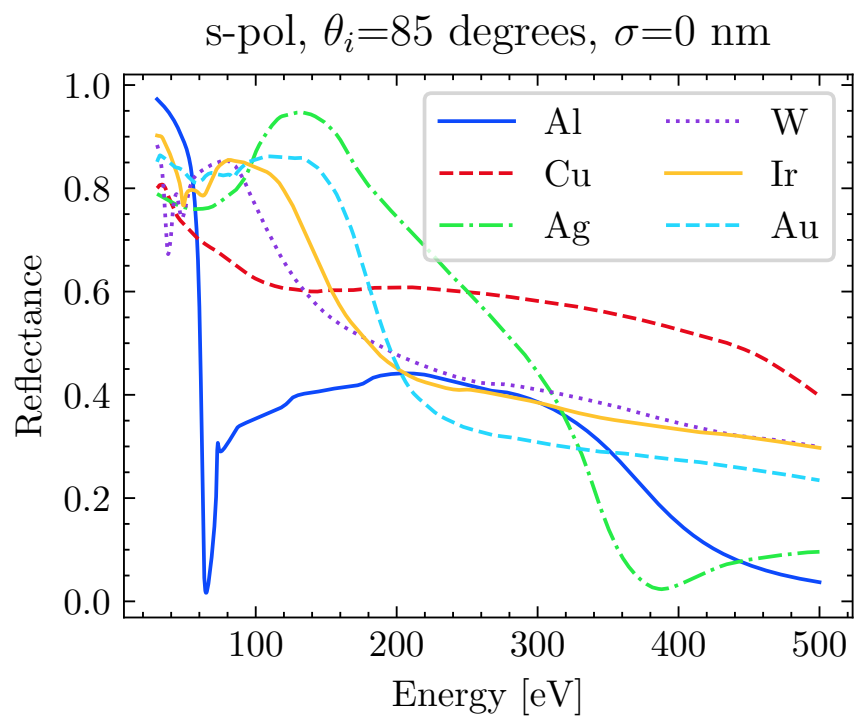


Figure 2.16: Fresnel reflectance for s-polarized light on smooth metal mirrors at a grazing angle of 5 degrees. Refractive index data obtained from [7, 11]. Calculation follows Eqs. (2.16) and (2.19).

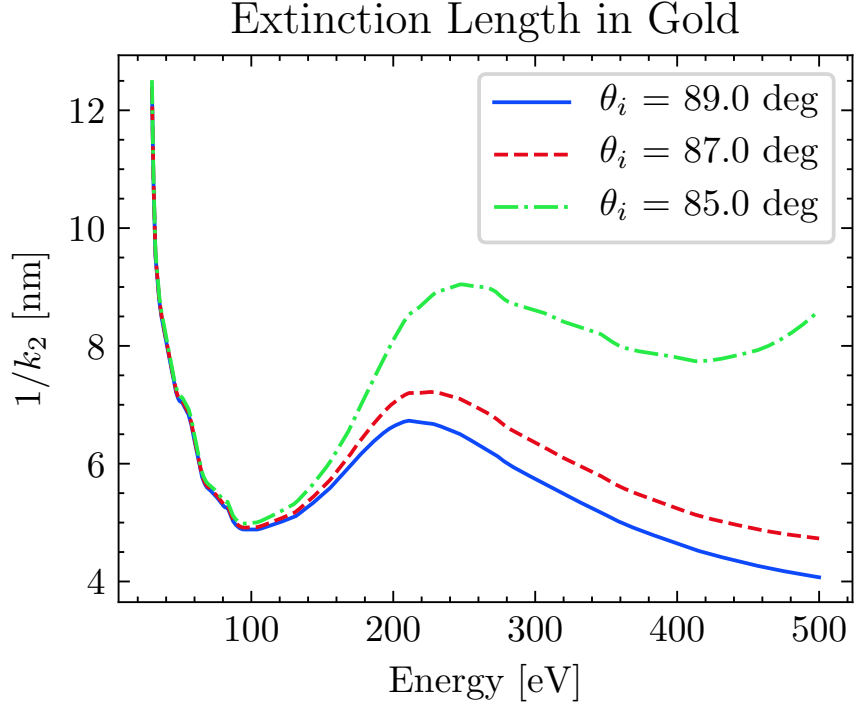


Figure 2.17: Extinction length in gold at various incident angles. Refractive index data obtained from [7, 11].

the extremely thin and fragile optical coating, it is not possible to clean the XUV optic if it becomes dirty, damaged or tarnished. Gold was chosen to maximize the lifetime of the optic.

The Fresnel analysis used above is valid for an infinitely thick medium, but one must question whether this is valid for a thin film gold coating. To answer this question, we plot the extinction length ($1/k_2$) in Fig. 2.17, with k_2 defined as $k_2 = (2\pi/\lambda) \sqrt{\sin \theta_i^2 - \text{Re } \hat{n}_2}$ [77]. We can see that above 30 eV, the extinction length remains below 13 nm; above 40 eV the extinction length is bounded by 10 nm. Based on this information, we decided to use the standard 40 nm coating offered by Zeiss. An adhesion layer (Cr) was applied to the substrate to prevent flaking of the gold coating. It should be noted that over time, the adhesion layer will diffuse into the gold and change the reflectivity.

Figure 2.18 shows the reflectivity of a single gold mirror for various incident angles. As expected, the best performance occurs at small grazing angles. However, for a fixed beam size, the required optic size increases as the grazing angle decreases. The footprint (area) F of a rectangular beam on the optic is given by the geometric projection [80]:

$$F = \frac{t_1}{\cos \theta_i} t_2. \quad (2.20)$$

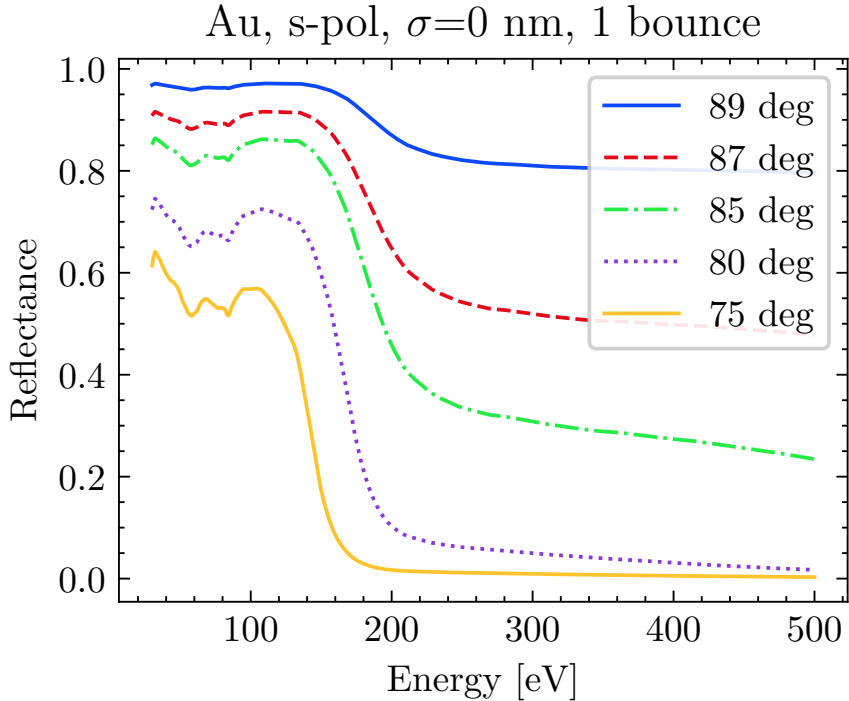


Figure 2.18: Fresnel reflectance for *s*-polarized light from a single smooth gold mirror as a function of incident angle. Calculation follows Eqs. (2.16) and (2.19).

Here, t_1 and t_2 are the rectangular dimensions of the input beam and θ_i is the incident angle of the light. If we do not scale the mirror size with the incident angle, we will clip the beam and lose XUV flux. Our desire to have a modular vacuum apparatus with a demagnifying XUV optic is therefore in direct conflict with our desire to have high XUV flux. The exit arm of the mirror, which is proportional to the demagnification factor, must be large enough so that the interaction region can be contained within a separate chamber from the rest of the beamline. We clearly cannot achieve the specifications of a typical x-ray mirror in a synchrotron facility (≈ 0.5 degree grazing angle, ≈ 1 m lateral dimension). Returning to Fig. 2.18, we can see that an 87 degree mirror drastically outperforms an 85 degree mirror above 200 eV, but according to Eq. (2.20), it will be 67% larger in the horizontal dimension. Larger mirrors have more mass, which increases the requirements for the *in vacuo* motorization, further increasing the cost and required chamber size. Finally, the manufacturing cost and lead time of the mirror is proportional to the polished area. Through an iterative design process involving the optical, motorization and vacuum chamber design elements, as well as Zeiss' manufacturing considerations, we decided to use an 85 degree mirror in the TABLE. This allowed us to place the interaction region in a separate chamber, minimized the cost of the mirror, and delivered better than 50% reflectivity below

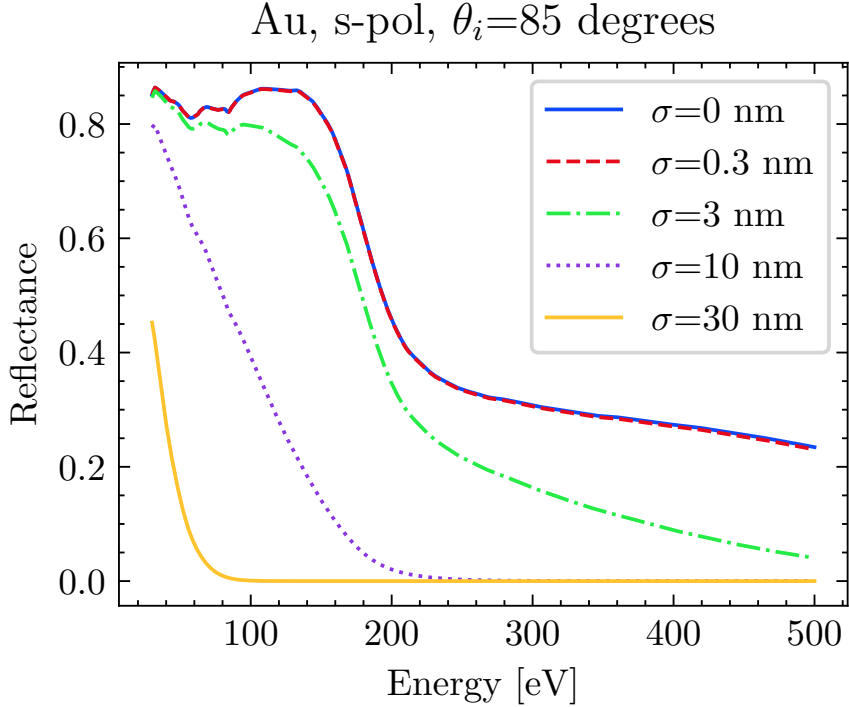


Figure 2.19: Effect of surface roughness on reflectance. Calculation follows Eqs. (2.16) and (2.19).

200 eV while utilizing small form factor motors and stages.

The effect of the surface roughness is shown in Fig. 2.19. When polishing glass surfaces, a surface roughness of 0.3 nm is considered state of the art and approaches a height variation of a single atomic layer. Below 500 eV, the difference between a surface with 0.3 nm roughness and an ideal interface is negligible.

2.4.3 Aberration-Free Focusing

XUV mirrors are typically simple rotational solids (cylinder, toroid, ellipsoid, etc.), and we considered several configurations during the planning stage. It is well known that reflective optics operating at grazing angles can cause aberrations at the focus. These aberrations introduce phase nonuniformity, smearing the XUV pulse out in time and reducing the effective temporal resolution of the apparatus [82]. Additionally, aberrations change the shape of the XUV focal spot, which results in a larger range of MIR intensities throughout the XUV-MIR interaction volume for a fixed MIR focusing geometry. Therefore it is critical to minimize or eliminate aberrations through optical design.

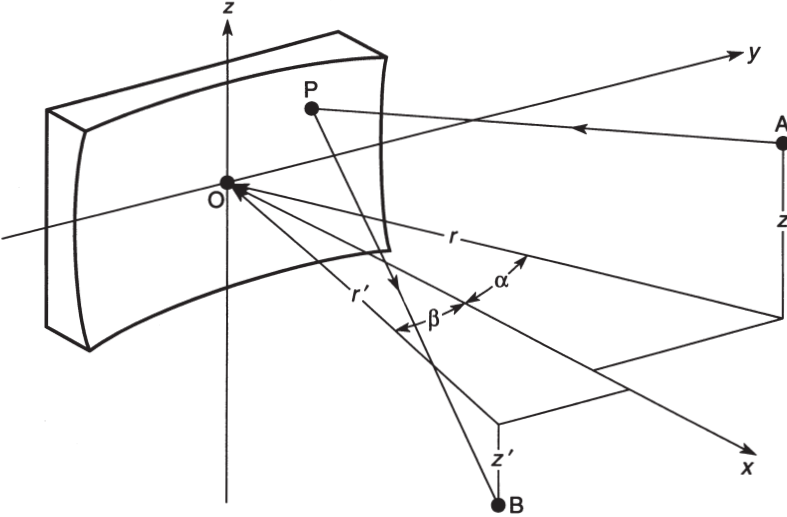


Figure 2.20: Coordinate system used for the light path function F . Source point A is located a distance r from the center of the mirror at angle α and height z . Focus point B is located a distance r' away, with angle β and height z' . The impact point P of an individual ray is located on the mirror surface at point $(y, z) = (w, l)$. The curvature of the mirror is used to calculate the distance x between $P(w, l)$ and the yz plane. Figure adapted from [12].

The Light Path Function

Aberrations are mathematically analyzed using the *light path function* [12, 83, 84]. Consider a reflective optic with an optical surface in the yz plane as shown in Fig. 2.20. The height of the optic surface x can be described by the following power series:

$$x = \sum_{i=0}^{\infty} \sum_{j=0}^{\infty} a_{ij} y^i z^j, \quad a_{00} = a_{10} = 0, \quad j = \text{even} \quad (2.21)$$

This expansion can be used to describe spherical, cylindrical, toroidal, ellipsoidal, or other aspheric surfaces given proper values of the coefficients a_{ij} .⁷ Now consider the situation shown in Fig. 2.20, where a ray is emitted from a point source A and passes through point B after reflecting off the surface of the optic at point P . The distance this ray travels is called the light path function, $F = \overline{AP} + \overline{PB}$. We are primarily concerned with aberrations at the focus which are proportional to the derivative of F with respect to impact coordinates w and l . So, we drop the zeroth-order constant $r + r'$ and perform a power series expansion

⁷Tables 2 and 3 in reference [12] provide a_{ij} values for an ellipsoidal and toroidal mirror, respectively.

i	j	0	1	2	3	4
0		0		S	0	$\frac{4a_{02}^2 - S^2}{r} - 8a_{04} \cos \alpha$
1		$-\sin \alpha$	0	$\frac{S \sin \alpha}{r} - 2a_{12} \cos \alpha$	0	*
2		T	0	$\frac{4a_{20}a_{02} - TS - 2a_{12} \sin 2\alpha}{r} + \frac{2S \sin^2 \alpha}{r^2} - 4a_{22} \cos \alpha$	0	*
3		$\frac{T \sin \alpha}{r} - 2a_{30} \cos \alpha$	0	*	0	*
4		$\frac{4a_{20}^2 - T^2 - 4a_{30} \sin 2\alpha}{r} + \frac{4T \sin^2 \alpha}{r^2} - 8a_{40} \cos \alpha$	0	*	0	*

Table 2.1: Values of $E_{ij0}(\alpha, r, 0)$ up to 4th order, used in the calculation of the light path function F . Terms in excess of 4th order are indicated by *. See text for definitions of S and T . Table adapted from [12].

with respect to the impact point $P(w, l)$:

$$\begin{aligned} F = & wF_{100} + wF_{102} + lF_{011} + \frac{1}{2}w^2F_{200} + \frac{1}{2}l^2F_{020} \\ & + \frac{1}{2}w^3F_{300} + \frac{1}{2}wl^2F_{120} + wlF_{111} + \frac{1}{8}w^4F_{400} + \frac{1}{4}w^2l^2F_{220} \\ & + \frac{1}{4}w^2F_{202} + \frac{1}{2}l^2F_{022} + \frac{1}{2}l^3F_{031} + \frac{1}{2}w^2lF_{211} + \dots \quad (2.22) \end{aligned}$$

This expression is valid for both mirrors and gratings, but it can be greatly simplified for our application. For a non-holographic grating, the coefficients of F must take the form $F_{ijk} = E_{ijk}(\alpha, r, z) + E_{ijk}(\beta, r', z')$. Next, if points A and B are within the symmetry plane of the mirror ($z = z' = 0$), then subscript k must be equal to zero. Finally, from the law of reflection, we have $\alpha = -\beta$. Putting it all together, the coefficients of the series expansion of F have the form:

$$F_{ij0} = E_{ij0}(\alpha, r, 0) + E_{ij0}(-\alpha, r', 0) \quad (2.23)$$

The values of $E_{ij0}(\alpha, r, 0)$ can be found in the literature and in Table 2.1. The terms S and T used in this table are defined below:

$$T = \frac{\cos^2 \alpha}{r} - 2a_{20} \cos \alpha \quad (2.24)$$

$$S = \frac{1}{r} - 2a_{02} \cos \alpha \quad (2.25)$$

Note that information about the shape of the mirror is connected to the F_{ij0} expansion coefficients via the a_{ij} mirror surface expansion coefficients. Therefore, we can apply this framework to calculate the aberrations at the focus for a given mirror shape and geometry.

A consequence of Fermat's Principle of Least Time is that F will be an extrema for any

point P on the mirror's surface. Therefore, aberration-free image focusing can be obtained if $\delta F/\delta w = \delta F/\delta l = 0$. This condition must hold for any value of w and l on the mirror's surface, from which it follows that all F_{ij0} terms are identically zero. We can quantify aberrations at the focus using a geometric ray approximation, in which we calculate the displacements of the rays from the image point B :

$$\begin{aligned}\Delta y'_{ij0} &= \frac{r'}{\cos \alpha} \left(\frac{\delta F}{\delta w} \right)_{ij0} \\ \Delta z'_{ij0} &= r' \left(\frac{\delta F}{\delta l} \right)_{ij0}\end{aligned}\tag{2.26}$$

The total ray aberration in the $\Delta y'$ ($\Delta z'$) direction is the algebraic sum of the above terms for all values of i and j . Therefore, the total ray aberration (to 4th order) is:

$$\begin{aligned}\Delta y' &= \frac{r'}{\cos \alpha} \left(F_{100} + F_{200}w + \frac{1}{2}F_{120}l^2 + \frac{3}{2}F_{300}w^2 + \frac{1}{2}F_{400}w^3 + \frac{1}{2}F_{220}wl^2 \right) \\ \Delta z' &= r' \left(F_{020}l + F_{120}wl + \frac{1}{2}F_{220}w^2l + \frac{1}{2}F_{040}l^3 \right)\end{aligned}\tag{2.27}$$

We now have expressions for the aberrations as a function of the shape of the XUV mirror, which will be applied to different mirror configurations.

Toroidal Mirrors

A toroidal mirror is a section of the interior surface formed by a torus (similar to a bicycle tire) described by radii R and ρ . There are many advantages to using a toroid in an XUV beamline. Toroidal mirrors operated in a $2f - 2f$ configuration can re-image the source point without introducing any aberrations at the focus [63]. Additionally, the toroid's constant curvature allows it to be manufactured to a higher degree of accuracy than other shapes [12]. As a result they are very affordable, starting as low as \$5,000.

The toroidal mirror can be designed to reduce aberrations. Owing to its symmetry, a toroid naturally has $F_{100} = F_{120} = 0$. An analysis of the F_{ij0} expansion coefficients reveals F_{200} and F_{020} will also equal zero if the toroid's radii are set to the following values:

$$\begin{aligned}\rho &= \frac{2rr' \cos \alpha}{r + r'} \\ R &= \frac{2rr' \sec \alpha}{r + r'}\end{aligned}\tag{2.28}$$

With these radii, the remaining non-zero terms of Eq. (2.22) are $F_{040}, F_{220}, F_{300}$ and F_{400} . Introducing the *demagnification factor* $M = r/r'$, the non-zero terms have the following

values:

$$\begin{aligned}
F_{300} &= - \left(\frac{M^2 - 1}{M} \right) \frac{\cos^2 \alpha \sin \alpha}{2(r')^2} \\
F_{040} &= - \frac{(M^2 - 1)(M + 1)}{M^3(r')^3} \\
F_{220} &= \frac{2(M^3 + 1) - (3M^3 - M^2 - M + 3) \cos 2\alpha}{4M^3(r')^3} \\
F_{400} &= - \frac{(1 + M) \cos^2 \alpha [-4 + 6M - 4M^2 + (5 + M(-8 + 5M)) \cos 2\alpha]}{4M^3(r')^3}
\end{aligned} \tag{2.29}$$

Recalling Eq. (2.27), we see that F_{300} corresponds to a second-order aberration, and F_{040}, F_{220} and F_{400} correspond to third-order and fourth-order aberrations. For the special case of $M = 1$, Eq. (2.29) simplifies to:

$$\begin{aligned}
F_{300} &= 0 \\
F_{040} &= 0 \\
F_{220} &= \frac{2 \sin^2 \alpha}{(r')^3} \\
F_{400} &= \frac{2 \cos^2 \alpha \sin^2 \alpha}{(r')^3}
\end{aligned} \tag{2.30}$$

So, the toroid only has third-order aberrations if $M = 1$, but second-order aberrations exist if $M \neq 1$.

Simulations of a demagnifying ($M = 3$) toroidal mirror were performed using numerical complex ray tracing techniques, implemented via Photon Engineering's FRED software [13, 85]. The results of this simulation are shown in Fig. 2.21. We can see strong aberrations are present at the focus that would be detrimental to the performance of the TABLe apparatus. For this reason, we decided against using a toroid in our beamline.

Spherical Mirrors

It is well known that spherical mirrors introduce significant aberration when operated away from normal incidence [12]. This is because a spherical mirror is simply a toroidal mirror with equal radii of curvature ($R = \rho$). For this reason, we did not pursue a spherical mirror solution.

Dual Mirror Configurations

Introducing a second XUV optic can counteract the aberrations introduced by the first [12]. The most common configuration is the Kirtpatrick-Baez (KB) mirror pair, which is commonly used in synchrotrons [86]. A KB mirror pair consists of two cylindrical mirrors

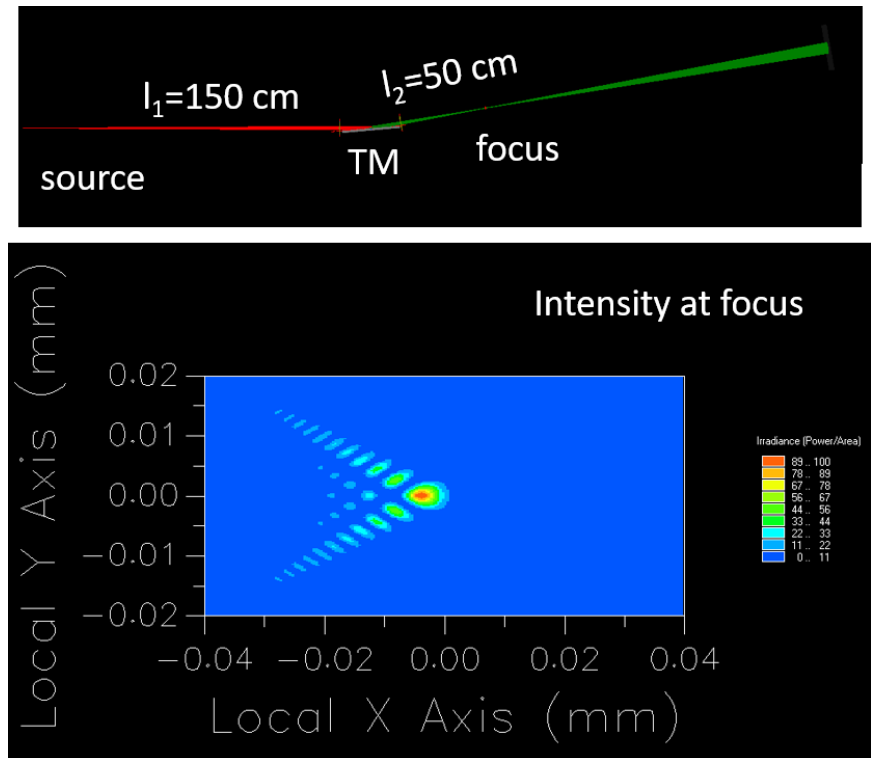


Figure 2.21: Complex ray tracing simulation showing severe aberrations at the focus of a demagnifying toroidal mirror (TM). The entrance arm l_1 is 150 cm, the exit arm l_2 is 50 cm, and the grazing angle is 5 degrees. Top panel: overhead view of the simulation showing the source rays (red) and the focused rays (green). Bottom panel: intensity at the focal plane in arbitrary units. Calculations were performed using Photon Engineering's FRED software [13].

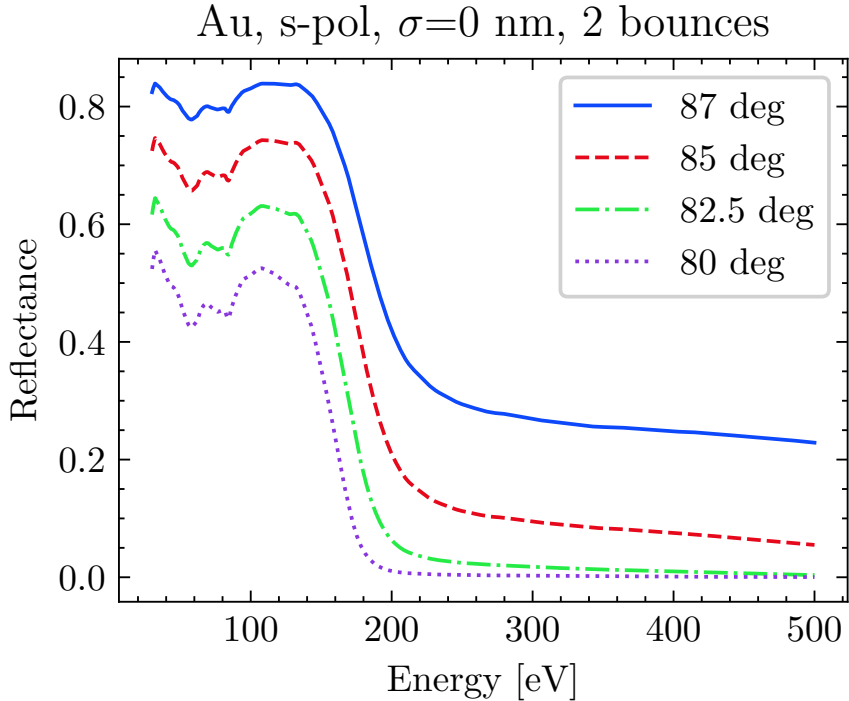


Figure 2.22: Fresnel reflectance for *s*-polarized light from two smooth gold mirrors as a function of incident angle. Calculation follows Eqs. (2.16) and (2.19).

with the normal direction of their optical surfaces placed orthogonally to each other and the beam propagation direction. In this geometry, each mirror focuses along one direction, and together they act as a single optic that focuses in both transverse directions. Another option is a dual toroid configuration, which has a real focus located between the two mirrors [84]. Both of these ideas were considered but ultimately deemed impractical.

Figure 2.22 illustrates the problem with a dual optic design design. Two 85 degree optics have a reflectance of only 20% at 200 eV, and have at least twice the footprint as a single 85 degree optic. To achieve the performance of a single 85 degree optic at 200 eV, the mirror pair needs to be operated at 87 degrees. As discussed above, this 87 degree pair will be 3.33 times larger than a single 85 degree optic in the beam propagation direction. On the other hand, if we want our two mirror configuration to maintain the footprint of a single 85 degree optic, it needs to be operated at 80 degrees. This geometry yields a reflectivity of only 1% at 200 eV, which is insufficient for our experimental requirements. Clearly, a single-optic solution is preferable.

Ellipsoidal Mirrors

We can apply the same light path function analysis to the ellipsoidal mirror. If we do the analysis, we will see that most of the terms in Eq. (2.22) are identically zero. The only non-zero term is F_{220} , which evaluates to:

$$F_{220} = \frac{(1+M)[-3-M(2+3M)+3(M-1)^2\cos 2\alpha](\cot \alpha + \tan \alpha - 2)}{16M^3(r')^3}. \quad (2.31)$$

As a result, the light path function for an ellipsoid is simply $F = \frac{1}{4}w^2l^2F_{220}$. Therefore, the largest aberrations from an ellipsoid are third-order in the aberration expansion, which is a significant improvement upon the performance of a toroidal mirror.

We have shown that an ellipsoidal mirror is able to demagnify a point source without introducing significant aberrations at the focus. As a single optic solution, it avoids the reflectivity losses of a dual mirror configuration. However, its variable radius of curvature provides manufacturing challenges that have only been overcome in the past several years [87]. This requires the use of special manufacturing techniques that significantly raise the cost and lead time of the optic. At the time of purchase, Carl Zeiss Laser Optics GmbH was the only company that could manufacture and verify the shape of an ellipsoidal mirror that met our technical requirements.

The shape of the rotational ellipsoid can be completely described by three parameters: the two semiaxes (a, b) and the horizontal⁸ off-axis position y_M . An alternative set of parameters are the entrance and exit arm lengths (l_1, l_2) and the grazing angle α . Additionally, the spatial extent (clear aperture) of the optic is specified by the tangential length L and the out-of-plane width W . Below, we will show how these quantities are related.

In a Cartesian coordinate system, an ellipsoid of revolution is described by parameters a and b :

$$\frac{x^2}{a^2} + \frac{y^2 + z^2}{b^2} = 1 \quad (2.32)$$

where the xy plane is the (horizontal) optical plane and z is the direction orthogonal to the optical plane (vertical).⁹ Due to the symmetry between y and z , much of the analysis can be done in the optical plane ($z = 0$):

$$\frac{x^2}{a^2} + \frac{y^2}{b^2} = 1 \quad (2.33)$$

In the xy plane, the surface of the mirror is a segment of the curve formed by Eq. (2.33), which is shown in Fig. 2.23. The center of the mirror (off-axis position) is denoted by

⁸Our mirror has vertical symmetry, so $y_M = 0$.

⁹Note that this coordinate system differs from the one used to describe the mirror surface in the previous section.

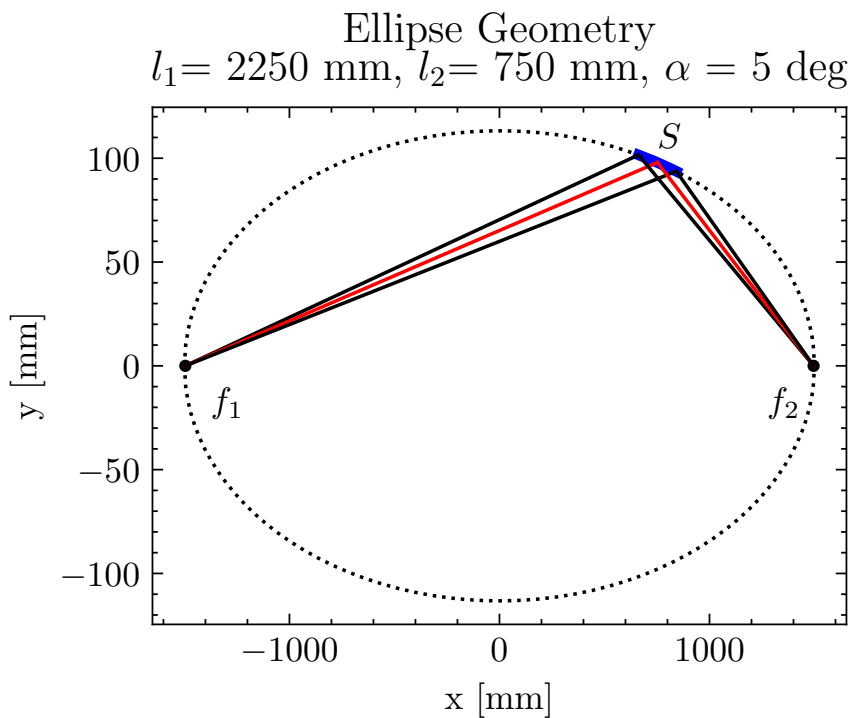


Figure 2.23: Overhead view of the ellipsoidal mirror geometry used in our beamline. Mirror surface S is shown in blue; foci $f_{1,2}$ are represented by black dots. Rays that strike the center (red) and the edges (black) of the mirror are depicted as lines. Vertical scale is enlarged to show detail. Drawing is otherwise to scale to match the dimensions in Table 2.2.

substrate		
surface geometry	concave rot. ellipsoid	
material	fused Silica HOQ310	
dimensions ($L \times W \times H$)	240 × 76 × 45 ± 0.2 mm	
optical surface		
clear aperture ($L \times W$)	180 × 16 mm	
footprint geometry	rectangular	
geometry parameters		
semiaxis a	1500 mm	alternative set
semiaxis b	113.219 mm	entrance arm l_1 2250 mm
off-axis position x_M	752.146 mm	exit arm l_2 750 mm
surface quality		
tangential slope error	≤ 2.0 arcsec (rms)	grazing angle 5 deg
sagittal slope error	≤ 10.0 arcsec (rms)	
mid spatial frequency roughness	≤ 0.3 nm (rms)	
coating material		
40 ± 5 nm Au w/ Cr binding layer	spatial sampling rate	
	2 – 180 mm	
	2 – 16 mm	
	1.0 – 200 μm	

Table 2.2: Specifications of the ellipsoidal mirror. Data provided by Carl Zeiss Laser Optics GmbH.

$(x, y) = (x_M, y_M)$. The ellipse has eccentricity ϵ ,

$$\epsilon = \sqrt{1 - \frac{b^2}{a^2}}, \quad (2.34)$$

and focal points at positions $(x, y) = (\pm a\epsilon, 0)$. Consider a light source at the first focal point, $f_1 = (-a\epsilon, 0)$: rays emanating from f_1 will strike surface of the ellipse at some point $S = (x_0, y_0)$ and focus to $f_2 = (a\epsilon, 0)$. This optical system has an entrance arm $l_1 = f_1 S$, exit arm $l_2 = S f_1$, and demagnification M given by:

$$l_1 = \sqrt{(x_0 + a\epsilon)^2 + y_0^2} \quad (2.35)$$

$$l_2 = \sqrt{(x_0 - a\epsilon)^2 + y_0^2} \quad (2.36)$$

$$M = \frac{l_1}{l_2} \quad (2.37)$$

Once the f_1 , f_2 and S are defined, the grazing angle α of reflection can be found by applying the Law of Cosines:

$$\alpha = \frac{1}{2} \arccos \left(\frac{(2a\epsilon)^2 - l_1^2 - l_2^2}{2l_1 l_2} \right) \quad (2.38)$$

Our Ellipsoidal Mirror

We used the results of the previous sections to specify the parameters of our XUV mirror, which can be found in Table 2.2. A picture of the mirror can be seen in Fig. 2.12. A rotational ellipsoid was chosen for its aberration-free focusing when used in a demagnifying geometry. A demagnification factor of $M = 3$ and a grazing angle of 5 degrees were chosen because they represent a compromise between our optical requirements of high flux at high photon energies and the mechanical limitations of a modular beamline. When performing ATAS experiments, this demagnification factor gives us a $\simeq 50\%$ signal improvement compared to a 1-to-1 geometry (see Section 4.3.1 for details). The exit arm was set to be as short as possible while keeping the mirror and target chambers separate, which resulted in an exit arm of 750 mm. A substrate with a 0.3 nm microroughness and a gold coating delivers excellent reflectivity out to 300 eV.

The clear aperture was chosen to match the expected footprint of the harmonics on the optic divergence of the harmonics, which we assumed would have a half-angle divergence of 3.5 mrad. This resulted in a polished region of size 180×16 mm with an rms roughness of 0.3 nm. A 30 mm border region surrounds this area with a moderately high polish. Zeiss estimates that the surface roughness smoothly increases from the specified 0.3 nm at the edge of the clear aperture to 3 nm at the edge of the substrate.

The finite spatial extent of a physical mirror will result in a range of grazing angles across its surface, as shown in Fig. 2.24. For our mirror, the grazing angle ranges from 4.8 to 5.25 degrees, which does not significantly change the reflectance shown in Fig. 2.18. Finally, the spatially resolved height error is shown in Fig. 2.25, which shows the excellent manufacturing tolerances of our mirror's surface.

2.4.4 Metallic Filters

We use a thin metallic filter in transmission geometry to block the infrared field after the HHG process (located in chamber F_1 in Fig. 2.8) and shape the XUV spectrum. The XUV transmission of the most commonly used filters is shown in Fig. 2.26. Aluminum is favored for experiments below 100 eV, zirconium is useful between 70 and 160 eV, and tin is best suited above 160 eV.

2.5 MIR Optics

Next, we discuss the infrared optics used in the generation and pump arms. This includes the optics used for generating harmonics in the generation arm; in the pump arm we have the pulse energy and delay control optics and the focusing optics. We also have the beamsplitter and the hole mirror, which mark the beginning and end of the interferometer, respectively.

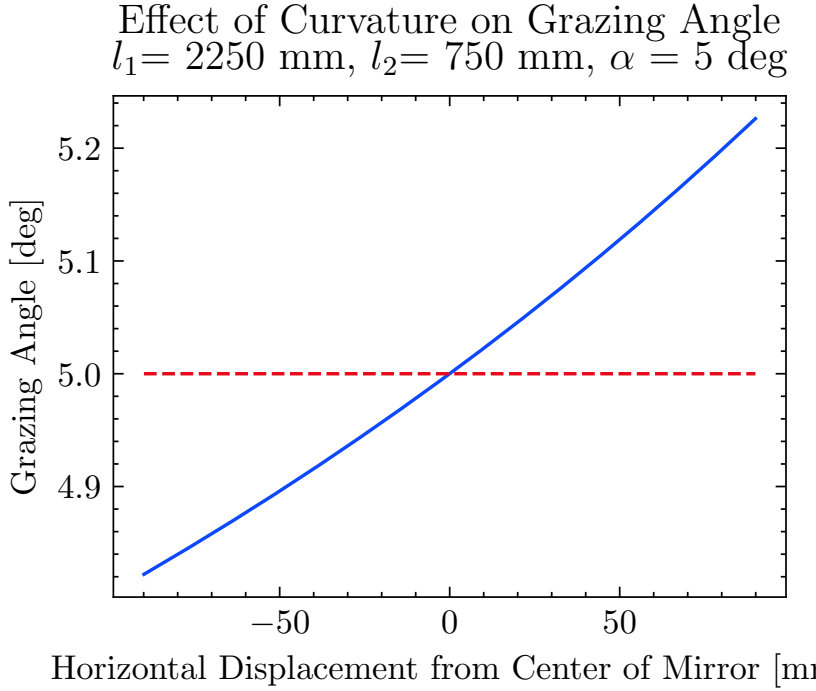


Figure 2.24: The effect of curvature on the local grazing angle along the mirror's symmetry axis ($z = 0$). Light that strikes the edges of the mirror will experience a slightly different grazing angle than the design angle.

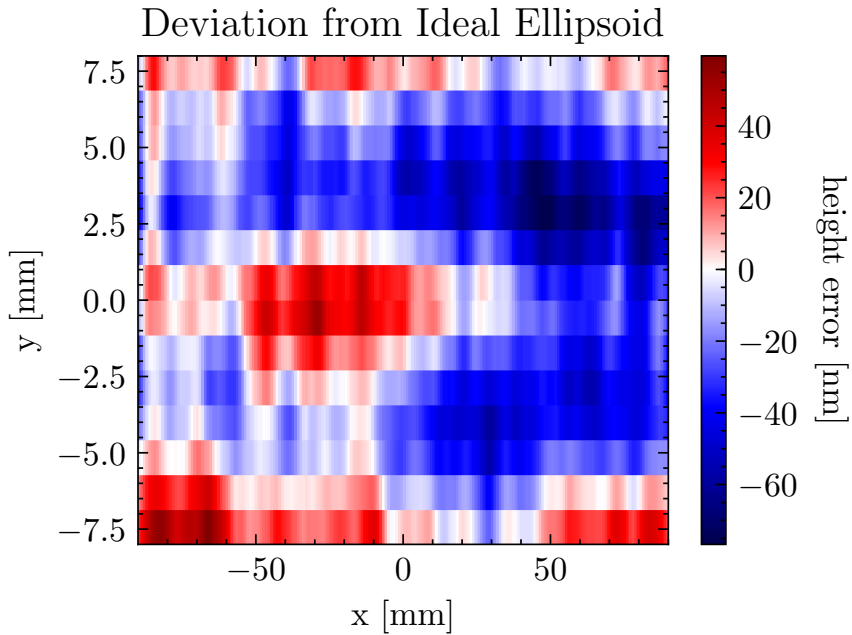


Figure 2.25: Height deviation of our ellipsoidal mirror from an ideal surface, as measured by a Carl Zeiss M400 precision tactile measurement device. Data provided by Carl Zeiss Laser Optics GmbH.

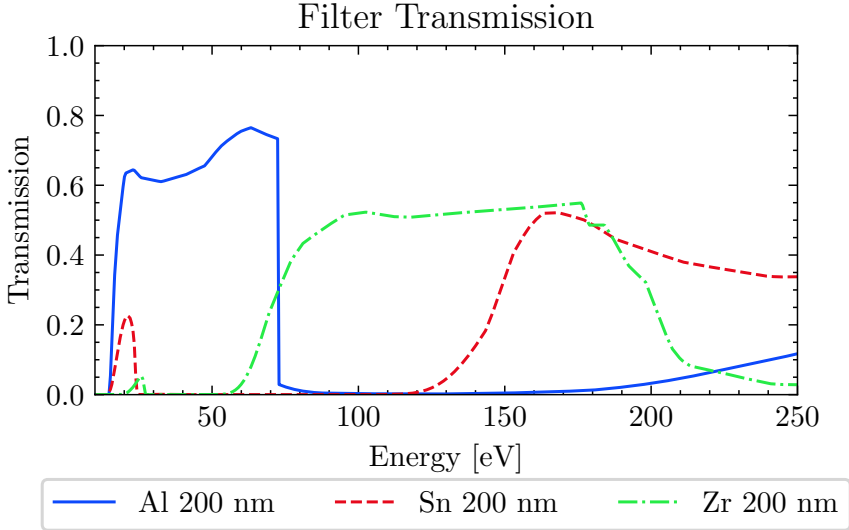


Figure 2.26: Calculated XUV transmission of various metallic filters. Data from [7].

We wanted the infrared optics to be as achromatic as possible, which would allow us to perform wavelength scans using the TOPAS, or to switch from the signal to the idler or the depleted 800 nm pump without having to completely rebuild the interferometer. Additionally, we wanted the ability to easily access the pump arm's optics, which meant keeping the pump arm out of vacuum until right before recombination with the XUV arm. This has the extra benefit of allowing future exotic upgrades to the pump arm, such as THz generation, DFG, SHG, etc. With the exception of the hole mirror, all MIR optics are outside the vacuum system.

2.5.1 The Generation Arm

We use 2" diameter silver optics throughout the beamline unless otherwise specified. As a future upgrade, we purchased high reflectivity dielectric mirrors (Lambda Optics BHR-5012B-1200-1600-45U, coated for $\lambda = 1.2 - 1.6 \mu\text{m}$) for use with the signal wavelengths.

The generation arm takes the transmitted light from a 4% reflected / 96% transmitted beamsplitter (BS, Thorlabs UVFS BSF20-C). A telescope (L1, $f = -300 \text{ mm}$; L2, $f = +500 \text{ mm}$) enlarges the beam, allowing for tighter focusing in the generation chamber, which is useful when operating at longer wavelengths, where the TOPAS is less efficient. A focusing lens (L3, $f = 400 \text{ mm}$) and an adjustable aperture (iris) are located immediately before a CaF₂ window (3 mm thick) on the entrance flange of the generation chamber. The distance between the outer surface of the CaF₂ window and the center of the chamber is 23.8 cm. This geometry supports focal lengths 30 cm or longer outside the chamber. It is possible to mount shorter focal length optics inside the generation chamber using the

internal breadboard. There is enough room outside the chamber to implement an $f = 40$ cm reflective focusing setup, but reflective setups using shorter focal lengths will require in-vacuum optics or modifications to the chamber. A metallic filter blocks the MIR light about 1 meter after the MIR focus (chamber F_1 in Fig. 2.8).

A computer controlled home-built shutter (S in Fig. 2.15) is located before telescope. This shutter is used to block the laser, which is useful when performing certain operations (finding overlap, moving the sample holder in the target chamber, manipulating the filter assembly, etc.).

For experiments that require additional harmonic bandwidth, we insert additional optics (a BBO crystal, 200 μm of calcite, and a zero-order 1310 nm $\lambda/2$ waveplate) between $L3$ and the vacuum window. When aligned correctly, these optics create a spatially and temporally overlapped ω and 2ω fields at the focus.

2.5.2 The Pump Arm

The pump arm takes the reflected light (4%) from the beamsplitter and propagates in air on the upper deck of the split-level optical table.

A 1 μm longpass filter (Thorlabs FELH1000, OD > 5) is positioned before the waveplate-polarizer assembly to filter out the OPA's visible parasitic wavelengths. This is necessary to suppress short-wavelength excitation of condensed matter samples. The MIR intensity incident on the sample is controlled by a motorized achromatic $\lambda/2$ waveplate (Thorlabs AHWP10M-1600, $\lambda = 1100 - 2000$ nm) and a pair of ultra broadband wire grid polarizers (Thorlabs WB25M-UB, each with a 1000:1 extinction ratio for $\lambda = 0.6 - 4 \mu\text{m}$) in the pump arm (see Fig. 2.15).

The XUV-MIR delay is coarsely adjusted using a retroreflector on a manual translation stage, with $\Delta\tau = 2\Delta x/c = 6.67 \ [\text{fs}/\mu\text{m}] \Delta x$. Motorizing this retroreflector could enable the study of ps-scale dynamics. Fine delay control is achieved by sending the laser through a pair of fused silica (Infrasil) opposing wedges. The insertion amount of one wedge into the beam path is controlled by a stepper motor, while the other wedge is fixed in place. Inserting the wedge by an amount Δx increases the thickness of glass in the beam path, delaying the pump arm by an amount $\Delta\tau$ [54]:

$$\Delta\tau = \frac{\Delta x}{c} \left[n \tan \theta - \frac{\sin \theta}{\cos \varphi} - n \tan \theta \left(\frac{\sin (\varphi - \theta)}{\cos \theta} \right) \right] \quad (2.39)$$

where n is the refractive index of the wedge material, θ is the wedge angle and $\varphi \equiv \arcsin(n \sin \theta)$ is calculated from Snell's law. For $\lambda = 1430$ nm and $\theta = 4.5$ degrees, $n = 1.4454$ [68] and Eq. (2.39) evaluates to:

$$\Delta\tau = \left(102 \left[\frac{\text{as}}{\mu\text{m}} \right] \right) \Delta x \quad (2.40)$$

A translation range of $\Delta x = 14$ mm provides a delay range of $\Delta\tau = 1.4$ ps.

During an experiment, the intensity is measured using an InGaAs photodiode (Thorlabs DET10D) mounted with a OD = 2.0 absorptive neutral density filter and 1 μm longpass filter (Thorlabs FELH1000), which detects light scattered off a mirror in the pump arm and is monitored using an oscilloscope (LeCroy). Absolute measurements of the average MIR power are taken with a power meter (Gentek) located before the diverging lens L4. A computer controlled home-built shutter S is located after the photodiode so that the intensity can be adjusted while the pump arm is blocked.

We use a pair of AR-coated N-BK7 lenses ($\lambda = 1050 - 1700$ nm) in the pump arm to minimize the losses from the hole mirror. Diverging lens L4 (Thorlabs LF1015-C, $f = -300$ mm) expands the beam and converging lens L5 (Thorlabs LA1380-C, $f = +500$ mm, located 68.5 cm after L4) focuses it into the target chamber. After L5, the MIR beam passes through a 3 mm thick CaF_2 window to enter the mirror chamber.

The two arms of the interferometer are combined using a hole mirror (HM), located 53 cm after L5 and 20 cm after the ellipsoidal mirror. The hole mirror is a 2" diameter silver mirror with a 10 mm diameter aperture in the center [88]. The XUV light passes through the aperture from the backside of the mirror, and the MIR light reflects off the annular disk on the front face. This geometry allows us to have a collinear XUV-MIR geometry without having to resort to bandwidth limiting XUV-MIR optics. However, this geometry clips the center of the MIR beam and is responsible for MIR diffraction at the focus.

Calculation of MIR intensity at Focus

The spatial intensity profile $I_0(x, t)$ of the $\lambda=1500$ nm TOPAS pulse was measured immediately before the pump arm's diverging lens (L4 in Fig. 2.15) using an Electrophysics PV320 thermal camera. We numerically calculated the transverse profile of the MIR pulse at the focus $I_{\text{diff.}}(x, y)$ by successively applying several operators to $I_0(x, t)$:

$$I_{\text{diff.}}(x, y) = \mathbf{M} I_0(x, y), \quad (2.41)$$

with $\mathbf{M} \equiv \mathbf{L}^+(d_{\text{focus}}) \mathbf{A}_{\text{HM}} \mathbf{L}^+(d_{\text{HM}}) \boldsymbol{\tau}(f_5) \mathbf{L}^+(d_{4,5}) \boldsymbol{\tau}(f_4)$.

In the above, $\mathbf{L}^+(d)$ is the free-space propagation operator for distance d under the Fresnel approximation evaluated using an FFT method, $\boldsymbol{\tau}_f$ is the complex transmittance of a lens of focal length f (see Eq. (1.47)), and \mathbf{A} is a spatially-dependent amplitude mask. This calculation was performed using the Python package *Lighthpipes for Python* [60] using a grid size of $2^{13} \times 2^{13}$, and the result is shown in Fig. 2.27. Clear apertures of 22.86 mm (L4), 45.72 mm (L5) and 50.8 mm (HM) were used for this calculation. The focal lengths were $f_4 = -300$ mm, $f_5 = +500$ mm and the distances were $d_{4,5} = 68.5$ cm, $d_{\text{HM}} = 53$ cm, $d_{\text{focus}} = 48.63$ cm. The input profile $I_0(x, y)$ was assumed to have 1 μJ of energy and a

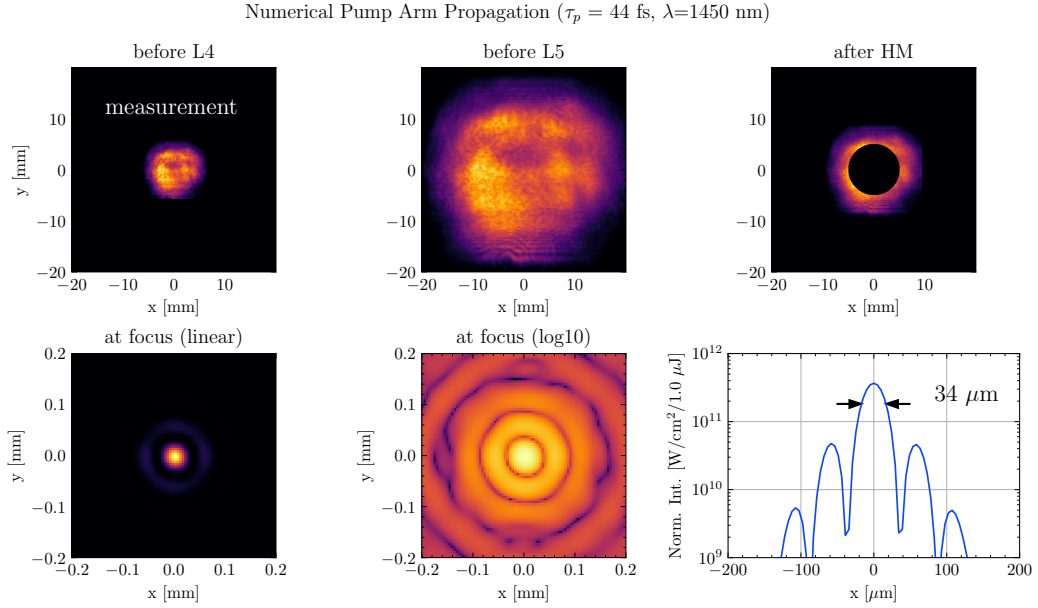


Figure 2.27: Numerical propagation of the MIR ($N = 2^{13}$, $\lambda=1450$ nm, $\tau_p = 44$ fs) beam through the pump arm for vacuum ($n = 1$). The beam path layout follows Fig. 2.15. From top left to bottom right, each panel shows the intensity profile of the beam as the beam propagates towards the focus. The top left panel shows the measured intensity and the remaining panels are calculations. The peak intensity at the focus is $3.68 \times 10^{11} \text{ W/cm}^2$ per $1 \mu\text{J}$ input energy.

$\tau_p = 48$ fs (FWHM) Gaussian temporal profile.

Reflection losses from 2 Ag mirrors, 2 AR-coated lenses and uncoated CaF₂ vacuum window are responsible for a 26.2% reduction in transmitted power. Additionally, the geometry of the hole mirror causes only 56% of incident power to be incident on a reflective surface (the rest is lost to the central aperture). In total, the pump arm transmits 41.3% of the power from before L4 to the focus.

The MIR intensity makes an Airy-like diffraction pattern at the focal plane. There is an intense bright spot surrounded by a series of rings, with the intensity of each ring decreasing as the distance from the center increases. The rings exhibit a periodic modulation in intensity with respect to angle ϕ . This four-fold symmetry is due to the square-like spatial profile of the TOPAS output, whereas the clipping from the hole mirror's aperture is responsible for the central peak and ring structure. The central lobe has a peak intensity of $\sim 3.68 \times 10^{11}$ W/cm² per 1 μ J input pulse energy and a FWHM of 34 μ m. The first ring has a radius of 59 μ m and a peak intensity $\sim 4.8 \times 10^{10}$ W/cm² per input μ J pulse energy. Thus the central lobe's peak intensity is about an order of magnitude larger than the ring's intensity. However, the central spot only contains about 49% of the total power, as the rings cover a much larger area.

Note that the above calculations assume perfect alignment into the hole mirror (i.e., the MIR beam is centered on the central aperture of the hole mirror). If the MIR beam is misaligned to the hole mirror, then the transmission to the focus will increase as the most intense part of the beam is no longer clipped by the central aperture. Therefore, a drift in the laser's pointing during an experiment can affect the sample's interaction intensity.

2.5.3 Aligning into the TABLE Interferometer

We use an Electrophysics PV320 thermal camera for daily alignment into the TABLE interferometer.¹⁰ The camera is located between S and L4, and we use two irises (the 1st is located between BS and CF, the 2nd is located just before S) to define the aligned beam path. Two motorized mirror mounts located on the TOPAS table control the pointing of the input beam. The beam is considered to be aligned when the Airy rings from the partially closed 1st iris are centered on the 2nd iris, and when the centroid of the beam is centered on the 2nd iris. Alignment is achieved by iteratively correcting the beam pointing while checking these two metrics.

¹⁰Special thanks to Eric Moore who wrote a LabVIEW program to semi-automate this process.

2.6 XUV Photon Spectrometer

2.6.1 Optical Description

Below is a brief overview of the XUV photon spectrometer's optics. For a complete description, see [54].

The XUV spectrometer utilizes one of two available concave variable line spaced (VLS) Hitachi gratings, depending on the desired spectral range. Owing to their small grazing angles (1200 lines/mm: 3 deg, 2400 lines/mm: 1.3 deg), they spectrally disperse the light in the horizontal plane while maintaining the vertical spatial profile. The groove spacing is engineered to a flat field across a wide spectral range (1200 lines/mm: 5 - 20 nm, 2400 lines/mm: 1-5 nm). Outside this spectral range, the gratings continue to disperse the light but the focal plane is no longer within the specified flat field. By adjusting the incident angle, we can control both the entrance arm and the flat field spectral range.

The dispersed light hits a 75 mm diameter imaging microchannel plate array¹¹ (MCP, Photonis) which converts the XUV photons into an electron shower via an avalanche process [89, 90]. A type P47 phosphor screen (P, Photonis) converts the spatially-resolved electron shower into light (370 - 480 nm range, peaked at 400 nm), which is sent outside the chamber via a glass window. The MCP-P assembly is mounted directly to an 8" flange, which is connected to the chamber via an edge welded bellows. An external mechanical assembly controls the angle and position of the detector array relative to the grating. The detector position is adjusted in conjunction with the grating's incident angle to make the flat field coincident with the detector plane for a given spectral range.

A computer-controlled digital 16-bit CMOS camera (Andor Neo DC-152Q-C00-FI) is equipped with a Rodagon 50 mm lens with an adjustable aperture and modular focus (QI Optiq) to image the output light of the phosphor. The camera image is recorded to the TABLE computer's hard drive. The camera images have a maximum resolution of 2560×2160 ($6.5 \mu\text{m}$ pixel size) with a sensor size of 16.6×14.0 mm.

2.6.2 Spectral Calibration

The photon spectrometer measures XUV counts as a function of position along the camera sensor (i.e., in the spectral pixel basis p). Owing to the grating equation, the position in the spectral pixel basis is proportional to the photon wavelength λ and inversely proportional to the photon energy E . However, the position of the detector relative to the grating (set by the cage & crank and the grating's piezo motors) introduces geometric factors which shift and skew the position of the light on the sensor. It is not practical to measure the

¹¹We use an imaging MCP to get a spatially- and spectrally-resolved two dimensional signal from our spectrometer. This is in contrast to a metal anode MCP, which integrates the signal across the detector's surface and records a zero-dimensional signal (voltage or current).

exact distances between these two elements, so we perform a numerical fit.

Generally speaking, we calibrate the spectrometer by assigning energies E_i to known spectral features in the data located at spectral pixel p_i . These features can be absorption features, resonances, or the harmonics themselves. This yields a set of coordinate pairs $\{(p_i, E_i)\}$ that can be fit to a polynomial $E(p)$. Below, we will discuss the methods used to create these coordinate pairs.

One-Source Harmonic Counting Scheme

The most prominent spectral features on the detector are the harmonics themselves. If we have more than an octave of XUV bandwidth, then we can exploit the grating equation and the regular spacing of the harmonics to determine the order of every harmonic on the detector. Below, we will explain this process.

First, consider the grating equation:

$$d(\sin \theta_i - \sin \theta_m) = m\lambda \quad (2.42)$$

where θ_i is the incident angle, θ_m is the diffraction angle, m is the diffraction order, and λ is the photon wavelength. Inspection of Eq. (2.42) reveals that a light of a particular wavelength will appear at multiple locations on the detector, corresponding to each diffraction order ($m = 1, 2, 3, \dots$). The grating is designed to deliver most of the light to the 1st order, but an appreciable amount of energy winds up in the 2nd and 3rd orders [54, 75].

We will assume that over the spectral region of interest, the wavelength of the i^{th} harmonic is $\lambda_i = \lambda_1/i$, where λ_1 is the effective fundamental wavelength. That is, we assume that all of the harmonics on the detector have the same fundamental wavelength and are evenly spaced in energy. Furthermore, we will assume that only odd-order harmonics are present during the calibration step.

As a result of the equal harmonic spacing and having more than an octave of XUV bandwidth, there will be regions of the detector that have light from both 1st and 2nd order diffraction. From the grating equation, a 1st order diffraction of the i^{th} harmonic will coincide with the 2nd order diffraction of the $(2i)^{th}$ harmonic. This is shown in Fig. 2.28.

Figure 2.28 schematically shows the effect of having more than an octave of XUV bandwidth on the detector. The vertical axis is proportional to divergence (unused in this application) and the horizontal axis is proportional to wavelength, with photon energy increasing to the right. The harmonics are denoted as vertical line segments, with 1st order harmonics colored blue and 2nd order harmonics colored red. Harmonics are labeled with their harmonic order (9 through 31 are shown), but generally speaking we do not have *a priori* knowledge of the harmonic order in the lab. Below, we will introduce a scheme to determine the absolute harmonic order.

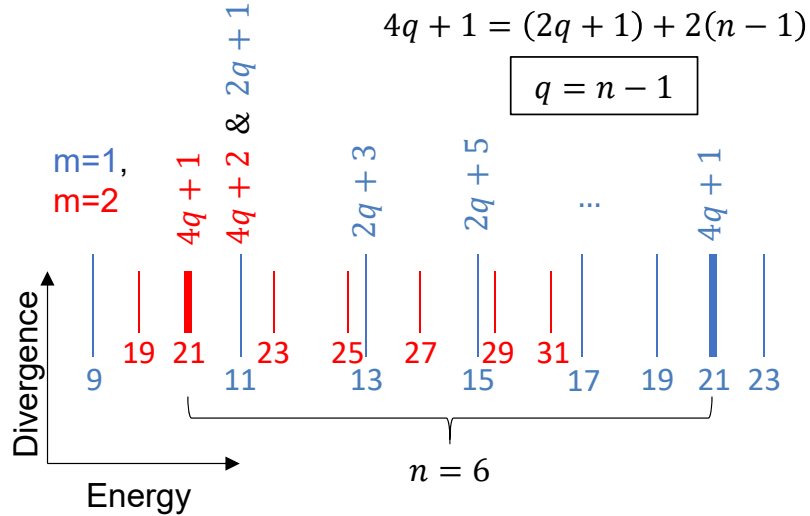


Figure 2.28: Counting scheme to determine the absolute harmonic order.

If we are able to identify a matched pair of diffraction orders, then we can determine the absolute harmonic order as follows. Let the harmonic order of this matched pair be $i = 4q + 1$. This pair is bolded in Fig. 2.28. If we look at the $m = 2$ copy of the $4q + 1$ harmonic, there will be an $m = 1$ harmonic immediately to the right of it. In $m = 2$ space, this position would correspond to $i_{m=2} = 4q + 2$, which is even. However we are only creating odd harmonics, so this light must be from an odd diffraction order ($m = 1, 3, \dots$). Of the odd diffraction orders, $m = 1$ is the brightest, so this harmonic order is $i_{m=1} = (4q + 2)/2 = 2q + 1$. We now count the number of $m = 1$ harmonics between the matched pair (including the right endpoint), which we will call n . In doing so, we are counting the number of $m = 1$ harmonics between $i = 2q + 1$ and $i = 4q + 1$. We therefore determine q via the following relation:

$$(m = 1) : 4q + 1 = (2q + 1) + 2(n - 1) \rightarrow q = n - 1 \quad (2.43)$$

In the cartoon, we count $n = 6$ 1st order harmonics (blue line segments) between the bolded matched pair. From Eq. (2.43), we determine that $q = 6 - 1 = 5$, and therefore the matched pair has harmonic order $4q + 1 = 21$. Once we know the numerical value of $4q + 1$, we can label the remaining harmonics sequentially, as shown in the figure.

At this point, we have a set of N coordinate pairs of spectral pixel and harmonic orders $\{(p_i, HO_i)\}$. We can now fit to a polynomial function and create a functional map between the spectral pixel and the harmonic order, $HO(p)$. If we can identify a single spectral feature located at pixel p_i with a known energy E_i , then we can scale the harmonic order function to an energy function: $E(p) = (E_i/HO(p_i)) \times HO(p)$. Usually, the sharp aluminum L -edge

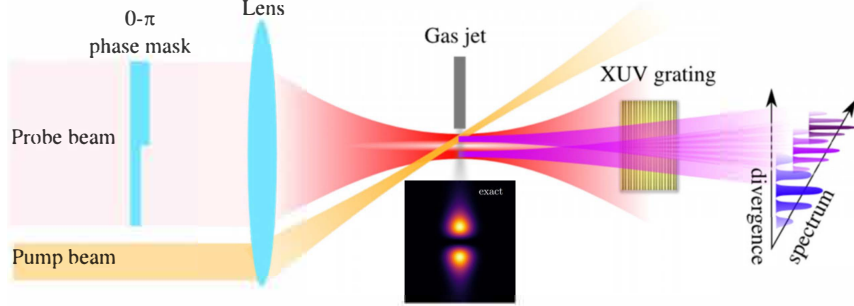


Figure 2.29: Two-source harmonic generation scheme. The pump beam is not used in this application. Extraneous XUV optics are omitted for visual clarity. Figure adapted from [14].

at 72.3 eV is used for this purpose.

Two-Source Harmonic Counting Scheme

We can use the divergence axis of the spectrometer to identify matching pairs of harmonic orders. We do this by inserting the π -plate into the laser beam upstream of the generation lens. Recalling the main result of Section 1.5, the π -plate transforms a TEM_{00} beam into a TEM_{01} -like beam. The two phase-locked intensity lobes at the focus of the MIR beam have a separation Δy_p :

$$\Delta y_p \approx \frac{\lambda_1 f}{\sigma}$$

For $\lambda = 1350$ nm, $f = 40$ cm and $\sigma = 12.8$ mm, the MIR spot separation is about 42 μm . By placing a gas jet at the MIR focus, each intensity lobe will locally drive the HHG process. As a result, we will have two spatially separated phase-locked XUV light sources that will interfere in the far field with a spatial frequency \tilde{k}_q [14]:

$$\tilde{k}_q = q \frac{2\pi a}{\lambda_1 D} \quad (2.44)$$

where D is the source-to-screen distance, a is the distance between the two sources, λ_1 is the fundamental wavelength, and q is the harmonic order. This setup is schematically shown in Fig. 2.29. By performing a Fourier transform along the spatial dimension, we can identify matching pairs ($m = 1, 2, 3, 4$) of harmonics. Once we have identified these pairs, we can apply the method described above to find the absolute harmonic order. For more details on two-source harmonic generation, see Stephen Hageman's dissertation [54].

The top panel of Fig. 2.30 shows a harmonic spectrum generated with the 1350 nm π -plate using argon gas in the low pressure cell (see Section 3.2.3), a fundamental wavelength of $\lambda = 1350$ nm, a zirconium filter, and an exposure time of 650 seconds. Along the spectral

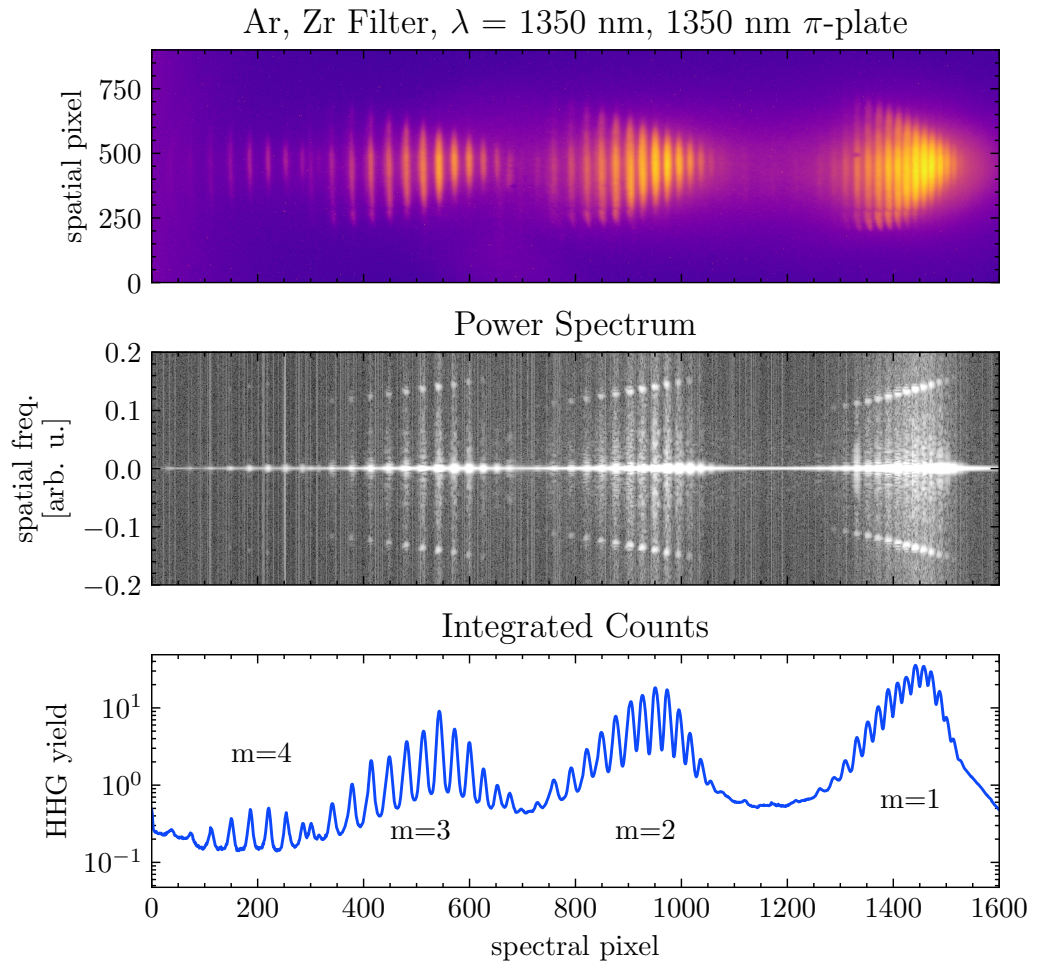


Figure 2.30: Two-source harmonic spectrum. Top panel: log scale 2D detector image. Middle panel: log scale of the power spectrum, computed by taking the FFT of the top panel along spatial dimension. Bottom panel: vertical integration of the top panel.

axis, we see four “clusters” of harmonics spanning the horizontal axis. We will show below that each “cluster” corresponds to a different grating diffraction order, with $m = 1$ on the right and $m = 4$ on the left of the sensor. As m increases, the counts decrease and the dispersion changes, but the clusters are otherwise identical to each other. The finite noise floor of the detector limits our ability to resolve the weakest harmonics. Normally, the $m = 3$ and $m = 4$ harmonics are too faint to be seen, but they are visible here due to the combination of the Zr filter (which blocks light below 60 eV, see Fig. 2.26) and an abnormally long exposure time. The cutoff energy of this spectrum is approximately 80 eV.

A discrete Fourier transform (FFT) is performed along the spatial dimension of the data shown in the top panel, and the power spectrum is shown in the middle panel of Fig. 2.30. As discussed above, we expect the spatial frequency of the interference pattern to be proportional to the harmonic energy, and this is exactly what we see. Within a given diffraction order, the spatial frequency increases as the harmonic number increases. Across the harmonic clusters, we see the same increase of spatial frequency with respect to increasing harmonic order, which confirms our hypothesis that each harmonic cluster corresponds to a unique grating diffraction order.

The bottom panel of Fig. 2.30 shows the spatial integration of the detector image. We can see that the efficiency of the grating decreases with increasing m , and only a few $m = 4$ harmonics are visible.

Any two harmonic orders with the same dominant spatial frequency must have the same wavelength and therefore must be the same harmonic order. We can use this fact to match harmonic orders across the different diffraction orders. Figure 2.31 shows the power spectrum, integrated around the width of each harmonic, for seven matching harmonics orders. The $m = 4$ harmonic signal is too weak to resolve most of the spatial frequencies, except for two harmonics.

Now that we have identified matching harmonics, we can calculate the relative grating efficiency, but we must take care in doing so. First, the spectral dispersion is different for each diffraction order, so the height of the harmonic is not a valid metric – we must use the integrated harmonic yield¹². Secondly, only a few $m = 4$ diffraction orders are visible, so we should take care to integrate over the same spectral region for each diffraction order. Finally, the harmonics overlap each other, and we can see the amount of overlap varies for each diffraction order – so we can’t just numerically sum the signal over a discrete number of harmonics. We get around this problem by fitting the harmonic spectrum to a sum of Gaussians and using the fitted values to analytically integrate the contribution of a subset of common harmonics.

This analysis is shown in Fig. 2.32. For each diffraction order, we fit the spectra to a

¹²Note that for this calculation, there is no need to include the Jacobian or convert the spectral axis to the energy basis, as the following quantity is conserved: $\int f_p(p) dp = \int f_E(E) dE$. See the later section on the Jacobian for more details.

Matching Harmonic Orders

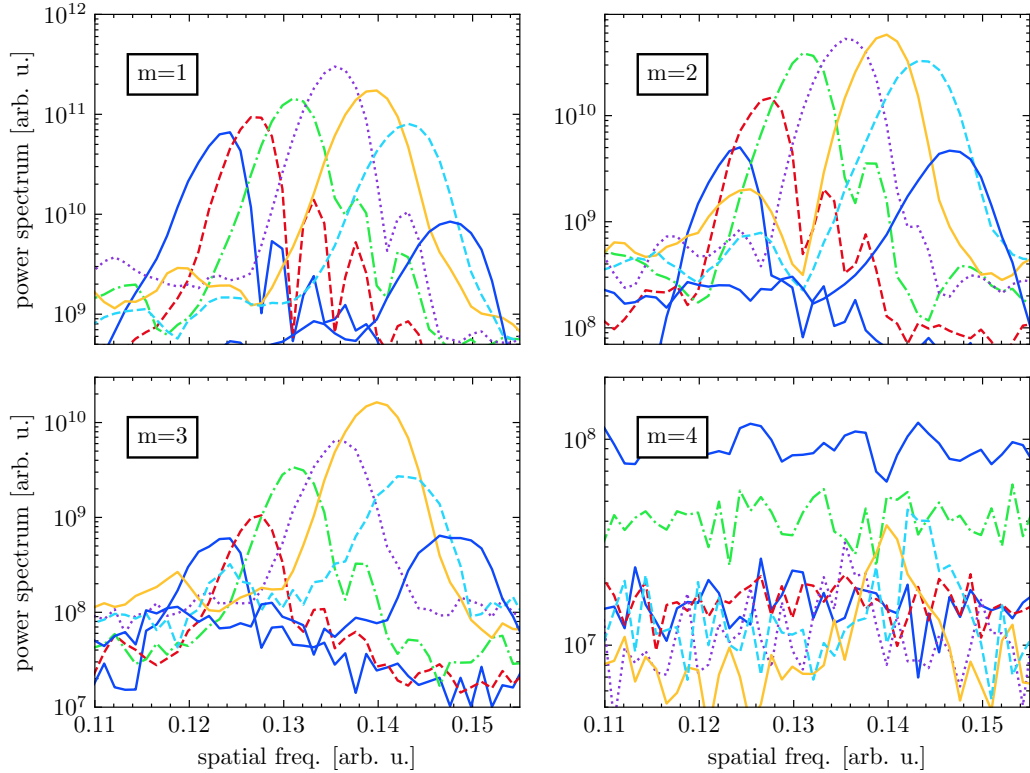


Figure 2.31: Integrated power spectrum (middle panel of Fig. 2.30) for selected harmonic orders and different diffraction orders. Harmonics with the matching spatial frequencies share the same line style and color. Note the poor visibility of the $m = 4$ peaks in the integrated power spectrum follows from the weak spatial interference pattern in the raw power spectrum.

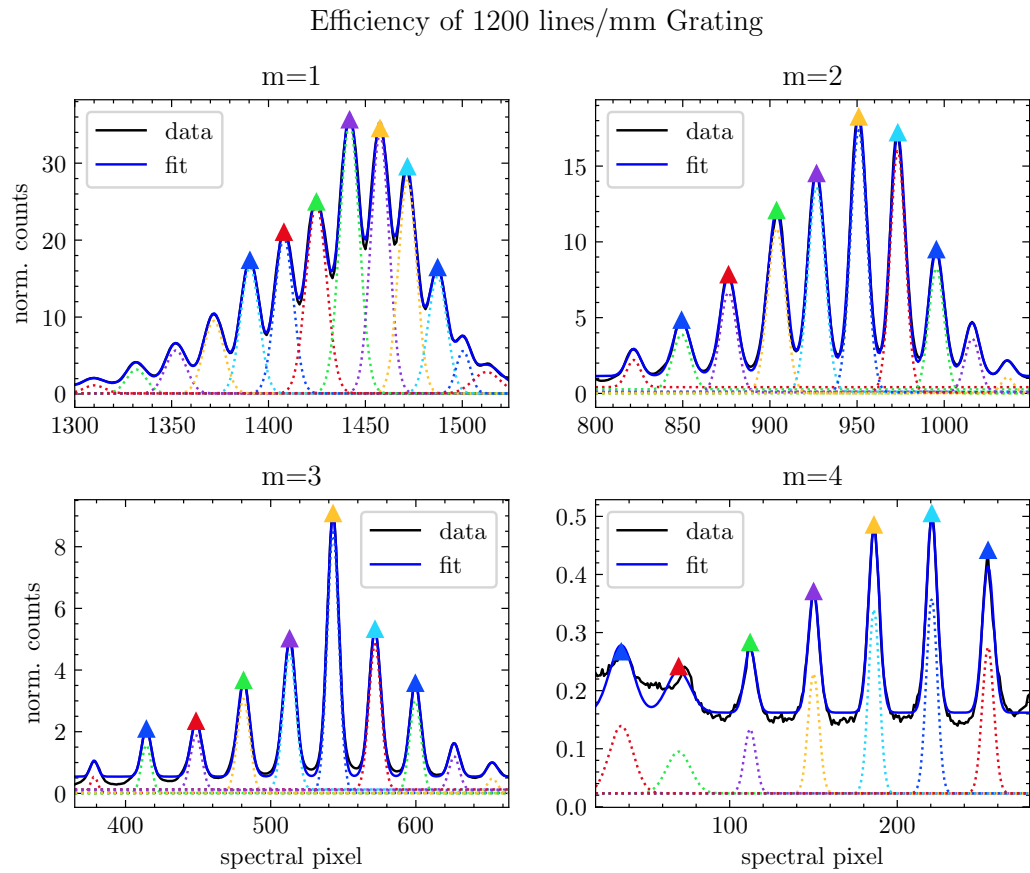


Figure 2.32: Gaussian fit to the HHG yield in Fig. 2.30. Triangles indicate the harmonics used in the grating efficiency calculation; matching colors indicate matching harmonic orders across the different diffraction orders ($m = 1, 2, 3, 4$), following Fig. 2.31.

series of Gaussians (dashed lines, each of the form $y_i = a_i \exp \left[(x - b_i)^2 / (2c_i^2) \right] + d_i$). The matching harmonics, identified in Fig. 2.31, are indicated with red triangles. For each diffraction order, we integrate the total yield of the tagged harmonics via $\eta_i = \Sigma_i \sqrt{2\pi} a_i |c_i|$. Next, we calculate the grating efficiency (relative to the $m = 1$ diffraction). The result is:

$$\begin{aligned}\frac{\eta_2}{\eta_1} &= 42.2\% \\ \frac{\eta_3}{\eta_1} &= 13.0\% \\ \frac{\eta_4}{\eta_1} &= 0.6\%\end{aligned}\tag{2.45}$$

If we neglect the zero-order diffraction and the contributions of higher order terms ($1 = \Sigma_{i=1}^4 \eta_i$), then we can calculate the absolute diffraction efficiency of the grating:

$$\begin{aligned}\eta_1 &\simeq 64.2\% \\ \eta_2 &\simeq 27.1\% \\ \eta_3 &\simeq 8.4\% \\ \eta_4 &\simeq 0.4\%\end{aligned}\tag{2.46}$$

These grating efficiencies are consistent with the values found in the manufacturer's specification sheet.

Argon Fano Resonances

The spectrometer can also be calibrated over a limited spectral range using a collection of known spectral features. The Fano resonance, which is due to an interference between bound and continuum states, can be used for this purpose. The Fano cross section σ is parameterized by [18, 91]:

$$\sigma = \frac{(q + \epsilon)^2}{1 + \epsilon^2} \sigma_a + \sigma_b\tag{2.47}$$

where σ_a is the amplitude of the resonance, σ_b is the slowly varying background scattering, q is the asymmetry parameter and ϵ is the normalized distance from the resonance, defined as:

$$\epsilon \equiv \frac{\hbar\omega - E_r}{\Gamma/2}\tag{2.48}$$

where $\hbar\omega$ is the photon energy, E_r is the resonance energy and Γ is the width. Taking the derivative, we find that the cross section σ has extrema at the following photon energies:

$$\hbar\omega^+ = E_r + \frac{\Gamma}{2q}\tag{2.49}$$

$$\hbar\omega^- = E_r - \frac{q\Gamma}{2}\tag{2.50}$$

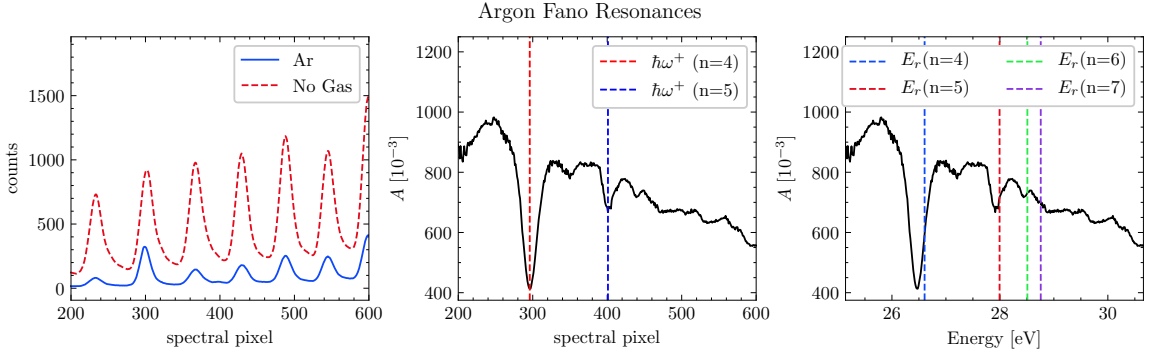


Figure 2.33: Fano resonances used for low energy spectral calibration. Left panel: XUV spectra with and without argon gas at the XUV focus. Middle panel: measured absorbance A of argon showing the absorption profile of the $n = 4$ and $n = 5$ $3s3p^6np$ resonances. Right panel: calibrated spectra showing the expected locations of the higher resonances.

n	E_r [eV]	Γ [meV]	q
4	26.605	80.2	-0.286
5	27.994	28.5	-0.177
6	28.509	12.2	-0.135
7	28.757	4.5	-0.125

Table 2.3: Experimentally measured Fano parameters for the $3s3p^6np$ resonance series in argon [18].

In argon, the $3s3p^6np$ Fano resonance series occurs between 26.6 and 29 eV. We can observe the Fano cross section in argon by recording XUV spectra with and without gas at the XUV focus, as shown in the left panel of Fig. 2.33. A low pressure cell located at the XUV focus delivers the gas in the target chamber (see Section 3.2.3). The middle panel shows the absorption A of the gas sample, defined as the logarithm of the ratio of the collected spectra S :

$$A = -\log_{10} \left(\frac{S_{\text{Ar}}}{S_{\text{No gas}}} \right) \quad (2.51)$$

Overall, we see a broad absorption with prominent emission peaks ($\hbar\omega^+$), corresponding to the $n = 4, 5$ resonances in the $3s3p^6np$ series. The location of these peaks is used to calibrate the spectrometer in the low photon energy region using the literature values of the Fano profile (see Table 2.3). The right panel shows the calibrated Fano absorption spectra and highlights the expected locations of the higher resonances.

The Jacobian

Once we have the calibration function, we need to scale the measured signal by the Jacobian in order to conserve energy [92]. Let $f_p(p)$ be the function that represents the measured XUV counts at spectral pixel p :

$$f_p(p) : \text{spectral pixel} \rightarrow \text{counts} \quad (2.52)$$

During the calibration step, we convert the spectral pixel axis to energy [eV] using a function $E(p)$, usually a polynomial:

$$E(p) : \text{spectral pixel} \rightarrow \text{energy [eV]} \quad (2.53)$$

$$E(p) = a_0 + a_1 p + a_2 p^2 + a_3 p^3 + a_4 p^4 + \dots \quad (2.54)$$

Likewise, we define the inverse of $E(p)$ to be:

$$p(E) : \text{energy [eV]} \rightarrow \text{spectral pixel} \quad (2.55)$$

$$p(E) \equiv E^{-1}(p) \quad (2.56)$$

We want calculate the XUV counts in the energy basis. That is, we want to convert $f_p(p)$ to $f_E(E)$ using the Jacobian. By conservation of energy, we have the relation:

$$f_p(p) dp = f_E(E) dE \quad (2.57)$$

Rearrangement of the above equation leads us to the desired result:

$$f_E(E) = f_p(p) \frac{dp}{dE} = f_p(p) \frac{d}{dE} p(E) \quad (2.58)$$

2.7 Conclusion

In this chapter, we described the laser system, including the active pointing correction system, the external compressor and TOPAS. The pulse duration was characterized using the FROG technique and the interaction pulse duration was estimated to be 44 fs. Next, the home-built vacuum system was described. Different XUV refocusing optics were discussed within the goal of maximizing reflectivity and minimizing aberrations at the focus. The aberrations of two candidate mirror geometries were analyzed, and it was found that an ellipsoidal mirror was superior to a toroidal mirror when used in a demagnifying configuration. The MIR optics were described and numerically modeled, and we obtained an intensity profile at the sample focal plane that will be used in Chapter 4 to model the laser-sample interaction. Finally, the XUV spectrometer was described and methods to spectrally calibrate it were developed.

Chapter 3

XUV LIGHT SOURCE DESIGN AND APPARATUS PERFORMANCE

3.1 Introduction

Compared to RABBITT measurements, condensed matter transient absorption experiments require a very high XUV photon flux. First, the sample thickness is usually chosen such that the XUV transmission is roughly 50% near the spectral feature of interest. This optical density represents a compromise between the incompatible goals of having a strong ground state absorption (enabling the detection of small changes in the optical density) while simultaneously avoiding the noise floor of the detector (which is required for good statistics). Second, a high XUV flux will reduce the number of laser shots required for a given data point, which in turn reduces the total MIR flux on the sample and minimizes the effects of long-lived excited states on the measurement. Finally, a high flux reduces the overall time required to complete an experiment. This increases data fidelity by reducing the effects of unavoidable experimental noise sources such as long-term laser drift (either pointing or energy) and environmental changes caused by the building's HVAC system.

This chapter will detail the development of bright XUV sources which were required for ATAS experiments. It will also quantify the performance of the available XUV sources and the TABLE beamline as a whole.

3.2 HHG Gas Sources

This section will discuss the HHG gas sources used to generate harmonics for ATAS experiments. For each gas source, we will describe the device, model the gas flow and discuss their XUV output in the context of the physical principles discussed in Section 1.3.

3.2.1 Introduction

Recalling the arguments of Section 1.3.2, there exists an optimal phase matching pressure P_{opt} for which the XUV flux is maximized. According to Eq. (1.31), P_{opt} is proportional to the square of the fundamental wavelength. From Eq. (1.34), we expect the harmonic yield of a perfectly phase matched HHG process to scale as the square of the pressure-length product, $(PL)^2$. Additionally, we expect the harmonic yield to scale with the fundamental wavelength as $\lambda^{-(5-6)}$, as explained in Section 1.3.1. These factors indicate that a high interaction pressure is critical for a successful ATAS experiment.

Experimentally, the interaction pressure is a consequence of the gas flow dynamics and the design of the gas delivery device. The interaction pressure can be increased by increasing the backing pressure into the device, but this is limited by the finite pumping speed of the vacuum system. Significant improvements to both the interaction pressure P and the interaction length L can be made by modifying the design of the gas delivery device. The simplest and most common gas delivery device (a free expansion nozzle) cannot reach P_{opt} at $\lambda_1 = 800$ nm before the vacuum system is overwhelmed. Since most of our experiments are performed at longer wavelengths using the signal output of the TOPAS, and because ATAS experiments require a high XUV flux, more advanced gas delivery systems were required.

Providing the lab with a brighter harmonic source was the ultimate goal of the high pressure cell, and for the most part this goal was achieved. Below, we will review the basic design considerations, drawbacks and advantages of the four main types of gas sources used in this thesis: the free expansion nozzle, the low pressure cell (LPC), the high pressure cell (HPC) and the Amsterdam pulsed piezovalve. A primer on how to install and use the high pressure cell can be found in Appendix A.3.

3.2.2 Free Expansion Nozzle

We use an *in vacuo* gas nozzle to deliver a localized plume of gas near the MIR focus. Generally, when gas flows from a high pressure region (P_0) to a low pressure region (P_b) through a small aperture of diameter d , a supersonic plume may form in the low pressure region. If the pressure ratio P_0/P_b exceeds a critical value G , given by

$$G \equiv ((\gamma + 1)/2)^{\gamma/(\gamma-1)} \leq 2.1, \quad (3.1)$$

then the gas flow at the aperture will be equal to the speed of sound, and the pressure will be equal to $P_0/G \approx P_0/2$. The highest chamber pressures in our experiments are on the order of $P_b \approx 10$ mTorr, and typical backing pressures for harmonic generation generally exceed 50 Torr, so we are always operating with a supersonic jet. The on-axis spatial extent

Source	j	γ	C_1	C_2	C_3	C_4	A	B
3D	1	5/3	3.232	-0.7563	0.3937	-0.0729	3.337	-1.541
3D	1	7/5	3.606	-1.742	0.9226	-0.2069	3.190	-1.610
3D	1	9/7	3.971	-2.327	1.326	-0.311	3.609	-1.950
2D	2	5/3	3.038	-1.629	0.9587	-0.2229	2.339	-1.194
2D	2	7/5	3.185	-2.195	1.391	-0.3436	2.261	-1.224
2D	2	9/7	3.252	-2.473	1.616	-0.4068	2.219	-1.231

Table 3.1: Gas parameters used in Eq. (3.4). Table recreated from Ref [19].

of the supersonic gas plume is estimated by the Mach disk location, x_M :

$$x_M/d = 0.67\sqrt{P_0/P_b}. \quad (3.2)$$

For a chamber pressure of 3 mTorr and a backing pressure of 450 Torr, $x_M = 260d = 51.9$ mm for a 200 μm diameter aperture. As will be shown below, our laser-gas interaction region is well within the structure of the gas jet.

The physics of supersonic gas flow have been discussed at length in the literature, so we will only go over the relevant highlights [19, 93]. The ratio of the velocity of the gas V to the speed of sound a is called the *Mach number* $M = V/a$. It can be shown that all thermodynamic parameters within the supersonic structure (density, pressure, velocity and temperature) can be expressed in terms of the Mach number and the heat capacity ratio γ . For harmonic generation, we are primarily concerned with the on-axis ($y = 0$) mass density ρ and pressure P :

$$\frac{\rho}{\rho_0} = \frac{n}{n_0} = \left(\frac{T}{T_0}\right)^{1/(\gamma-1)} = \left(1 + \frac{\gamma-1}{2}M^2\right)^{-1/(\gamma-1)}, \quad (3.3a)$$

$$\frac{P}{P_0} = \left(\frac{T}{T_0}\right)^{\gamma/(\gamma-1)} = \left(1 + \frac{\gamma-1}{2}M^2\right)^{-\gamma/(\gamma-1)}. \quad (3.3b)$$

Here, ρ_0 is the mass density at the nozzle aperture ($x = 0$), and n is the number density. The Mach number is found by solving the fluid mechanics equations dealing with the conversation of mass, momentum and energy for a given nozzle geometry. For a complete discussion, see [19]. Below we present the on-axis result, which is an analytic fit to a numerical solution of the thermodynamic equations:

$$\frac{x}{d} > 0.5 : \quad M = \left(\frac{x}{d}\right)^{(\gamma-1)/j} \left[C_1 + \frac{C_2}{\left(\frac{x}{d}\right)} + \frac{C_3}{\left(\frac{x}{d}\right)^2} + \frac{C_4}{\left(\frac{x}{d}\right)^3} \right], \quad (3.4a)$$

$$0 < \frac{x}{d} < 1.0 : \quad M = 1.0 + A \left(\frac{x}{d}\right)^2 + B \left(\frac{x}{d}\right)^3. \quad (3.4b)$$

The fitting coefficients for Eq. (3.4) are listed in Table 3.1. We can see that M scales with

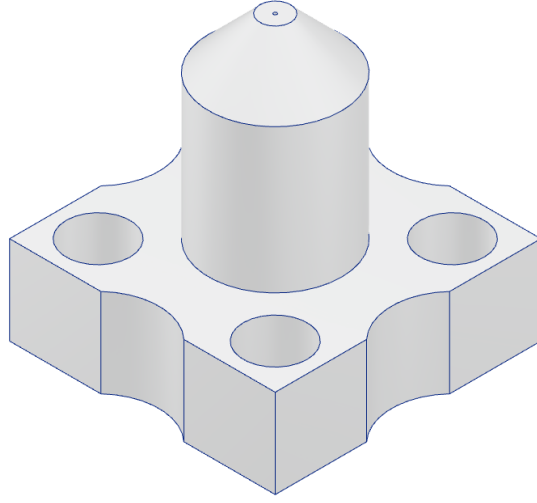


Figure 3.1: Rendering of the continuous free expansion nozzle. Gas flows from the base of the nozzle (bottom) and out of the $200 \mu\text{m}$ aperture (top). The top surface is beveled so the nozzle can be brought closer to the MIR focus without clipping the beam.

powers of x/d , the number of nozzle diameters away from the nozzle aperture.

The gas nozzle throughput \hat{T} is proportional to the area of the aperture and the backing pressure:

$$\hat{T} \text{ (Torr} \cdot \text{l/s}) = c \left(\frac{T_C}{T_0} \right) \sqrt{\frac{300}{T_0}} P_0 d^2, \quad (3.5)$$

where c is a gas constant¹³, T_C and T_0 are the vacuum chamber and backing temperatures, respectively, and d is the nozzle diameter in cm. Ignoring the effect of the generation chamber's vacuum aperture, we can estimate the operating pressure of the generation chamber P_b using the following equation [94]:

$$P_b \text{ (Torr)} = \frac{\hat{T}}{S}, \quad (3.6)$$

where S is the pumping speed of the turbo pump in liters per second. To avoid overloading our turbo pumps, we are typically limited to operating pressures below 5 - 10 mTorr.

The basic design of our continuous free expansion nozzle is shown in Fig. 3.1. The nozzle is an aluminum cylinder with a small diameter hole drilled into the top surface. Gas is delivered to the aperture via a universal gas receiver (not shown), which attaches to base of the nozzle. To reduce the gas load on the pumps, we used a $200 \mu\text{m}$ diameter aperture, which was the smallest size hole the machine shop could readily drill into aluminum. A

¹³Values of c for common gas species are listed here: 45 [He], 20 [Ne], 14 [Ar], 16 [N₂] in $\text{l/cm}^2/\text{s}$. For a full table of values, see Table 2.5 in [19].

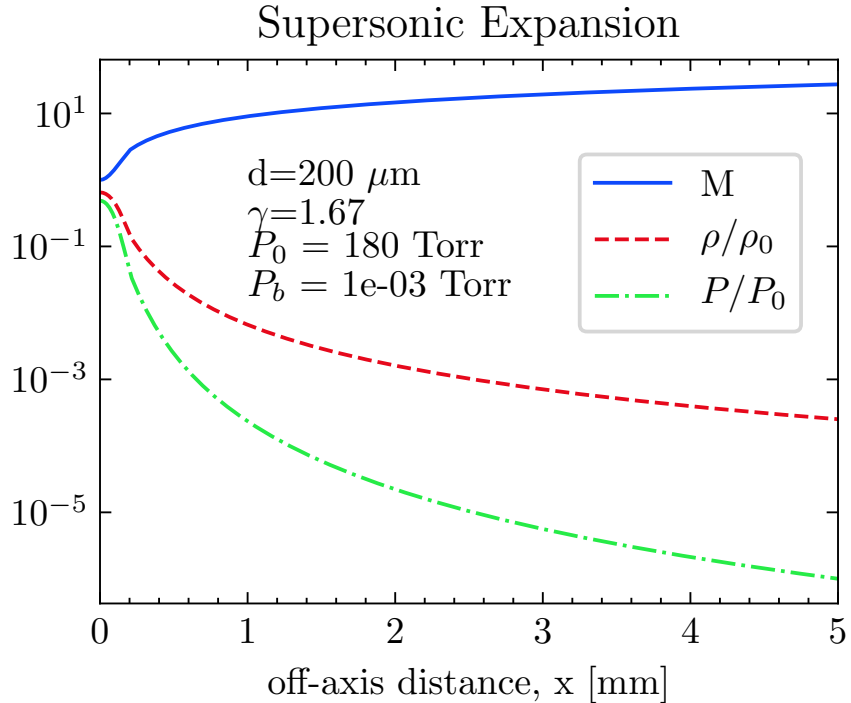


Figure 3.2: On-axis Mach number M , mass density ρ and pressure P for a free expansion nozzle.

$200 \mu\text{m}$ diameter aperture backed with 180 Torr of argon will deliver a gas throughput of approximately $1 \text{ Torr} \cdot \text{l/s}$. With a pumping speed of $S = 1000 \text{ l/s}$, the generation chamber pressure will be around $P_b = 1 \text{ mTorr}$. For a monatomic gas, $G = 2.05$, and the pressure at the nozzle aperture is $P_0/G \approx 87 \text{ Torr}$.

The on-axis Mach number, density and pressure for a monatomic gas are shown in Fig. 3.2. We can see the on-axis gas density drops off precipitously with increasing distance from the nozzle aperture x . Recalling Fig. 1.11, we want to bring the nozzle as close to the optical axis to maximize the interaction density. However, if nozzle face enters the focal volume it will be drilled by the high intensity light and the resulting metallic plume will coat the generation chamber's vacuum window. Under normal operating conditions, we estimate the optical axis is located at $x = 100 \mu\text{m}$.

The left panel of Fig. 3.3 shows the on-axis interaction pressure for He and Ar ($\gamma = 5/3$) as a function of the nozzle backing pressure at various on-axis distances. Vertical dashed lines correspond to the highest sustainable backing pressure for each gas. For $x/d = 1$, the maximum interaction pressure for argon is $\sim 120 \text{ Torr}$ and for helium it is $\sim 35 \text{ Torr}$; for $x/d = 2$, $P_{int}(\text{Ar}) \sim 360 \text{ Torr}$ and $P_{int}(\text{He}) \sim 110 \text{ Torr}$.

Recalling the results of the 1D reabsorption model discussed in Section 1.3.2, ideal phase

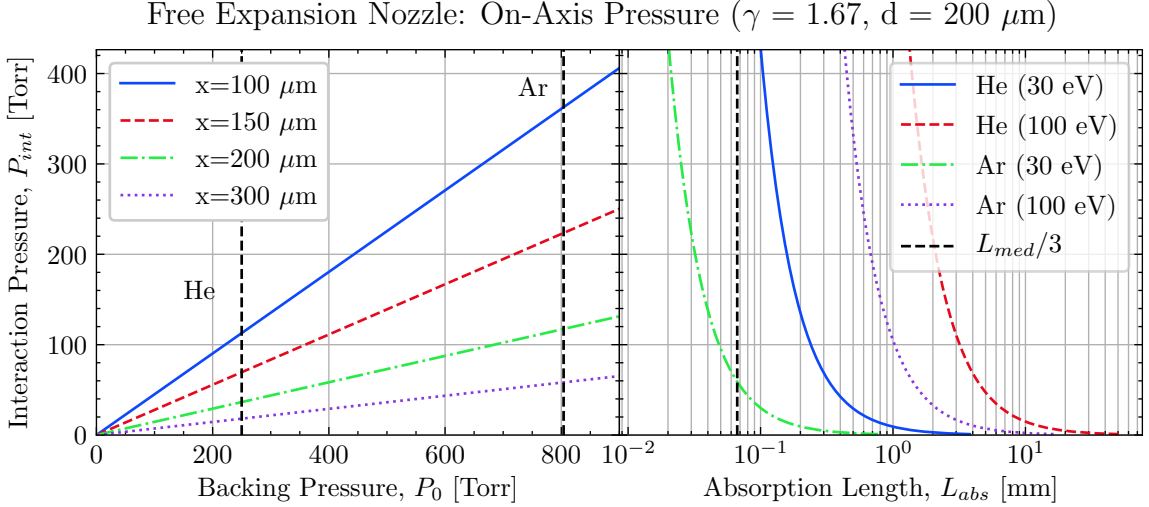


Figure 3.3: On-axis interaction pressure and absorption length for the free expansion nozzle. Left panel: On-axis pressure as a function of nozzle backing pressure for various on-axis distances x . Vertical dashed lines indicate pressures at which the vacuum system is overwhelmed (5 mTorr). Right panel: Required average interaction pressure as a function of absorption length L_{abs} for both gasses at 30 and 100 eV.

matching occurs if $L_{med} > 3L_{abs}$. We can estimate the absorption length of the gas plume by assuming a boxcar function density profile of width d . Note that this approximation overestimates the average density in the interaction region, as the off-axis density profile at large values of x/d is proportional to $\cos^4 \theta$, where $\tan \theta \equiv y/x$ [19]. Therefore $d/3$ represents a hard upper bound for L_{abs} , which is 67 μm for a 200 μm nozzle. The right panel of Fig. 3.3 shows the absorption length for both gasses at 30 and 100 eV. We can see that the free expansion nozzle is only capable of phase matching argon at lower photon energies, where the XUV absorption cross section is larger. The free expansion nozzle is incapable of properly phase matching helium at any photon energy.

3.2.3 Low Pressure Cell

We have shown that the free expansion nozzle cannot provide sufficiently high pressure-length product to phase match high energy photons. The low pressure cell (LPC), shown in Fig. 3.4, was designed to improve the ratio L_{abs}/L_{med} while maintaining a relatively simple nozzle geometry [72].¹⁴ The LPC consists of an aluminum disk with rectangular block at the center of the top surface. Gas flows from the universal gas receiver (which is mated to the bottom of the disk) through a thin capillary and into the rectangular block. A through

¹⁴Special thanks to Zhou Wang for designing the original LPC. The LPC used in this work has been slightly modified to work with our universal gas receiver.

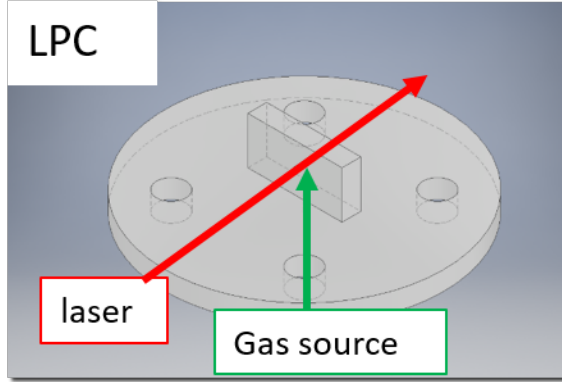


Figure 3.4: Rendering of the low pressure cell (LPC). The interaction region is contained within the rectangular block. The circular disk is attached to the universal gas receiver (not shown) via the four through holes.

hole drilled into the front face of the rectangular block intersects the capillary and serves as the gas-laser interaction volume. Below, we will model the gas density profile of the LPC and show that the thickness of the block ($W = 2.032$ mm) sets the gas-laser interaction length.

Gas Flow in the LPC

Figure 3.5 shows a gas flow model of the LPC inside the generation vacuum chamber. The green arrows indicate the direction of gas flow, and the red shaded region indicates the laser focus. The gas receiver is considered to be an infinite reservoir of gas with pressure P_1 . This region supplies the laser interaction region with gas via a thin capillary of diameter $R = 101.5 \mu\text{m}$, length $L = 5 \text{ mm}$ and volumetric flow rate Q_2 , modeled as an ideal isothermal gas [95–97]. The interaction region with pressure P_2 acts as a pressure source for two diametrically opposed supersonic gas jets [19], each with diameter d and throughput \hat{T}_n . The generation chamber has a turbopump with pumping speed S_t and an equilibrium pressure P_3 . We justify this treatment by noting that we are in the supersonic regime, as $P_2 \sim 100 \text{ Torr}$ and $P_3 \sim 10^{-3} \text{ Torr}$. Additionally, the mean free path l :

$$l = \frac{\mu}{P} \sqrt{\frac{\pi R T}{2M}} \quad (3.7)$$

is much shorter than either physical dimension (d, W) of the rectangular block. For helium at 100 Torr, $l \sim 1.5 \mu\text{m}$ and for argon $l \sim 0.5 \mu\text{m}$. Therefore, we can think of the interaction region as a reservoir of gas for two diametrically opposed supersonic jets. This approach

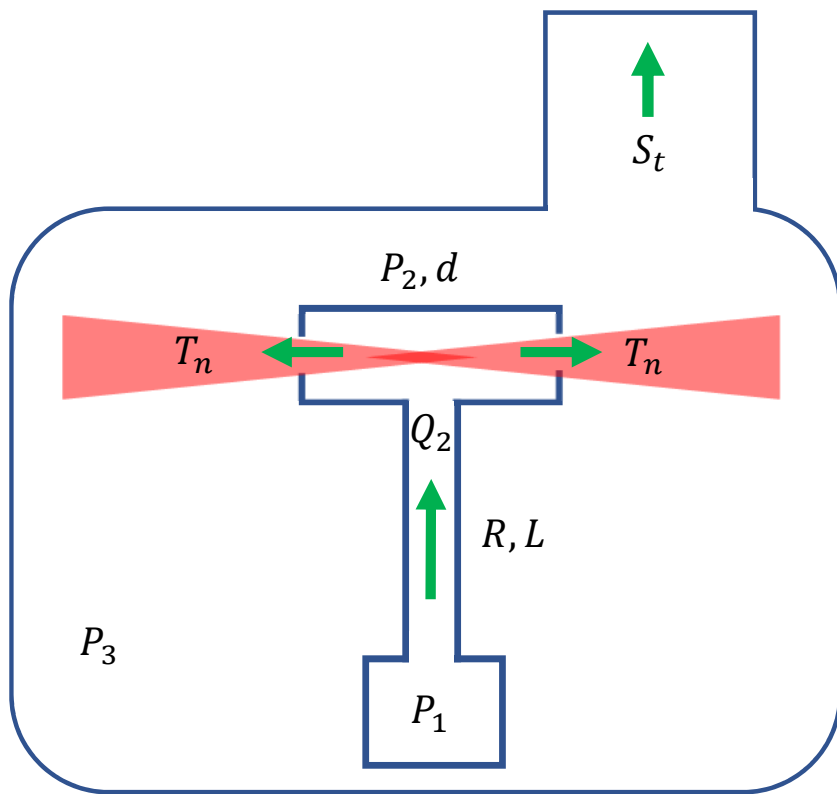


Figure 3.5: Conceptual gas flow schematic of the LPC. Arrows indicate direction of gas flow. Red shaded region indicates laser path.

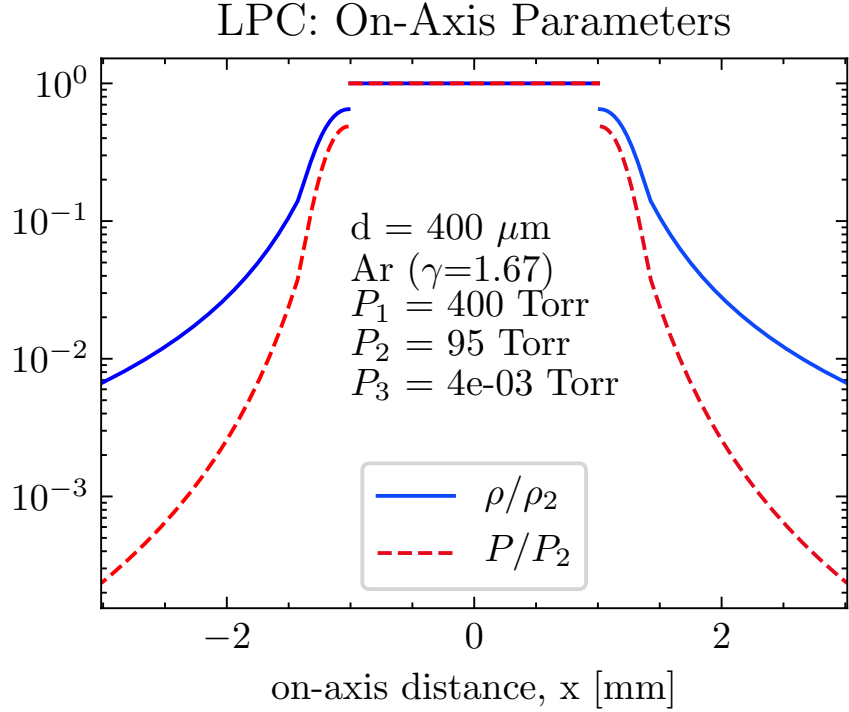


Figure 3.6: Calculated on-axis density and pressure for the low pressure cell.

results in the following coupled equations (SI units):

$$P_1^2 - P_2^2 = \frac{16\mu L Q_2 P_2}{\pi R^4}, \quad (3.8)$$

$$Q_2 P_2 = 2\hat{T}_n, \quad (3.9)$$

$$P_3 = \frac{2\hat{T}_n}{S_t}, \quad (3.10)$$

$$\hat{T}_n = C P_2 d^2, \quad (3.11)$$

where C is the gas constant expressed in m/s (see Eq. (3.5)) and μ is the dynamic viscosity in Pas. Solving for the interaction pressure P_2 and chamber pressure P_3 , we obtain:

$$P_2 = -\frac{16Cd^2L\mu}{\pi R^4} + \sqrt{P_1^2 + \frac{256C^2d^4L^2\mu^2}{\pi^2R^8}}, \quad (3.12)$$

$$P_3 = \frac{2Cd^2}{S_t} \left(-\frac{16Cd^2L\mu}{\pi R^4} + \sqrt{P_1^2 + \frac{256C^2d^4L^2\mu^2}{\pi^2R^8}} \right). \quad (3.13)$$

Equation (3.3) can be used to calculate the on-axis density and pressure of the LPC, which are shown in Fig. 3.6. Our simplified model yields a constant pressure in the LPC assembly and a sharp drop off in the plume region. Note that due to the G factor (see

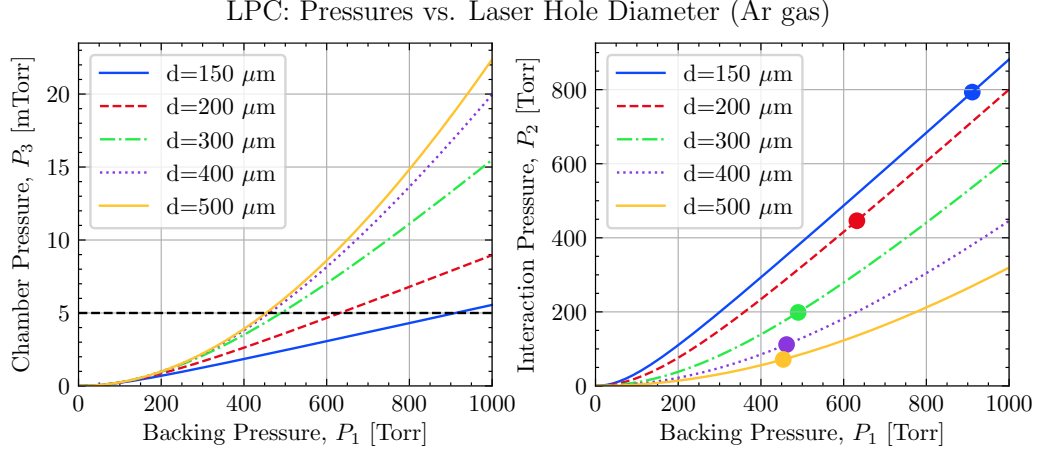


Figure 3.7: Effect of the laser hole diameter d on the LPC gas flow. Left panel: chamber pressure. Dashed horizontal line indicates maximum sustainable operating pressure. Right panel: interaction pressure. Circles indicate the interaction pressure at the maximum sustainable backing pressure.

Eq. (3.1)), the FWHM of the pressure and density is simply the width of the LPC's rectangular block, W . When considering XUV reabsorption, we will neglect the existence of the gas plumes and treat the gas density pressure as a boxcar function with a thickness $L_{\text{med}} = W$.

Figure 3.7 shows the effect of the laser hole diameter d on the chamber and interaction pressures when using argon gas. As d increases relative to the capillary dimensions (R, L), the pressure of the interaction region decreases, and the overall conductance of the LPC assembly increases. As a result, gas is no longer efficiently trapped in the interaction region, but instead escapes out to the greater vacuum chamber. We therefore want to minimize the diameter of the laser hole as much as possible within manufacturing and optical constraints. Note that when misaligned, the laser will drill into the rectangular block, increasing the effective value of d over time. For this reason, the LPC is considered a consumable part that should be replaced when its maximum operating pressure is insufficient for experimental needs.

Figure 3.8 shows the corresponding absorption length for a given backing and interaction pressure. In the left panel, we have selected pressure curves for $d = 400\ \mu\text{m}$ (bright lines) and $d = 200\ \mu\text{m}$ (faint lines) for both helium (blue) and argon (red). As in Fig. 3.7, the filled circles indicate the maximum sustained operating pressure before the vacuum system is overwhelmed. In the right panel, we show the corresponding absorption length L_{abs} for low and high energy photons in both gas media. Applying the arguments of Section 1.3.2, we compare the absorption length to the upper bound required for efficient phase matching,

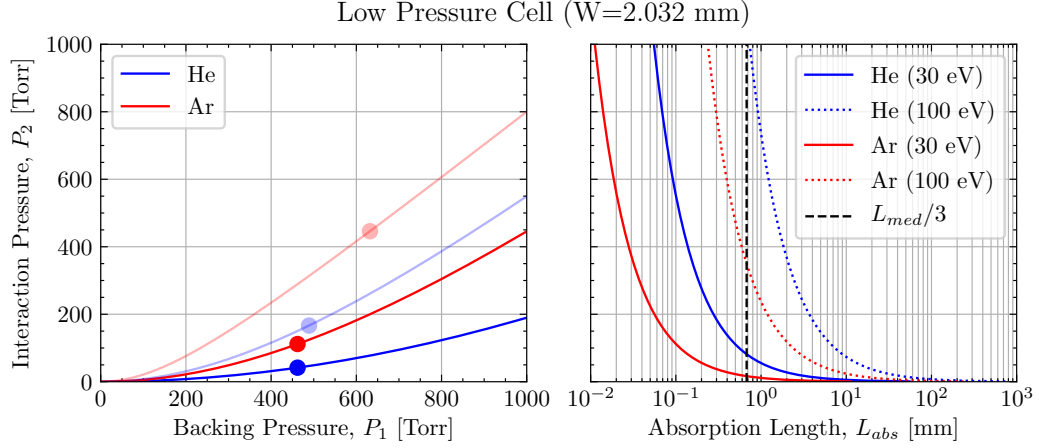


Figure 3.8: Interaction pressures and XUV absorption lengths for the low pressure cell (LPC). Left panel: interaction pressure of helium (blue) and argon (red) as a function of backing pressure. Bright lines correspond to $d = 400 \mu\text{m}$, faint lines are for $d = 200 \mu\text{m}$. Right panel: absorption length for the interaction pressures shown in the left panel.

$L_{abs} = L_{med}/3$ (black vertical dashed line). We can see that a $200 \mu\text{m}$ LPC is capable of efficiently phase matching 100 eV photons in argon, whereas a $400 \mu\text{m}$ LPC cannot.

HHG in LPC

To test the feasibility of the LPC for transient absorption experiments, we recorded HHG spectra under various experimental conditions.

Figure 3.9 shows the pressure scaling of the LPC's harmonic yield when using an 800 nm pulse, a $f = 40 \text{ cm}$ lens, and helium gas. The interaction pressure is calculated from the backing pressure and the geometry of the nozzle using Eq. (3.13) using an assumed laser hole diameter of $d = 400 \mu\text{m}$. The pulse energy was controlled using a combination of neutral density (ND) filters and by closing an iris before the generation chamber; average power was measured after the ND filters and before the lens using a power meter. The peak intensity was calculated assuming a 65 fs pulse duration, two 4% transmission losses from the lens and CaF_2 window, and ignoring the iris-induced diffraction at the focus [98]. From this figure, we can see that the harmonic yield increases with increasing interaction pressure regardless of input pulse energy. Using the reabsorption model of Section 1.3.2, this trend indicates that we are operating with a sub-optimal interaction pressure, and increasing the pressure-length would improve our harmonic yield. At the higher operating pressures, the harmonic yield is saturated when the peak intensity is $2.32 \times 10^{15} \text{ W/cm}^2$.

The red curve in Fig. 3.22 shows an optimized harmonic spectrum from the LPC (17 Torr interaction pressure, $2.32 \times 10^{15} \text{ W/cm}^2$). Recalling Section 2.6.2, a harmonic spectrum

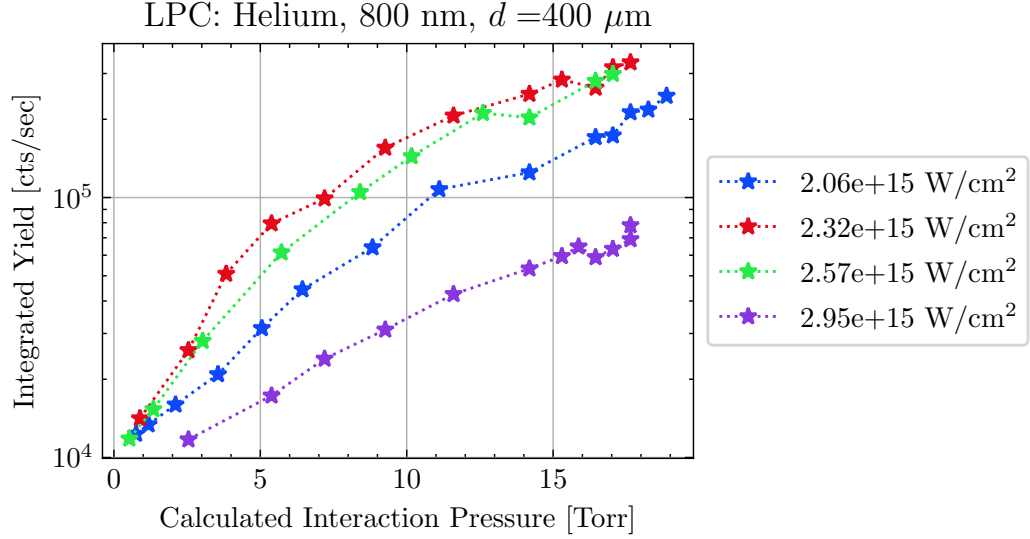


Figure 3.9: Total harmonic yield of the LPC as a function of interaction pressure. To calculate the integrated yield, harmonic spectra are background subtracted, normalized for exposure time and integrated over the sensor area.

with more than an octave of bandwidth will have both $m = 1$ and $m = 2$ diffraction orders present on the screen. The highest resolvable harmonic is at 107 eV, which we identify as the observable cut-off energy. As such, the spectrum below 52 eV is contaminated with $m = 2$ light and the shape of the lower energy harmonics should be ignored. From Eq. (1.16), we estimate $U_p = 26.0$ eV and from Eq. (1.2), we estimate the intensity to be $I_0 = 3.5 \times 10^{14}$ W/cm². Both of these estimates are nearly an order of magnitude lower than the peak intensity calculated from the input pulse energy.

Figure 3.10 shows the on-axis ionization fraction within a single pulse for these experimental conditions. The peak intensity is sufficiently high to completely ionize the gas medium well before the peak of the field. The on-axis ionization fraction quickly exceeds the critical ionization fraction (see Fig. 1.9) a full 50 fs before the peak of the field, as shown in the shaded regions below the blue curve. This narrow on-axis phase matching window indicates that the majority of the light is coming from the larger off-axis volume, which experiences a lower peak intensity. Nevertheless, the interaction density is too low to accommodate ideal phase matching.

Relative to the continuous free expansion gas jet, the low pressure cell has an increased interaction length but cannot reach optimal phase matching pressures. While the flux is higher than the free expansion jet, it is insufficient for an ATAS experiment.

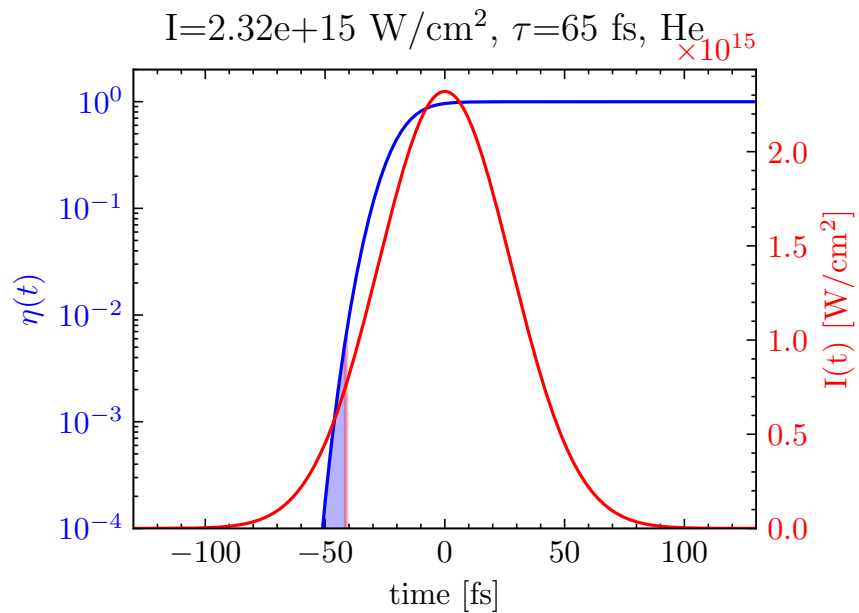


Figure 3.10: On-axis ionization fraction of helium (blue) and pulse envelope (red) at the focus of an 800 nm $\tau = 65$ fs, $I_0 = 2.32 \times 10^{15} \text{ W/cm}^2$ pulse. Times on the rising edge of the pulse where the ionization fraction is below the critical ionization fraction η_c are shaded to indicate when harmonics are phase matched. The blue region denotes times when $\eta < \eta_c \simeq 0.55\%$ for photons with energies above 50 eV. The red region shows the additional times where lower energy (< 50 eV) photons can be phased matched as their critical ionization fraction is slightly higher ($\eta_c \simeq 0.7\%$).

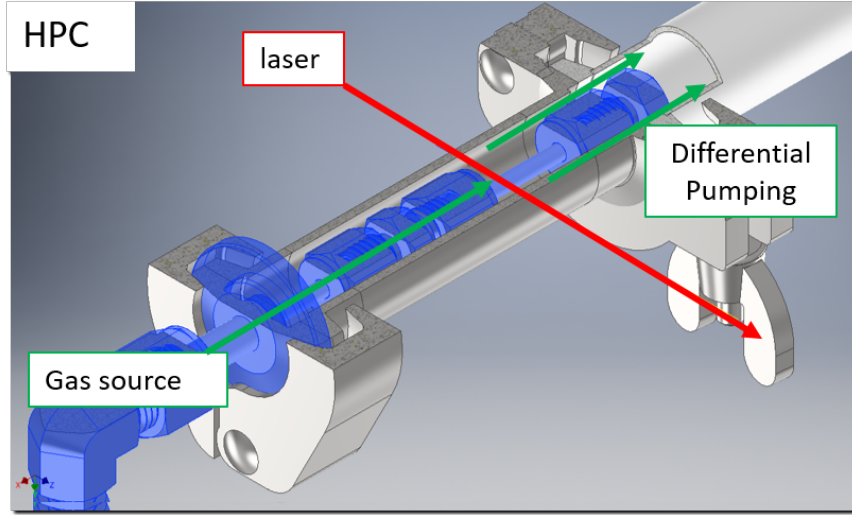


Figure 3.11: Cutaway view of the HPC interaction region. From bottom left to top right: welded gas feedthrough, concentric inner & outer pipes, connection to edge-welded bellows. The high pressure region is shaded blue. The green lines indicate the gas flow direction; the red line indicates the laser propagation direction.

3.2.4 High Pressure Cell

Design of HPC

The high pressure cell (HPC) was designed to be a drop-in upgrade to the previously available HHG gas sources. As such, we did not consider a semi-infinite gas cell design which would require disruptive chamber modifications. We also did not want to implement a waveguide solution, as its performance would be strongly effected by the coupling (and therefore the laser pointing) into the assembly [99, 100]. Finally, we wanted to avoid the complications of a servicing a pulsed solenoid valve [101], so the HPC was designed to be user-serviceable with low-cost replacement parts. As such, it consists of standard Swagelok and KF fittings with minimal modifications and a custom bellows assembly. The only consumable part is the stainless steel pipe housing the interaction region, and it only needs to be replaced when the HPC is installed or the focusing condition is changed.

The design of the HPC is shown in Figs. 3.11 and 3.12. It features two concentric cylinders: a stainless steel inner pipe which serves as the interaction region and gas source, and an outer shroud connected to an external rough pump which provides differential pumping. The inner pipe is connected to a gas line with continuous flow. Laser-drilled diametrically opposed pinholes on the inner pipe wall allow for light propagation while minimizing gas flow to the outer shroud. A small portion of the gas within the outer shroud flows into the generation chamber via the machined holes, but most of the gas flows towards the exhaust

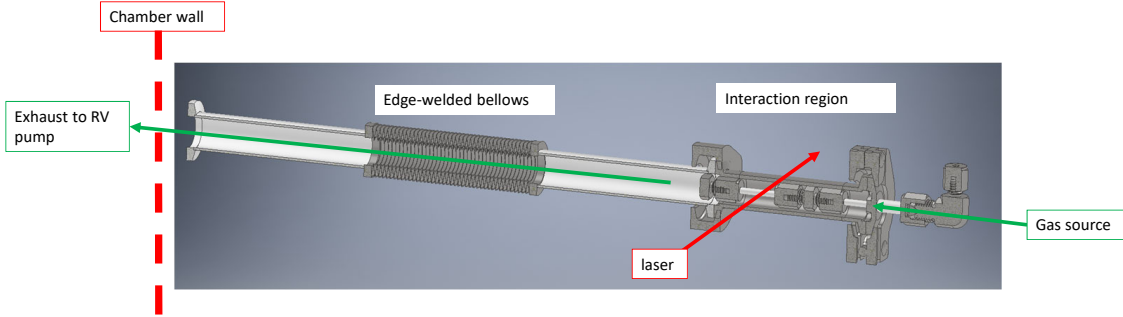


Figure 3.12: Cutaway view of the HPC assembly showing the flexible bellows connection and connection to the chamber wall.

and into a dedicated rough pump.

The relative positions of the inner pipe and the outer shroud are fixed by the KF hardware connections upon assembly. However, this positioning is not repeatable within the tolerances imposed by the laser transmission requirements. As a result, a new section of stainless steel pipe must be laser drilled every time the HPC is disassembled or removed from the generation chamber. The HPC assembly's position relative to the laser is adjustable via the same vacuum XYZ manipulator used for the free jet and LPC assemblies. A set of flexible bellows, visible in Fig. 3.12, allows for this movement while maintaining a vacuum-tight connection between the outer shroud and the chamber wall. A Baratron pressure gauge monitors the pressure of the KF tubing just outside the chamber wall.¹⁵ The flexible bellows has enough slack to allow the HPC to move below the optical axis, allowing the beam to pass over the top of the outer shroud. This is useful when aligning downstream optics.

The laser passes through the HPC assembly perpendicular to its symmetry axis; therefore the gas-laser interaction length is approximately equal to the diameter of the inner pipe. The outer shroud has two diametrically opposed machined 600 μm holes for the laser to pass through the assembly. During installation, the user aligns the two apertures in the outer shroud to the laser and fixes its position. Next, the inner pipe is installed and the unattenuated laser drills through the inner pipe walls. As a result, the four apertures are automatically collinear and aligned to the laser propagation axis.

Figure 3.13 is a photograph of the inner pipe, taken with a 0.5x telecentric lens (Edmund Optics part number 62-911). This photo shows the laser-drilled hole at the end of an experimental run. Laser drift and misalignment, as well as daily harmonic optimization procedures over the course of several months have opened up these holes from their original

¹⁵Note: while the bellows can withstand an external pressure differential of 1 atm, they will become damaged if they are overpressured by 120 Torr. See Appendix A.3 before operating this system.

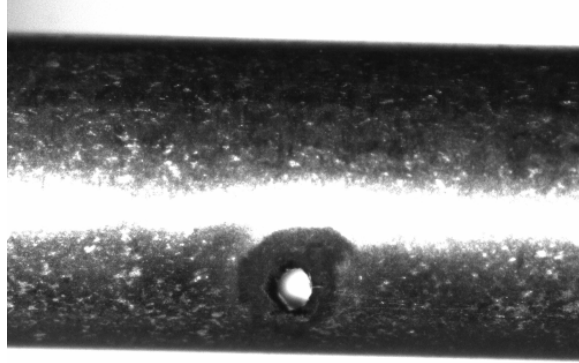


Figure 3.13: Photograph of the HPC's inner pipe showing the laser-drilled hole (bottom center of pipe).

diameter of approximately $100 \mu\text{m}$ to a final diameter of $430 \mu\text{m}$.

Gas Flow in HPC

The differential pumping of the HPC assembly allows the user to use much higher interaction pressures than other continuous gas sources in the DiMauro lab. In this section we will model the gas flow through the HPC to see why this is the case. Figure 3.14 shows a simplified gas flow of the HPC assembly. With the HPC cell installed, there are three distinct pressure regions within the generation chamber: the high pressure inner pipe (region H , with pressure P_H), the medium pressure outer shroud (region M , with pressure P_M), and the rest of the generation chamber remains at low pressure (region L , with pressure P_L). Two pairs of supersonic jets form at the boundaries of the three pressure regions. For each boundary, the gas jet serves as a gas sink for the higher pressure region, and as a gas source for the lower pressure region. Due to the large conductance of the tubing between the gas cylinder and the H region, we treat P_H as spatially constant and equal to the pressure reading on the regulator / inline pressure gauge. In the M region, the majority of the gas flows orthogonal to the laser axis, down the roughing line to the floor pump; a small portion flows to the L region via the machined apertures as supersonic jets. The large pressure differential (2-3 orders of magnitude) between each region justifies the assumption of supersonic flow [19].

In Fig. 3.14, the dark blue region represents the high pressure region (H), the light blue region represents the medium pressure region (M), and the low pressure region is represented by the white region (L). Red arrows and text indicate gas sources, green arrows and text indicate flow towards the vacuum pumps; blue arrows and text indicate physical dimensions. S_{turbo} , S_{eff} and C_{annular} are the turbo pumping speed, effective rough pumping speed and annular conductance, respectively; \hat{T}_H (\hat{T}_M) is the gas throughput from

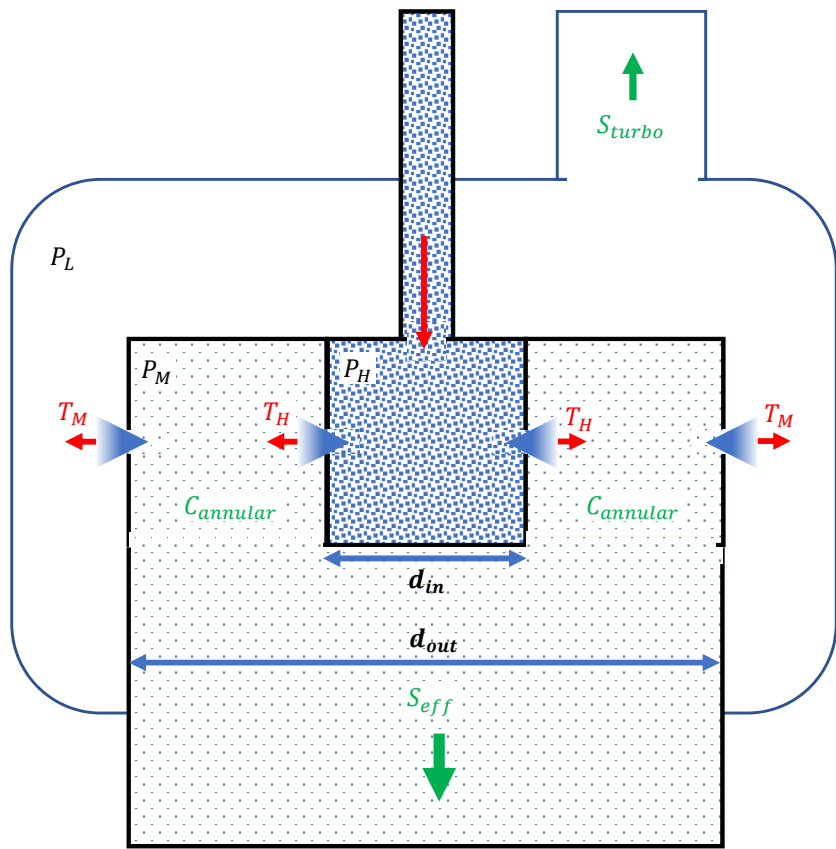


Figure 3.14: Schematic used to calculate the pressures inside the HPC and generation chamber.

the H (M) region into the M (L) region from each supersonic jet.

By balancing the throughputs, we arrive at the following coupled equations:

$$\begin{aligned}\hat{T}_H &= cP_H a_H^2, \\ P_M &= \frac{2(\hat{T}_H - \hat{T}_M)}{S_{\text{eff}}}, \\ \hat{T}_M &= cP_M a_M^2, \\ P_L &= \frac{2\hat{T}_M}{S_{\text{turbo}}}.\end{aligned}\tag{3.14}$$

In the above equations, P_M and P_L refer to the average background pressures in the M and L volumes, and the gas constant c is the same as in Eq. (3.5). That is, we ignore the structure of the plume in these calculations, which is justified because the size of each gas plume is smaller than the distance between the aperture and the next vacuum region.¹⁶ Rearranging Eq. (3.14), we see that P_M and P_L are proportional to P_H , with prefactors that depend on the local effective pumping speed and aperture geometry:

$$\begin{aligned}P_M &= \frac{2ca_H^2}{S_{\text{eff}} - 2ca_M^2} P_H = \frac{S_{\text{turbo}}}{2ca_M^2} P_L, \\ P_L &= \frac{4c^2 a_M^2 a_H^2}{S_{\text{turbo}}(S_{\text{eff}} - 2ca_M^2)} P_H.\end{aligned}\tag{3.15}$$

The maximum achievable interaction pressure P_H is only limited by the internal bellows burst pressure ($P_M \sim 120$ Torr) and the load on the turbopumps (P_L). From Eq. (3.15), we can see that we can reduce P_M and P_L by maximizing the effective rough pump speed S_{eff} and minimizing the aperture sizes (a_H, a_M). The aperture sizes are set by the laser beam size and divergence, while S_{eff} is conductance-limited by the roughing line connecting the M region to the floor pump. Note that we do not need to know S_{eff} to calculate P_M , provided we have accurate measurements of a_M and P_L . However, it can be instructive to analyze how the geometry of the HPC assembly affects the effective pumping speed.

We need to make a few key assumptions before we can calculate the effective pumping speed, S_{eff} . First, we assume that the pressure in the rough line is on the order of a few Torr (this was later confirmed experimentally using the Baratron gauge). Assuming a characteristic internal length scale of $L = 1$ cm and mean free path of $\lambda = (5 \text{ Torr}/760 \text{ Torr}) \times 80 \text{ nm}$, we can calculate the *Knudsen number*, $Kn = \lambda/L \sim 0.001$, which meets the criteria for continuum flow ($Kn < 0.01$). Next, assuming an effective pump speed of 5 l/s and a pipe diameter of 2 cm, we can calculate the *Reynolds number*: $Re = \rho ud/\mu \sim 1$, which meets

¹⁶For $P_H = 760$ Torr, $P_M = 0.7$ Torr and $a_H = 100 \mu\text{m}$, $x_M = 22.1a_H = 2.21$ mm, which is smaller than the distance between the laser drilled aperture and the outer shroud's machined aperture (6.2825 mm). For $P_L = 3 \times 10^{-4}$ Torr and $a_M = 600 \mu\text{m}$, we have $x_M = 32a_M = 19.4$ mm, which is much smaller than the distance between the HPC and the next vacuum chamber (25 cm).

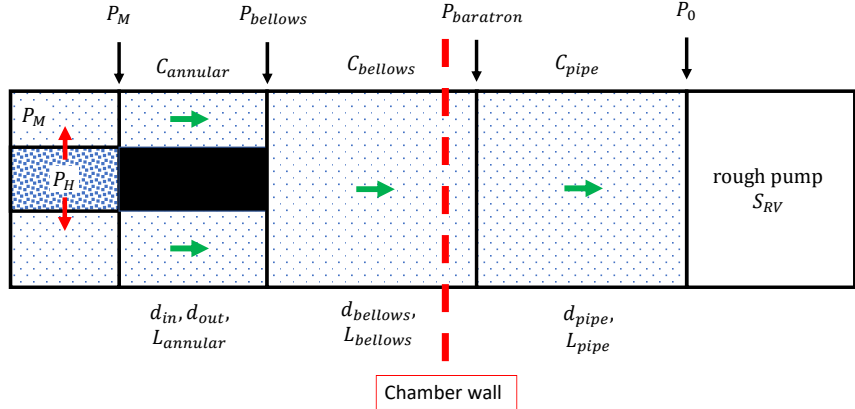


Figure 3.15: Schematic showing the geometry and pressure profile of the HPC's rough vacuum line.

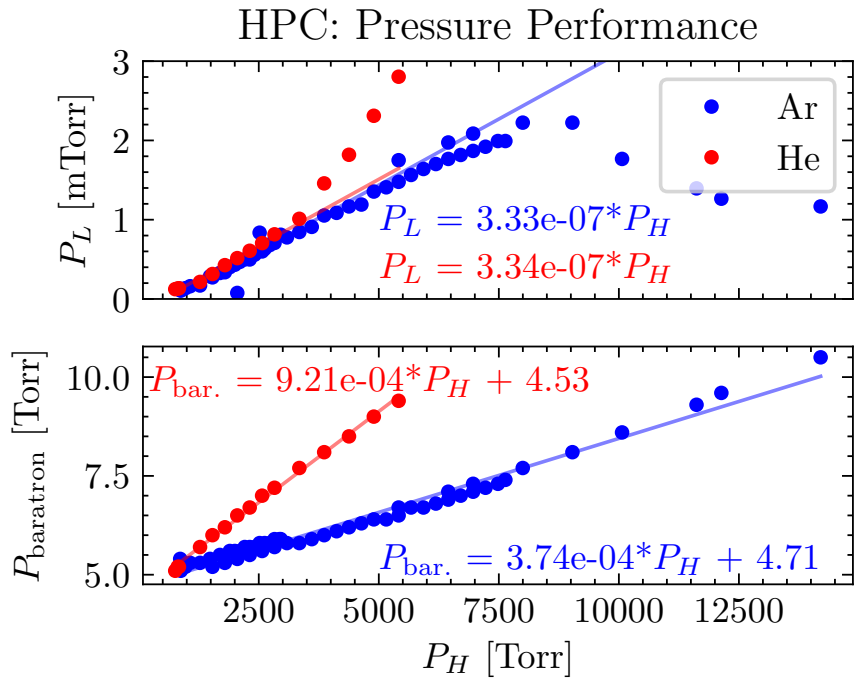


Figure 3.16: Measured HPC pressure performance using the temporary spectroscopy station. P_H is measured from the gas source's inline pressure regulator; P_{baratron} is measured using a diaphragm gauge immediately outside the chamber wall; P_L is measured using a cold cathode gauge (PTR90) and corrected using values from the manufacturer's datasheet. Linear fits to P_{baratron} and P_L are performed for $P_H < 3000$ Torr. Regulators were changed at $P_H \sim 3000$ and ~ 8000 Torr, which account for the discontinuities.

the criteria for laminar flow ($Re < 2300$). By making reasonable assumptions, we have shown that vacuum tubing between the M region and the floor pump is well within the laminar flow regime. Again, this analysis ignores the structure of the supersonic plume; the flow is likely turbulent near the boundary of the plume. The effective pumping speed in the medium pressure region S_{eff} can therefore be calculated using standard conductance formulae for laminar flow (SI units) [93]:

$$\begin{aligned}\frac{1}{S_{\text{eff}}} &= \frac{1}{C_{\text{annular}}} + \frac{1}{C_{\text{bellows}}} + \frac{1}{C_{\text{pipe}}} + \frac{1}{S_{\text{RV}}}, \\ C_{\text{annular}} &= \frac{\pi}{128} \frac{1}{\eta} \frac{1}{L_{\text{annular}}} \left(d_{\text{out}}^4 - d_{\text{in}}^4 - \frac{(d_{\text{out}}^2 - d_{\text{in}}^2)^2}{\ln[d_{\text{out}}/d_{\text{in}}]} \right) \frac{P_M + P_{\text{bellows}}}{2}, \\ C_{\text{bellows}} &= \frac{\pi}{128} \frac{1}{\eta} \frac{d_{\text{bellows}}^4}{L_{\text{bellows}}} \frac{P_{\text{bellows}} + P_{\text{baratron}}}{2}, \\ C_{\text{pipe}} &= \frac{\pi}{128} \frac{1}{\eta} \frac{d_{\text{pipe}}^4}{L_{\text{pipe}}} \frac{P_{\text{baratron}} + P_0}{2},\end{aligned}\tag{3.16}$$

where the pressures are measured in Pa, η is the dynamic viscosity of the gas in Pa·s, distances are in meters, and S_{RV} is the rated pump speed of the floor pump in m^3/s . The geometry of the rough line system is defined in Fig. 3.15. We include in the calculation of S_{eff} the three main vacuum elements between the outer shroud of the HPC and the floor pump:

1. the short annular region formed between the inner pipe's Swagelok fittings and the inner wall of the shroud (see Fig. 3.11), defined by inner diameter $d_{\text{in}} = 1.283$ cm, outer diameter $d_{\text{out}} = 1.575$ cm, length $L_{\text{annular}} = 2$ cm, entrance pressure P_M and exit pressure P_{bellows} ;
2. the edge-welded bellows assembly, defined by length $L_{\text{bellows}} = 27.6$ cm, interior diameter $d_{\text{bellows}} = 1.7272$ cm, entrance pressure P_{bellows} and exit pressure P_{baratron} ;
3. the length of flexible PVC pipe connecting the exterior of the chamber to the floor pump, defined by length $L_{\text{pipe}} = 150$ cm and interior diameter $d_{\text{pipe}} = 2$ cm, entrance pressure P_{baratron} and exit pressure P_0 .

Given the above dimensions, the annular region has an outsized impact on the total conductance of the differential pumping system:

$$\begin{aligned}C_{\text{annular}} &= (5.83 \times 10^{-10} \text{ m}^3) \times (\bar{p}_{\text{annular}}/\eta), \\ C_{\text{bellows}} &= (7.91 \times 10^{-9} \text{ m}^3) \times (\bar{p}_{\text{bellows}}/\eta), \\ C_{\text{pipe}} &= (2.62 \times 10^{-9} \text{ m}^3) \times (\bar{p}_{\text{pipe}}/\eta),\end{aligned}$$

where \bar{p}_i is the average pressure in each element. For a floor pump speed with $S_{\text{RV}} = 5 - 11 \text{ l/s}$, the effective pump speed S_{eff} in the M region will be between 20% and

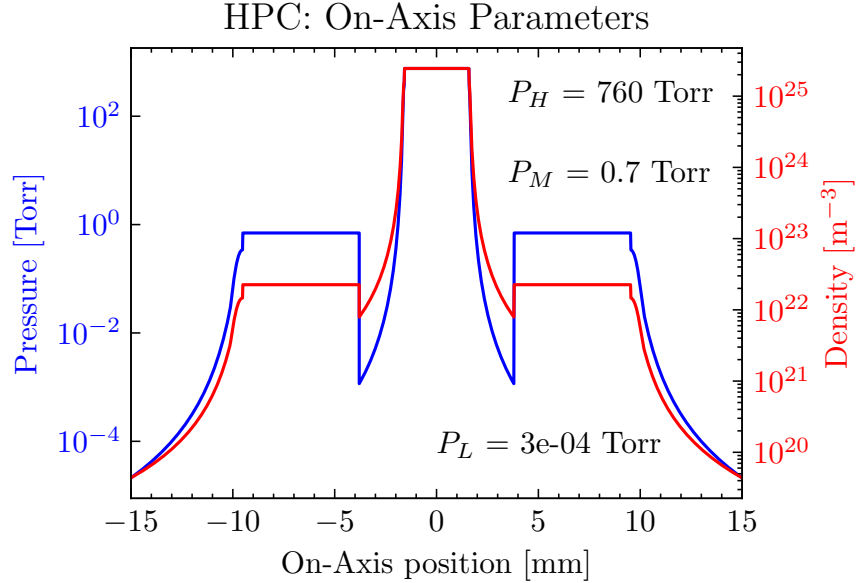


Figure 3.17: Calculated on-axis pressure and density profiles for helium with $P_H = 760$ Torr, $P_M = 0.7$ Torr and $P_L = 3 \times 10^{-4}$ Torr.

88% of S_{RV} , assuming a constant average pressure \bar{p} in the range 1 – 30 Torr.

The HPC was initially tested in a simplified vacuum system, called the *temporary spectroscopy station*, as the TABLE’s interferometer was being used by another graduate student at the time. The temporary spectroscopy station consisted of the TABLE’s target chamber (repurposed as a generation chamber) connected to the photon spectrometer via a differential pumping chamber. There was no XUV refocusing optic. Instead of using the TABLE’s high throughput RV system (see Fig. 2.14), individual floor pumps to back the turbos. The generation turbo was backed by a Leybold D40B ($S_{RV} = 13.3$ l/s); the HPC rough line was pumped by a scroll pump ($S_{RV} \sim 10$ l/s), and two smaller Leybold D16B pumps ($S_{RV} = 5.5$ l/s) were used to back the differential and photon spectrometer turbos.

Figure 3.16 shows the HPC’s pressure performance for helium and argon gas as measured in the temporary spectroscopy station. Pressures were measured with a Baratron diaphragm gauge (P_{baratron} , located immediately outside the chamber wall) and a Leybold PTR90 cold cathode gauge (P_L , attached to the generation chamber). The pressure readings from the cold cathode gauge are corrected using the manufacturer’s datasheet; the Baratron’s readings are gas species-independent. Here, we see that P_{baratron} , which is approximately equal to P_M , scales linearly with respect to the backing pressure P_H over a wide range of pressures. Note that the slope for helium is approximately 3 times that for argon, which is consistent with their gas constants ($c = 14$ l/cm²/s for Ar, $c = 45$ l/cm²/s for He).

Turning our attention to the chamber pressure (P_L), we see a rollover in argon around

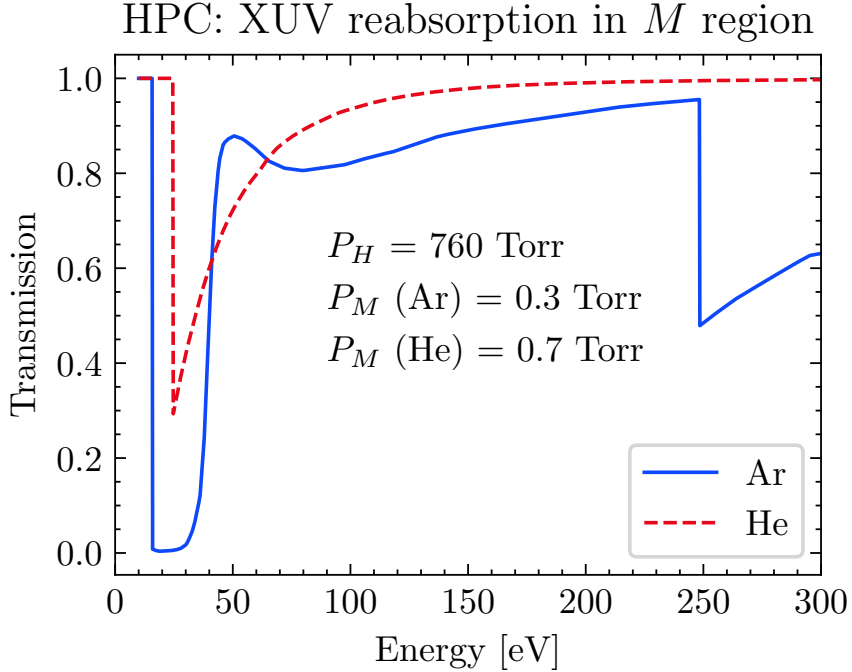


Figure 3.18: Expected XUV reabsorption in the P_M region for different generating media. P_M calculated using $P_H = 760$ Torr via Eq. (3.15). Absorption data from [7].

$P_H \sim 8000$ Torr, and in helium we see a discontinuity in the slope at $P_H \sim 3000$ Torr. These features are unphysical and are likely caused by the cold cathode gauge malfunctions. Regardless, we can see that the chamber pressure stays in the milliTorr regime even when $P_H \simeq 5,000$ Torr for helium and $P_H \simeq 14,000$ Torr for argon.

Figure 3.17 shows the calculated on-axis density and pressure profile of the HPC for helium and an interaction pressure of 760 Torr. The intermediate pressure P_M is assumed to be equal to P_{baratron} and is calculated using the linear coefficient obtained in Fig. 3.16. In calculating P_M , we omit the offset of 4.53 Torr which is a measurement artifact of the Baratron gauge. The on-axis pressure shows that there is a non-negligible amount of gas in the M region, which is several millimeters long. If we assume that HHG occurs solely in the H region, then XUV flux may inadvertently be reabsorbed when propagating through the M region.

Figure 3.18 estimates the XUV transmission (via $T = \int_M dz \exp(-\rho(z)\mu_a z)$) in the M region assuming the aforementioned pressure profile, and Fig. 3.19 shows the XUV transmission in the M region for 30 and 100 eV photons over a range of pressures. In both figures, XUV absorption in the L region is neglected due to its low pressure. Figure 3.19 also compares the absorption length ($L_{\text{abs}} = 1/\rho\mu_a$) to the medium length L_{med} . We can see that the HPC can reach sufficiently high interaction pressures and length to meet the

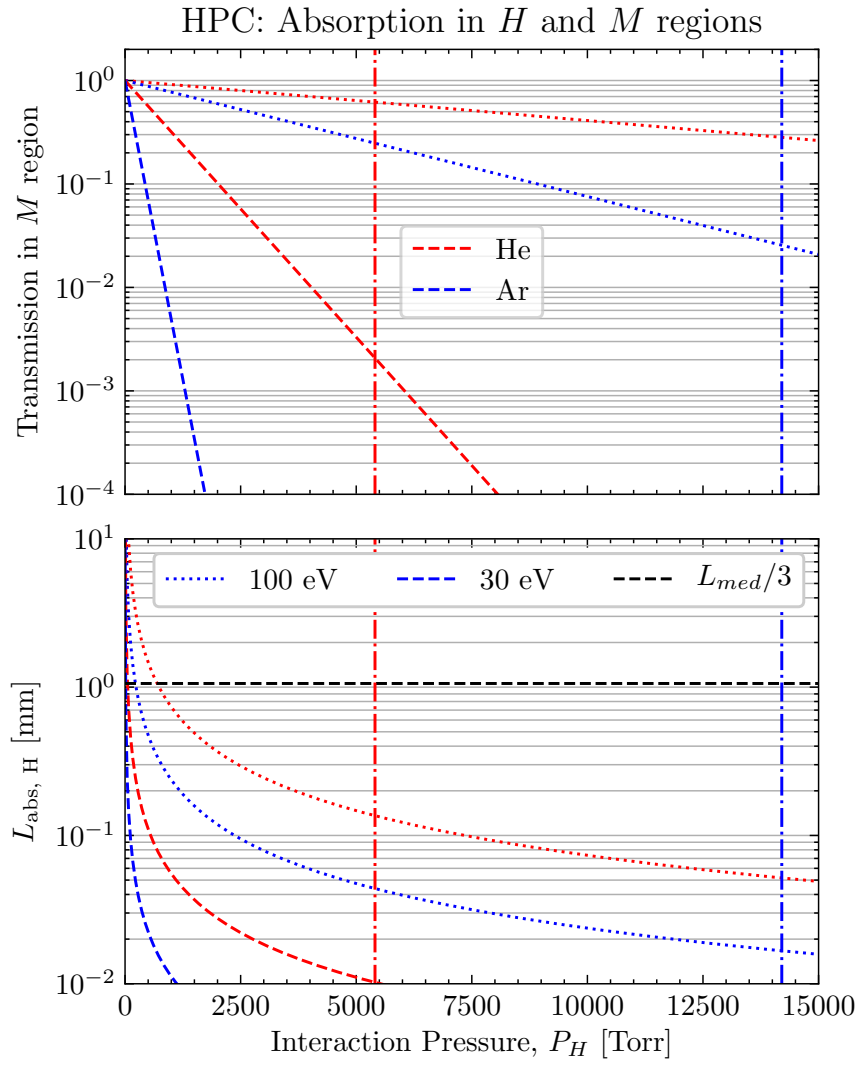


Figure 3.19: HPC calculated performance as a function of interaction pressure, assuming $a_H = 100 \mu\text{m}$ and the fit from in Fig. 3.16. For both panels, blue (red) lines correspond to argon (helium), dashed (dotted) lines correspond to 30 (100) eV photons. Vertical dashed lines indicate the highest experimentally achieved pressures.

phase matching guidelines laid out in Section 1.3.2.

HHG in the HPC

An effort was made to increase the XUV flux in the energy range 90 - 130 eV, which would allow the measurement of the Si *L*-edge in an ATAS experiment. To this end, HHG experiments were performed in the temporary spectroscopy station using the HPC and an $f = 40$ cm CaF₂ lens. Input power and phase matching were simultaneously controlled using an adjustable aperture located before the focusing optic. The interaction pressure was controlled with the gas cylinder's regulator and measured using an inline digital pressure gauge (Ashcroft model 2274). The fundamental and < 50 eV harmonics were blocked using a 200 μm Zr filter located approximately 75 cm downstream of the HPC. The spectrometer's energy axis was crudely calibrated by counting the harmonics above the Al *L*-edge and assuming $2\omega_1$ spacing, and fitting to a 5th degree polynomial (see Section 2.6.2), and all HHG yields shown are scaled by the Jacobian. To isolate the effects of pressure scaling, phase matching conditions were optimized at low pressure and held constant as the interaction pressure was controlled. To maximize harmonic flux, the HPC's position relative to the focus was optimized (at the focus for helium and downstream of the focus for argon). Phase matching conditions were optimized for photon energies above 100 eV. Pulse energy was measured using a power meter immediately before the generation chamber; the reported values do not take into account any transmission losses of the fundamental due to the two HPC vacuum apertures between the generation chamber's window and the interaction region (*H*). Calculating the interaction intensity is complicated by diffraction and transmission losses resulting from the HPC's apertures; we report the intensities that would occur in the absence of the HPC assembly with the caveat that the actual intensities are likely lower.

The total harmonic yield for helium using 800 nm light as a function of interaction pressure is shown in Fig. 3.20. Unlike the LPC, we can see a maximum in the harmonic yield with respect to interaction pressure, indicating that we are no longer limited by the vacuum performance of the gas source. The total yield is maximized for $P_H \sim 600$ Torr. Helium's high ionization potential ($I_p = 24.5874$ eV) necessitates high laser intensities to efficiently drive the HHG process, and we see that a $\simeq 0.36 \times 10^{15}$ W/cm² increase in peak intensity increases total harmonic yield by nearly an order of magnitude. In contrast to the LPC, where we saw a saturation in harmonic yield at around $\simeq 2.32 \times 10^{15}$ W/cm², the HPC's yield does not saturate until $\simeq 2.67 \times 10^{15}$ W/cm². This is likely due to the lower transmission of the HPC's vacuum apertures, estimated at $\simeq 90\%$. In the following discussion we report the normalized yield, which is obtained by background subtracting, integrating over the spatial dimension of the sensor, and normalizing by integration time. In the event that multiple spectra are obtained for identical conditions, we average the results together.

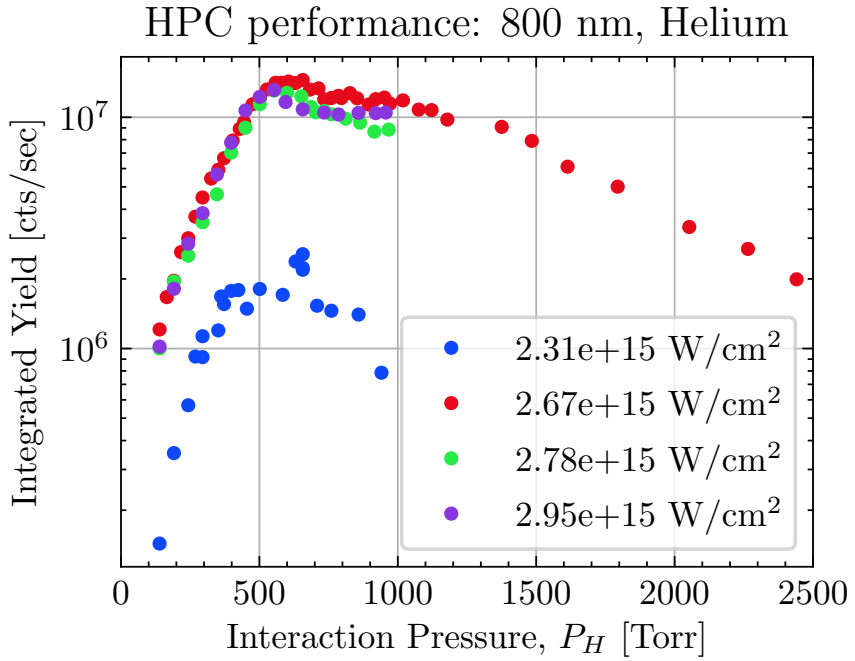


Figure 3.20: Total harmonic yield as function of interaction pressure in the HPC. To calculate the integrated yield, harmonic spectra are background subtracted, normalized for exposure time and integrated over the sensor area (divergence and energy).

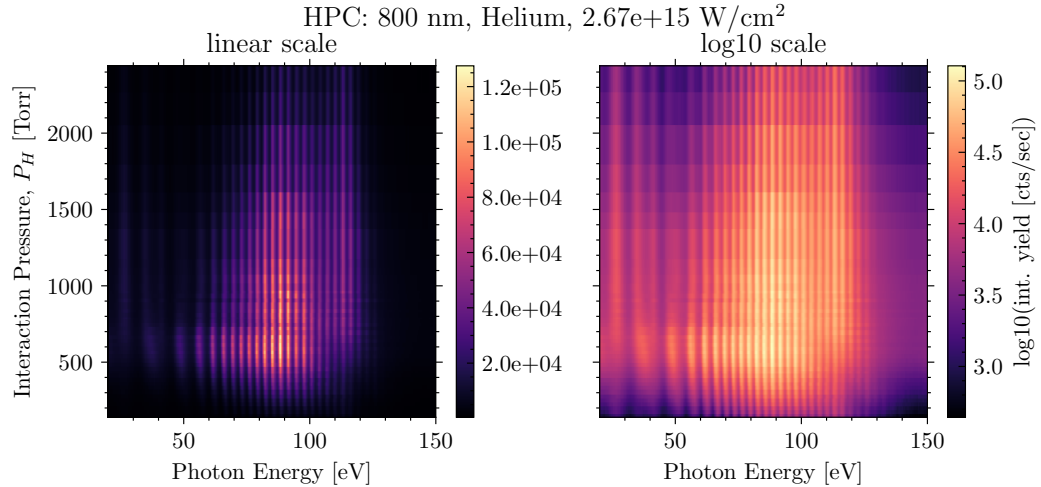


Figure 3.21: Harmonics generated from helium as a function of interaction pressure for $\lambda_1 = 800 \text{ nm}$, a peak intensity of $2.67 \times 10^{15} \text{ W/cm}^2$ and a $200 \mu\text{m}$ Zr filter. Note that different energy harmonics are phase matched at different pressures. To calculate the integrated yield, harmonic spectra are background subtracted, normalized for exposure time and integrated over the sensor area.

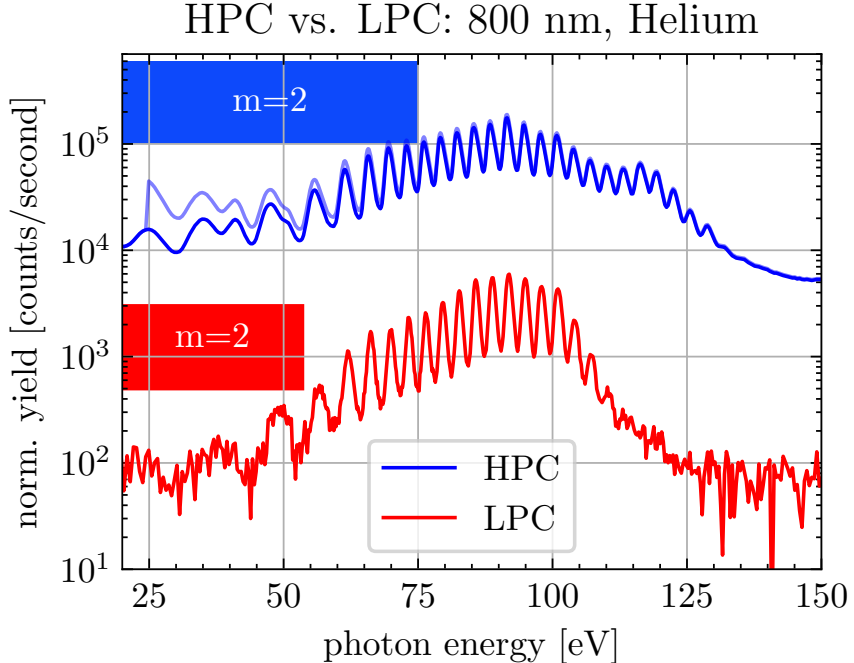


Figure 3.22: Comparison of the LPC and the HPC in helium at 800 nm. Generation conditions for each were optimized (LPC: 17 Torr interaction pressure, $2.32 \times 10^{15} \text{ W/cm}^2$; HPC: 650 Torr, $2.67 \times 10^{15} \text{ W/cm}^2$) in helium at 800 nm. The higher interaction pressure extends the phase matched region from ~ 110 eV to ~ 130 eV, and increased pressure-length product increases the XUV brightness by at least two orders of magnitude across the spectrum. Note that harmonics with energies less than half the cutoff are contaminated by 2nd order diffraction from the XUV spectrometer's grating. Faint blue line removes the calculated absorption losses in the medium pressure (M) region. Normalized yield is calculated by background subtracting the 2D spectra, integrating the spatial dimension of the sensor, normalizing by exposure time and applying the Jacobian.

Figure 3.21 shows a spectrogram of the 800 nm $2.67 \times 10^{15} \text{ W/cm}^2$ helium dataset. We can see a broad maximum in yield for energies below ~ 100 eV below 650 Torr. Harmonic yield above 100 eV is maximized above 700 Torr at the expense of lower energy light; light below 80 eV is suppressed when $P_H > 1600$ Torr. This observed dispersion matches the general $1/\Delta n$ pressure scaling in Fig. 1.10 and the absorption in Fig. 3.19.

Figure 3.22 compares the spectra of the LPC and the HPC. The portion of the sensor that is contaminated with $m = 2$ XUV light (lower half of the spectra) is indicated by a red or blue box. Other than the gas source, these datasets were taken under identical circumstances¹⁷, so we can compare their spectral amplitudes. We can see that the total harmonic yield of the HPC exceeds that of the LPC by about two orders of magnitude.

¹⁷Nominal differences in pulse energy are attributed to lower MIR transmission of the HPC's apertures. Both experiments were conducted at the threshold of saturation intensity.

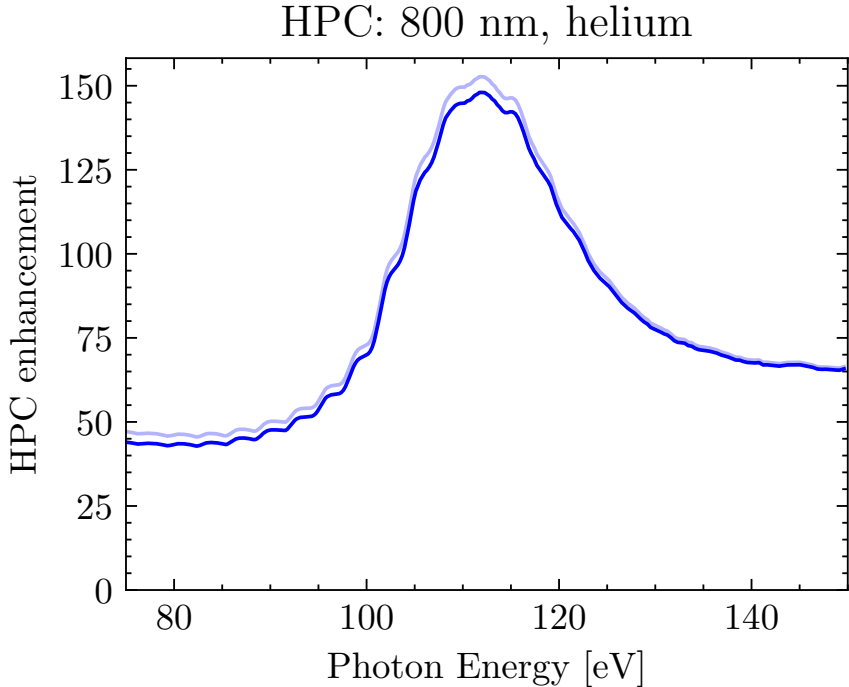


Figure 3.23: Relative performance of the HPC compared to the LPC in the energy range 75 - 150 eV. Faint blue line includes the calculated transmission factor in the M region. Datasets are the same as in Fig. 3.22.

Additionally, the highest observable harmonic is increased from ~ 110 eV to ~ 130 eV. Taking into account the calculated pressure profile in the M region and the photoabsorption cross section of helium, we plot the absorption-free yield ($P_M = 0$) in faint blue.

Figure 3.23 shows the relative enhancement of HHG using the HPC compared to the LPC. Over the energy range 75 - 150 eV, we can see a 50 - 60x improvement in yield, with a ~ 150 x enhancement centered at 110 eV. The position of this enhancement peak is very sensitive to generation conditions and can be shifted by tens of eV by adjusting the iris.

We can compare the measured performance to what was expected from our previous discussions on HHG. From Eq. (1.34), we expect the harmonic yield to scale as $(PL_{\text{med}})^2$, and when considering the pressure models developed above, we would expect the HPC to outperform the LPC by a factor of roughly 3500. After taking into account the XUV absorption in the M region, we measured a factor of 150, which is significantly less than the expected value. This discrepancy (factor of ~ 23) may be attributed to a smaller effective MIR spot size and a diffraction-induced non-Gaussian beam shape at the focus. The higher interaction pressures may result in an ionization-induced defocusing of the fundamental beam, lowering the interaction intensity and therefore the harmonic yield [102].

Similar experiments were performed using argon using signal wavelengths. Figure 3.24

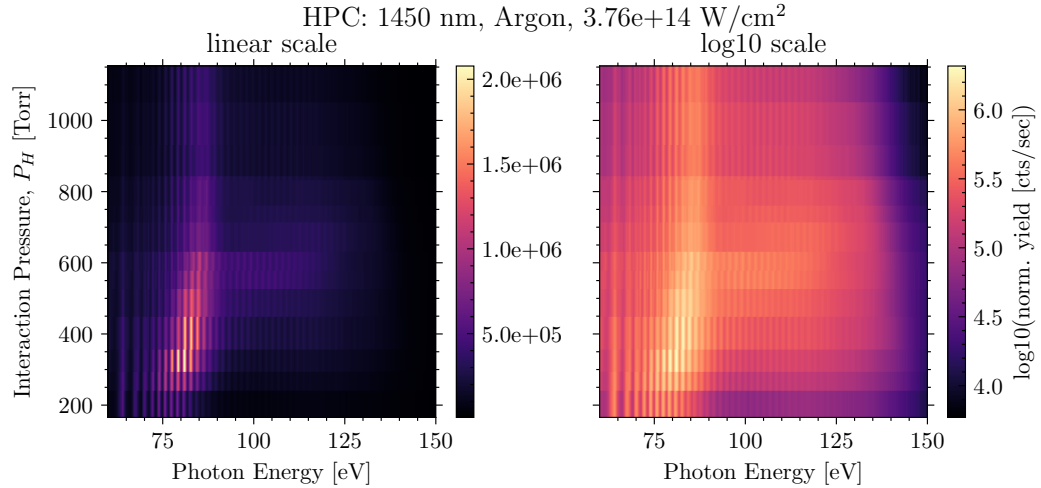


Figure 3.24: Performance of the HPC using argon at 1450 nm. Normalized yield is calculated by background subtracting the 2D spectra, integrating the spatial dimension of the sensor, normalizing by exposure time and applying the Jacobian.

shows a spectrogram of argon’s harmonic yield at 1450 nm under typical operating conditions. Note that the lower ionization energy ($I_P = 15.75962$ eV) translates into a lower peak intensity for optimal harmonic generation. We observe a rolling maximum in the harmonic yield, from 70 to 90 eV, as the interaction pressure is increased from 200 to 600 Torr. At higher energies (> 90 eV), we see a broad maximum between 250 and 850 Torr. As the pressure increases past 850 Torr, harmonic yield uniformly decreases.

Figure 3.25 shows spectral lineouts of Fig. 3.24 for lower interaction pressures. In this figure, we see that the harmonic yield above 90 eV increases about an order of magnitude as the interaction pressure is increased from 165 to 527 Torr, which is perfectly in line with the expected P^2 scaling ($527^2/165^2 = 10.2$). At 450 Torr and above, we observe a blueshifting of the harmonic comb, which is suggestive that the fundamental is experiencing nonlinear propagation effects near the focus. This effect was not observed in helium, which has a significantly higher ionization potential.

Although we do not have a directly comparable LPC HHG dataset, we can make some general comparisons between the two gas sources. Recalling Fig. 3.8, the LPC is limited to a maximum interaction pressure of between 50 and 175 Torr (depending on laser aperture size). If HHG follows the observed P^2 scaling, then the HPC would be between 9 and 110 times brighter than the LPC if both systems are optimized for maximum HHG yield.

We note that the increased XUV absorption of argon results in a lower overall enhancement factor than for helium [100]. The pressure model developed above predicts an XUV transmission between 85 and 90% for $P_H = 527$ Torr for photon energies between 75 and 150 eV.

HPC: 1450 nm, Argon, 3.76e+14 W/cm²

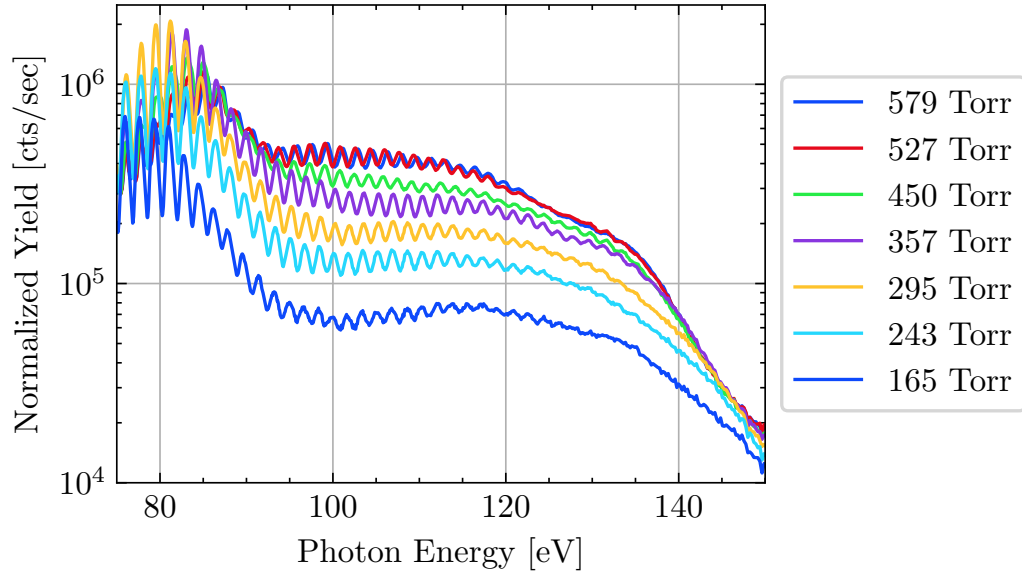


Figure 3.25: Spectral lineouts of Fig. 3.24 for pressures below the maximum in harmonic yield. Normalized yield is calculated by background subtracting the 2D spectra, integrating the spatial dimension of the sensor, normalizing by exposure time and applying the Jacobian.

We observe that at 100 eV, the optimized 1450 nm Ar dataset is $\sim 3x$ brighter than the 800 nm He dataset, despite being performed at a longer wavelength. Assuming λ^{-4} scaling of the yield at a single harmonic (see Section 1.3.1), we lose a factor of ~ 10 in yield by increasing from 800 to 1450 nm. Therefore, for optimized generation conditions using the same fundamental wavelength, we should expect Ar to be 30x brighter than He at a given photon energy dE .

3.2.5 Pulsed Amsterdam Piezo Valve

We can reduce the gas load on the turbopumps while achieving a moderately high interaction pressure by using a pulsed gas source, as the gas throughput scales approximately with the valve’s duty cycle [103]. Typical valve opening times are on the order of tens of microseconds [104–106], which results in a duty cycle of 1 – 10% percent when operating at 1 kHz. Commercially available valve designs consist of either a plunger-solenoid [101] or a piezoelectric flapper [104–106].

In our experience the plunger-solenoid design is prone to mechanical failure, which necessitates the device be sent back to the manufacturer for repairs. Unfortunately, it is not uncommon to experience months of equipment downtime during these regular service events. For this reason, we eschewed the use of a plunger-solenoid valve in favor of a simpler



Figure 3.26: Labeled picture of the Amsterdam Piezovalve showing dimensions (mm). The gas and electrical connections are located on the rear of the device; the nozzle aperture is located at the center of the front face (flat side).

CW gas delivery solution when designing the beamline.

We briefly had access¹⁸ to a commercial pulsed valve (Amsterdam Piezo Valve by MassSpecpecD BV), as shown in Fig. 3.26. The Amsterdam piezo valve utilizes an o-ring mounted to a cantilever piezoelectric flapper to briefly open an internal gas inlet port. This device has a $d = 500 \mu\text{m}$ diameter straight-channel nozzle and a backing pressure range of 0 - 15 bar. The delay was controlled using a Quantum Composer, the valve opening time was $75 \mu\text{s}$ and the operating voltage was 150 V.

The primary motivation for using this device was to complete a two-source harmonic generation experiment (for details, see [54]), but we performed basic diagnostics on the nozzle after installing it into the TABLE. Recalling Fig. 3.2, the gas density falls off sharply with increasing on-axis distance from the nozzle aperture. However, due to the flat face of the piezo valve assembly, the recessed nozzle aperture and the divergence of the beam, it is difficult to bring the aperture close to the laser axis without obscuring the laser beam and damaging the nozzle. We do not have a direct measurement of the on-axis distance x , but we can estimate it using the harmonic yield.

¹⁸Special thanks to fellow graduate student Andrew Piper for letting us borrow his equipment. For more detail and characterization of the piezo valve, see Andrew Piper's dissertation [73].

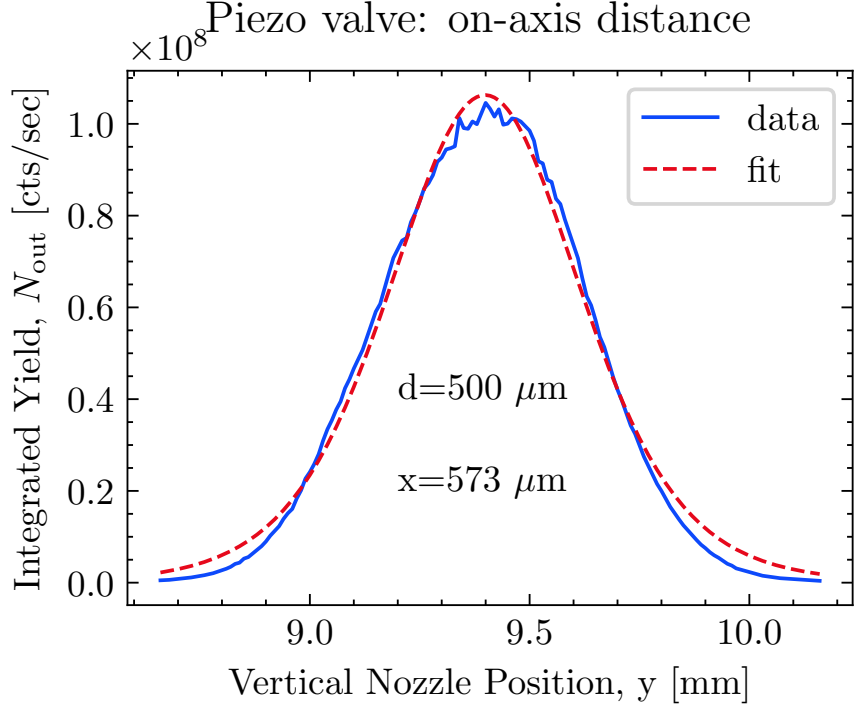


Figure 3.27: Integrated yield as a function of off-axis nozzle distance used to determine the on-axis distance, x . A fit of Eq. (3.19) to the data yields an on-axis distance of $573 \mu\text{m}$.

The off-axis density $\rho(x, y, z)$ of a free expansion gas jet is given by [19]:

$$\frac{\rho(x, y, z)}{\rho(x, 0, 0)} = \cos^2 \theta \cos^2 \left(\frac{\pi \theta}{2\phi} \right), \quad (3.17)$$

$$\text{with } \tan \theta \equiv \frac{\sqrt{y^2 + z^2}}{x}, \quad (3.18)$$

where x is the on-axis distance from the nozzle aperture, y and z are the off-axis distances from the nozzle's centerline axis (with z parallel to the laser propagation direction), and ϕ is a gas constant with values $\phi = 1.365, 1.662$, and 1.888 for $\gamma = 5/3, 7/5$ and $9/7$, respectively. If we assume an on-axis gas density distribution $\rho(x, 0, 0)$ given by Eqs. (3.3a) and (3.4a) and make the following approximation to Eq. (1.32) for the harmonic yield N_{out} :

$$N_{\text{out}}(x, y) \approx \alpha \left| \int_{-\infty}^{\infty} dz \rho(x, y, z) \right|^2, \quad (3.19)$$

where α is a scaling constant, then we can extract the on-axis distance x if we measure the harmonic yield as a function of the off-axis distance y .

To determine the minimum on-axis distance, we recorded the harmonic yield as a function of the vertical position of the piezo valve relative to a fixed laser focus. This scan was

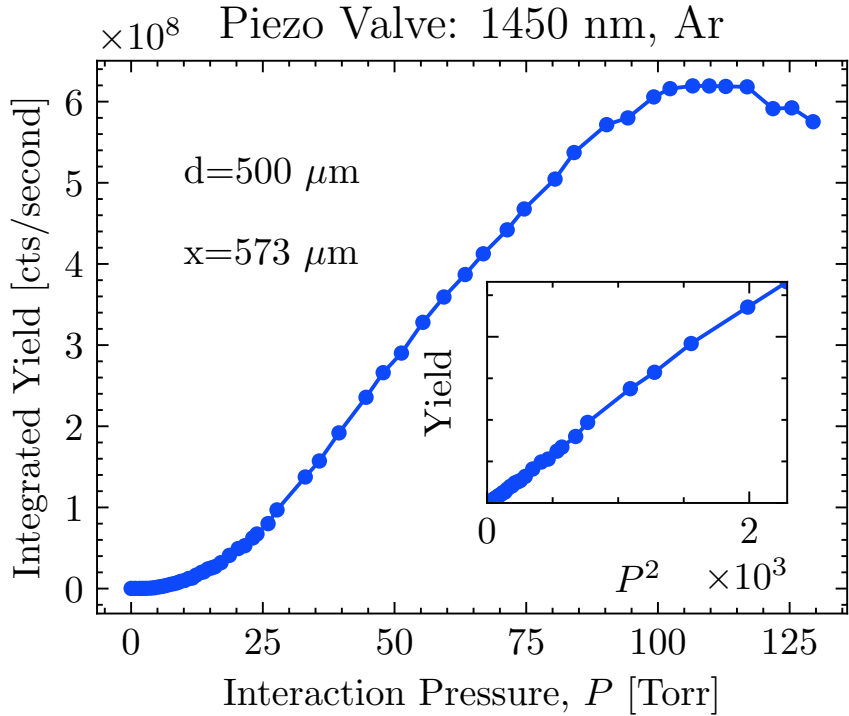


Figure 3.28: Integrated harmonic yield from the piezo valve as a function of interaction pressure. The inset shows excellent quadratic behavior with respect to interaction pressure. Assumed on-axis distance is $x = 573 \mu\text{m}$. To calculate the integrated yield, harmonic spectra are background subtracted, normalized for exposure time and integrated over the sensor area. The total yield has been multiplied by 4 to account for the 250 Hz rep. rate to compare it to the 1 kHz datasets.

performed using the following optimized generation conditions: a pulse energy of 961 mJ, a fundamental wavelength of 1450 nm at 250 Hz, a CaF₂ generation lens ($f = 40$ cm) and 29.3 psig backing pressure of Ar gas. The interaction intensity is estimated to be $3.67 \times 10^{14} \text{ W/cm}^2$. A 200 μm metallic aluminum filter located downstream of generation was used to block the fundamental. The experimental data and a fit to Eq. (3.19) are shown in Fig. 3.27. Assuming a nozzle diameter of 500 μm , we obtain a fit result of $x = 573 \mu\text{m}$, which represents the closest we can get the laser to the nozzle aperture without damaging the piezo valve assembly. At this distance, the calculated on-axis interaction pressure is 11.7% of the backing pressure.

As part of a diagnostic process, we recorded harmonic spectra as a function of backing pressure using the aforementioned generation conditions and with the piezo valve centered on the optical axis ($y = 0$). The interaction pressure was calculated using Eqs. (3.3a) and (3.4a) and assuming $x = 573 \mu\text{m}$, which was unchanged from the previous measurement. The total harmonic yield (below 72.7 eV) is shown in Fig. 3.28. The main figure shows a

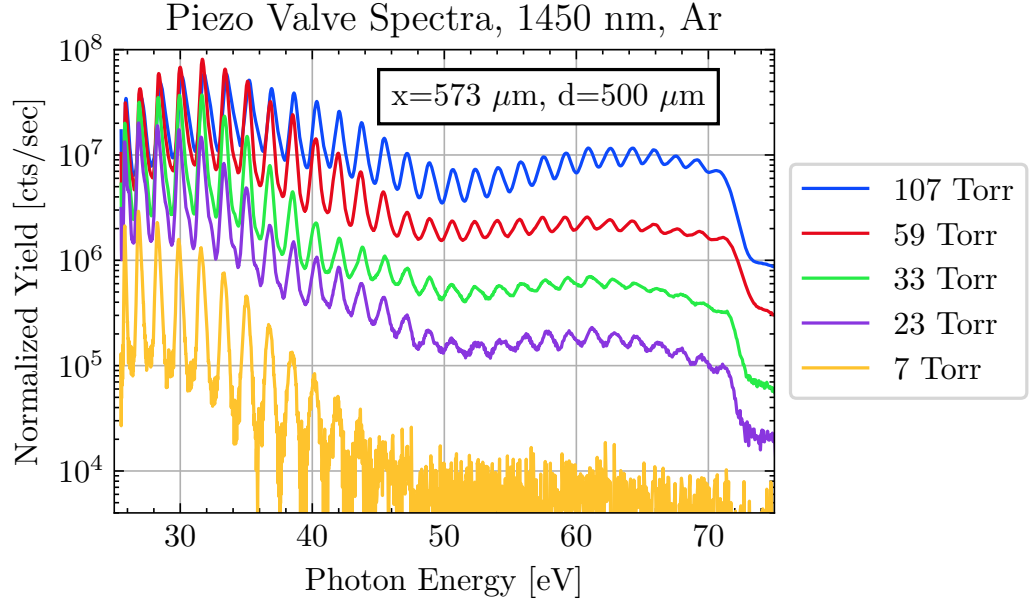


Figure 3.29: A selection of piezo valve spectra as a function of interaction pressure. Assumed on-axis distance is $x = 573 \mu\text{m}$. Normalized yield is calculated by background subtracting the 2D spectra, integrating the spatial dimension of the sensor, normalizing by exposure time and applying the Jacobian. Total yield is multiplied by 4 to account for the 250 Hz rep. rate.

steadily increasing harmonic yield until a maximum is reached at ~ 107 Torr, after which the yield starts to decrease. The inset plots the yield as a function of the square of the interaction pressure, which shows excellent quadratic scaling up to 50 Torr.

A select few spectra from this dataset are shown in Fig. 3.29. The sharp decrease in counts at 72.7 eV is due to absorption of the aluminum filter's *L*-edge. As seen in other datasets, the spectral envelope shifts to higher energies with higher pressures, which is consistent with our understanding of the macroscopic phase matching principles discussed in Section 1.3.2.

Figure 3.30 compares the performance of the piezo valve compared to the HPC under similar generation and detection conditions. The harmonics were generated using 1450 nm in argon gas, with the spectrometer configured to collect lower energy photons. As before, the spectra have been normalized for exposure time and laser repetition rate. The piezo valve spectra was intentionally blue-shifted for the purposes of an argon spectroscopy experiment [54], but this did not affect the overall yield. Note that this data was collected using the full TABLE setup and therefore the absolute XUV yields are not directly comparable to the previous HPC datasets shown in Section 3.2.4 due to the additional transmission losses introduced by the ellipsoidal mirror and extra vacuum apertures. Nevertheless, we can see

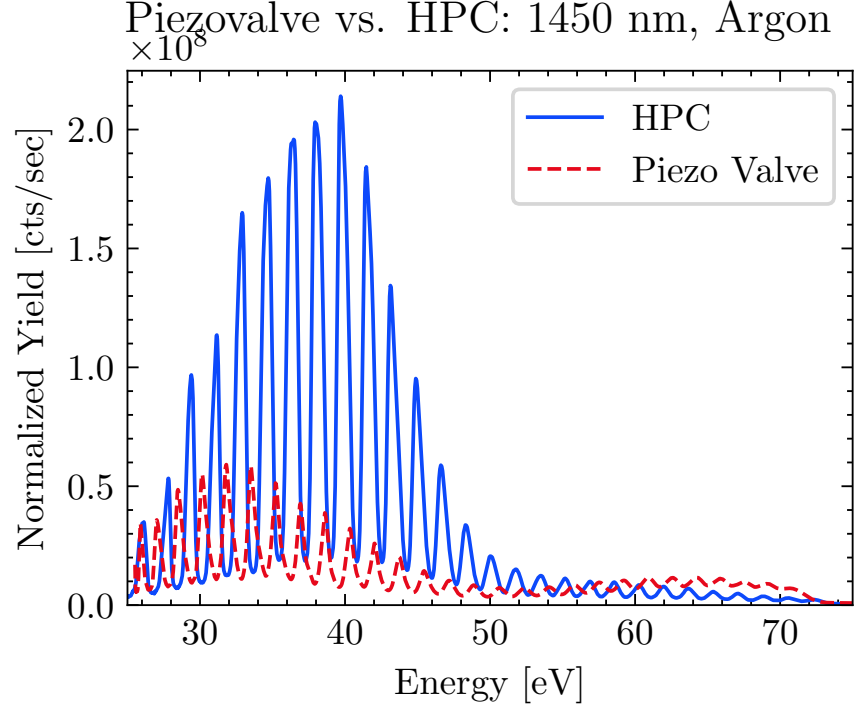


Figure 3.30: A comparison of the HPC and piezo valve harmonic yield under typical operating conditions.

that the HPC's higher interaction pressures and longer effective medium length result in significantly higher yields.

3.3 XUV Focal Spot Size

A simple knife edge measurement does not give a complete description of the beam profile, but it can be used for basic diagnostic purposes [107–109]. The knife edge measurement allows us to locate the XUV focus relative to the sample holder, which is critical for pump-probe measurements. Additionally, it can verify the performance of the ellipsoidal mirror and estimate the basic properties of the harmonic generation process.

The edge of a Si frame mounted to the target chamber's sample holder (see Fig. 4.4) as our knife edge. The coordinate system geometry is defined in Fig. 3.31. For this analysis, we assume a Gaussian beam profile with an XUV focus at position (x_0, y_0, z_0) [110]:

$$I(x, y, z) = I_0 \left(\frac{w_0}{w(z)} \right)^2 \exp \left[-2 \frac{(x - x_0)^2 + (y - y_0)^2}{w(z)^2} \right], \quad (3.20)$$

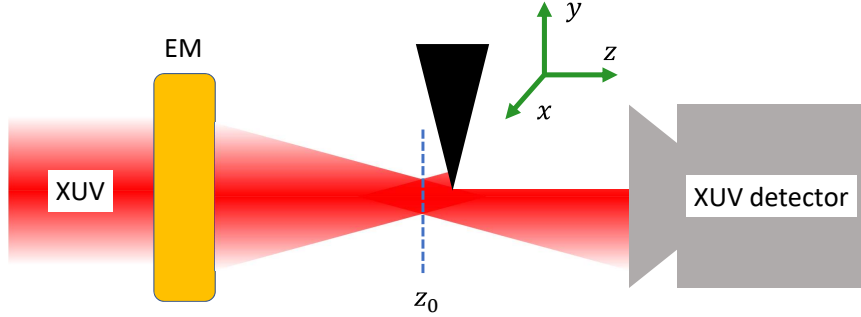


Figure 3.31: Schematic of XUV knife edge measurement. EM: ellipsoidal mirror, z_0 : XUV focal plane.

The beam waist $w(z)$ will evolve as:

$$w(z) = w_0 \sqrt{1 + \left(\frac{z - z_0}{z_R}\right)^2}, \quad (3.21)$$

where z_R is the Rayleigh range. If we use the knife edge to block the transmission as depicted in Fig. 3.31, then the transmitted power will be:

$$P(y, z) = P_0 + \frac{P_{max}}{2} \left(1 - \text{erf} \left[\frac{\sqrt{2}(y - y_0)}{w(z)} \right] \right), \quad (3.22)$$

where y is the insertion of the knife in the beam, z represents the location of the knife plane in the propagation direction, and $\text{erf}(\dots)$ is the error function. To ensure numerical stability during the fitting procedure, we approximate the error function in Eq. (3.22) using an analytic function, f [111]:

$$\begin{aligned} P(y, z) &\approx P_0 + P_{max} f(-s), \\ \text{with } f(s) &\equiv \frac{1}{1 + \exp(a_1 s + a_3 s^3)}, \\ \text{and } s &\equiv \frac{2(y - y_0)}{w(z)}, \\ a_1 &= -1.5954086, \\ a_3 &= -7.3638857 \times 10^{-2}. \end{aligned} \quad (3.23)$$

We performed knife edge measurements on harmonics created in argon using a 1430 nm / 715 nm two-color generation scheme (see Section 1.3.1). These HHG conditions were later used to perform ATAS experiments in germanium. Figure 3.32 shows the total harmonic signal as the knife edge is inserted into the beam path at a z -position near the XUV focal plane. By fitting the data to Eq. (3.23), we obtain the local waist radius $w(z)$. This

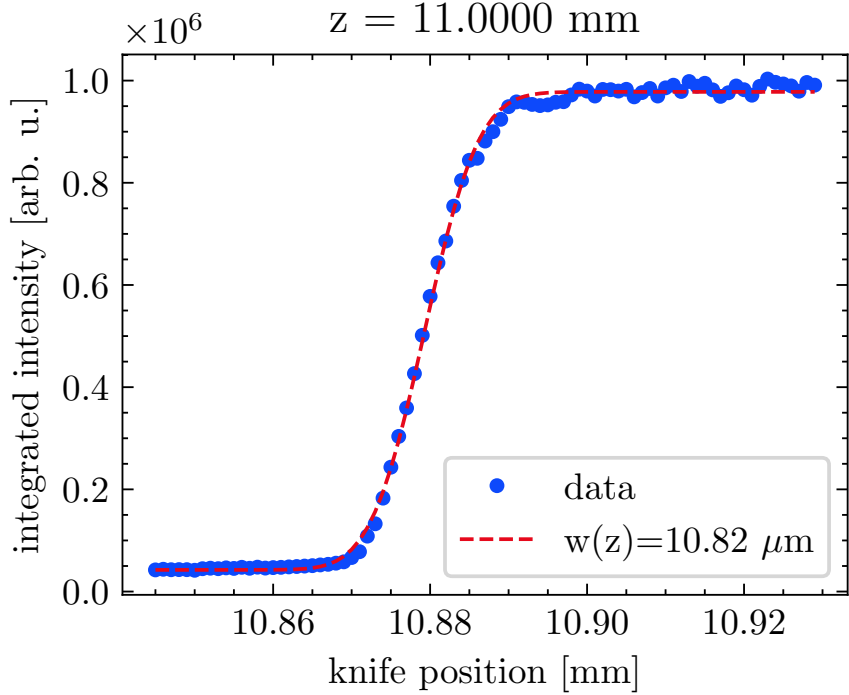


Figure 3.32: A typical XUV knife edge measurement near the focal plane. The total harmonic yield was used in this calculation.

measurement is repeated for different z values until the focal plane is found, as shown in Fig. 3.33. The Rayleigh range z_R and focal spot size w_0 are found by fitting the evolving beam waist data to Eq. (3.21).

This calculation was performed for each harmonic in the spectrum. Figure 3.34 shows the energy-resolved parameters for 37 harmonics ranging from ~ 23.4 eV to ~ 54.5 eV. The far-field divergence half-angle θ is calculated from the fit parameters in Eq. (3.21) via $\theta = \arctan(w_0/z_R)$. Neglecting geometric losses from the finite aperture of the ellipsoidal mirror, we estimate the divergence of the harmonics after generation to be $M = 3$ times smaller than at the XUV focus. This gives us a harmonic divergence immediately after generation ranging from $\theta \simeq 1.1 - 2$ mrad, which is consistent with what is reported in the literature [112].

We don't know the size of the XUV generating volume in the generation chamber, so we can't use the measured spot size to comment on the performance of the ellipsoidal mirror. However, we note that this XUV spot size is what we expect given our generation conditions. For a focal length of $f = 40$ cm and an input beam diameter of $D = 10$ mm, the 1430 nm light will have a beam waist radius $w_0 = (2\lambda/\pi)(f/d) = 36.4 \mu\text{m}$, and the 715 nm light will have $w_0 = 18.2 \mu\text{m}$. With a demagnification factor of $M = 3$, an XUV beam waist

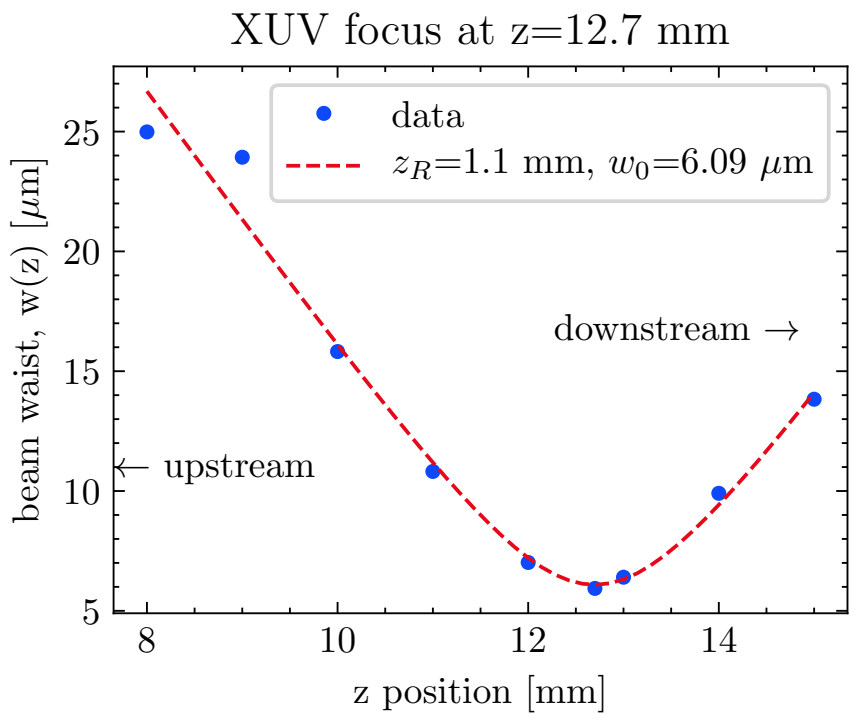


Figure 3.33: Evolution of XUV beam waist as a function of propagation direction, z . The Rayleigh range z_R and beam waist w_0 are extracted from the fit to Eq. (3.21). The total harmonic yield was used in this calculation.

XUV Knife Edge Measurements

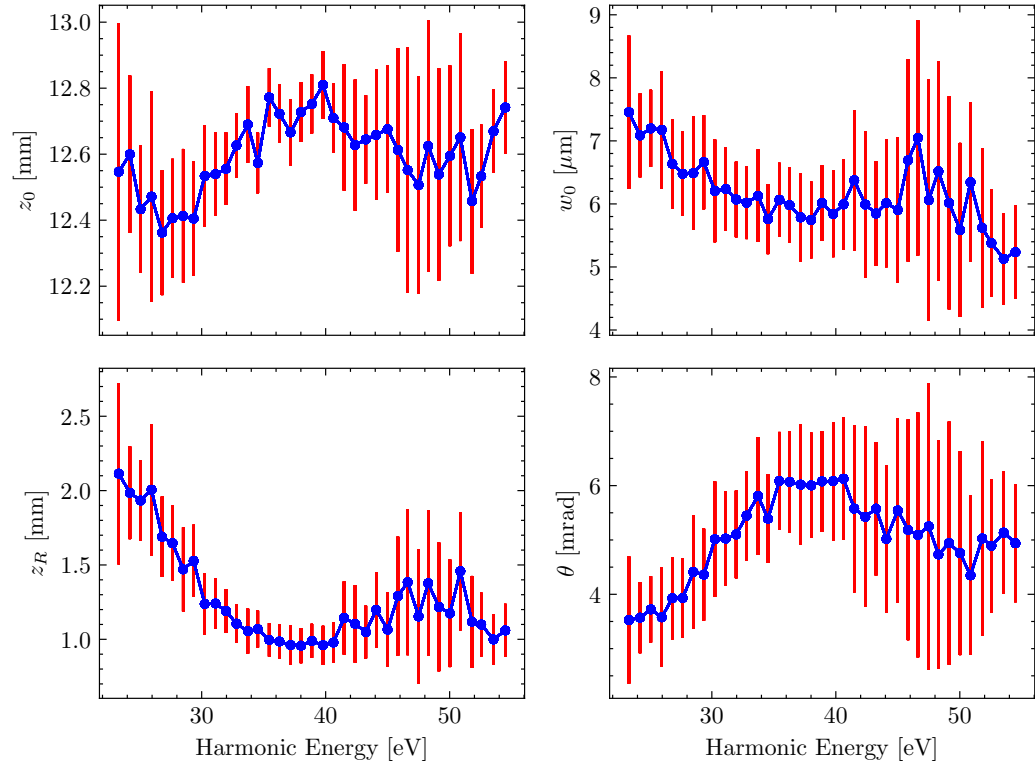


Figure 3.34: Energy-resolved fit parameters following a knife edge measurement of two-color harmonic spectrum generated in argon using 1430 nm / 715 nm light. The focal plane position (z_0), beam waist radius (w_0), Rayleigh range (z_R), and half-angle divergence (θ) are calculated for each harmonic. Error bars represent one standard deviation on the parameters.

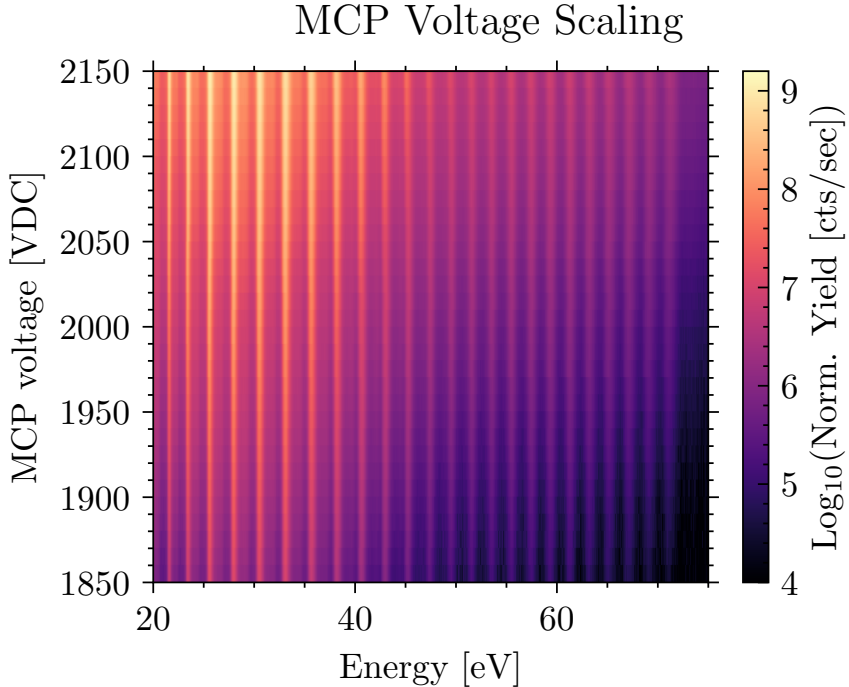


Figure 3.35: Harmonic spectra as a function of MCP voltage. Harmonics were generated in argon gas with a 1250 nm fundamental. The aluminum *L*-edge is visible at 72.7 eV.

radius of $6 \mu\text{m}$ in the target chamber corresponds to an $18 \mu\text{m}$ beam waist in the generation chamber. This means that the XUV light is generated in a volume approximately half the size of the fundamental beam's spot size.

3.4 MCP response

The gain of the MCP can be controlled by adjusting the accelerating voltage between the microchannel plates. This scaling is demonstrated experimentally in Figs. 3.35 and 3.36 using harmonics generated in argon gas with a 1250 nm fundamental. Near typical operating voltages, the measured harmonic yield Y follows a power law of the form [89, 90]:

$$Y = b * 10^{mV}, \quad (3.24)$$

where b and m are fitting coefficients, and V is the operating voltage of the MCP array in Volts.

In Fig. 3.35, we see that the MCP signal increase is spatially uniform across the sensor. Equation (3.24) shows the integrated yield for two generating conditions (GC1 and GC2) and a fit to Eq. (3.24). The slopes m are noted in the figure. We see that an increase of 100 V increases the measured signal by a factor of ~ 4.5 .

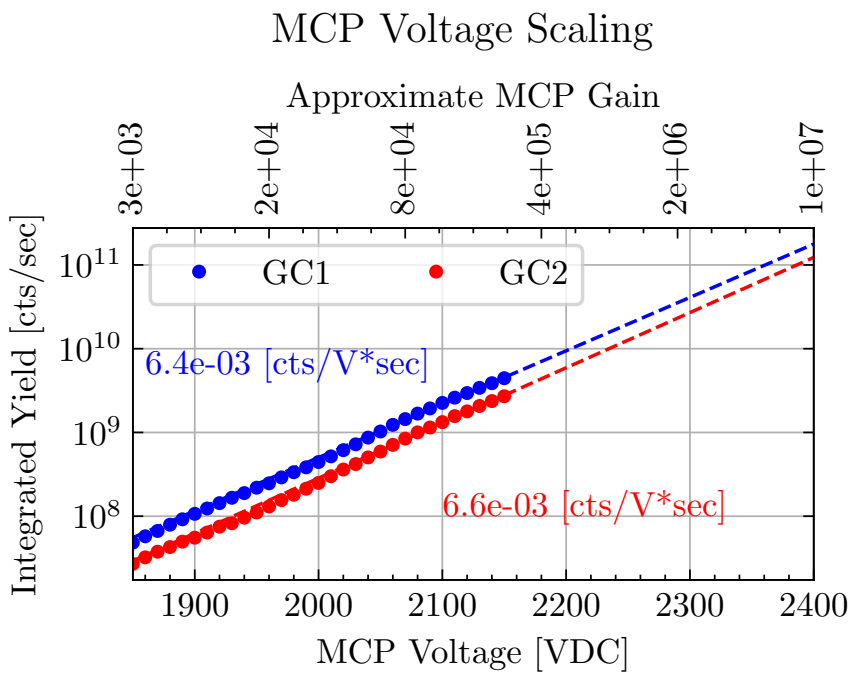


Figure 3.36: Integrated harmonic yield Y as a function of MCP voltage. GC1 was obtained by summing the spectra in Fig. 3.35, GC2 was taken under similar but slightly less efficient harmonic generation conditions. Approximate gain is calculated assuming $G = 10^7$ at 2400 VDC and using the fitting coefficient from GC1.

According to the manufacturer, typical gain values are at least 10^7 at 2400 VDC. As we do not have access to a known-brightness XUV source, we are unable to measure the gain directly. We estimate the MCP's gain G by assuming $G = 10^7$ at 2400 VDC and scaling it using the fitting coefficients obtained from the GC1 dataset. Using this assumption, we estimate $G(2000 \text{ VDC}) \approx 3 \times 10^4$, and $G(2150 \text{ VDC}) \approx 3 \times 10^5$.

According to the manufacturer, dielectric breakdown may occur when the voltage across the plates is in excess of 2400 VDC. Additionally, the plates are consumable, as they only support a finite amount of charge transfer before needing replacement. In the interest of extending the lifetime of the equipment, it is good practice to optimize experimental conditions at a relatively low voltage (2000 VDC) and only increase the voltage to higher values when collecting data for sensitive experiments. For this reason, most experiments are performed with the plate voltage below 2200 VDC.

3.5 Conclusion

We have developed a new gas source for high harmonic generation (the HPC) and modeled the gas flow within it. The measured vacuum performance was shown to agree with this model, which was then used to calculate the interaction pressure during the high harmonic generation process. The high harmonic yield of the HPC was measured under a variety of generating conditions, and it compared favorably to the other HHG gas sources available in the lab. When generating in helium at 800 nm, the XUV flux of the high pressure cell is up to 150 times brighter than the LPC, and 4 times brighter than the piezo valve when generating in argon at 1450 nm. Although we don't have direct measurements for comparison, we estimated the HPC would be between 1 and 2 orders of magnitude brighter than the LPC when operated at 1450 nm using argon. Since the optimal interaction pressure P_{opt} scales with λ^2 , we expect the HPC to become more relevant at longer wavelengths, for example when using the lab's fiber compressor to achieve few-cycle pulses at $\lambda = 1.8 \mu\text{m}$ [64]. The performance of the XUV focusing element was also validated using a knife edge measurement at the sample focus, and we characterized the divergence of the beam across its bandwidth. Finally, we validated the performance of the microchannel plate (MCP) and we estimated its gain over a range of operating voltages. In the next chapter, we use the increased harmonic flux to perform transient absorption measurements in germanium.

Chapter 4

ATAS EXPERIMENTS IN GERMANIUM

4.1 Introduction

Recalling the discussion in Section 1.4, in an attosecond transient absorption spectroscopy (ATAS) experiment the MIR laser induces electron and phonon dynamics in the sample, and the sample response is probed by an XUV pulse arriving at a variable delay τ . ATAS is a relatively new technique, but it is a blossoming field. There are several reviews of the technique available in the literature [17, 49, 113–115]. Studies have been performed in gases [116–125], molecules [126–128], liquids [129], nanorods [130], and various condensed matter samples. Several simple materials have been studied, including Si [131, 132], Si-Ge blends [133], Ge [16, 50], α -Fe₂O₃ [134], Co₃O₄ [135], TiO [136], PbI₂ [137], Ti [138], MgO [139], and even some heterostructures [51, 52].

Almost all of the aforementioned studies were done with a pump laser wavelength at 800 nm (or shorter), given the ubiquity of the ultrafast Ti:Sapph laser system and frequency-doubling optics. To our knowledge, there is no published ATAS work in solids using a mid-IR driving laser. At longer wavelengths, the electrons experience a higher ponderomotive energy U_p , as well as a lower adiabatic Keldysh parameter γ . When $\gamma \ll 1$, the excitation process is best described as tunneling (rather than multiphoton, which occurs when $\gamma \gg 1$). As such, the work presented in this chapter should be viewed as a continuation of two papers on germanium: a transient absorption measurement by Zürch in 2017 [16] and a complementary transient reflectivity measurement by Kaplan in 2018 [50], both done with ultrafast, ultra-broadband 780 nm sources.

Zürch performed the first ATAS measurement in germanium using a 780 nm, < 5 fs excitation pulse. Given these pulse parameters, over 90% of the observed signal was due to direct bandgap single-photon absorption. After applying a novel spectral decomposition algorithm to the data, Zürch was able to observe electron, hole, phonon dynamics in response to the laser excitation over a ~ 1 ps timescale. However, given the limited experimental delay range (~ 1.5 ps), they were not able to directly measure the evolution of the phonons.

Kaplan repeated the measurement on bulk germanium in reflection geometry using a 3.7 fs pulse centered at 800 nm. This reflection-absorption measurement was sensitive to both the real and imaginary parts of the refractive index and provided additional insight into the electron, hole and phonon response. Additionally, the delay range was extended out to ~ 9 ps, allowing for a more direct study of the phonon dynamics.

In the present work, we perform transient absorption measurements in germanium using a mid-IR (1430 nm), ultrafast (60 fs) pulse. Simulations show that our value of γ is approximately 1, about four times smaller than the estimated value of 4.18 for previous experiments. As a result, the strong MIR field dramatically shifts the valence and conduction bands, which has important implications for the excitation dynamics.

This chapter is organized as follows. Section 4.2 explains the experimental considerations for an ATAS measurement, including a motivation for using thin membrane samples. In Section 4.3, we consider the effects of performing an ATAS measurement with finite MIR and XUV spot sizes, and we calculate the TABLE's experimental sensitivity. In Section 4.4, we model the nonlinear excitation using the Keldysh formalism, taking into account the thin-film nature of the sample and the finite beam sizes of the MIR pump and XUV probe. Section 4.5 presents the experimental ATAS results in germanium and analyzes the observed dynamics using a two-state electronic model that includes phonon-mediated intervalley and intravalley scattering mechanisms.

4.2 Experimental Considerations

4.2.1 Sample Requirements

There are several sample requirements for a successful condensed matter transient absorption experiment. First and foremost, the sample needs to have an absorption edge within the bandwidth of the XUV source. Second, the material must have the correct thickness for a transmission measurement, given the capabilities of the XUV light source and detector. If the material is too thick, the ground state will absorb most of the XUV flux and the recorded spectrum will be too close to the noise floor of the apparatus. If it is too thin, insufficient XUV absorption will occur and the laser-induced change of the ground state (on the order of 1 – 10%) will be lost in the noise floor. As a general guideline, a sample that absorbs roughly 50% at the spectral feature of interest provides a good compromise between these conflicting requirements [115]. Figure 4.1 shows the expected transmission of several materials, calculated from the atomic scattering factors [7]. We can see that a typical sample will be on the order of 10 - 200 nm thick, depending on the material.

Another upper bound for sample thickness comes from material dispersion. In any material, the XUV light ($n_{\text{XUV}} \sim 1$) will outpace the MIR light ($n_{\text{MIR}} > 1$). This effect can be significant even for thin films. In order to keep the phase slippage between the XUV

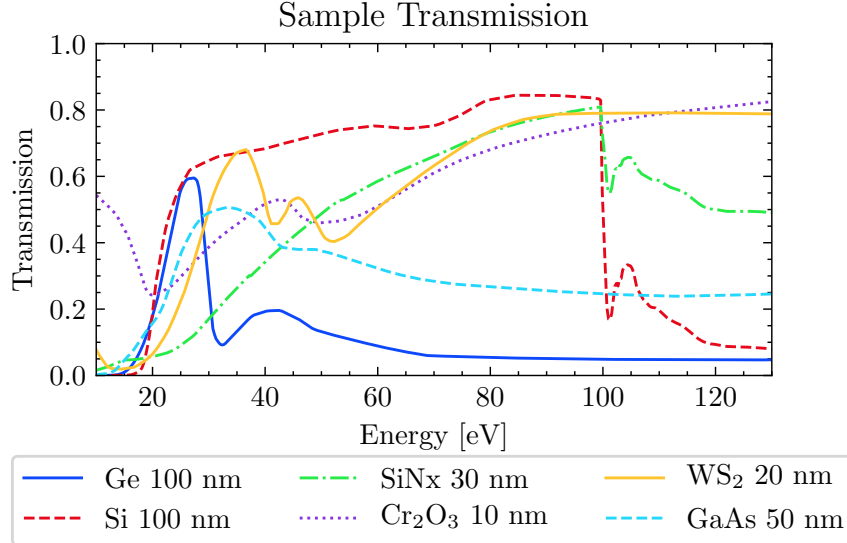


Figure 4.1: Calculated XUV transmission of various materials. Data from [7].

and MIR light below half an MIR period, the sample thickness L must obey the following relationship:

$$L \leq \frac{1}{2} \frac{\lambda_{\text{MIR}}}{n_{\text{MIR}} - n_{\text{XUV}}} \quad (4.1)$$

For germanium excited with $\lambda_{\text{MIR}} = 1430$ nm and probed with 30 eV XUV at the $M_{4,5}$ edge, $n_{\text{MIR}} = 4.2481$ [140] and $n_{\text{XUV}} = 0.992536$ [7], which gives a maximum thickness of 220 nm.

Next, the sample needs to be excitable using laser sources present in our lab (i.e., ultrafast pulses with wavelengths between 800 nm and a couple of microns). To minimize the slow build up of heat (on the order of seconds) and laser-induced damage, the sample needs to be rastered through the laser focus as the experiment is performed. This rastering method necessitates both a large clear aperture ($\sim 1 \text{ mm}^2 - 1 \text{ cm}^2$) and good sample uniformity. Samples that meet the above thickness and clear aperture requirements are extremely delicate, with thicknesses between 5,000 and 100,000 times smaller than their freestanding lateral dimensions. As such, one should expect most samples to break before, during and after measurements, so a successful experiment should have a materials pipeline that is capable of producing multiple, consistent samples in a short time frame.

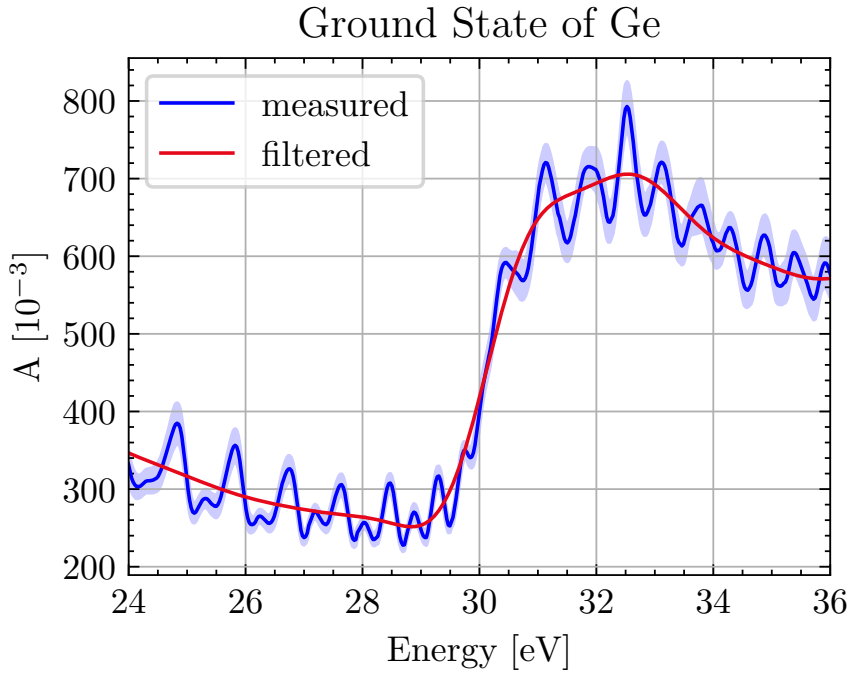


Figure 4.2: Spatially averaged ground state absorbance A of our 100 nm germanium sample. The ground state absorbance is defined by $A_{g.s.} = -\log_{10}(\bar{S}_{Ge+SiN}/\bar{S}_{SiN})$, where the overbar denotes a spatial average over the sample area (182 points for Ge+SiN, 196 points for SiN). The blue line is the average absorbance of the Ge, with the shaded region representing ± 1 std. The red line shows the result of frequency filtering to eliminate the oscillations, which originate from a measurement artifact of the harmonic comb (see Section 4.5.2 for details). The $M_{4,5}$ edge of Ge is visible around 30 eV.

4.2.2 Data Collection Sequence

The absorbance A of the ground state is defined as the negative logarithm of the transmission $T_{\text{g.s.}}$:

$$A_{\text{g.s.}}(E) = -\log_{10}(T_{\text{g.s.}}) = -\log_{10}\left(\frac{S_{\text{g.s.}}(E)}{S_{\text{vac.}}(E)}\right) \quad (4.2)$$

In Eq. (4.2), $S_{\text{g.s.}}$ is the XUV spectrum transmitted by the sample in its ground state and $S_{\text{vac.}}$ is the spectrum without the sample present. Therefore we can measure the sample's ground state absorbance by measuring the harmonic spectrum with and without the sample in the XUV beam. Likewise, we can measure the absorbance of a thin film on a membrane by comparing the transmission of the film+membrane heterostructure to that of a bare membrane. Figure 4.2 shows the ground state absorption of a germanium sample as measured using the TABLE's XUV light source.

The *change in absorbance* ΔA between the ground and laser-induced states is therefore:

$$\begin{aligned} \Delta A(E, \tau) &= A_{\text{e.s.}}(E, \tau) - A_{\text{g.s.}}(E) \\ &= -\log_{10}\left(\frac{S_{\text{e.s.}}(E, \tau)}{S_{\text{vac.}}(E)}\right) + \log_{10}\left(\frac{S_{\text{g.s.}}(E)}{S_{\text{vac.}}(E)}\right) \\ &= -\log_{10}\left(\frac{S_{\text{e.s.}}(E, \tau)}{S_{\text{g.s.}}(E)}\right). \end{aligned} \quad (4.3)$$

In Eq. (4.3), the excited state spectrum $S_{\text{e.s.}}(E, \tau)$ results from an MIR pulse hitting the sample, followed by an XUV pulse after a delay of $\tau \equiv t_{\text{MIR}} - t_{\text{XUV}}$. Note that negative delays mean the XUV arrives at the sample before the MIR. Also note that for technical reasons, the experiment is performed using a pulsed laser with a *laser repetition rate* RR , and the XUV detector integrates the sample response over hundreds or thousands of laser shots. Therefore, the sample experiences a train of MIR excitation pulses with temporal spacing $1/RR$. For the sake of discussion, let τ_p be the longest timescale of the sample's laser-induced dynamics, and assume that this long-lived excitation decays to the ground state exponentially.¹⁹ Therefore, we can relate the experimentally observed change in absorbance (ΔA) to what would be observed *in the absence of a pulse train* (denoted by ΔA_{ideal}) via the relation:

$$\Delta A(E, \tau) = \sum_{m=0}^{\infty} \Delta A_{\text{ideal}}\left(E, \tau + \frac{m}{RR}\right) \times \exp\left(-\frac{\tau + \frac{m}{RR}}{\tau_p}\right). \quad (4.4)$$

In other words, a pulse train $\Delta A(\tau)$ measurement is actually a superposition of single-shot ideal measurements at delays $\tau + \frac{m}{RR}$. If the time between laser pulses is much greater than the time required for the sample to return to the ground state, then $\exp(-1/(RR\tau_p)) \approx 0$ and we can neglect the influence of the previous laser shots ($m \geq 1$) on the measurement.

¹⁹This assumption is justified by the observations presented in Section 4.5.1.

Equivalently, an excited state spectrum $S_{\text{e.s.}}$ at sufficiently negative delays ($\tau < -\tau_L$, where τ_L is the laser pulse duration) will be indistinguishable from a ground state measurement if the repetition rate is low enough:

$$S_{\text{e.s.}}(E, \tau < -\tau_L) = S_{\text{g.s.}} \quad (4.5)$$

For this reason, negative time delay measurements are sometimes referred to as “negative infinity” measurements by the ultrafast community. Conversely, if the repetition rate is too high, then we will see a non-zero contribution to ΔA at delays $\tau < -\tau_L$. We will revisit these concepts in Section 4.5.1.

An ATAS experiment is simply a collection of recorded spectra taken over a range of delay points with otherwise identical experimental conditions. However, we have implemented several techniques to improve the fidelity of our data.

As an extremely nonlinear process, HHG’s conversion efficiency is highly dependent on the input laser pointing, peak power, pulse duration, spatial mode, etc. – all of which are affected by laboratory environmental conditions and the activity of other group members within our lab complex. As a result, even under “ideal” experimental conditions, the total harmonic yield drifts slowly throughout the course of the experiment. To minimize the effect of this slow drift, we take a ground state spectrum for each delay point. A computer-controlled home-built shutter system blocks the MIR laser in the pump arm between measurements (S in Fig. 2.15). Taking back-to-back ground and excited state spectra significantly lowers the harmonic stability requirements; we require stability on the order of twice the exposure time (several seconds), rather than the entire experimental run (several hours).

Our spectrometer’s CMOS camera has a bit depth of 16, corresponding to a maximum value of $2^{16} = 65,535$ counts before saturation. The exposure time is set so that the amplitude of the brightest harmonic on the detector is about 10% below this limit, which allows for an upward drift in harmonic yield to occur without invalidating the dataset. An exposure time of 3 seconds is typical for a 200 nm Al filter with a 100 nm Ge sample at 125 Hz (375 laser shots), an MCP voltage of +2200 VDC, and 2×2 camera pixel binning.

Although the SpitFire laser system has a maximum repetition rate of 1 kHz, we perform solid state ATAS experiments at a much lower rate (125 or 250 Hz) by adjusting the amplifier’s Pockels cell firing rate. The lower repetition rate allows the sample to more fully relax between laser shots, reducing the effects of millisecond ($1 \text{ ms} = 10^{-3} \text{ s}$) thermal processes on our measurements. It also reduces the average power on the sample for a given pulse energy, which lowers the steady state temperature of the sample. On the other hand, it allows us to increase the pulse energy while maintaining a constant average power on the sample.

During the experiment, the sample is rastered across the focus to reduce any deleterious

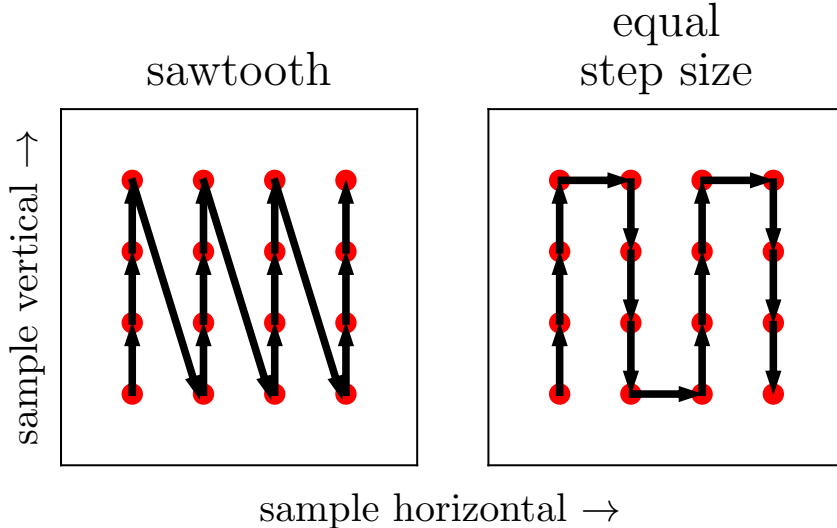


Figure 4.3: Schematic of competing raster methods, shown in the sample’s reference frame. The clear aperture of the sample is represented by the interior of the black square. The laser propagation direction is out of the page. The laser focal spots are shown as red circles, and the movement of the sample holder relative to the laser focus is indicated by arrows. A $200 \mu\text{m}$ border exists between the raster array and the perimeter of the sample’s clear aperture. This diagram is to scale for a $1 \times 1 \text{ mm}^2$ clear aperture sample, a $60 \mu\text{m}$ diameter MIR focal spot and a $200 \mu\text{m}$ step size.

effects of long term uninterrupted laser exposure.²⁰ During motor movement, the MIR beam is blocked with a shutter but the relatively weak XUV beam is allowed to remain on the sample. Each pair of measurements (ground state, excited state) in a delay scan has a unique position on the sample. Typical step sizes are $200 \mu\text{m}$, which is larger than the measured XUV spot size of $\simeq 12 \mu\text{m}$ and the MIR spot size of $\simeq 34 \mu\text{m}$. Two raster schemes are schematically shown in Fig. 4.3. The method shown in the left panel produces a sawtooth pattern on the sample. This method gives very accurate positioning, as the vertical motor is almost always approaching the final position from the same direction. However, the diagonal steps are $\sqrt{N^2 + 1}$ times longer than the vertical steps, where N is the number of vertical steps in the pattern. As a result, there is a bimodal distribution of motor transit times between measurements. If the sample is not fully relaxed between motor movements, this will lead to an inconsistent measurement of the ground state $S_{\text{g.s.}}(E)$. Additionally, if the sample is heated by the laser outside of the raster step size, then the average distance between points can affect the measurement of the ground state. The method shown in the

²⁰Note that sample heating provides a deleterious but unavoidable effect. Short of eliminating heating via *in vacuo* sample cooling or a rapidly spinning sample, the best approach is to ensure that all datapoints are collected using a *consistently* heated sample.

right panel alleviates both problems by requiring equal step sizes, and therefore equal travel times. All measurements presented in this work were acquired using the method shown in the right panel.

This rastering method has its limitations, as thousands of laser shots hit the sample between each movement. A future upgrade to the beamline could include a rapidly spinning sample mount, as described in [141]. Another option would be to directly cool the sample with an *in vacuo* pulsed gas jet pointed at the interaction region, timed such that the valve fires between laser shots.²¹

Before measuring a sample's response for the first time, or after a major optical alignment, an XUV transmission map of the sample must be created. Creating this map serves two purposes: it verifies sample XUV absorption uniformity and it determines the motor coordinates of the sample's clear aperture. To avoid edge effects, the edges of the raster area are chosen to be 200 μm away from the edge of the clear aperture (see Fig. 4.3).

The transient data collection sequence can be summarized as *excited state \rightarrow ground state \rightarrow move motors*. Details of this sequence are as follows. First, the sample moves to a given raster position and delay wedge position, the MIR shutter opens and an excited state spectrum $S_{\text{e.s.}}(E, \tau)$ is recorded, followed by a ground state measurement $S_{\text{g.s.}}(E, \tau)$. To minimize the duration of the experiment, an XUV reference spectrum $S_{\text{vac.}}$ is not recorded. Finally, the sample moves to the next raster position as the delay wedge pair moves to the next delay position. The system is programmed to wait for the wedges to become stationary before the next measurement begins.

Note that in this sequence, the time between the i^{th} excited state and the i^{th} ground state measurement is equal to the exposure time, but the time between the i^{th} ground state measurement and the $i+1^{\text{th}}$ excited state measurement is equal to the motor transit time. This sequence is preferable to the alternative (*ground state \rightarrow excited state \rightarrow move motors*), which would result in a delay step size-dependent relaxation time between the i^{th} excited state and the $i+1^{\text{th}}$ ground state measurement.

To further improve our signal-to-noise ratio, we average multiple delay scans together. A typical ΔA measurement will be repeated between 5 and 50 times. Each delay scan uses the raster points of the previous delay scan so there is a one-to-one mapping of delay to sample position.

4.2.3 The Supporting Nitride Membrane

While most materials have an absorption edge within the range 25 - 150 eV, there are very few commercially available prefabricated materials with both the requisite large clear aperture and thickness. Note that either characteristic is relatively easy to achieve individually,

²¹Private communication with Prof. Stephen Leone of University of California, Berkeley.

but their combination presents unique materials challenges. We considered three synthesis methods to produce this quasi-2D sample:

1. sample growth on a traditional substrate, followed by chemical back-etching or milling of the substrate until sub-micron thickness of the heterostructure is achieved;
2. sample growth on a traditional substrate, followed by mechanical transfer onto a membrane;
3. sample growth on a membrane.

Sample quality and composition is heavily impacted by local growth conditions such as substrate temperature, deposition rate, substrate crystal cut, substrate-sample lattice mismatch, etc. Many of these characteristics are changed when growing on a substrate of a different cut, or by replacing a substrate with a membrane. In general, one should not expect success when applying a substrate-optimized growth recipe to a freestanding membrane. Therefore, methods 1 and 2 will yield the highest quality samples, as they leverage already-developed sample recipes. However, both methods require a technically difficult second step that is prone to failure.

Selective chemical etching recipes exist for certain compounds, but they usually require an additional chemically inert layer in the heterostructure to protect the sample. Adding this layer will come at the expense of the total XUV flux transmitted by the heterostructure. Additionally, the chemical etching rates are highly dependent on local chemistry, fluid convection and temperature [142], which ultimately means that the amount of material removed is uncontrollable and unrepeatable within our requirements ($499.9 \mu\text{m} \pm 10 \text{ nm}$ removed from a $500 \mu\text{m}$ substrate). For these reasons, we decided to not pursue a chemical etch recipe. Ion or electron milling is more controllable, but too expensive to implement on a large scale. The above reasons preclude the use of Method 1.

Mechanical transfer of thin samples is a tried and true method, but it usually results in flakes with lateral dimensions on the order of $100 \mu\text{m}$. Repeated transfer of many flakes is possible, but there little control over their exact positioning on the membrane. This results in a random distribution of flakes with the possibility of folded or overlapping flakes. These mishaps increase the effective optical density of the sample, changing the MIR and XUV absorption properties significantly.

An XUV spatial measurement needs to be taken prior to any ATAS experiment, but a non-uniform distribution of flakes on a membrane would require a much higher resolution map. This is because the flakes are on the order of the XUV and MIR foci, so it is critical that the raster points in Fig. 4.3 correspond to the center of each flake to avoid edge diffraction and to minimize the effects of slow laser pointing drift. For a uniform film, a map can be taken using $200\text{--}250 \mu\text{m}$ step sizes, as the most important feature is the border

of the clear aperture. On the other hand, each flake would have to be sampled ~ 5 times in each direction to find its center. As a conservative estimate, a membrane covered with $100 \times 100 \mu\text{m}^2$ flakes would require a step size of $20 \mu\text{m}$, which increases the number of raster points by a factor of $10^2 = 100$. Considering that a $3 \times 3 \text{ mm}^2$ clear aperture sampled with $200 \mu\text{m}$ steps takes ~ 45 minutes to map, a random distribution of flakes would take a prohibitively long time to map out.

With the first two methods ruled out, we turn to the third method of growing directly on a freestanding membrane. Although it will result in a lower quality sample, it does not have the same technical hurdles of the previous two methods. However, the large clear area makes the heterostructure extremely fragile. We initially attempted to circumvent this problem by using an array of smaller clear apertures.

As shown in Fig. 4.3, most of the sample's area isn't directly used by the laser - it exists as a buffer between the grid of sample points. An alternative to a single clear aperture is an array of micro-apertures, each with a diameter on the order of the MIR spot size. The micro-apertures exist within a mechanically robust substrate and a thin membrane lies on top of the structure. This configuration significantly eases the material strength requirements by reducing the size of the unsupported area from cm-scale to sub-mm-scale. The regular grid of apertures avoids the difficulties of a randomly distributed sample, easing the XUV mapping step size requirements. Fortunately, these arrays are commercially available from Silson, Norcada (silicon nitride membranes) and US Applied Diamond (diamond membranes) but we encountered technical difficulties in their implementation. Because the aperture size is on the order of the size of the MIR focal spot, there is very little room for positioning error, and our motors were insufficiently precise for this application. Further, these arrays are typically only available in at most a 3×3 array, which provides an insufficient number of raster points for an ATAS experiment.

With these limitations in mind, we decided to use large aperture x-ray windows from Norcada. These windows consist of a mechanically robust Si frame substrate with a square clear aperture cut through the center. The structure is fabricated so that a thin membrane covers the clear aperture. A schematic of the cross section is shown in Fig. 4.4.

Norcada offers these structures with either a silicon (polycrystalline or single-crystal) or a silicon nitride membrane. An ideal membrane is transparent to both XUV and MIR wavelengths with a high damage threshold. Referring to Fig. 4.1, 100 nm of Si provides a relatively flat transmission curve from 25 to 100 eV. In contrast, 30 nm of silicon nitride has poor, but featureless, transmission at lower energies. Both materials transmit light below their bandgaps (5 eV for SiN and 1.14 eV for Si). Finally, silicon nitride's higher bandgap results in a significantly higher laser damage threshold [29, 143, 144]. Taking all these factors into account, we decided to use 30 nm silicon nitride membranes for germanium transient absorption experiments. The measured transmission of a typical membrane is

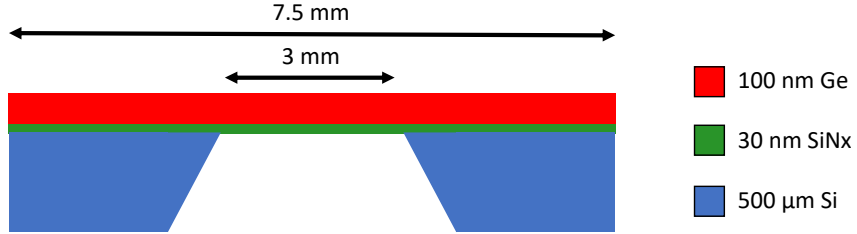


Figure 4.4: Cartoon showing the cross section of the free standing sample heterostructure. A 500 μm thick Si frame supports a freestanding 30 nm low stress silicon nitride membrane (Norcada QX7300X), upon which 100 nm of germanium has been deposited. The Si frame has a 3x3 mm^2 square clear aperture and a 7.5x7.5 mm^2 square external dimension. The taper of the Si frame thickness along the perimeter of the clear aperture forms a knife edge. In an ATAS experiment, the XUV and MIR pulses propagate from the top to bottom of the figure.

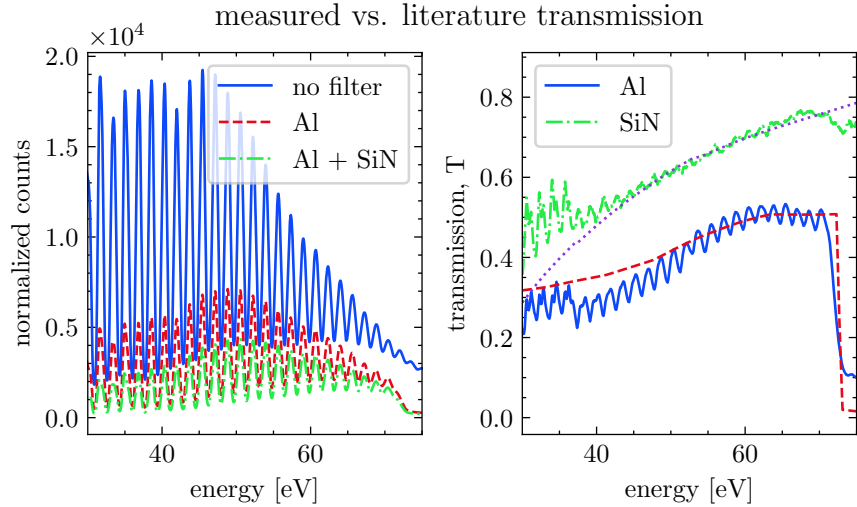


Figure 4.5: XUV transmission measurements of Al metallic filter and silicon nitride membrane. Left panel: normalized XUV counts for i) unfiltered HHG signal, ii) HHG going through a 200 nm Al filter and iii) HHG going through a 200 nm Al filter and 30 nm of silicon nitride. Counts are scaled by the Jacobian. Right panel: transmission curves obtained from the left panel's data. Also shown are literature values for 20 nm of silicon nitride (purple dots) and 200 nm of Al with two 4 nm oxide layers (red dashes) [7]. Multilayer interference is not taken into account. Oscillations in measured transmission are numerical artifacts originating from a finite detector noise floor and XUV brightness instabilities. The deviation between the measured and literature transmission for SiN below 40 eV, and for Al between 36 and 55 eV, is due to a measurement artifact as will be discussed in Section 4.5.2.

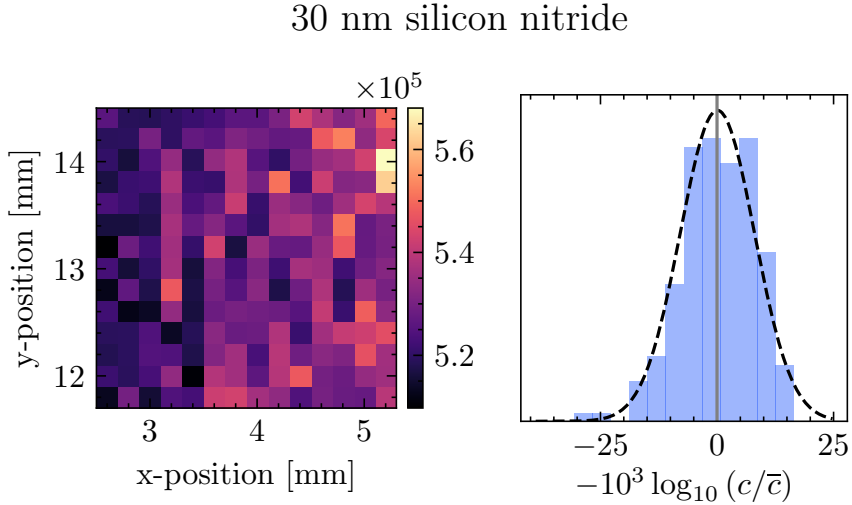


Figure 4.6: XUV transmission map of 30 nm silicon nitride freestanding membrane. Left panel: integrated XUV counts in the range 30 – 34 eV. Sample holder motor positions are indicated by x- and y-positions. Right panel: histogram of logarithmic deviation of counts from the average. Dashed line shows a normal distribution.

shown in Fig. 4.5. The commercial membranes have very uniform transmission, as shown in Fig. 4.6.

4.2.4 Laser Damage

Unlike the gas-phase samples traditionally used in the DiMauro lab, condensed matter samples can suffer permanently laser-induced damage which frustrates any intensity-dependent investigation. The delicate nature of a $\simeq 100$ nm freestanding membrane further complicates these studies. The exact damage mechanism was not studied but we have observed two modes of membrane failure, which will be discussed presently. Occasionally, the volume near the MIR focal spot will be ablated by the laser, leaving the rest of the freestanding sample undamaged. The most common failure mode results in the immediate destruction of the entire membrane, often within a single camera exposure ($\simeq 1$ second).

Sample damage is apparent in both the visible and the XUV. The top left panel of Fig. 4.7 shows our *in-situ* method of imaging the samples using visible light. The top right panel shows a false color image of our sample holder within the chamber. The 3×3 grid of 5 mm diameter clear apertures is visible as dark circles. The bottom three panels of Fig. 4.7 show close ups of three samples. On the left, we have a pristine Si membrane; in the middle panel, we have a Si membrane with a $< 200 \mu\text{m}$ laser-drilled pinhole (visible as a bright point in the center of the membrane); the right panel shows a completely obliterated SiN membrane (visible as ragged edges).

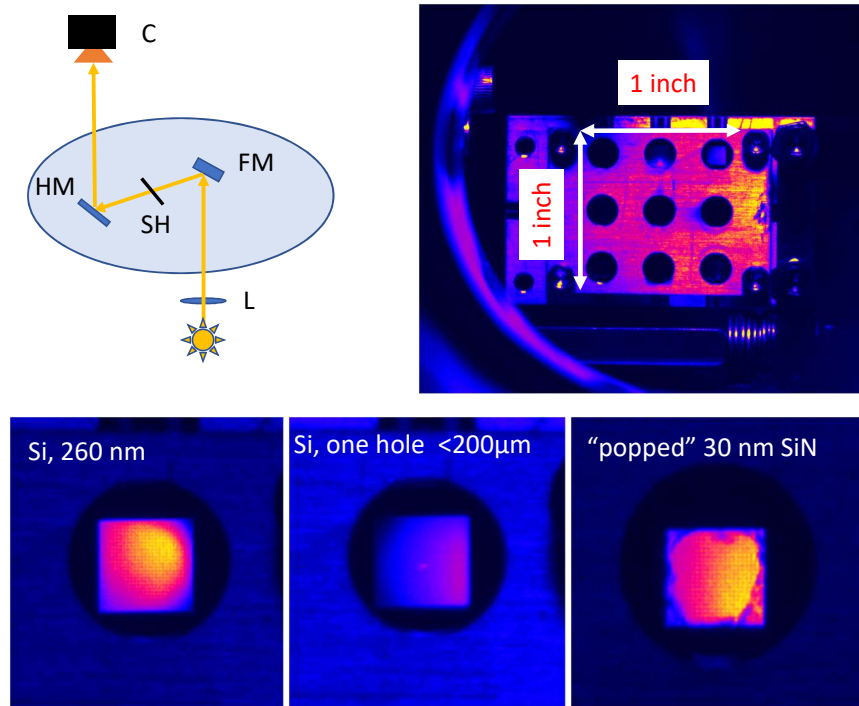


Figure 4.7: *In-situ* imaging of the samples within the target chamber. Left: optical setup for *in-situ* imaging of samples. C: Si CCD camera, HM: hole mirror, SH: sample holder, FM: translatable silver mirror, L: lens. Right: false color image showing the sample holder with a 3 x 3 grid of 5 mm diameter clear apertures. Samples are held in a clamshell design centered in the clear apertures and are backlit using a flashlight.

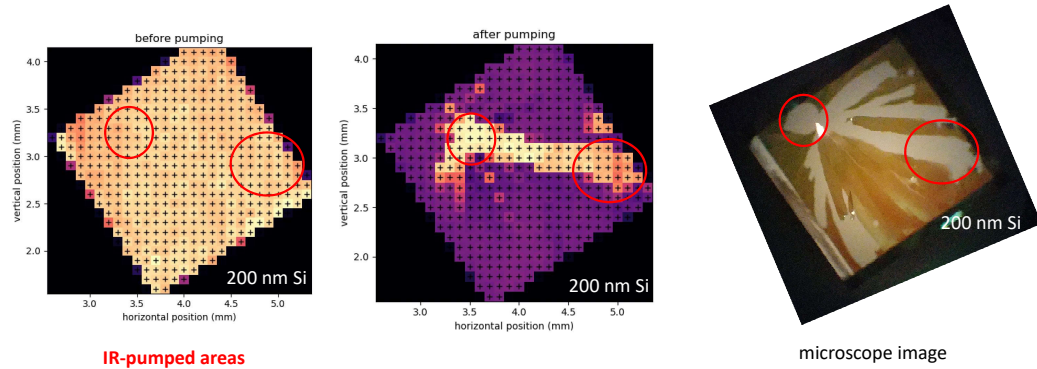


Figure 4.8: Laser damaged 200 nm silicon membrane samples. Left panel: XUV map of pristine Si before being exposed to MIR laser. Center panel: XUV map of damaged sample after being pumped with $\approx 65 \mu\text{J}$ of $\lambda = 1500 \text{ nm}$ at 1 kHz repetition rate in two locations. Right panel: microscope image of damaged sample (beige) showing large sections of missing material (white). Red circles in all three pictures indicate the two locations that were exposed to MIR laser light.

Figure 4.8 shows a 200 nm thick freestanding Si membrane before and after it was laser damaged. The first two panels show the integrated XUV transmission ($E \simeq 60 - 100$ eV) as the sample is rastered across the XUV focus; each image consists of over 100 individual measurements. The small black “+” signs correspond to the center of the coordinates for each exposure, and the sample is rotated $\simeq 30$ degrees relative to the motor axes. In the left panel, we see the XUV transmission of a pristine sample before it was exposed to the MIR laser. The center panel shows the same sample shortly after it was briefly pumped with $\simeq 65 \mu\text{J}$ of $\lambda = 1500$ nm light at 1 kHz in the two locations indicated by red circles. Damage occurred within the first camera exposure (2 seconds). We see high transmission (beige) in a horizontal stripe across the membrane; the remaining parts of the sample have lower transmission (purple), although there are signs of increased transmission in the bottom-center area of the sample. The right panel shows a microscope image of the sample after it was removed from the chamber. We can see that while the areas exposed to the laser are missing, the entire membrane is shattered and is unusable.

Ultrafast melting has been identified as a possible mechanism for mid-IR laser induced damage [144, 145], which can be understood as the following. At the microscopic level, the germanium lattice consists of a multitude of electronic bonds between valence electrons. In the ground state, there exists an energetic balance between the attractive bonding force and an electrostatic repulsion of inner electrons and nuclei. As the VB electrons are excited to the CB, the attractive force is weakened and the bond distance increases. If we continue to excite the VB, it will become depleted to the point where the repulsive forces destroy the bonds. Thereafter, the material no longer resists shear forces - much like a liquid. Experiments have shown that the lattice is destroyed within 100 fs after the electron-hole plasma is created, and the crystal melts 500 fs later. In semiconductors, tight-binding calculations predict that ultrafast melting occurs when the conduction band density N_{CB} is about 8-12% of the valence band density N_{VB} [144, 146].

We estimate the valence band electron density of the ground state as the product of the number of valence electrons per atom and the number of atoms per unit cell divided by the unit cell volume. Germanium has a diamond cubic lattice with a unit cell volume of $a^3 = (5.658 \text{ \AA})^3 = 1.81129 \times 10^{-22} \text{ cm}^3$, and an electron configuration of $[\text{Ar}]3\text{d}^{10}4\text{s}^24\text{p}^2$. With 8 atoms per unit cell and 4 valence electrons per atom, the valence band electron density of the ground state is $N_{\text{VB}} = 1.767 \times 10^{23} \text{ cm}^{-3}$. Therefore, we would not expect ultrafast melting to occur unless N_{CB} exceeds $\simeq 1.767 \times 10^{22} \text{ cm}^{-3}$. Although the simulations don't predict excitation densities in excess of this threshold, they do not take into account the temperature-dependence of the bandgap. The indirect bandgap is reduced at elevated temperatures, and we would expect a commensurate increase in the excitation rate.

4.3 Finite Beam Size Considerations: Measuring ΔA

In a transient absorption experiment, we measure the change in absorbance of the sample in response to a laser-induced electronic excitation. We measure macroscopic properties in the lab, but the coefficients are determined by the local conditions at the microscopic level. In this section, we will describe how the two quantities are related given the XUV and excited fraction spatial profiles. We will use this formalism to calculate the sensitivity of our measurement to the relative spot sizes of the MIR excitation laser and the XUV probe beam. Additionally, we will calculate the sensitivity of the measurement to misalignment of the two focal spots.

4.3.1 Relating Macroscopic and Microscopic Absorbance

The XUV absorption within the sample is linear, so we can write the measured spectrum S_i as the product of the input XUV brightness I_{XUV} and a transmission factor T_i :

$$\begin{aligned} S_i(E, \tau) &= I_{\text{XUV}}(E) T_i(E, \tau), \\ \text{with } T_i &= 10^{-A_i}, \\ \text{and } A_i &= \int_0^L \alpha_{10}(E, z) dz, \end{aligned} \tag{4.6}$$

where A_i is the absorbance and $S_i(E, \tau)$ is the recorded XUV spectrum with photon energy E at XUV-MIR delay τ . The subscript i denotes a ground state (g.s.) or excited state (e.s.) measurement. Note that Eq. (4.6) assumes no transverse spatial structure of the excitation fraction or the XUV light, so S_i , I_{XUV} , T_i , A_i and $\alpha_{10}(z)$ are effectively macroscopic quantities. In our experiments, we measure the area integral of the spectrum in the far-field:

$$S_{\text{meas},i} = \iint dx dy I_{\text{XUV}}(x, y) t_i(x, y), \tag{4.7}$$

where $t_i(x, y)$ is the *local transmission* of the sample/heterostructure at sample position (x, y) .²² Therefore, the (macroscopic) transmission and absorbance of the excited or ground state relative to a vacuum reference can be expressed as:

$$\begin{aligned} T_i &= \frac{S_i}{S_{\text{vac}}} = \frac{\iint dx dy I_{\text{XUV}}(x, y) t_i(x, y)}{\iint dx dy I_{\text{XUV}}(x, y)} \\ A_i &= -\log_{10}(T_i) \end{aligned} \tag{4.8}$$

²²In the following discussion, we drop the explicit energy- and time-dependence to make the equations more readable. The time dependence comes from the evolution of the excitation fraction η , and the energy dependence comes from the energy-dependent excitation and ground state of the sample. Also note that the transverse XUV beam spot size does not appreciably change over the sample thickness (since $z_R \simeq 1 \text{ mm} \gg 100 \text{ nm}$), so we omit the z -dependence in writing $I_{\text{XUV}}(x, y)$.

Using this notation, the *change in absorbance* between the excited and ground states is:

$$\Delta A \equiv A_{\text{e.s.}} - A_{\text{g.s.}} = -\log_{10} \left(\frac{\iint dx dy I_{\text{XUV}}(x, y) t_{\text{e.s.}}(x, y)}{\iint dx dy I_{\text{XUV}}(x, y) t_{\text{g.s.}}(x, y)} \right) \quad (4.9)$$

Now, let us write the cross section α of the sample as a ground state term plus an excitation-dependent perturbation term:

$$\begin{aligned} \alpha(x, y, z) &= \alpha_{10}(1 + \eta(x, y, z)) \\ \text{with } \alpha_{10} &\equiv \frac{\alpha_e}{\ln 10} = \frac{4\pi \text{Im}[\tilde{n}]}{\lambda \ln 10}. \end{aligned} \quad (4.10)$$

From Eq. (4.6), the absorbance of a sample of thickness L is:

$$\begin{aligned} A_{\text{g.s.}} &= \alpha_{10}L, \\ A_{\text{e.s.}} &= \alpha_{10}L + \bar{\eta}_z(x, y)L. \end{aligned} \quad (4.11)$$

where we have defined the *depth-averaged excitation fraction*, $\bar{\eta}_z(x, y)$ as:

$$\bar{\eta}_z(x, y) \equiv \frac{1}{L} \int_0^L \eta(x, y, z) dz. \quad (4.12)$$

Since $t_{\text{g.s.}}(x, y)$ is spatially invariant, Eq. (4.9) simplifies to:

$$\Delta A = -\log_{10} \left(\frac{\iint dx dy I_{\text{XUV}}(x, y) 10^{-\alpha_{10} L \bar{\eta}_z(x, y)}}{\iint dx dy I_{\text{XUV}}(x, y)} \right). \quad (4.13)$$

Therefore, the measured macroscopic sample response is the integral of the local absorbance weighted by the local XUV probe intensity. Equation (4.13) will reduce to the Eq. (4.6) if and only if $\bar{\eta}_z(x, y)$ is constant for all values of x and y . Since $\bar{\eta}_z(x, y)$ is created in response to the MIR laser, this is equivalent to making the plane wave approximation for the pump arm. In the case of finite excitation and probe beams, the measured macroscopic response of the sample will always be lower than that predicted by the *peak sample response*, $\text{Max}[\eta(x, y, z)]$.

Our condensed matter experiments are limited by our ability to measure weak signals. We can improve the measured signal by increasing the depth-averaged excitation fraction, but we are constrained by the ultrafast melting condition ($N_{\text{CB}} \simeq 0.1 N_{\text{VB}}$), which puts an upper limit on $\text{Max}[\eta(x, y, z)]$. Our detection efficiency, defined as the measured ΔA divided by ΔA at $\text{Max}[\eta(x, y, z)]$, is an important experiment parameter. In the following discussion, we consider the effect of the transverse profile on the measurement efficiency. In Section 4.4.5 we will see that the thin film interference causes a strong z -dependence of $\eta(x, y, z)$ that will further diminish the measurement efficiency.

We can gain intuition about the situation by numerically evaluating Eq. (4.13) using

mathematically convenient expressions for I_{XUV} and $\bar{\eta}_z$:

$$I_{\text{XUV}}(x, y, z) = \frac{2}{\pi w(z)^2} \exp \left[-\frac{2(x^2 + y^2)}{w(z)^2} \right],$$

$$\bar{\eta}_z(x, y) = \eta_0 \exp \left[-\frac{2(x^2 + y^2)}{w_1^2} \right],$$

with $w(z) = w_0 \sqrt{1 + (z/z_R)^2}$,

and $w_1 \equiv a * w_0$.

(4.14)

In the above, we have made the radius of the depth-averaged excited fraction a times larger than the XUV spot radius. Additionally, the XUV intensity is normalized such that the denominator in Eq. (4.13) evaluates to 1. In Fig. 4.9, we numerically integrate Eq. (4.13) using the assumptions of Eq. (4.14) to better understand the importance of the relative sizes the XUV and depth-averaged excitation fraction spot sizes. The left panel shows the efficiency of measuring the amplitude η_0 for a given ratio of spot sizes. We see an error function-like curve which approaches unity as $a \rightarrow \infty$, which is consistent with the plane wave approximation. Equal spot sizes result in a measured ΔA that is only 40.7% of the amplitude $\alpha_{10} L \eta_0$, and an XUV spot size 1/3 of the excited fraction results in an efficiency of 89%. In our experiment, the XUV beam waist radius is $\simeq 6 \mu\text{m}$ and the MIR FWHM is $\simeq 34 \mu\text{m}$, which yields $a \simeq 5$ and a detection efficiency of $\simeq 96\%$. In the right panel, we plot the expected measured signal as a function of the effective excitation cross section for different values of a .

Note that we obtain $a = 5$ using our XUV optic with a demagnification factor of 3. If instead we used a 1-to-1 toroid to focus the XUV onto the sample, we would have $a = 5/3$, and the measurement efficiency would be $\simeq 65\%$. Therefore, the ellipsoid's demagnification yields a nearly 50% increase in signal compared to a 1-to-1 XUV optic.

4.3.2 XUV-MIR Misalignment

We now consider the effect of having slightly misaligned MIR and XUV spots. For this calculation, we assume the sample excitation is purely linear: $\eta(x, y) \propto I_{\text{MIR}}(x, y)$. We numerically integrate Eq. (4.9) using the simulated MIR intensity profile $I_{\text{MIR}}(x, y)$ from Fig. 2.27 and an XUV spot with a $6 \mu\text{m}$ waist and a transverse offset of $x \rightarrow x + \Delta x$. The result is shown in Fig. 4.10. As in Fig. 4.9, we see that the finite beam sizes lead to a maximum measurement efficiency of about 96%. The measurement is very sensitive to misalignment; a $10 \mu\text{m}$ offset will reduce the efficiency to 76%, a $20 \mu\text{m}$ deviation yields 37%, and the minimum of $\simeq 0.8\%$ is near $\Delta x = \pm 37 \mu\text{m}$. The local maximum at $\Delta x = \pm 58 \mu\text{m}$ is due to the 1st lobe of the MIR diffraction pattern, yielding an efficiency of $\simeq 10\%$.

In our chamber, a $10 \mu\text{m}$ displacement of the MIR at the sample corresponds to a $15 \mu\text{rad}$ tilting of the hole mirror (HM). There are two ways misalignment can affect exper-

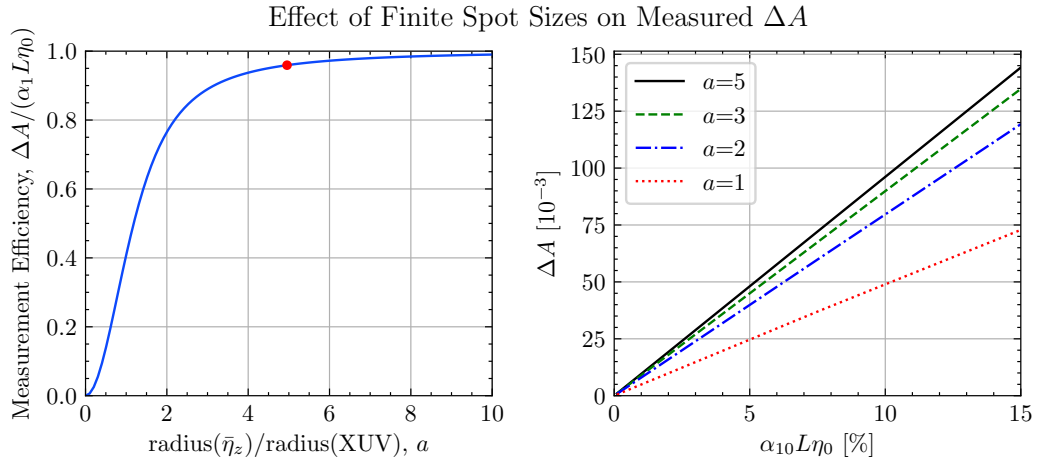


Figure 4.9: The effect of finite pump and probe sizes in measuring the change in absorbance in an ATAS experiment. Left panel shows the relative sensitivity of ΔA as a function of the relative sizes of the XUV and $\bar{\eta}_z$ spots. The red dot represents our experimental configuration ($a \simeq 5$), which yields $\simeq 96\%$ measuring efficiency. The right panel shows the expected ΔA amplitudes as a function of both a and $\alpha_{10}L\eta_0$. See Eq. (4.13) and surrounding text for details.

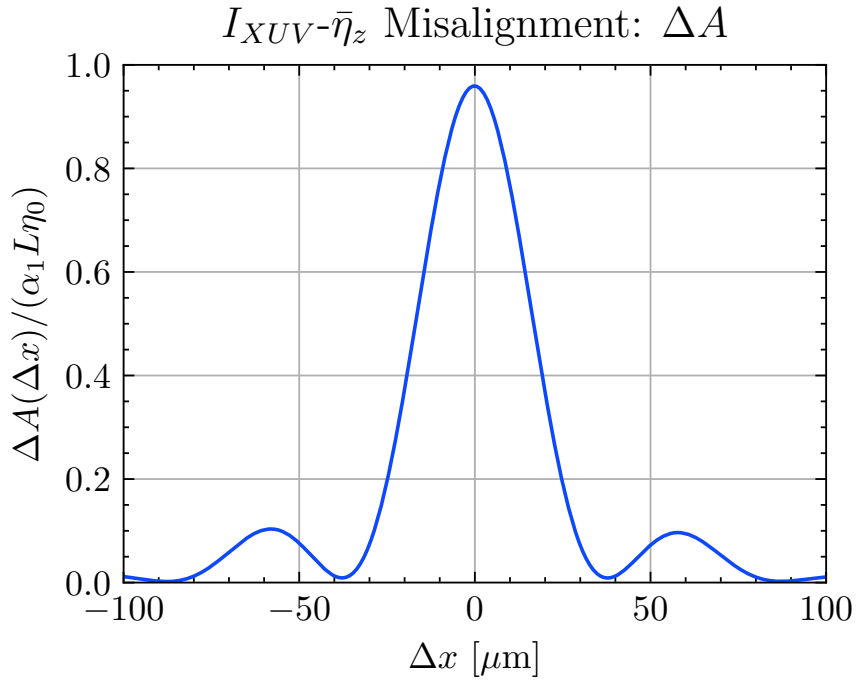


Figure 4.10: The effect of relative misalignment of the MIR and XUV spots. Linear excitation is assumed for this calculation.

imental results. If the relative positions of the XUV and MIR focal spots changes as an experiment is performed, then the recorded ATAS signal would be a function of both the laser-induced dynamics and the XUV-MIR spatial misalignment. On the other hand, if the entire experiment is performed using a constant misalignment, we would be exciting the sample to some peak excitation fraction f , but our probe would be measuring a lower excitation fraction ($\approx fa/a_{max}$). Consequently, the measured ATAS signal would be lower than otherwise expected, and any attempts to boost the signal by increasing the interaction intensity could result in permanent laser-induced sample damage.

A condensed matter ATAS experiment has much tighter alignment tolerances than a gas phase experiment. This discrepancy is a simple consequence of sample geometry and density. In either experiment, the measured signal comes from the region of space where the sample density, XUV intensity and MIR intensity overlap. The transmission of XUV through the sample is, to first order, $T = \exp(-n\mu_a L)$, where n is the number density, L is the sample thickness and μ_a is the photoabsorption cross section. As discussed above, for technical reasons the experiment should be designed with $T \approx 1/2$. Therefore, the product $n\mu_a L$ will be approximately constant for any transient absorption experiment.

The number density of a condensed phase sample is determined by the chemistry of the compound and is on the order of 4×10^{22} atoms/cm³. The experimentalist is free to engineer clever sample geometries, heterostructures and/or nanopatterns, but the high atomic density (and thus absorption coefficient) dictates a total sample thickness on the order of 100 nm. On the other hand, the spatial profile and density of a gas phase sample is determined by the gas nozzle design and its backing pressure, respectively. A typical nozzle used in our lab produces a gas plume with lateral dimensions on the order of 200 - 500 μm . This effectively creates a sample that is three orders of magnitude thicker than a condensed phase sample, which relaxes the alignment constraints significantly. This has important consequences for the alignment of the sample.

If the XUV and MIR are perfectly collinear, then the beam overlap region is effectively infinite in the propagation direction. In this case, the measured ΔA will be finite regardless of any displacement of the sample plane from the focal plane, and maximal when the sample lies in the focal plane. However, if there is a small angle $\delta\theta$ between their k -vectors, then the beams will only spatially overlap within a finite region. In this case, the position of the sample plane relative to the beam crossing plane becomes a critical experimental parameter. For an infinitely thick sample (i.e., a chamber effusively filled with gas), it wouldn't matter where the beams crossed as long as they overlapped somewhere within the chamber. Then, the XUV- η overlap integral would decrease as a function of $\delta\theta$, but it would never go to zero. For a thin sample, the bounds of Eq. (4.12) must enclose the beam overlap region, or else the integral will be zero. Thus, the signal strength of a condensed phase ATAS experiment is roughly 3 orders of magnitude more sensitive to the z -position of the sample

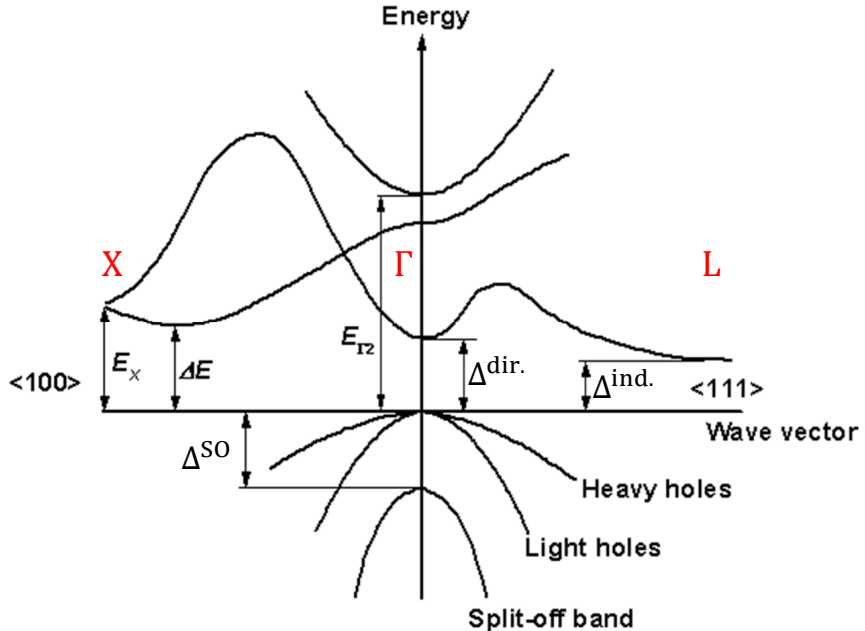


Figure 4.11: Band structure of germanium. Transition energies are labeled in black; the X , Γ and L valleys are labeled in red. Figure adapted from [15].

relative to the focal plane than a gas phase ATAS experiment.

4.4 Nonlinear Excitation of Germanium

Germanium's band structure is shown in Fig. 4.11 and additional material parameters are listed in Table 4.1. Germanium has a direct bandgap of $\Delta^{\text{dir.}} = 0.8$ eV, an indirect bandgap of $\Delta^{\text{ind.}} = 0.66$ eV, and a split-off band that is $\Delta_{\text{SO}} = 0.29$ eV below the heavy and light hole valence bands.

When considering the effect of an external electric field in a condensed matter sample, it is natural to compare the magnitude of the external field to that of the crystal lattice field, E_{CR} . We estimate the crystal field by:

$$E_{CR} \approx \frac{\Delta}{ae}, \quad (4.15)$$

where Δ is the field-free bandgap, a is the lattice constant and e is the electron charge. For germanium with an indirect bandgap of 0.66 eV and lattice constant $a = 0.5658$ nm, the crystal lattice field is approximately 11.7 MV/cm. This electric field corresponds to a laser peak intensity, I_{CR} :

$$I_{CR} = \frac{1}{2}cn\epsilon_0|E_{CR}|^2. \quad (4.16)$$

effective masses	
m_{CB} , for direct transitions	$0.041 * m_e$
m_{CB} , for indirect transitions	$0.0815 * m_e$
m_{VB} , from HH	$0.33 * m_e$
m_{VB} , from LH	$0.043 * m_e$
m_{VB} , from SO	$0.084 * m_e$
field-free excitation energies	
indirect transitions, from LH/HH	0.66 eV
direct transitions, from LH/HH	0.8 eV
indirect transitions, from SO	0.95 eV
direct transitions, from SO	1.09 eV
electron-phonon collision time, Γ^{-1}	47 fs

Table 4.1: Material parameters used in the Keldysh simulation for germanium. Abbreviations used are as follows: CB: conduction band; VB: valence band; HH: heavy hole band; LH: light hole band; SO: split-off band.

At $\lambda = 1430$ nm, $n = 4.2200$ and we obtain $I_{CR} \approx 760$ GW/cm², which isn't that much larger than the estimated peak intensity in our experiments (≈ 600 GW/cm²). As a result, the laser significantly distorts germanium's band structure in ways that cannot be treated by regular time-dependent perturbation theory [149]. We are therefore forced to employ non-perturbative approaches to approximate the laser-induced electronic dynamics within the sample.

There are two major categories of non-perturbative approaches to describe the interaction between a strong laser field and a semiconductor. The first approach is to numerically solve time-dependent quantum mechanical equations such as the time-dependent Schrödinger equation (TDSE), or to use time-dependent density functional theory (TDDFT). Alas, these approaches are computationally very expensive (which limits the XUV-MIR delay range and number of crystallographic unit cells used in the analysis) and their “black box” nature makes it difficult to interpret the physical origins of their main features. The second category, employed below, uses analytical equations for the cycle-averaged electron excitation rates.

We use the Keldysh formalism to calculate²³ the rate of field-driven interband transitions from the valence to the conduction bands [29, 147, 148]. The rate is then integrated using population coefficients to obtain the excited electron (hole) density in the conduction (valence) bands. This approach ignores the electron-particle collision and intraband absorption rates of conduction band electrons. The electric field is calculated from the en-

²³Special thanks to Dr. Drake Austin for performing the simulations, and to Prof. Enam Chowdhury for arranging the collaboration and participating in helpful discussions.

velope of the laser pulse, which ignores the sub-cycle effects of the laser field's oscillations. Additionally, the incident pulse is treated as a monochromatic source, which is valid for sufficiently long pulses. Finally, the dispersion of both the valence and conduction bands are modeled using simple functions of crystal momentum.

The remainder of this section is organized as follows. Section 4.4.1 describes the nonlinear model, and Section 4.4.2 provides a method for handling indirect transitions. Section 4.4.3 discusses the bandwidth of the MIR pulse as it relates to our model's assumptions. Section 4.4.4 presents the main results of the nonlinear calculation for a laser pulse with a spatially uniform intensity. However, this is an intermediate result as diffraction and thin film interference cause a broad distribution of MIR intensities throughout the interaction region. Section 4.4.5 performs the thin film interference calculations for our sample geometry. In Section 4.4.6, these results are combined with transverse diffraction calculations (see Section 2.5.2 and Fig. 2.27) to determine the focal volume averaged contribution to the measured signal. Finally, we comment on the steady state sample temperature in Section 4.4.7.

4.4.1 Description of the Nonlinear Model

This simulation considers photoexcitation from the top of the three valence bands to the bottom of the first conduction band²⁴ and includes both direct and indirect transition pathways. In the following paragraphs, we provide a brief physical motivation of the laser-induced modification of the band gap, which is an essential part of the Keldysh model and our subsequent analysis. First, we consider the laser-matter interaction while neglecting Coulomb-type interactions and applying the single-electron and dipole approximations. With these approximations, we can write down the time-dependent Schrödinger equation in the length gauge to describe the laser-electron interaction [149]:

$$i\hbar \frac{\partial \Psi(\vec{r}, t)}{\partial t} = \hat{H}_0(\vec{r})\Psi(\vec{r}, t) - e\vec{F}(t) \cdot \vec{r}, \quad (4.17)$$

where $\hat{H}_0(\vec{r})$ is the space-periodic field-free Hamiltonian of the crystal and $\vec{F}(t)$ is the electric field of the MIR laser. An approximate solution to Eq. (4.17) is given by the non-steady Bloch functions:

$$\Psi(\vec{r}, t) = u_{CB}(\vec{p}(t), \vec{r}) \exp\left(\frac{i}{\hbar}\vec{p}(t) \cdot \vec{r}\right) \exp\left(-\frac{i}{\hbar} \int_{-\infty}^t \epsilon_{CB}(\vec{p}(\tau)) d\tau\right), \quad (4.18)$$

where $u_{CB}(\vec{p}(t), \vec{r})$ is the amplitude of a steady Bloch function of the field-free crystal Hamiltonian and $\epsilon_{CB}(\vec{p})$ is the dispersion relationship for the conduction band. We use the

²⁴In germanium, the gap between the bottom of the first conduction band and vacuum is about 4 eV, so photoemission can be neglected.

Bloch acceleration theorem to calculate the time-dependent electron momentum, $\vec{p}(t)$:

$$\vec{p}(t) = \vec{p}_0 - e \int_{-\infty}^t \vec{F}(\tau) d\tau, \quad (4.19)$$

where \vec{p}_0 is the initial value of the 3D momentum. Equation (4.19) shows that the laser induces electron oscillations in crystal momentum-space. Due to the dispersion relationship, these momentum oscillations increase the energy of the conduction electron on the order of the ponderomotive energy, U_p ; the exact increase depends on the shape of the dispersion relationship. Note that the above argument equally applies to both electrons and holes in the valence band.

Having motivated the strong-field distortion of the bandgap, we will summarize without proof the relevant results of Keldysh theory below. The energy of the heavy and light hole bands are described using the Kane energy-momentum dispersion relation:

$$\epsilon_i(p) = \Delta \sqrt{1 + \frac{p^2}{m_i^R \Delta}}, \quad i = \text{HH, LH}, \quad (4.20)$$

which was the dispersion relationship used to derive the original Keldysh model. Here m_i^R is the *reduced electron mass* calculated from the conduction-band m_{CB} and valence band m_i effective masses (see Table 4.1 for values):

$$\frac{1}{m_i^R} = \frac{1}{m_{\text{CB}}} + \frac{1}{m_i}, \quad i = \text{HH, LH, SO}, \quad (4.21)$$

and Δ is the field-free excitation energy between the conduction and valence bands. The following results are valid for both direct and indirect transitions assuming the appropriate value of Δ is used. Consequently, we can use Keldysh's result for the effective band gap, Δ_i^{eff} :

$$\Delta_i^{\text{eff}} = \frac{2}{\pi} \Delta \left[\frac{\sqrt{1 + \gamma_i^2}}{\gamma_i} E \left(\frac{1}{\sqrt{1 + \gamma_i^2}} \right) \right], \quad i = \text{HH, LH}. \quad (4.22)$$

Here, $E(x) = \int_0^{\pi/2} \sqrt{1 - x^2 \sin^2 \theta} d\theta$ is the complete elliptic integral of the second kind²⁵, and γ_i is the Keldysh adiabatic parameter, which can be written as:

$$\gamma_i = \frac{\omega \sqrt{m_i^R \Delta}}{e F(t)}, \quad i = \text{HH, LH}, \quad (4.23)$$

where e is the elementary electric charge, m_i^R is the reduced carrier mass, and $F(t)$ is the time-dependent electric field of a slowly varying envelope of the pulse with peak amplitude

²⁵Note that this is a non-standard convention for the elliptic integral. The standard convention, $E(x) = \int_0^{\pi/2} \sqrt{1 - x \sin^2 \theta} d\theta$, will yield an unphysical result for small values of γ .

E_0 , pulse width τ_p and carrier frequency ω .

The *Keldysh adiabatic parameter* γ is used as a metric to distinguish between two mechanisms of photoexcitation: multiphoton excitation ($\gamma \gg 1$) and tunnel excitation ($\gamma \ll 1$); when $\gamma \simeq 1$ both mechanisms play a role in excitation. Physically, the electron sees the bandgap as a barrier of physical width $l = \Delta/(eF)$ and it has velocity $v \simeq \sqrt{\Delta/m_i^R}$. Then, the time it takes to tunnel through the barrier is $t_t \simeq v/l = eF/\sqrt{m_i^R \Delta}$. The Keldysh parameter is simply the ratio of the laser frequency to the tunneling frequency: $\gamma \equiv \omega/\omega_t$. When $\omega \ll \omega_t$, the electron will tunnel through the barrier quickly and the laser field can be considered to be quasi-static. On the other hand, if $\omega \gg \omega_t$, the field oscillates much faster than the tunneling time, and the excitation becomes frequency-dependent.

The split-off band (SO) is assumed to have a parabolic dispersion relationship:

$$\epsilon_{\text{SO}}(p) = (\Delta + \Delta_{\text{SO}}) \left(1 + \frac{p^2}{2m_{\text{SO}}^R(\Delta + \Delta_{\text{SO}})} \right), \quad (4.24)$$

where $\Delta + \Delta_{\text{SO}}$ is the total energy required to ionize an election from the split-off band in the absence of an external field, and p is the crystal momentum. Likewise, the effective excitation threshold for the split off-band is given by:

$$\begin{aligned} \Delta_{\text{SO}}^{\text{eff}} &= (\Delta + \Delta_{\text{SO}}) \cdot \left[1 + \frac{1}{4\gamma_{\text{SO}}^2} \right] \\ &= (\Delta + \Delta_{\text{SO}}) \cdot \left[1 + \frac{e^2 F(t)^2}{4m_{\text{SO}}^R(\Delta + \Delta_{\text{SO}})\omega^2} \right] \end{aligned} \quad (4.25)$$

where the adiabatic parameter has the same form as Eq. (4.23), but includes the additional excitation potential due to the split-off energy Δ_{SO} :

$$\gamma_{\text{SO}} = \frac{\omega \sqrt{m_{\text{SO}}^R(\Delta + \Delta_{\text{SO}})}}{eF(t)}. \quad (4.26)$$

Note that the effective bandgaps are always greater than the field-free bandgaps.

Even for small values of γ , where the multi-photon picture breaks down, it can still be instructive to compare the effective band gap to the photon energy. The minimum number of simultaneously absorbed photons required to cover the effective band gap of the interband transition from each valence band i is:

$$n_i = \left\langle \frac{\Delta_i^{\text{eff}}}{\hbar\omega} + 1 \right\rangle, \quad i = \text{HH, LH, SO}, \quad (4.27)$$

where $\langle x + 1 \rangle$ means a minimum integer exceeding x .

Figure 4.12 shows the effective band gaps and the Keldysh parameter as a function of peak intensity. The effective bandgap (solid lines, values on left axes) is significant for all initial states and transition types. For example, for a peak intensity of 640 GW/cm^2 and

Effective Band Gaps and Keldysh Parameters in Ge

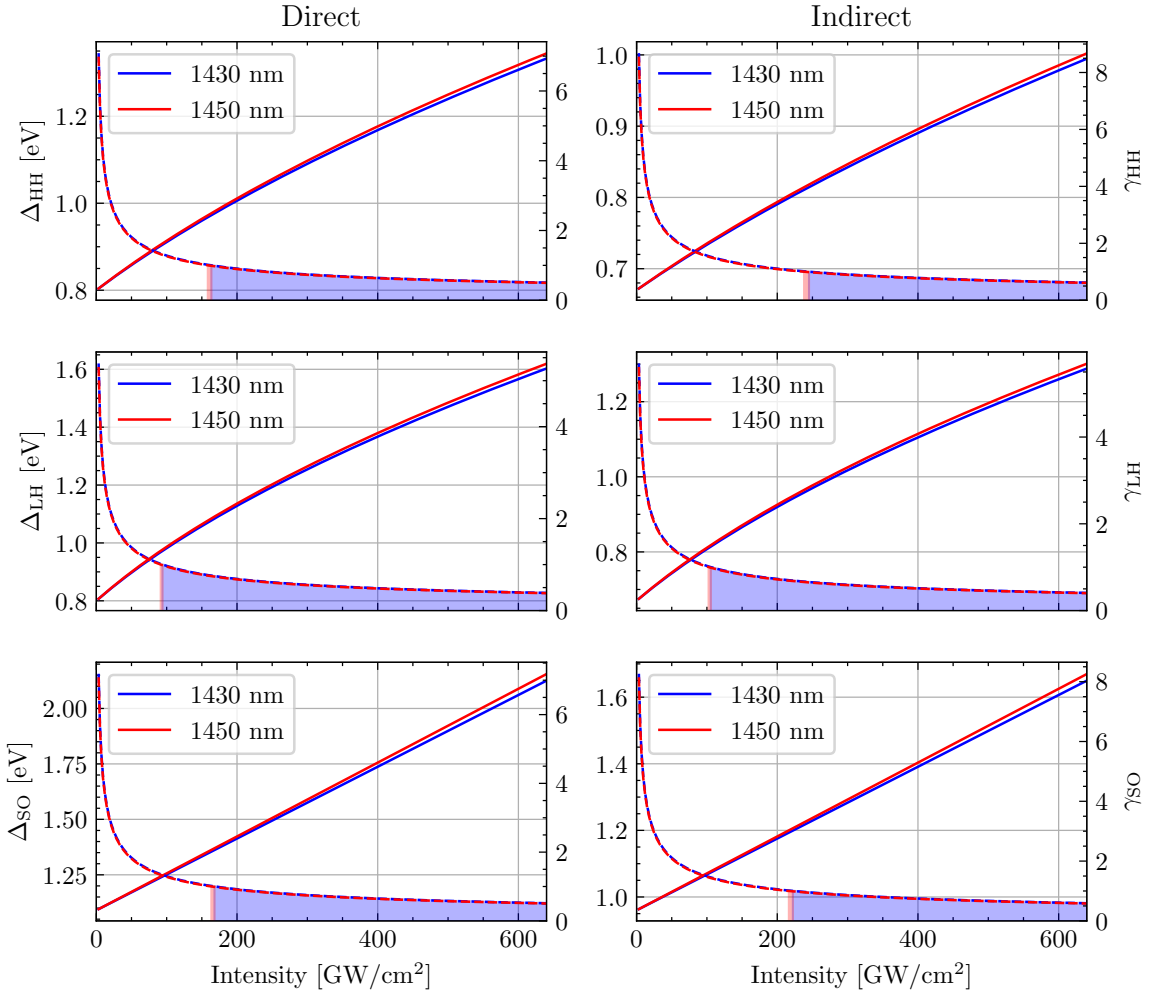


Figure 4.12: Channel- and initial band-resolved effective bandgaps Δ_i (solid line, left axes) and Keldysh parameters γ_i (dashed lines, right axes) as a function of peak intensity. The shaded region under γ_i corresponds to intensities where $\gamma_i < 1$ for 1430 nm (blue) and 1450 nm (red).

$m_i^R \Delta^{\text{eff}}$ [meV m_e]	direct	indirect
HH	29.18	43.14
LH	16.79	18.58
SO	30.03	39.30

Table 4.2: Values for the intensity-scaling factor $m_i^R \Delta^{\text{eff}}$, calculated using Eq. (4.21) and Table 4.1.

$\lambda = 1430$ nm, the energy required to excite from the light hole band to the conduction band via a direct transition is $\simeq 1.6$ eV, which is double the ground state value of 0.8 eV. The dashed lines (values shown on right axis) show the Keldysh parameter γ_i for each wavelength. Since $\gamma_i \propto \omega$, the difference between γ_i for the two wavelengths is negligible at this scale (about 1.5%). The shaded region under each γ_i curve denotes the intensities at which $\gamma_i < 1$. Most intensities result in $\gamma < 1$ or $\gamma \simeq 1$, meaning that both tunnel excitation and multiphoton excitation play an important role in the photoexcitation process. By 225 GW/cm², $\gamma < 1$ for all possible excitation channels.

Recalling Eqs. (4.23) and (4.26), γ is proportional to $\sqrt{m_i^R \Delta^{\text{eff}} / I}$, where I is the peak laser intensity. Therefore, the ratio of $m_i^R \Delta^{\text{eff}}$ to the intensity I is the most important parameter when considering the behavior of γ across the different bands and transitions. The six values of this intensity-scaling factor are shown in Table 4.2. Larger values of $m_i^R \Delta^{\text{eff}}$ will lead to correspondingly larger values of γ at the same intensity. The LH band has significantly lower values of $m_i^R \Delta^{\text{eff}}$ compared to both the HH and SO bands, and this is responsible for the relatively low values of γ experienced by the LH band as shown in Fig. 4.12.

We now turn to the excitation rate and population densities. The time-dependent electron density per unit energy in the conduction band N is the sum of contributions from the three valence bands i and two transition pathways j :

$$N(t, \epsilon) = \sum_{i,j} N_{i,j}(t, \epsilon), \quad (4.28)$$

where the subscript i denotes either the heavy-hole (HH), light-hole (LH) or split-off (SO) valence bands, and j denotes the transition type (direct or indirect).²⁶ The contribution from each band is determined by the following rate equation:

$$\frac{dN_i(t, \epsilon)}{dt} = f_i(t) W_i[F(t)], \quad (4.29)$$

where the interband excitation rate densities W_i (units of cm⁻³ fs⁻¹) are evaluated by the

²⁶In this section, we will restrict the discussion to direct transitions and therefore we will omit the subscript j ; indirect transitions will be considered in Section 4.4.2.

Keldysh formula for heavy and light hole energy bands [29] and by the parabolic version of the Keldysh formula for the split-off valence band [150]. Note the expressions for W_i only depend on γ_i , ω , and η_i , and that this treatment naturally includes both linear and nonlinear electronic excitation across the bandgap. The relaxation and electron-trapping contributions to the rate equation are neglected, as are electron-electron collisions and impact ionization. The prefactor $f_i(t)$ is a unitless population coefficient equal to the unexcited population density fraction, which accounts for state blocking:

$$f_i(t) = 1 - \frac{1}{N_{i0}} \int_{\Delta_i^{\text{eff}}}^{\infty} N_i(t, \epsilon) d\epsilon. \quad (4.30)$$

Here, N_{i0} is the initial total population of each valence band (units of cm^{-3}) and Δ_i^{eff} is the instantaneous minimum required transition energy for the i^{th} channel (see Eqs. (4.22) and (4.25)). The initial conduction band population is assumed to be zero, as the sample is at room temperature:

$$N_i(t = 0) = 0. \quad (4.31)$$

Using the aforementioned theoretical framework, the simulation calculates contributions to the photoexcitation rate from both direct and indirect excitations across the bandgap as the pulse propagates through the material. Integration of Eq. (4.29) yields the initial band-and excitation channel-resolved contributions to the conduction band. The total excited electron density in the conduction band N is obtained by summing over all valence bands and excitation channels via Eq. (4.28). For computational and theoretical details on how this code is implemented, see Appendix B of [145] and Reference [147], respectively.

4.4.2 Indirect Transitions

An indirect transition, where the final crystal momentum is substantially different than its initial value, is mediated by an electron-phonon scattering process. This additional process must occur within the timescale of the laser pulse, and thus we expect the pulse duration and the scattering cross section to impact the relative prevalence of indirect transitions in our experiments. If we assume these collisions occur independent of one another (and, therefore, follow a Poisson distribution), we can calculate the indirect transition excitation rate $W_i^{\text{ind.}}$ by multiplying the direct transition rate $W_i^{\text{dir.}}$ by a correction factor:

$$W_i^{\text{ind.}} = W_i^{\text{dir.}} * (1 - \exp(-\Gamma\tau_p)), \quad (4.32)$$

where τ_p is the pulse duration and Γ is the electron-phonon collision rate. The factor in Eq. (4.32) represents the probability that any given electron will undergo one or more phonon collisions in the time τ_p , assuming the collisions follow a Poisson distribution. For germanium, we estimate $1/\Gamma \approx 47$ fs, which is an estimate inferred from measurements

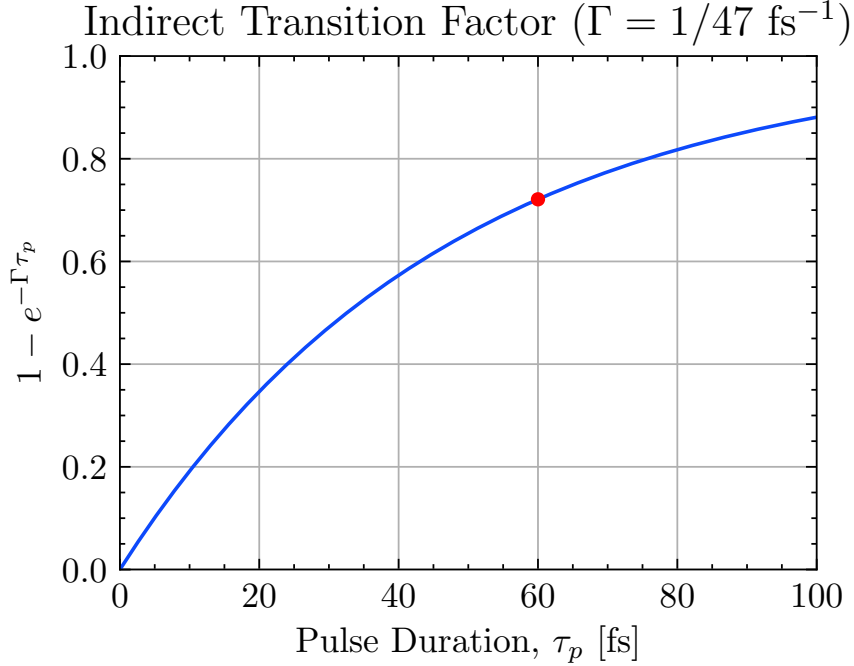


Figure 4.13: Prefactor for indirect transition rates assuming a Poisson distribution. For germanium and a pulse duration of 60 fs, the indirect transition factor is about 0.7.

of laser-induced periodic surface structures on Ge [145]. When calculating $W_i^{\text{dir.}}$, we use the local conduction band mass m_{CB} in the indirect valley and the indirect energy gap $\Delta_i^{\text{ind.}}$. Figure 4.13 shows the prefactor in Eq. (4.32) as a function of pulse duration. For our experiment, $\tau_p = 60$ fs and the prefactor evaluates to ~ 0.72 . We note that a shorter pulse duration of ~ 12 fs, which is achievable with our lab's fiber compressor [151], would give a prefactor of ~ 0.23 . The DiMauro lab thus has an avenue for future studies that probe the relative importance of direct and indirect transitions in the ensuing electron dynamics.

4.4.3 Spectral Content of the Laser Pulse

Since we are near the bandgap ($\Delta^{\text{dir.}} = 1550$ nm, $\Delta^{\text{ind.}} = 1879$ nm), it's possible that a portion of the MIR pulse's spectrum will be below the bandgap, which would have consequences for both the interference and Keldysh calculations. Figure 4.14 shows the spectral content of the TOPAS when it is set to 1400 nm.²⁷ We will use this spectrum to estimate the spectral content when operating at 1430 and 1450 nm. The red line shows the spectral intensity, the black line is the integrated sum of the red line, and the green dashed

²⁷Unfortunately, we did not measure the spectral content of the pulse when the TOPAS was set at $\lambda = 1430$ or 1450 nm. However, in our experience the shape of the spectral envelope is invariant under small wavelength shifts.

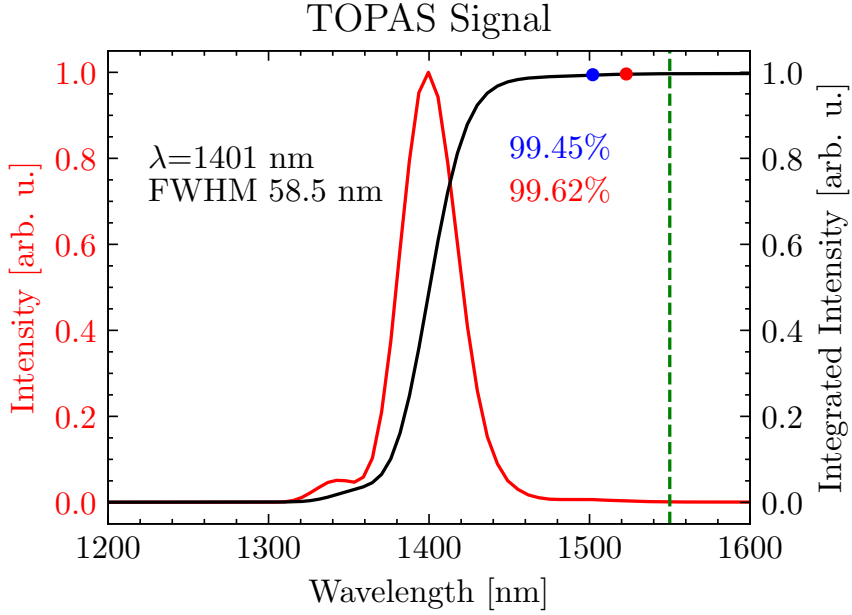


Figure 4.14: TOPAS spectral content at $\lambda = 1401$ nm.

vertical line represents the direct bandgap. When the TOPAS is operating at 1430 nm (1450 nm), the central wavelength λ_0 is 120 nm (100 nm) above the bandgap. According to this measurement, when the TOPAS is running at 1400 nm, 99.45% of the pulse energy is at wavelengths below the $\lambda_0 + 100$ nm (blue dot), and 99.62% of the pulse energy is at wavelengths below $\lambda_0 + 120$ nm (red dot). If we assume the spectral envelope is invariant under small wavelength shifts, then it stands to reason that when the TOPAS is run at 1430 or 1450 nm, over 99% of the pulse energy is above Ge's bandgap (1550 nm). Thus, we are justified in treating the pulse as if it were entirely above the band gap.

4.4.4 Keldysh Results

We now present the excitation results of the model introduced in Sections 4.4.1 and 4.4.2. We start with single-intensity calculations (i.e., what we would observe if we had a δ -function intensity distribution in Fig. 4.22), then proceed to focal volume average the results using the MIR intensity distributions in Section 4.4.5 and Fig. 2.27. Focal volume-averaged results are presented in Section 4.4.6.

The simulation was performed for two wavelengths ($\lambda = 1430, 1450$ nm) and 1000 different peak intensities, ranging from 3.26 to 640 GW/cm². A Gaussian pulse envelope was assumed with a pulse duration of $\tau_p = 60$ fs, and the time relative to the center of the pulse τ ranged from -120 to +120 fs in 1000 steps. For each set of input parameters, the simulation outputs an initial band- (HH, LH, SO) and transition type- (indirect, direct)

resolved electron population in the conduction band as a function of τ .

Figure 4.15 shows the main result of the Keldysh calculation. We plot the contributions from each excitation channel (direct & indirect) and for each of the three initial bands after the MIR pulse has left ($\tau = 120$ fs) as a function of peak intensity. In 5 of the 6 plots, we see an intensity-dependent effect where N_{CB} has a local maximum, a slight dip, and then an increase. At this scale, this feature is most prominent in for indirect heavy hole plot, but the general shape is the same whenever it appears. These features occur at intensities that coincide with an increase in the minimum number of photons required to cross the bandgap (n_i in Eq. (4.27)), akin to channel-closure [152]. The value of n_i is denoted in the plot on either side of the feature. Only the indirect split-off contribution lacks this feature, as $n_i = 2$ for all intensities in the simulation.

Figure 4.16 shows the total excitation (summed over all channels and initial bands) of the sample as a function of τ for the highest intensity ($I = 640 \text{ GW}/^2$). The result is a modified error function, owing to the nonlinearity of the sample's response. We see there is little difference between the two wavelengths in terms of total excitation. Because we use the pulse envelope, rather than the instantaneous field strength, we do not see steps in the excitation fraction every half-period [131].

Figure 4.17 shows the population of the conduction band after the MIR pulse has left ($\tau = 120$ fs) as a function of peak intensity. For all intensities, the signal is dominated by contributions by the heavy and light hole bands, which is to be expected as the split-off band has a higher excitation potential. For 1430 nm, we see that at $160 \text{ GW}/\text{cm}^2$, the heavy hole VB is responsible for about 56.8% of the CB population, followed by the light hole VB at around 36.2%, and finally the split-off VB at around 7.29%, with similar ratios for 1450 nm. Above $400 \text{ GW}/\text{cm}^2$ and as a result of $n_{\text{HH, ind.}}$ increasing by 1, the LH contribution begins to overtake the HH. In our experience, a peak intensity of above $640 \text{ GW}/\text{cm}^2$ corresponds to immediate sample damage, meaning that we can expect no more than $1.18 \times 10^{22} \text{ cm}^{-3} \simeq 6.6\% N_{\text{VB}}$ fractional excitation in our experiments. This indicates that ultrafast melting should not be a concern below $640 \text{ GW}/\text{cm}^2$.

Figure 4.18 shows the relative contribution of indirect and direct transitions to the total population density by the end of the pulse as a function of peak intensity. Recalling Eq. (4.32), the indirect transition rate is suppressed due to the product $\tau_p \Gamma \approx 0.7$. However, this factor is not enough to overcome the relative increase in excitation due to the lower bandgap of the indirect transition compared to the direct transition. Consequently, only 23 – 50% of the excited population are due to direct transitions. At the highest intensities, we see equal contributions by both channels.

The above calculations assume a single peak intensity throughout the sample, but a spatially invariant intensity profile is unphysical. In a real experiment, the sample experiences a spatially varying intensity profile, which results in a nonuniform excitation fraction. We

Initial State Contributions to Final CB Density ($\tau=120$ fs)

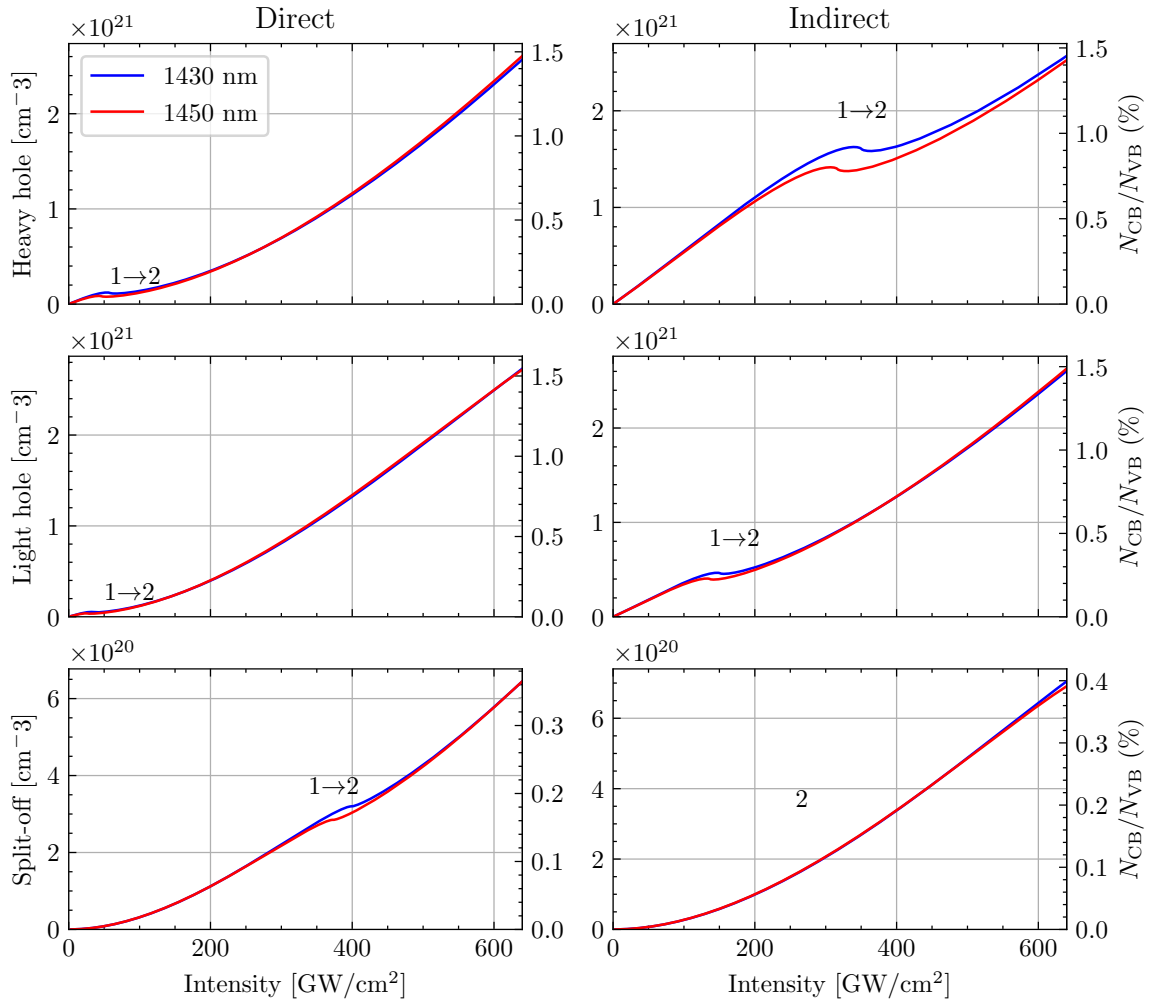


Figure 4.15: Transition type and initial band resolved contributions to the final conduction band density. Inset text denotes the values of n_i at the peak intensity (for $\tau = 0$ fs) as the minimum number of photons required to excite the electron across the gap increases by 1.

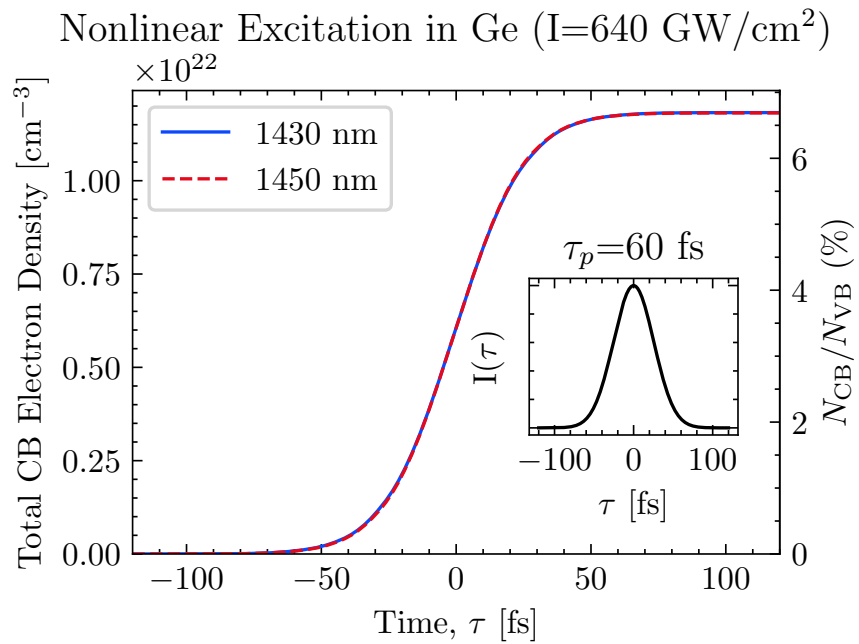


Figure 4.16: Total conduction band (CB) population as a function of laser pulse delay. Inset shows the pulse envelope.

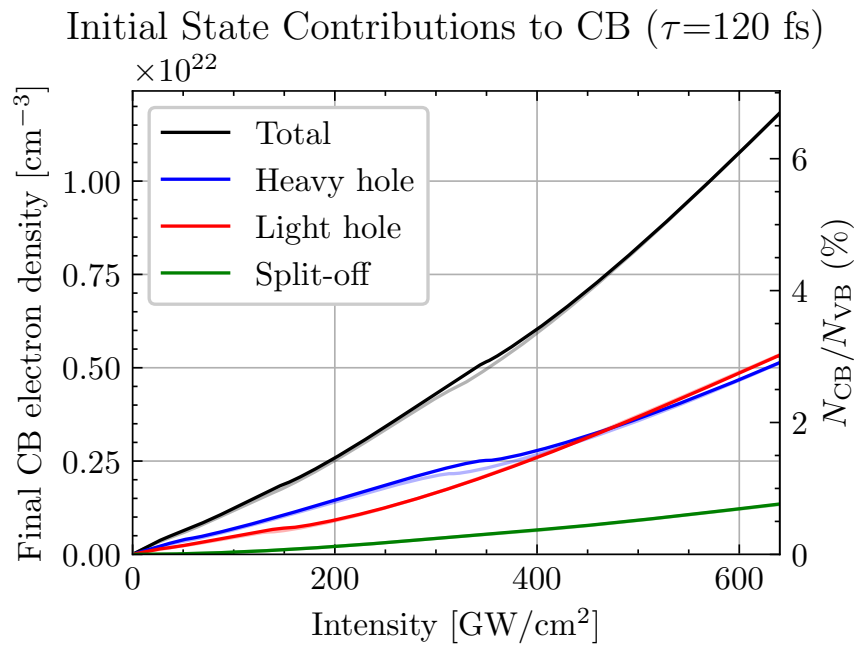


Figure 4.17: Contributions of the initial bands to the final conduction band (CB) density at the end of the pulse ($\tau = \infty$). Dark lines are for $\lambda = 1430$ nm, faint lines are for $\lambda = 1450$ nm.

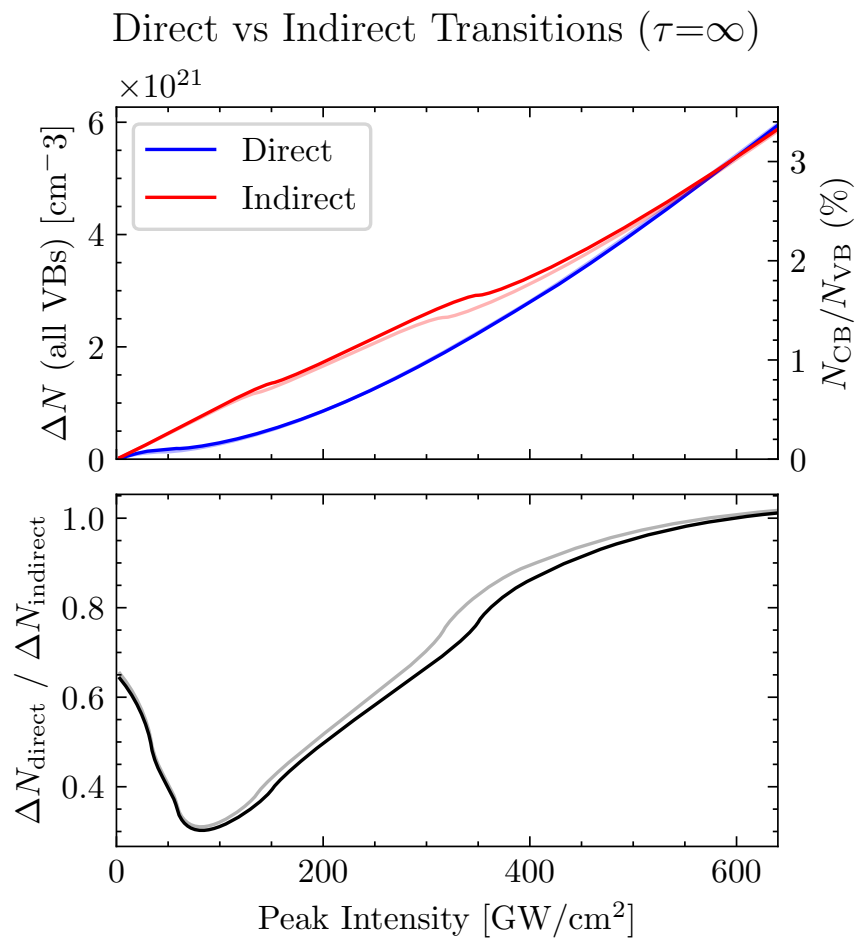


Figure 4.18: Contributions by indirect and direct transitions to the final conduction band (CB) density at the end of the pulse ($\tau = \infty$). Dark lines are for $\lambda = 1430$ nm, faint lines are for $\lambda = 1450$ nm.

have already addressed the diffraction-induced transverse intensity profile of the MIR focus (see Section 2.5.2). In the following section, we will calculate the intensity profile along the direction of propagation within the sample.

4.4.5 Thin Film Interference Calculations

The sample is a heterostructure of 100 nm germanium ($\tilde{n} = 4.2481 + 0.066041i$ at 1430 nm) on a 30 nm silicon nitride membrane ($\tilde{n} = 1.9997 + 0i$ at 1430 nm) with a total thickness measuring $\sim 9\%$ of the fundamental wavelength. As a result, we cannot ignore thin film interference effects that may arise from this geometry. To account for this, we calculated the intensity profile in the heterostructure for the two wavelengths of experimental interest (1430 and 1450 nm) using the transfer matrix method. We also calculate the intensity profile with the assumption that there is no internal interference pattern. As will be shown below, these two methods result in drastically different intensity profiles. The actual internal profile is likely somewhere between the two, as the sample is not an ideal thin film, nor is its quality so poor that it is completely incapable of supporting interference patterns. The resulting intensity profiles are later used as inputs to the Keldysh nonlinear photoexcitation code. Refractive index data for germanium [140] and the silicon nitride [153] were taken from the literature. Calculations were performed using the *TMM package for Python* [154, 155].

The TMM code assumes a multilayer planar stack of non-magnetic ($\mu = \mu_0$) and isotropic materials. The interfaces are considered ideal (i.e., zero surface roughness), so this result represents an upper limit on the interference effects present in our system. Nonlinear effects are excluded from this calculation. The electric field is expressed as a superposition of forward- and backward-propagating complex-valued waves:

$$\begin{aligned}\mathbf{E}(\mathbf{r}) &= \mathbf{E}_f^0 \exp(i\mathbf{k}_f \cdot \mathbf{r}) + \mathbf{E}_b^0 \exp(i\mathbf{k}_b \cdot \mathbf{r}), \\ \mathbf{k}_f &= \frac{2\pi n}{\lambda_{\text{vac}}} (\hat{\mathbf{z}} \cos \theta + \hat{\mathbf{x}} \sin \theta), \\ \mathbf{k}_b &= \frac{2\pi n}{\lambda_{\text{vac}}} (-\hat{\mathbf{z}} \cos \theta + \hat{\mathbf{x}} \sin \theta),\end{aligned}\tag{4.33}$$

where θ is the angle between \mathbf{k} and the surface normal. The code solves for the internal complex electric field by applying the transfer matrix method to the heterostructure assuming an input electric field of unit magnitude [156–160]. We obtain the physical field at any time t by multiplying the complex field by $e^{-i\omega t}$ and taking the real part of the resulting expression. We define the *peak normalized intensity* as the local peak intensity divided by

TMM: Coherent & Incoherent Properties

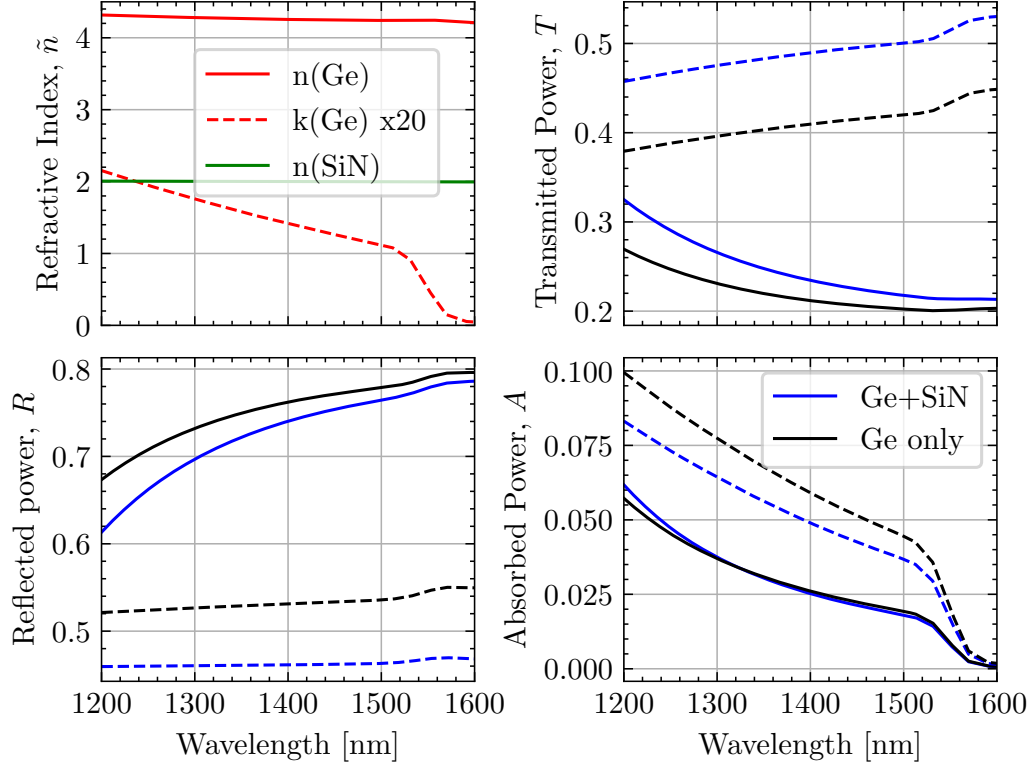


Figure 4.19: Optical properties of the Ge/SiN heterostructure and a freestanding 100 nm Ge membrane as a function of wavelength. For the R , A and T panels, solid lines represent the coherent calculations, and dashed lines represent the incoherent calculations. TMM calculations assume monochromatic light.

the peak intensity in the absence of the heterostructure²⁸:

$$\frac{I_p(z)}{I_{p,0}(z)} \equiv \operatorname{Re}\{\tilde{n}_{\lambda_0}(z)\} \max_t \left(\left| \sum_{\lambda} \mathbf{E}_{\lambda}(z, t) \right|^2 \right), \quad (4.34)$$

where $\tilde{n}_{\lambda_0}(z)$ is complex refractive index at the central wavelength λ_0 at position z . The normalized peak intensity will later be used to convert vacuum intensities to sample intensities. We also report the transmitted (T), reflected (R) and absorbed power (A) of the heterostructure.

We start by considering the wavelength dependence of the calculated optical properties. The top left panel of Fig. 4.19 shows the complex refractive index of germanium and silicon

²⁸We omit the denominator as it evaluates to unity with an input field of unit strength. That is, $\max_t \left(\left| \sum_{\lambda} \mathbf{E}_{\text{vac.}, \lambda} \right|^2 \right) = 1$.

nitride over the range 1200 – 1600 nm. Note that the vertical scale for $k(\text{Ge})$ has been enlarged for visual clarity. In the following discussion, we consider either a heterostructure (germanium sample at $z = 0 - 100$ nm, silicon nitride at $z = 100 - 130$ nm, and vacuum elsewhere) or a freestanding germanium film (germanium sample at $z = 0 - 100$ nm, and vacuum elsewhere). The MIR laser propagates in the $+z$ direction with a normal incidence angle ($\theta = 0$). The refractive index for silicon nitride is effectively constant over this range, and germanium's index is well-behaved below 1520 nm (near the direct bandgap at 1550 nm). The solid lines in the remaining three panels of Fig. 4.19 show the transmitted, reflected and absorbed power for both a freestanding 100 nm Ge film and a 100 nm Ge / 30 nm SiN heterostructure assuming full coherence of the beam. The dashed lines in these panels show the results of an *incoherent TMM calculation*, in which we discard the phase information of the light to approximate the effects of a rough surface or spatially varying film thickness.

As should be expected, interference effects are critical to understanding the optical properties when the structure's thickness is sub-wavelength. The coherence is responsible for nearly doubling the reflectance and reducing the absorbed power by a factor of ≈ 2.5 at 1400 nm. We can see that the reflected and transmitted power do not change appreciably over the range 1400 – 1500 nm, which encompasses the spectral envelope of a TOPAS signal centered at 1430 or 1450 nm. For both the heterostructure and the freestanding Ge film, about 75 percent of the incident power is reflected, about 23 percent is transmitted, and about 2 percent is linearly absorbed.

We note that at these wavelengths the coherence length, L , greatly exceeds the sample thickness [159]:

$$L = \frac{\lambda^2}{n\Delta\lambda}. \quad (4.35)$$

For a laser pulse with a central wavelength of 1430 nm and a bandwidth of 58.5 nm, $L(\text{Ge}) \approx 8.23 \mu\text{m}$ and $L(\text{SiN}) \approx 17.4 \mu\text{m}$, which is ≈ 80 and ≈ 580 times longer than the thickness of the germanium and silicon nitride films, respectively. We also note that a round trip reflection within the heterostructure will take 3.2 fs at 1430 nm, which is 18 times shorter than the laser pulse. For these reasons, we use standard interference calculation methods to estimate the intensity profile within the heterostructure.

Since the TMM model is linear, we can extend it to handle a broadband pulse by coherently summing the resulting electric field over the bandwidth of the pulse. Broadband TMM calculations were performed using $N = 500$ monochromatic TMM calculations over the spectral range 1300 - 1500 nm. Spectral weights for each wavelength were calculated by interpolating the square root of the spectral intensity in Fig. 4.14 after shifting the spectral envelope to the appropriate central wavelength.

We compare the TMM result to a simpler model which only includes Fresnel losses from

Broadband TMM: 100 nm Ge + 30 nm SiN

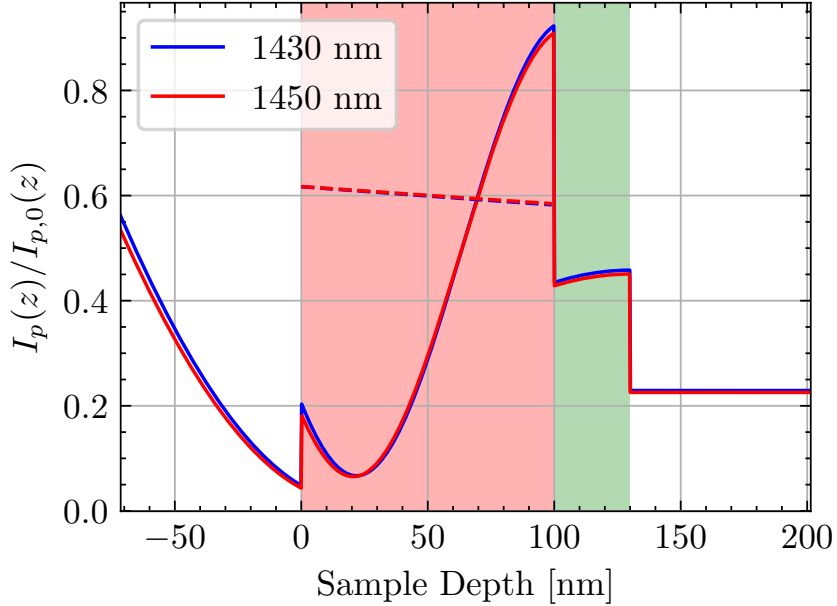


Figure 4.20: Broadband TMM calculations for a 100 nm Ge film and 30 nm SiN membrane. The red region represents Ge; green is SiN; white is vacuum. Solid lines are TMM results, dashed lines are Eq. (4.36).

the front interface (vacuum-Ge) and linear absorption thereafter [16]:

$$\frac{I_p(z)}{I_{p,0}(z)} = \text{Re}\{\tilde{n}\} \left| \frac{2}{1 + \tilde{n}} \right|^2 \exp \left[- \left(\frac{4\pi}{\lambda_0} \right) \text{Im}\{\tilde{n}\} z \right] \approx 0.60, \quad (4.36)$$

where \tilde{n} is the complex refractive index of Ge evaluated at the central wavelength of the pulse (λ_0) and z is the depth within the Ge sample. While this method does not calculate the intensity profile outside of the germanium, we note that this information is superfluous as SiN's large band gap ($\Delta \approx 5$ eV) precludes any linear absorption, and our XUV measurement is insensitive to any dynamics occurring within the SiN membrane.

Figure 4.20 shows the calculated peak normalized intensity profile of a heterostructure consisting of 100 nm of germanium on a 30 nm thick silicon nitride membrane for $\lambda = 1430$ and 1450 nm. The solid lines are broadband TMM calculations, and the dashed lines are the Fresnel absorption model (Eq. (4.36)). Starting with the TMM result, we note that the discrete jumps in intensity at the sample boundaries are due to the discrete jumps in the refractive index. Inside the Ge, we see a strong modulation of the intensity due to interference effects. Before the sample ($z < 0$), the intensity is suppressed by the coherent back reflection from the vacuum-Ge interface. Inside the sample, the intensity has a min-

Broadband TMM: 100 nm Freestanding Ge

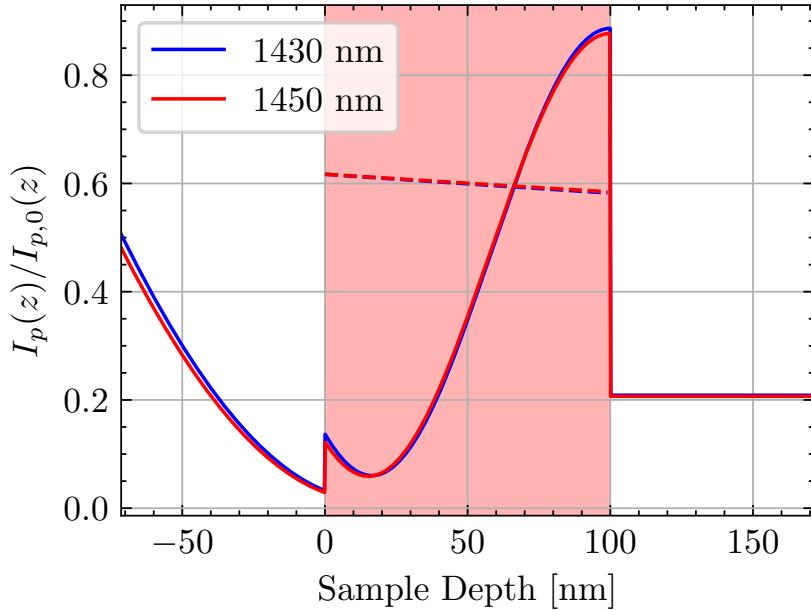


Figure 4.21: Broadband TMM calculations for a 100 nm freestanding Ge thin film. The red region represents Ge; white is vacuum. Solid lines are TMM results, dashed lines are Eq. (4.36).

imum about 20 nm below the vacuum-Ge interface. From $z = 20$ nm to $z = 80$ nm the normalized peak intensity increases linearly before asymptotically approaching a maximum value at the Ge-SiN boundary. Therefore, the broadband TMM model predicts that the highest intensities are located on the back face of the Ge sample, which can be understood as a combined reflection off the Ge-SiN and SiN-vacuum interfaces. In contrast to the TMM result, Eq. (4.36) yields an intensity profile that is very nearly linear over the limited 100 nm depth. In either model, changing the wavelength from 1430 nm to 1450 nm does not appreciably change the intensity profile.

The presence of the silicon nitride membrane was required for technical materials preparation reasons. To quantify the effect of its presence on the internal intensity distribution, we performed broadband TMM calculations for a 100 nm thick freestanding germanium membrane, as shown in Fig. 4.21. Comparing it to the previous result, we can see that the addition of the SiN membrane does not significantly change the optical properties of the sample, as the general shape of the intensity profile is the same as the heterostructure. By adding the SiN membrane, reflectivity increases by $\approx 2.5\%$, absorption decreases by $\approx 4.2\%$, and transmission increases by $\approx 9.6\%$. The increased reflection losses are not a concern, as we have sufficient flux in our pump arm to make up for the increased losses.

TMM Type	Structure	λ_0 [nm]	$\min\left(\frac{I_p(z)}{I_{p,0}(z)}\right)$ [%]	$\max\left(\frac{I_p(z)}{I_{p,0}(z)}\right)$ [%]
monochromatic	Ge/SiN	1430	6.62	92.62
		1450	6.49	91.24
	freestanding Ge	1430	5.93	88.50
		1450	5.86	87.53
broadband	Ge/SiN	1430	6.68	92.19
		1450	6.53	90.90
	freestanding Ge	1430	6.01	88.67
		1450	5.90	87.84

Table 4.3: TMM calculated internal intensity ranges for a 100 nm Ge / 30 nm SiN heterostructure and a freestanding 100 nm Ge film.

The dashed lines show Eq. (4.36), which does not take into account the presence or absence of the SiN membrane and is the same as in Fig. 4.20.

If the sample response was strictly linear, then the measured ATAS signal should be proportional to the average intensity within the XUV probe. For the Ge/SiN heterostructure, the average intensity of the TMM model is about 65% that of the Fresnel model. On the other hand, a nonlinear sample response gives the higher intensity regions outsized importance, and we see that the broadband TMM interference pattern has a maximum intensity 50% higher than the Fresnel model. These numbers are similar for the freestanding germanium geometry, albeit less pronounced.

As an aside, a simple monochromatic TMM calculation at the central wavelength of the pulse can reveal much of the same information in a fraction of the computational time. Table 4.3 shows intensity extrema for the different sample geometries, wavelengths and TMM calculation methods. For our relatively narrow bandwidth, including the coherent sum over all wavelengths changes the results by about 1%. Not shown are the monochromatic versions of Figs. 4.20 and 4.21, but the differences between the two methods are imperceptible at this scale.

The distribution of intensities within the sample is important when calculating the focal volume averaged Keldysh excitation, and anything short of a δ -function distribution of intensities will smear out intensity-dependent effects. Fig. 4.22 shows histograms ($N = 40$ bins) of the intensity distributions of the aforementioned sample geometries and experimental conditions. The dark colors are the results of the broadband TMM calculation, and the lighter colors follow from Eq. (4.36). The general shape of the TMM's distribution is similar for both wavelengths and sample geometries. In all four cases, most of the sample sees relatively low intensities (< 20% of the incident intensity), whereas on the volume closest to the rear face of the stack experiences high intensities (> 75% of the incident intensity). The distribution is flat for intermediate intensities (20 – 75 % of the incident in-

Broadband TMM: Intensities in Heterostructures

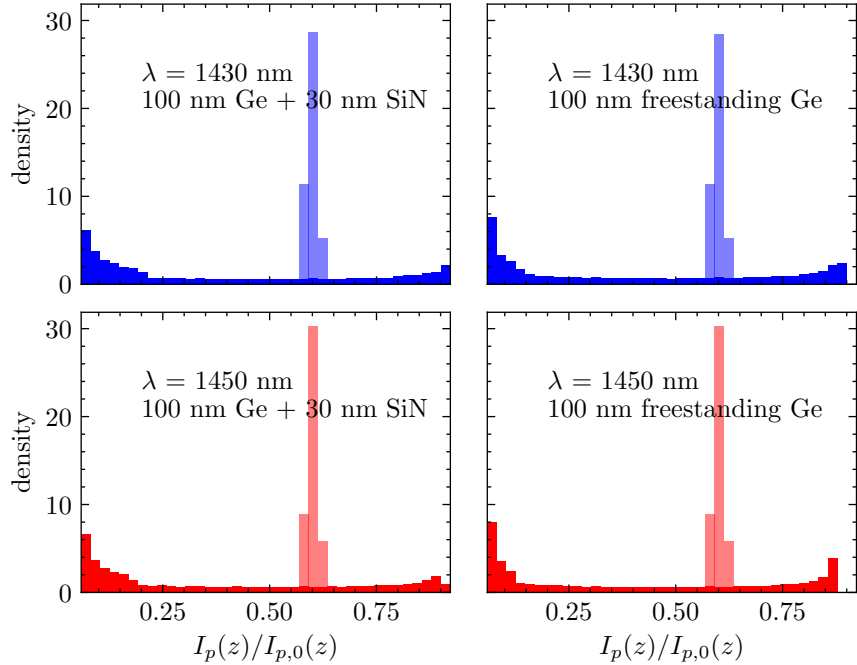


Figure 4.22: Calculated intensity distributions in Ge/SiN heterostructures and Ge thin films. Dark colors follow broadband TMM calculations, light colors follow Eq. (4.36).

tensity), owing to the linear increase of intensity with increasing z . It should be noted that the high-intensity tail of the freestanding Ge samples is slightly more pronounced than the Ge/SiN heterostructures, which could facilitate the measurement of intensity-dependent effects. In contrast, the Fresnel absorption model (Eq. (4.36)) predicts a much sharper intensity distribution.

These calculations were run over a range of incident angles. The resulting intensity distribution does not appreciably change for either s- or p-polarized light if the incident angle remains below 20 degrees (measured from normal). We did not carefully control the incident angle when installing our samples, but since this result is not sensitive to the incident angle, it is reasonable to assume that our sample experiences the intensity distribution shown in Fig. 4.22.

Having computed the intensity profile within the germanium sample, we can now apply the Keldysh model to our experiment.

4.4.6 Volume Averaging

We calculate the intensity inside the sample as the product of the sample-free vacuum intensity $I_{\text{vac.}}$, the transverse diffraction-induced term $I_{\text{diff.}}(x, y)$ (Fig. 2.27) and the inter-

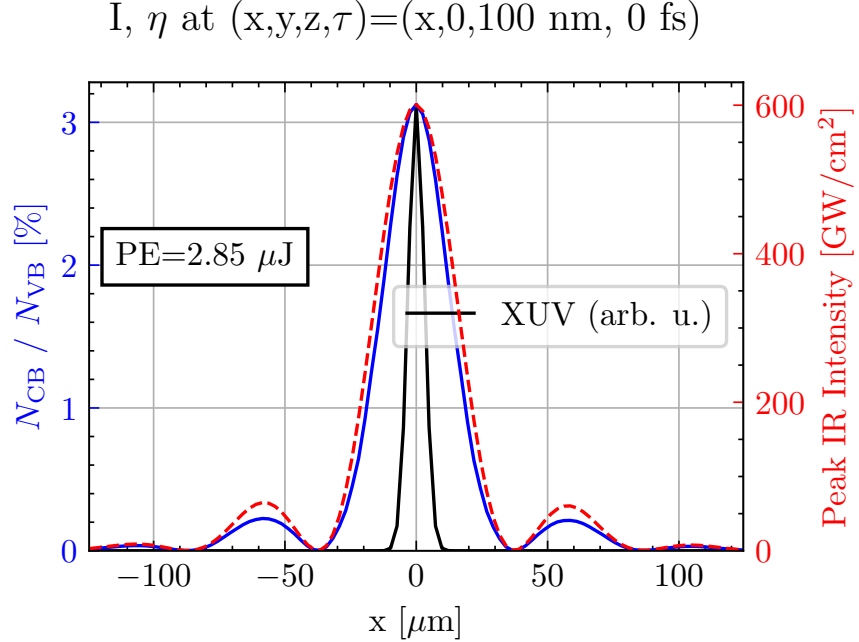


Figure 4.23: Cross sectional slice of the MIR intensity profile, XUV intensity profile and total excited state fraction at the rear of the Ge sample in a Ge/SiN heterostructure and the center of the MIR pulse ($\tau = 0 \text{ fs}$). The MIR intensity profile follows from a broadband TMM calculation for a 100 nm Ge / 30 nm SiN heterostructure and an input pulse energy of $2.85 \mu\text{J}$ of $\lambda = 1430 \text{ nm}$.

ference/absorption term $I_p(z)/I_{p,0}(z)$ (Section 4.4.5):

$$I_{\text{sample}}(\tau; x, y, z) \equiv I_{\text{vac.}}(\tau) \times I_{\text{diff.}}(x, y) \times \frac{I_p(z)}{I_{p,0}(z)} \quad (4.37)$$

We provide a brief summary of the aforementioned profiles here. Combining the first two terms, $I_{\text{vac.}} \times I_{\text{diff.}}$ has a peak intensity at the focus of $\approx 2.3 \times 10^{11} \text{ W/cm}^2$ per $1 \mu\text{J}$ input energy (as measured before lens L4), and $I_p(z)/I_{p,0}(z)$ has a maximum value of about 93% (for a Ge/SiN heterostructure). Therefore, the maximum peak intensity in the germanium sample for a 60 fs pulse is approximately $2.13 \times 10^{11} \text{ W/cm}^2$ per $1 \mu\text{J}$ input energy.

We map the Keldysh simulation result $N_{\text{CB}}(I, \tau)$ onto the intensity distribution $I_{\text{sample}}(x, y, z, \tau)$ to get the conduction band electron density distribution $N_{\text{CB}}(x, y, z, \tau)$ within the sample. Figure 4.23 shows an example lineout of the MIR intensity and the conduction band electron density in our sample. This slice was taken at the Ge/SiN interface ($z = 100 \text{ nm}$) at the peak of the pulse ($\tau = 0 \text{ fs}$), where the intensity is the highest. We see that the excitation (blue solid line) mostly follows the Airy-like diffraction pattern of the MIR intensity (red dashed line). Deviations between the two profiles are due to the nonlinear response of the sample to the laser. The XUV profile is also shown

(black solid line) in arbitrary units, which will be used to perform the volume averaging integral, Eq. (4.13).

Equation (4.13) was numerically evaluated using a literature value of $\alpha_{10}(32 \text{ eV}) = 1713.2 \text{ cm}^{-1}$ (see Eq. (4.10)). The resulting volume averaged ΔA is plotted as a function of input pulse energy in Fig. 4.24 for a delay corresponding to after the MIR pulse has left the sample ($\tau = 120 \text{ fs}$). To illustrate the importance of the thin film interference on the predicted ΔA signal, we plot Eq. (4.13) assuming three distinct intensity profiles $I_{\text{sample}}(\tau; x, y, z)$. Note that all three profiles incorporate the same transverse diffraction pattern $I_{\text{diff}}(x, y)$ but use different interference terms $I_p(z)$. The top panel (TMM: Ge/SiN) includes interference effects of both the germanium and nitride membrane (intensity profile shown in Fig. 4.20); the middle panel (TMM: freestanding Ge) only includes interference from the germanium sample and neglects the SiN membrane (profile shown in Fig. 4.21), and the bottom panel ignores all thin film interference effects (dashed lines in Figs. 4.20 and 4.21).

There is little difference between the Ge/SiN heterostructure and freestanding results, which follows from their similar internal intensity profiles. This confirms the implicit assumption that the SiN membrane does not strongly affect the experimental results, even when taking into account nonlinear excitation. On the contrary, the simple Fresnel absorption model has a narrow intensity distribution, and as a result the intensity-dependent features (visible at 0.4, 1.1 and 2.5 μJ) persist through the volume averaging. The higher average intensity of the Fresnel absorption model results in a ΔA signal that is about 45% higher than either TMM intensity distribution.

Figure 4.25 shows the time dependence of the ΔA signal at a fixed pulse energy (2.85 μJ). This figure is qualitatively very similar to Fig. 4.16. We see the $\simeq 45\%$ difference between the interference-free Fresnel and Ge/SiN TMM intensity profiles persists for all pulse delay times τ .

4.4.7 Sample Heating

In this section, we estimate magnitude of the laser-induced long-term heating of the sample.

Using the volume-averaged Keldysh results, we can estimate the total energy gained by the germanium sample in a single laser pulse by integrating the product of the excitation rate and the effective bandgap over the interaction volume:

$$E_{\text{abs}} \simeq \sum_{i,j} \int dV \int_{-\infty}^{\infty} dt W_{i,j}(x, y, z, t) \Delta_{i,j}^{\text{eff}}(x, y, z, t), \quad (4.38)$$

with $i = \text{HH, LH, SO}$,

and $j = \text{direct, indirect}$.

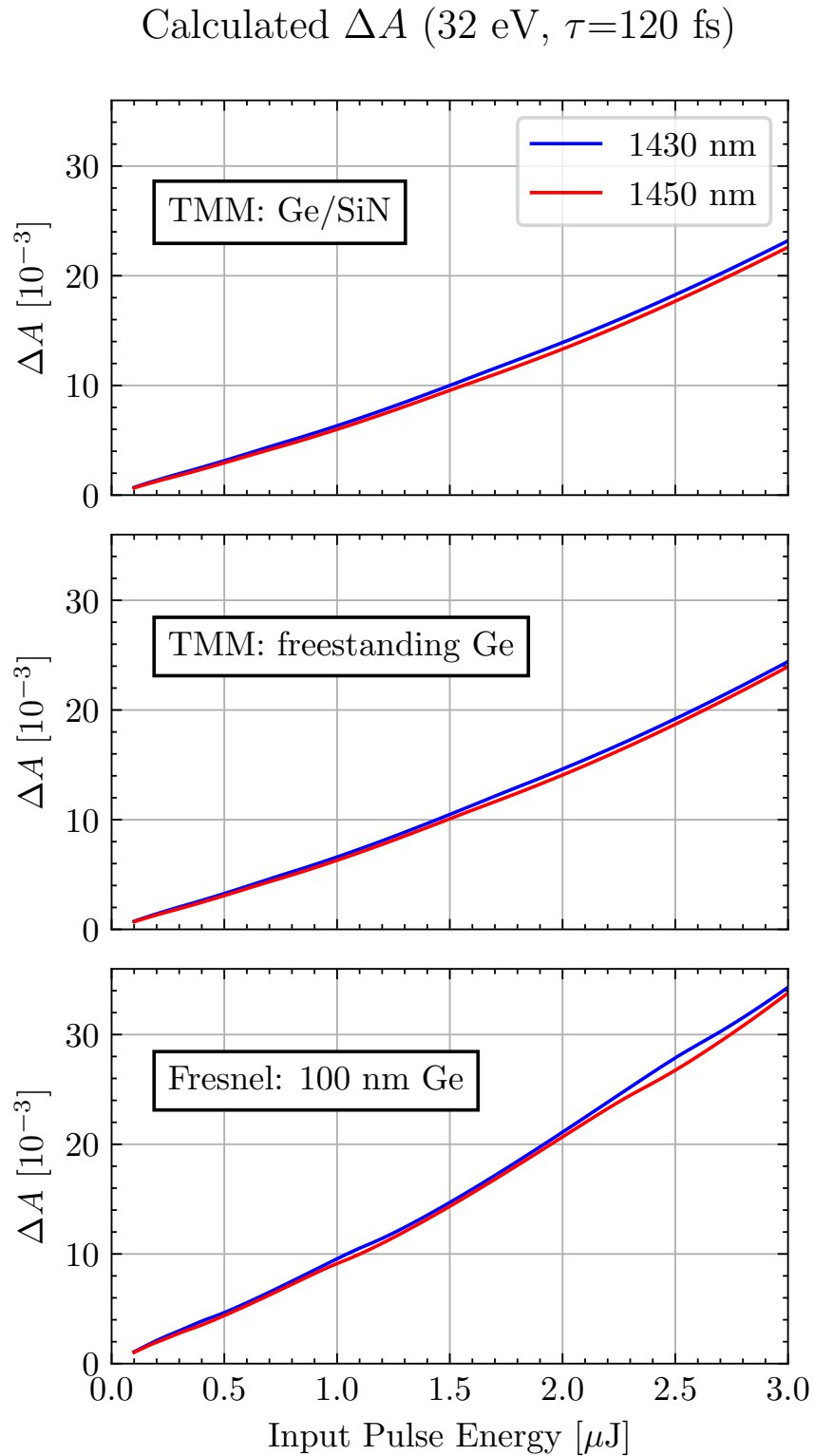


Figure 4.24: Calculated volume averaged final ΔA (Eq. (4.13)) as a function of input pulse energy. These curves were calculated using $\alpha_{10}(32 \text{ eV})$ and assuming different interference terms $I_p(z)$ (see Eq. (4.37)).

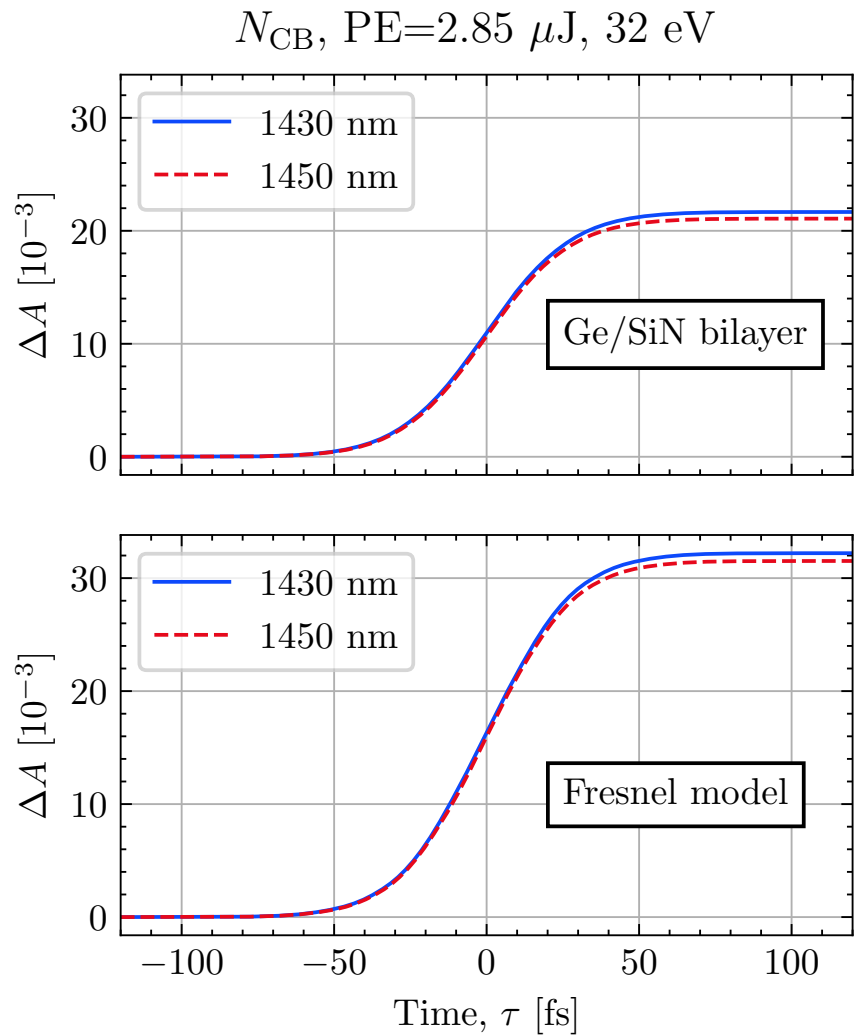


Figure 4.25: Calculated volume averaged ΔA (Eq. (4.13)) as a function of pulse delay time, τ . These curves were calculated using $\alpha_{10}(32 \text{ eV})$ and assuming different interference terms $I_p(z)$ (see Eq. (4.37)).

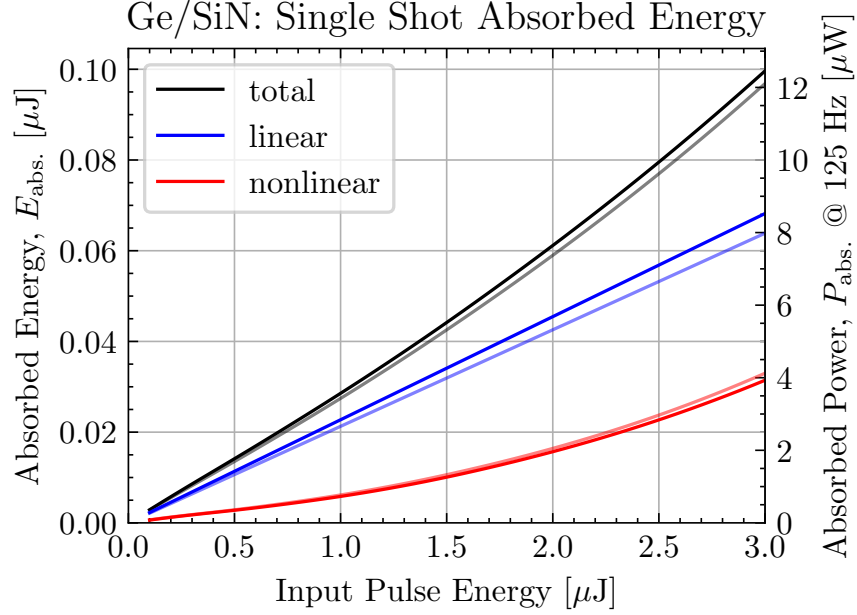


Figure 4.26: Calculated absorbed energy from a single $\tau_p = 60$ fs pulse at $\lambda = 1430$ nm (dark lines) and $\lambda = 1450$ nm (faint lines).

Here, we assume that all excited states eventually decay nonradiatively and that each electron is photoexcited to the bottom of the conduction band from the top of the valence band. The cycle-averaged absorbed power is found by multiplying by the laser repetition rate, RR :

$$P_{\text{abs.}} = E_{\text{abs.}} \times RR \quad (4.39)$$

Figure 4.26 plots the absorbed energy and average power for our experimental conditions. The total absorption is calculated using Eqs. (4.38) and (4.39), the linear contribution is calculated using the TMM-predicted effective absorption coefficient of the bilayer $A(1430 \text{ nm}) = 0.023$, and the nonlinear component is the difference between the total and the linear component. We see that the nonlinear absorption is responsible for one third of the energy transferred into the sample. For an input pulse energy of $2.75 \mu\text{J}$, only about $0.1 \mu\text{J}$ is absorbed by the sample, which corresponds to $12.5 \mu\text{W}$ at 125 Hz .

The literature reports two estimates of the steady-state thin film temperature for a free-standing Ge/SiN membrane with the same geometry as our sample [16]. In this experiment, they use a $\lambda = 760 \text{ nm}$, ≤ 5 fs pulse at a 100 Hz repetition rate and an NIR FWHM diameter of about $100 \mu\text{m}$ to excite the sample. At their interaction intensities, nonlinear effects are negligible, but the absorption coefficient ($A(760 \text{ nm}) = 0.23$) is about 10x higher than at our mid-IR wavelengths. It is reported that sample annealing occurs above 500 K , resulting in permanent sample damage and ultimately limiting the maximum input pulse energy

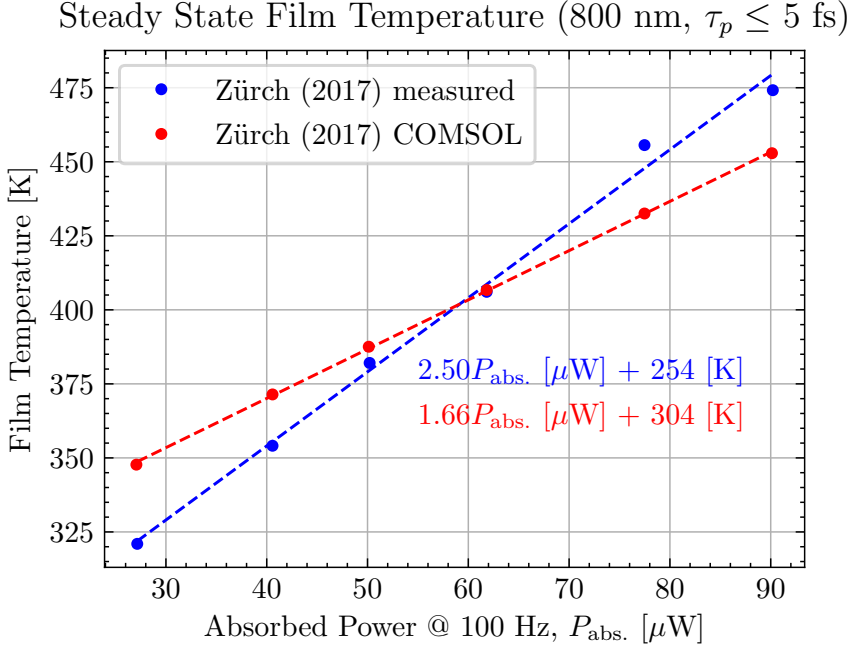


Figure 4.27: Thermal data for a 100 nm Ge/ 30 nm SiN heterostructure extracted from the literature [16].

and excitation fraction. Figure 4.27 shows these two estimates as a function of absorbed power. The first estimate of sample temperature uses a finite element numerical simulation (COMSOL) that takes into account linear absorption by the laser, three dimensional heat diffusion and radiation losses. The second method fits the temperature using the measured indirect bandgap shift to the empirical formula [161]:

$$\Delta E_{\text{ind.}} = a - \frac{\alpha T^2}{\beta + T}, \quad (4.40)$$

with $a = 0.741$ eV, $\alpha = 4.561 \times 10^{-4}$ eV K $^{-1}$, and $\beta = 210$ K. Both methods yield a linear increase in sample temperature with average absorbed power, albeit with slightly different slopes. The difference between the two estimates is ascribed to an erroneous heat conductivity value used in the COMSOL calculation.

We extrapolate the aforementioned linear fits to estimate our maximum sample temperature. For an absorbed power of $14 \mu\text{W}$, we would expect a steady state film temperature of $T = 289$ K using the CB shift estimate, and $T = 327$ K using the COMSOL estimate. Both temperatures are well below the reported annealing temperature of 500 K. Taking the higher of the two temperatures, Eq. (4.40) predicts $\Delta E_{\text{ind.}} = 0.65$ eV, which is 10 meV lower than the 0.66 eV value used in Table 4.1. We therefore conclude that we can ignore the effects of steady-state laser-induced heating on the band structure of our sample.

At first it may be surprising that the steady state temperature of two experiments operating near the laser-damage threshold in the same material would differ by nearly 150 K. However, this can be understood as a side effect of tightly focusing our MIR beam. By concentrating the MIR-induced heat to such a small volume (34 *vs.* $100\ \mu\text{m}$ spot size), the required absorbed power to reach a given excitation threshold is lower and therefore the steady-state temperature is reduced.

4.5 Experimental Results

In this section we will present the transient absorption results from a $100\ \text{nm Ge} / 30\ \text{nm SiN}$ thin film membrane sample. Section 4.5.1 presents the millisecond-scale (ms-scale) dynamics that obscure the fs & ps-scale dynamics when data is recorded at high repetition rates. Section 4.5.2 shows the need to apply frequency filter the spectral axis of our data. Section 4.5.3 goes into detail about the spectral decomposition algorithm, including the initial guess for the state blocking function. In Section 4.5.4, we develop an electronic population model and fit it to the state blocking data, and the physical implications are discussed in Section 4.5.5. Phonons are added to the population model in Section 4.5.6 to explain the observed band shift.

4.5.1 Long-Lifetime Excited States in Ge

Figure 4.28 shows a typical spectrogram for germanium at a $1\ \text{kHz}$ repetition rate. A broad, delay-independent increase in ΔA near $30\ \text{eV}$ is visible as a red horizontal band. The horizontal bands above and below this feature are a modulation of the random noise, the magnitude of which is inversely proportional to the harmonic yield. Further study suggests that this constant feature is an excited state with a millisecond-scale lifetime.

Recalling the arguments made in Section 4.2.2, negative delays correspond to dynamics from the previous laser shot, $\tau \simeq +1/RR$, which is $1\ \text{ms}$ for a $1\ \text{kHz}$ repetition rate. Following convention within the ultrafast community, these delays are often collectively referred to as $\tau = -\infty$. To investigate the nature of these signals, we average the $\tau < -50\ \text{fs}$ spectra, as shown in the left panel of Fig. 4.29 for three different pulse energies and for $RR = 1\ \text{kHz}$. The right panel of this figure plots the maximum value of $\Delta A(\tau = -\infty)$ between 29 and $31\ \text{eV}$ versus pulse energy, and we observe a linear response over this limited range. The existence of a non-zero $\Delta A(\tau = -\infty)$ contribution suggests the sample remains in an excited state from the previous laser shot. If this were true, we would expect to see the magnitude of the negative time signal decay with decreasing laser repetition rate.

Our experimental apparatus cannot directly investigate ms-scale dynamics, as our delay wedges have a range of roughly $2\ \text{ps}$. The only practical method to investigate this response is to measure the $\tau = -\infty$ response at various repetition rates. To this end, the repetition

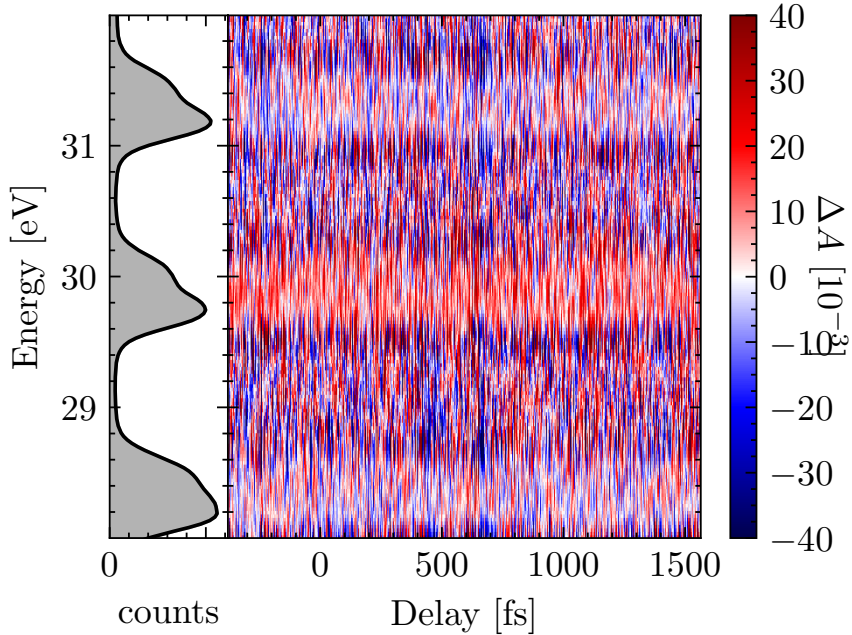


Figure 4.28: A delay-independent feature at 30 eV (red horizontal stripe) is observed in germanium for a repetition rate of 1 kHz, $\lambda = 1450$ nm and $1.75 \mu\text{J}$ pulse energy. The harmonic spectrum used for this measurement is shown in the left panel.

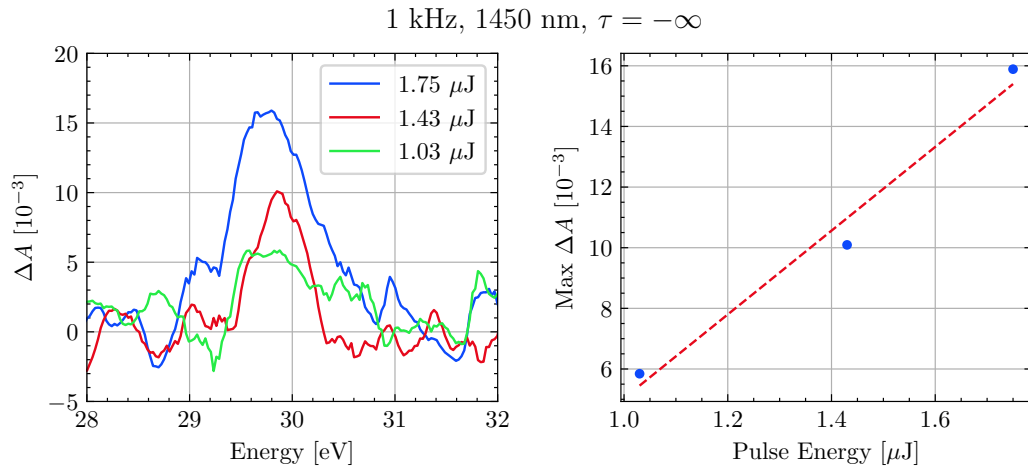


Figure 4.29: Evidence of a long-lifetime state in germanium. The left panel shows the $\Delta A(\tau = -\infty)$ lineouts for three pulse energies. A broad feature centered near 30 eV appears to scale with increasing pulse energy. The right panel plots the magnitude of the feature as a function of pulse energy, suggesting a linear scaling of the feature $\tau = -\infty$ feature.

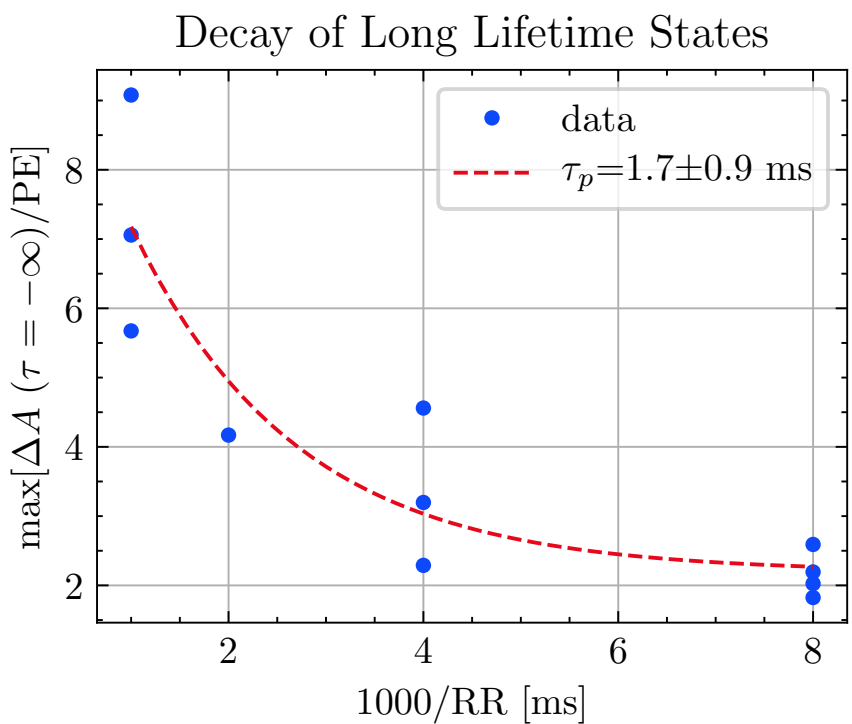


Figure 4.30: Estimating the lifetime of the negative time delay feature. The maximum sample response at $\tau = -\infty$ is normalized to the pulse energy (PE) and plotted as a function of the inverse laser repetition rate (RR). The data is fit to an exponential decay with $\tau_p = 1.7$ ms.

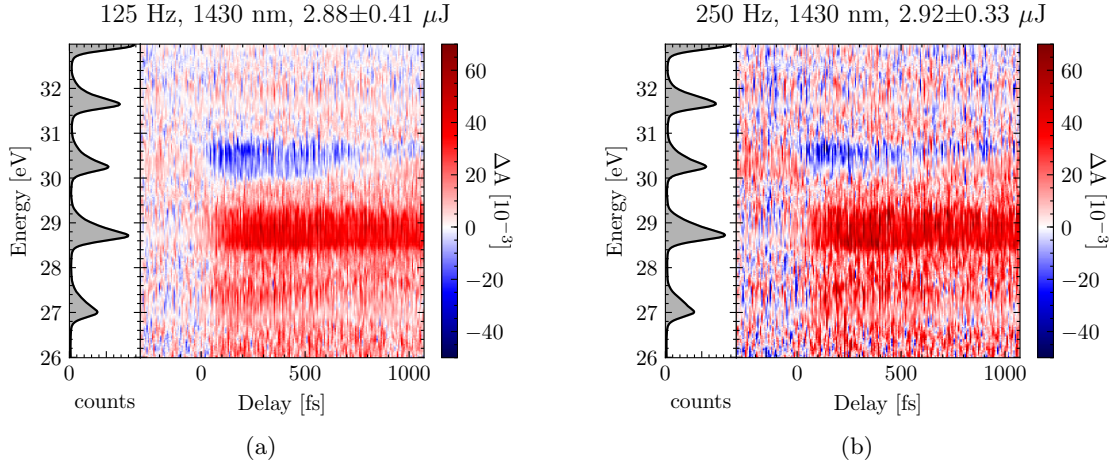


Figure 4.31: Low repetition rate ATAS measurements reveal ultrafast dynamics in germanium. Left panel: an average of 6 measurements at 125 Hz. Right panel: an average of 2 measurements at 250 Hz. Consistent with Fig. 4.30, a slight $\tau = -\infty$ contribution is present in both measurements between 30 and 31 eV, visible as a positive ΔA at negative time delays.

rate was adjusted from 1 kHz to 125 Hz in powers of two using a combination of the Spitfire’s repetition rate divider and a chopper placed immediately before the TABLE’s interferometer. Sample damage and the apparatus noise floor limited the pulse energy range, which was controlled using a HWP / polarizer. Figure 4.30 shows the maximum $\tau = -\infty$ sample response between 29 and 31 eV, normalized by the pulse energy in μJ , plotted against the time between laser shots. This normalization is justified by the linear behavior seen in Fig. 4.29. We see that the negative-delay feature decreases in amplitude with decreasing repetition rate, which is consistent with an excited state with a long lifetime on the order of 1 ms. The data is fit to an exponential decay function $y(\tau) = a \exp(-\tau/\tau_p) + y_0$, and a value of $\tau_p = 1.7 \pm 0.9$ ms is obtained.

At 500 and 1000 Hz, the millisecond lifetime excited state depletes the ground state and overwhelms the transient signal, making direct observation of faster dynamics impossible. By reducing the repetition rate, we give the sample enough time between laser shots for the ms-scale dynamics to more fully relax to the ground state between laser shots. Practically speaking, we cannot reduce the repetition rate below 100 Hz, as we are limited by the thermal stability of the laser and the time to complete the experiment. At repetition rates of 250 Hz or slower, we can begin to observe the transient fs- and ps-scale dynamics in our measurements.

The fundamental wavelength was decreased by 20 nm to 1430 nm, where the absorption length in Ge is about 5% shorter. For a fixed pulse energy, this increases the excitation

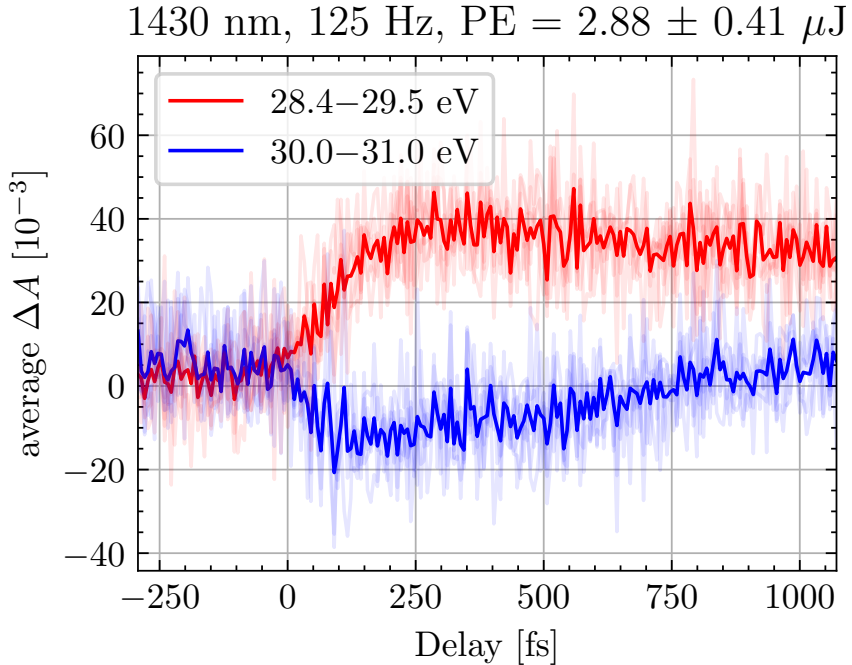


Figure 4.32: Integrated lineouts of Fig. 4.31a. Dark lines are the average of 6 measurements, faint lines show the individual measurements.

fraction and thus the strength of the ΔA signal. Using this shorter wavelength we can observe a more robust sample response, as shown in Fig. 4.31.

In this dataset, we can see a sample response from 25.7 to 31 eV. From 25.7 to 30 eV, there is a broad increase in absorption (red), with the largest increase occurring between 28.4 and 29.5 eV. A concurrent decrease in absorption (blue) occurs between 30 and 31 eV. The increase in absorption persists for at least 1100 fs, while the decrease in absorption tapers off after about 750 fs. These features are present in both the 125 and 250 Hz data. Note that the $\tau = -\infty$ feature at 30 eV negative delay persists in the 250 Hz dataset, but at 12×10^{-3} it does not overwhelm the rest of the sample response. Additional measurements were performed at either 125 Hz to suppress the static feature, or at 250 Hz to minimize data collection time.

Figure 4.32 shows the average spectral response for the 125 Hz dataset from Fig. 4.31a for two spectral regions. In the lower energy region (29.4–29.5 eV), ΔA starts at zero, rises to 40×10^{-3} over the course of about 250 fs, then slowly decays to about 30×10^{-3} over the next picosecond. In contrast, ΔA in the higher energy region (30–31 eV) has a non-zero $\tau = -\infty$ component, rapidly decays to about -15×10^{-3} in about 100 fs, then recovers to zero over the next picosecond.

In a later section we will perform spectral decomposition on this data (see Section 4.5.3),

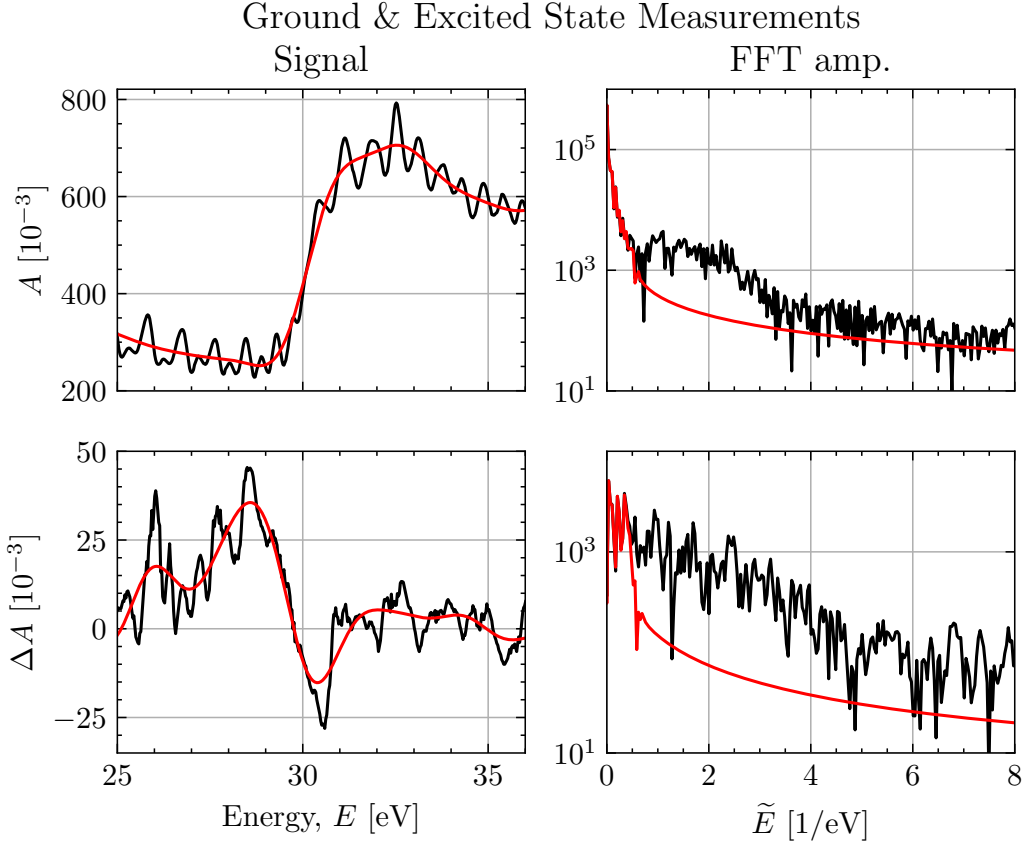


Figure 4.33: Details of the low pass filter (LPF) used for the measured ground and excited states of germanium. Black lines are interpolated data, red lines are filtered data. The same LPF (cut-off $f_L = 0.507 \text{ eV}^{-1}$, bandwidth $b_L = 0.5 \text{ eV}^{-1}$) has been applied to both datasets.

but first we must address the amplitude oscillations present along the energy axis in Figs. 4.2 and 4.31.

4.5.2 Frequency Filtering & Background Subtraction

Figure 4.33 shows the measured spectra and the Fourier amplitudes (black lines) of the ground state $A(E)$ and a typical excited state $\Delta A(E, \tau = 300 \text{ fs})$. For computational reasons, the measured spectra have been interpolated along the energy axis and resampled with constant energy spacing. This process faithfully reproduces the original dataset while facilitating numerical operations like frequency filtering. Starting with A in the top left panel, germanium's $M_{4,5}$ edge is visible as an abrupt increase in absorption near 30 eV. In the bottom left panel, we see ΔA has an asymmetric profile centered around the $M_{4,5}$ edge, with an increase in absorption below the M edge and a slight decrease in absorption above

it.

In both A and ΔA , we see small wiggles with $\simeq 0.5 - 1$ eV spacing. From our *a priori* knowledge of the ground state absorption profile, we know that A should be a slowly varying function devoid of any such oscillations [16]. We interpret the spurious features as the combination of two distinct measurement artifacts. First, slight nonlinearities of the MCP/P detector, coupled with the constant spacing of an unstable, high-contrast harmonic comb result in positive and negative contributions to the absorption on the rising and falling edges of the harmonics [53, 162]. This effect is visible throughout the A spectrum as an oscillation of magnitude $\simeq 50 \times 10^{-3}$ and spacing $\simeq 1$ eV. Secondly, the spectrometer's grating has nonzero efficiency η_m for higher order diffraction modes (see the discussion surrounding Fig. 2.30 and Eq. (2.45)) which pollutes the $m = 1$ signal with higher energy light. For example, the signal corresponding to nominally 30 eV light will have non-zero contributions from $m = 2$ (60 eV photons), $m = 3$ (90 eV) and $m = 4$ (120 eV) grating diffraction orders. Thus, the measured spectrum at a given nominal energy is a weighted contribution from all diffraction orders:

$$S_{\text{meas.}}(E) = \sum_{m=1}^{\infty} \eta_m S_{\text{XUV}}(mE) \quad (4.41)$$

The datasets in this chapter were collected using an XUV spectrum that extended at least to the aluminum L edge (72 eV), so 2nd order diffraction is present at energies below $\frac{1}{2} \times 72$ eV = 36 eV in our measured signal. This effect is most prevalent below 30 eV in the A signal as an oscillation of amplitude $\simeq 10 \times 10^{-3}$ and spacing $\simeq 0.5$ eV.

The spectral decomposition algorithm (see Section 4.5.3) is sensitive to these artifacts, so they must be removed before we can proceed. The Fourier amplitudes of A are shown in the top right panel of Fig. 4.33, and the artifacts' contributions are visible as a broad hump between 0.5 and 4 eV⁻¹. We use a low-pass filter (LPF) with a cut-off frequency $f_L = 0.507$ eV⁻¹ and a transition bandwidth $b_L = 0.5$ eV⁻¹ to remove these artifacts while preserving the underlying signal (red lines).

We expect a portion of the ΔA consists of these artifacts, albeit with higher significance given the signal's weak amplitude. Looking at the Fourier amplitudes of ΔA , we see an additional high-frequency tail that arises due to the signal being only slightly above the noise floor of the apparatus. For consistency, we must apply the same spectral filter to all datasets, and the high frequency tail of ΔA necessitates the use of a LPF rather than a band-reject filter (BRF). An unfortunate side effect of this treatment is a reduction of the effective energy resolution of the spectrometer. This problem could be mitigated in future experiments by generating a continuum of XUV light that spans less than an octave of bandwidth [16].

Figure 4.34 shows the data processing steps to prepare the data for spectral decom-

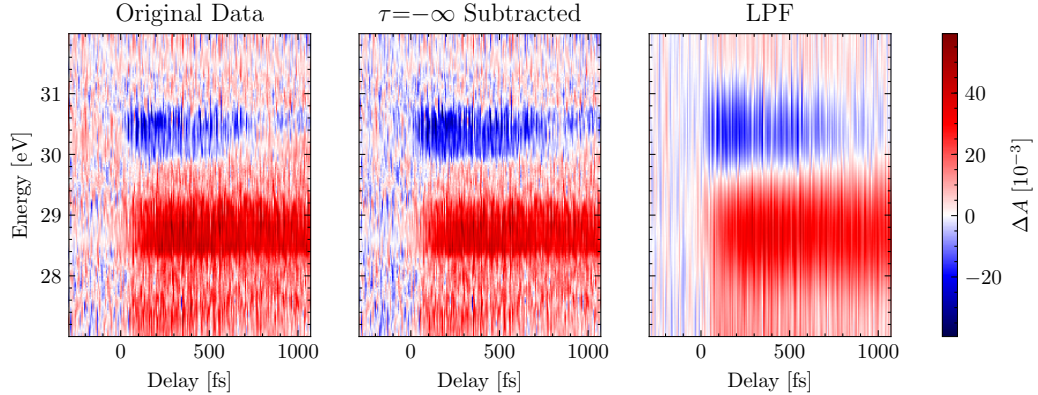


Figure 4.34: Preparing the spectrogram data ($RR = 125$ Hz, $\lambda = 1430$ nm, PE = 2.88 ± 0.41 μ J) for spectral decomposition analysis. Left panel: averaged spectrogram from $N = 6$ measurements. Middle panel: spectrogram after subtracting the average ΔA signal for $\tau < -50$ fs. Right panel: spectrogram after applying a low pass filter (LPF) along the energy axis. A common colorscale is used for all figures.

position. The left panel shows the average of $N = 6$ spectrograms taken under identical experimental conditions. In the original data, we see a slight positive ΔA signal at negative time delays between 30 and 31 eV. This response, detailed in Section 4.5.1, is assumed to be constant over the delay range of our experiment. Starting with the left panel's spectrogram, we compute the average spectral response for delays prior to $\tau = -50$ fs, which is then subtracted from the spectrogram to produce the middle panel of Fig. 4.34. A low pass filter (LPF) is then applied along the energy axis of the middle panel, which yields the right panel. No filtering is performed along the delay axis.

4.5.3 Decomposition of Spectral Response

The literature details a useful spectral decomposition algorithm, which we will briefly describe here [16]. It assumes that the ΔA measurement is the sum of three distinct features: a red shift of $A(E)$, a broadening of $A(E)$, and a state-blocking term. Physically, the red shift of the ground state can result from the presence of acoustic phonons distorting the lattice, as well as a reduced screening of the Coulomb potential due to an excited electron density. The broadening term arises from lifetime shortening of the excited state, which can be induced by electron-electron scattering, electron-phonon scattering, or field-induced effects. The state blocking term has an intuitive physical origin: an electron excited by the MIR field from the valence band to the conduction band will block, via the Pauli exclusion principle, an XUV transition from the $3d$ core states to the CB. Likewise, the hole created in the VB by the MIR-induced electronic excitation will open up a new allowed XUV-induced transition from the $3d$ core states to the VB. Thus, state blocking results

in increased (decreased) absorption at energies corresponding to the valence (conduction) band.

Computationally, the red shift and broadening terms are determined by performing operations on the measured $A(E)$, and it is assumed that the state blocking component makes up the remainder of the observed signal. The magnitude of these contributions are computed by iteratively fitting the data for a given time delay τ and for all energies E by minimizing the function ϵ_n :

$$\epsilon_n = \left| \Delta A_{\text{meas}}(E, \tau) - \Delta A_{\text{broad},n}(E, \sigma(\tau)) - \Delta A_{\text{shift},n}(E, \Delta E_{\text{shift}}(\tau)) - \Delta A_{\text{SB},n-1}(E, \tau) \right| \quad (4.42)$$

where n denotes the iteration step number ranging from 1 to N . Following the procedure introduced in Reference [16], we seed the algorithm with an initial guess for the state blocking term. The functional form of the initial guess is guided by our understanding of the initial excited electron and hole distribution in the sample.

The Keldysh simulation gives us excitation rates $W_{i,j}(t)$, but not the final energies. We assume that the electrons are excited with an energy equal to the effective bandgap at the time of excitation $\Delta_{i,j}^{\text{eff}}(t)$ as predicted by Eqs. (4.22) and (4.25). Here, $i = \text{HH, LH, SO}$ is the electron's initial band and $j = \text{direct, indirect}$ denotes the transition type. Furthermore, we assume that the initial and final states are energetically centered around the Fermi energy²⁹, $E_F = 29.2$ eV [16]. Then, the energy separation between a $3d$ core state and either the excited electrons (in the CB) or holes (in the VB) is given by:

$$\begin{aligned} 3d_{3/2} : \quad B_{i,j}(t) &= E_F + \frac{1}{2}f\Delta_{i,j}^{\text{eff}}(t) + E_{SO} \\ 3d_{5/2} : \quad B_{i,j}(t) &= E_F + \frac{1}{2}f\Delta_{i,j}^{\text{eff}}(t) \end{aligned} \quad (4.43)$$

where f is $+1$ for electrons in the CB and -1 for holes in the VB, and $E_{SO} = 0.58$ eV is the energy splitting between the two core states. In other words, the function $B_{i,j}(t)$ tells us the photon energy at which state blocking features will emerge in our experiment.

From Eq. (4.10), we expect the state blocking signal at a given photon energy E and delay τ to be proportional to the corresponding transient electron (and hole) populations $\Delta N(E, \tau)$:

$$\Delta A_{\text{SB}}(E, \tau) \propto \Delta N(E, \tau) \quad (4.44)$$

Consider the laser-induced change to the transient electron (and hole) population at time

²⁹Note that this experimentally convenient convention assigns the energy of the $3d_{5/2}$ orbital be to zero, while $3d_{3/2}$ has energy $-E_{SO}$.

$t \in [t, t + dt]$ and with photon energy E :

$$\delta_t \Delta N(E, t) = \sum_{i,j} f W_{i,j}(E, t) \delta(E - B_{i,j}(E, t)), \quad (4.45)$$

where δ is the Dirac δ -function and we have neglected decay channels for the purposes of this discussion. Then, the transient electronic density at delay τ will be the integrated excitation rate:

$$\Delta N(E, \tau) = \int_{-\infty}^{\tau} dt \sum_{i,j} f W_{i,j}(E, t) \delta(\epsilon - B_{i,j}(E, t)) \quad (4.46)$$

Note that Eq. (4.44) does not include the degeneracy of the core states, which is 4 for $3d_{3/2}$ and 6 for $3d_{5/2}$. Since the value of $B_{i,j}$ depends on the core state, we must weight the contributions of each state accordingly. Additionally, our detector has finite energy resolution, dE , so the initial guess for the state blocking function will have the form:

$$\begin{aligned} (\text{single intensity}) \quad \Delta A_{\text{SB},0}(E, \tau; I) \propto & \int_E^{E+dE} d\epsilon \int_{-\infty}^{\tau} dt \sum_{i,j} f W_{i,j}(\epsilon, t) \times \\ & \left[6\delta(\epsilon - B_{i,j}^{3d_{5/2}}(\epsilon, t)) + 4\delta(\epsilon - B_{i,j}^{3d_{3/2}}(\epsilon, t)) \right] \end{aligned} \quad (4.47)$$

The single intensity expression is plotted in Fig. 4.35 for a peak intensity of 640 GW/cm². We see that above (below) 29.5 eV, the state blocking signal is negative (positive), representing the presence of transient electrons (holes) in the conduction (valence) band. Along the energy axis, we see four main “bands”. Bands of the same sign are displaced copies of another, which reflects the fact that the $3d$ core states separated by E_{SO} both contribute to the signal. Each band has six “sub-bands”, which follows from the six possible values of $B_{i,j}(t)$ at any time (= 3 initial VB states \times 2 excitation channels). The central energy and width of each main band evolves in time as the effective bandgaps are distorted by the laser field. The amplitude of the bands grows with delay as the laser field grows in strength. Recall there is no decay mechanism in this model, and we assume an instantaneous response to the laser.

Note that the effective bandgap $\Delta_{i,j}^{\text{eff}}$ and excitation rate $W_{i,j}$ both depend on the instantaneous laser intensity, which has a strong spatial dependence within the sample. Therefore, we must perform the volume averaging integral on the single intensity result:

$$(\text{volume averaged}) \quad \Delta A_{\text{SB},0}(E, \tau) = -\log_{10} \left(\frac{\iint dx dy I_{\text{XUV}}(x, y) 10^{-\Delta A_z(x, y)}}{\iint dx dy I_{\text{XUV}}(x, y)} \right), \quad (4.48)$$

where $\Delta A_z(x, y)$ is the depth-integrated state blocking signal:

$$\Delta A_z(x, y) \equiv \alpha_{10} \int_0^L \Delta A_{\text{SB},0}(E, \tau; I(x, y, z)) dz. \quad (4.49)$$

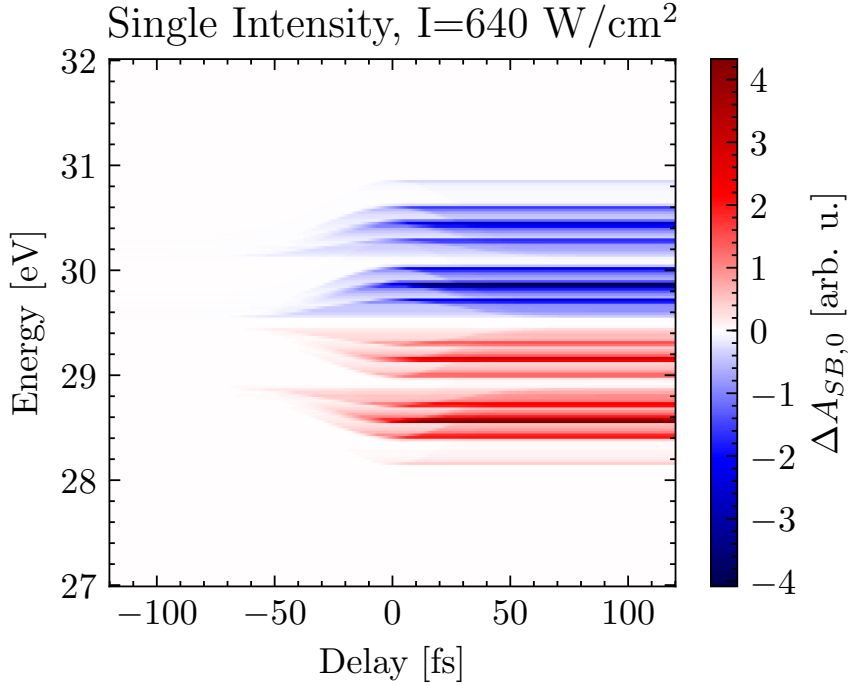


Figure 4.35: Single-intensity state blocking signal for a peak intensity of 640 GW/cm² ($\lambda = 1430$ nm), from Eq. (4.47).

The volume averaged expression is plotted in Fig. 4.36 for a pulse energy of 2.85 μ J. Compared to the single-intensity calculation, we can see that the sub-bands have been washed out, but the overall structure remains the same. This is a consequence of having a wide distribution of intensities, with each intensity depositing electrons (holes) at different final energies. When performing the spectral decomposition algorithm, Eq. (4.48) is scaled in amplitude to match the experimental data.

As an aside, the derived expressions are similar in form to that reported in the literature [16], which we present below for comparison:

$$\begin{aligned}
 \text{(linear abs.) } \Delta A_{\text{SB},0} \propto & \left(-6 \exp \left\{ - \left[\left(E - E_F - \frac{E_c}{2} \right) / \Delta E_{\text{BW}} \right]^2 \right\} \right. \\
 & - 4 \exp \left\{ - \left[\left(E - E_F - \frac{E_c}{2} - \Delta E_{\text{SO}} \right) / \Delta E_{\text{BW}} \right]^2 \right\} \\
 & + 6 \exp \left\{ - \left[\left(E - E_F + \frac{E_c}{2} \right) / \Delta E_{\text{BW}} \right]^2 \right\} \\
 & \left. + 4 \exp \left\{ - \left[\left(E - E_F + \frac{E_c}{2} - \Delta E_{\text{SO}} \right) / \Delta E_{\text{BW}} \right]^2 \right\} \right), \tag{4.50}
 \end{aligned}$$

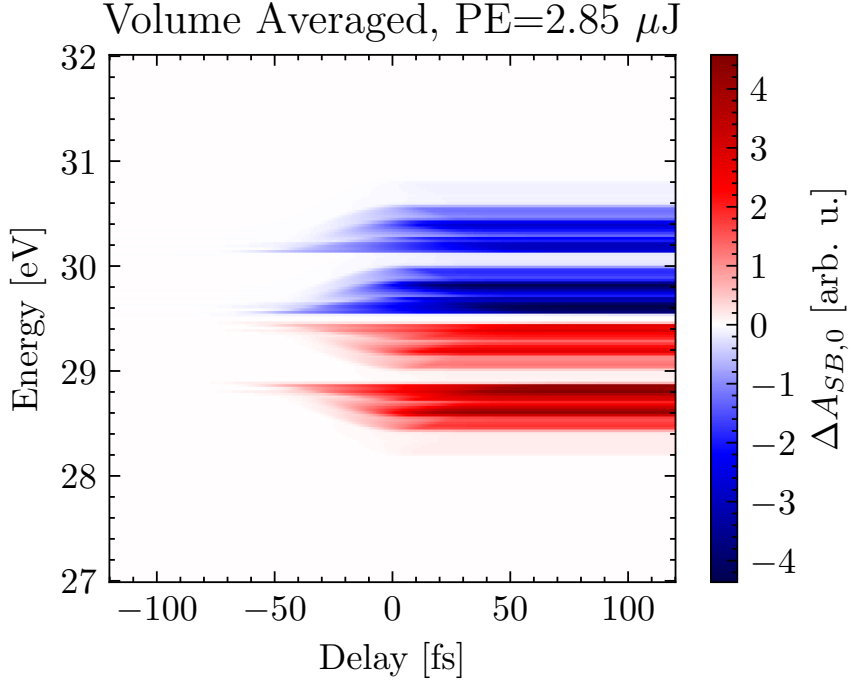


Figure 4.36: Volume-averaged state blocking signal for a pulse energy of $2.85 \mu\text{J}$ ($\lambda = 1430 \text{ nm}$) from Eq. (4.48).

where E_{BW} and E_c are the bandwidth and central photon energy of the exciting laser, respectively. Intuitively, Eq. (4.50) has four ($= 2 \times 2$) terms because there are two core states and a single expectation value for the energy of the excited electrons and holes.

The broadening term, $\Delta A_{\text{broad},n}$ is calculated by convoluting the measured ground state with a normalized³⁰ lineshape function, F :

$$\Delta A_{\text{broad},n}(E, \sigma(\tau)) = (A \star F)(E, \sigma(\tau)) - A(E), \quad (4.51)$$

where σ is the FWHM of a F . The lineshape function can have either a Gaussian (G) or Lorentzian (L) profile:

$$\begin{aligned} G(\epsilon, \sigma) &= \frac{2}{\sigma} \sqrt{\frac{\ln 2}{\pi}} \exp \left[-4 \ln 2 \left(\frac{\epsilon}{\sigma} \right)^2 \right] \\ L(\epsilon, \sigma) &= \left(\frac{2}{\pi \sigma} \right) \frac{1}{1 + 4 (\epsilon/\sigma)^2} \end{aligned} \quad (4.52)$$

The red shift contribution, $\Delta A_{\text{shift},n}$, is calculated by shifting the measured absorption

³⁰The \star operator in Eq. (4.51) denotes a convolution: $(A \star F)(E, \sigma) \equiv \int_{-\infty}^{\infty} A(\epsilon)F(E - \epsilon, \sigma) d\epsilon$. The lineshape function is normalized so that $\int_{-\infty}^{\infty} F dE = 1$. Using the properties of convolution, $\int_{-\infty}^{\infty} (A \star F) dE = \int_{-\infty}^{\infty} A dE$ and therefore $\int_{-\infty}^{\infty} \Delta A_{\text{broad}} dE = 0$.

Shifting & Broadening the Ground State

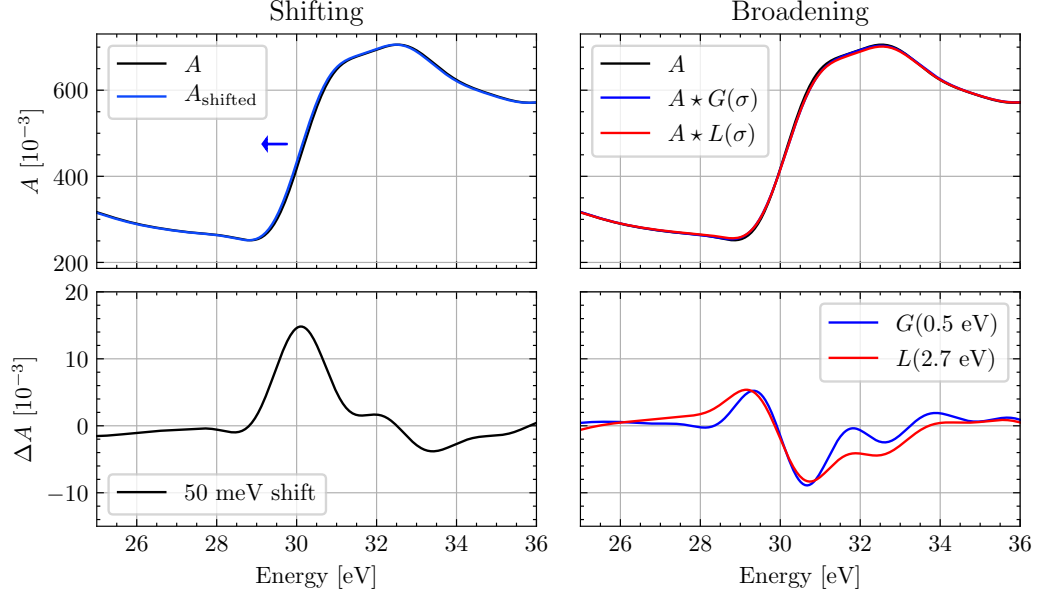


Figure 4.37: Illustrating the effects of numerically shifting and broadening the ground state absorption spectrum using Eqs. (4.51) and (4.53). Left panels: a band shift of 50 meV yields a ΔA_{shift} profile peaked at about 15×10^{-3} . Right panels: A Gaussian (Lorentzian) broadening of 0.5 eV (2.7 eV) yields a ΔA_{broad} profile with a magnitude of about 7×10^{-3} .

profile A by ΔE in the energy basis:

$$\Delta A_{\text{shift},n}(E, \Delta E(\tau)) = A(E - \Delta E(\tau)) - A(E). \quad (4.53)$$

The effects of the shifting and broadening operations are illustrated in Fig. 4.37. A positive energy shift will lead to a positive ΔA_{shift} centered at the inflection point of A , and a broadening of A results in a symmetric profile centered about the same point. We can see that ΔA_{shift} is proportional to dA/dE , and ΔA_{broad} is proportional to $d^2 A/dE^2$. It is for this reason that we employ a frequency filter on A and ΔA_{meas} , as was shown in Fig. 4.33. Additionally, these two terms enjoy a high degree of mutual orthogonality³¹ which ensures the fit is numerically stable.

After the initialization, the state blocking contribution is calculated as the weighted difference between the observed signal and the broadening & red-shifting terms:

$$\begin{aligned} \Delta A_{\text{SB},n}(E, \tau) &= \frac{2}{3} \Delta A_{\text{SB},n-1}(E, \tau) \\ &+ \frac{1}{3} [\Delta A_{\text{meas.}}(E, \tau) - \Delta A_{\text{broad},n}(E, \sigma(\tau)) - \Delta A_{\text{shift},n}(E, \Delta E(\tau))] \end{aligned} \quad (4.54)$$

³¹Orthogonal in the sense that $\int \Delta A_{\text{shift}} \Delta A_{\text{broad}} dE \approx 0$.

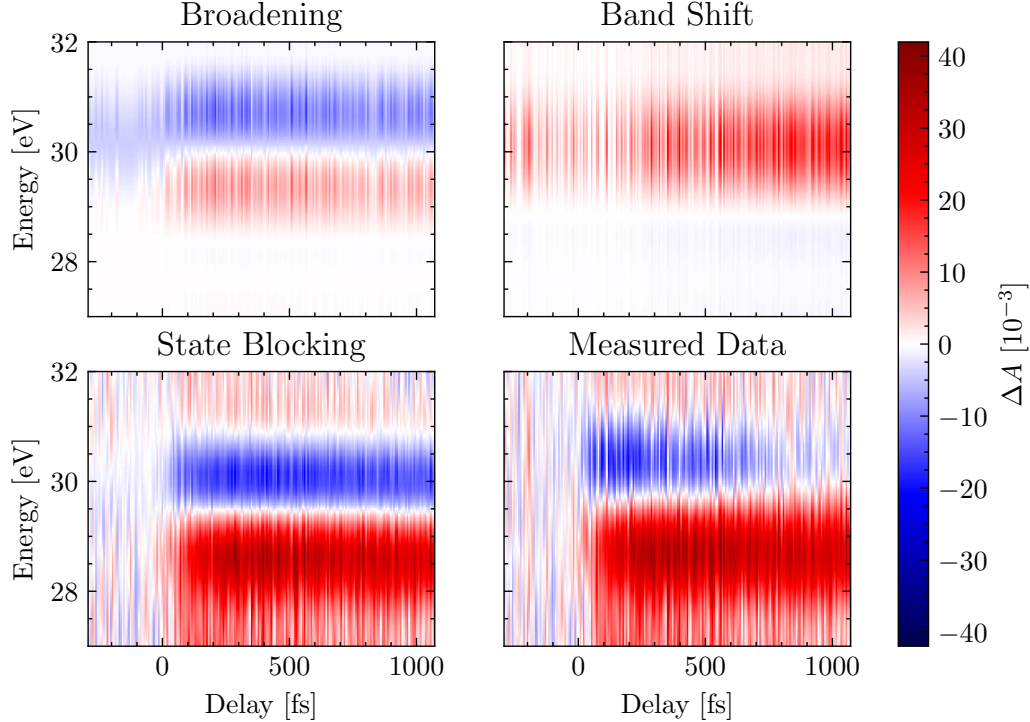


Figure 4.38: Spectral decomposition of the filtered data using a Gaussian broadening function. The contributions of broadening, band shifting, state blocking are compared to the filtered measured dataset.

The algorithm is run for $N = 5$ iterations over the energy range 27.5 to 34.0 eV. The components $\Delta A_{\text{broad}}(E, \tau)$, $\Delta A_{\text{shift}}(E, \tau)$ and $\Delta A_{\text{SB}}(E, \tau)$ are shown in Fig. 4.38. The delay-dependent parameters $\sigma(\tau)$ and $\Delta E(\tau)$, as well as the integrated state blocking signal are shown in Fig. 4.39.

It has been reported that when germanium is excited by a < 5 fs, 800 nm pulse, that the broadening term was negligible [16]. However, our decomposition shows a strong broadening component of roughly 10×10^{-3} . Looking at Fig. 4.38, we can see this corresponds to a Gaussian broadening of 0.6 eV, and a Lorentzian broadening of roughly five times that value. These numbers are not to be believed. From the uncertainty principle ($\Delta t \Delta E \sim \hbar/2$), we would expect a broadening of 1 eV to correspond to about 0.33 fs. Thus, a 0.6 eV broadening is unphysical considering that our MIR pulse duration is an order of magnitude longer than the study which found no substantial broadening. We can understand this error as a side effect of our low pass frequency filter. As was shown in Fig. 4.37, the amplitude of ΔA_{broad} depends on the sharpness of A , which was considerably softened by the LPF.

The decomposition algorithm was run again by setting σ to zero, and the results are shown in Figs. 4.40 and 4.41. Turning our attention to Fig. 4.40, we see that the band shift

Spectral Decomposition vs. Delay

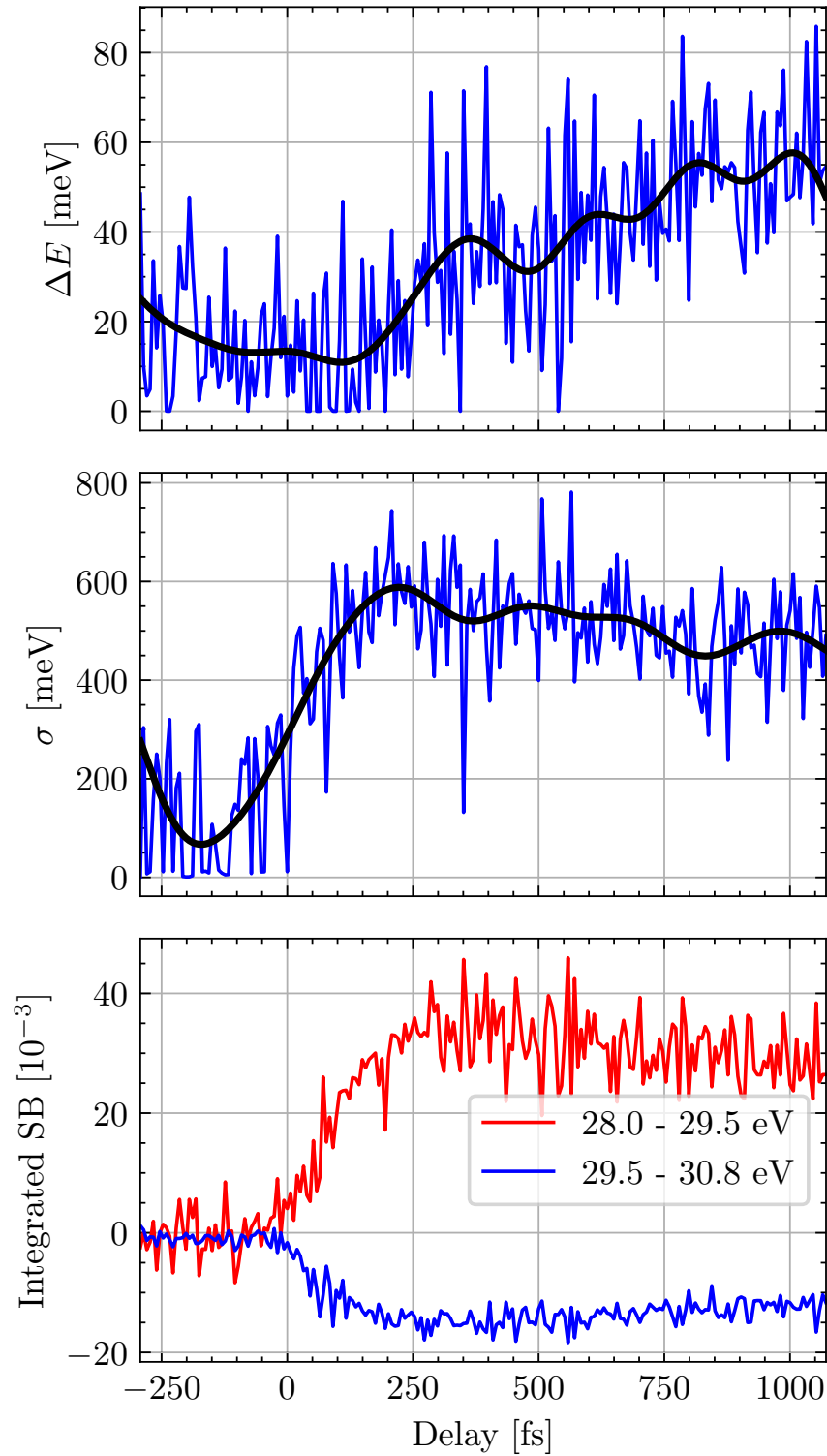


Figure 4.39: Time dependence of the spectral decomposition results. The black lines in the broadening and shifting plots are guides for the eye.

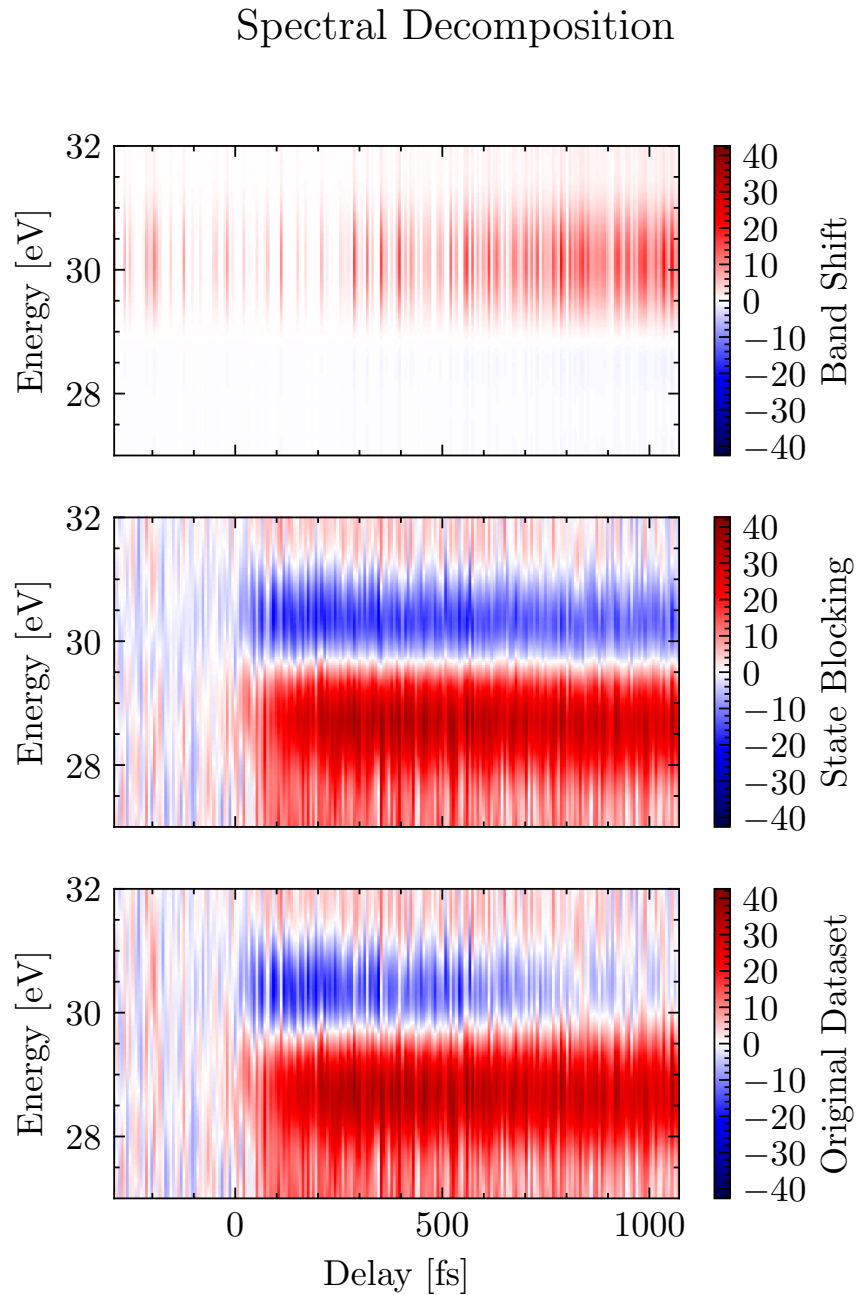


Figure 4.40: Spectral decomposition of the filtered data without broadening ($\sigma = 0$). The contributions of band shifting and state blocking are compared to the filtered measured dataset.

Spectral Decomposition

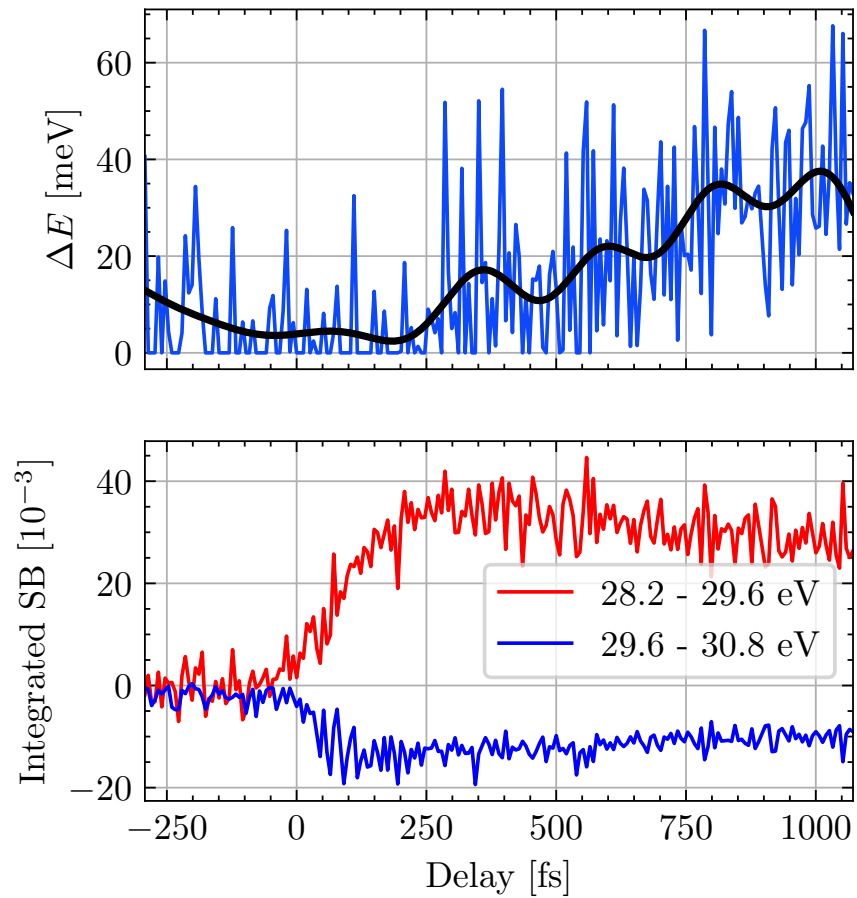


Figure 4.41: Delay-dependent parameters from the $\sigma = 0$ decomposition result in Fig. 4.40. The black line in the top panel is a guide for the eye.

component is responsible for the apparent shift in the zero-crossing of ΔA with respect to delay. The magnitude of the state blocking and band shift components are similar to what has been seen with a 5 fs, 780 nm excitation [16]. In Fig. 4.41, we see that the state blocking signal rises in amplitude from $\tau \sim 0$ fs before reaching a maximum at $\tau \sim 250$ fs and then slowly decaying. The band shift component $\Delta E(\tau)$ is within the noise floor until about $\tau \sim 250$ fs, after which it rises linearly over the next 825 fs. In the next section, we will develop a population model that explains this observed temporal evolution.

4.5.4 State Blocking Population Model

We can deduce the carrier dynamics from the temporal evolution of the state blocking signal. Notably, the observed rise of the state blocking amplitude occurs on a much slower timescale than would be expected from the Keldysh excitation simulation. Figure 4.42 shows the normalized excitation rate W for different initial bands and excitation channels as a function of peak intensity and delay. For each intensity, we fit the time dependence to a Gaussian of the form $W(\tau) = W_0 e^{\tau^2/2\tau_W^2}$ and extract an *effective excitation duration*, τ_W . The fit parameter τ_W is plotted for each band and transition in Fig. 4.43. We can see that although there is some variation in the effective pulse duration, it never exceeds 40 fs regardless of the initial band, transition channel or intensity. Furthermore, if we perform a volume-averaged excitation rate calculation for an input pulse energy of 2.85 μJ , we obtain an effective excitation duration of $\tau_W = 22.6$ fs.

As a thought experiment, let us assume the laser populates an excited state $a(t)$ directly from the ground state and there is no decay mechanism: g.s. $\xrightarrow{W} a$. For the purposes of this discussion, a is the electron (or hole) population density of a conduction (or valence) band. Then, the population density of the excited state is governed by the rate equation:

$$a'(t) = W(t), \quad (4.55)$$

If we assume the Keldysh excitation rate W is the aforementioned Gaussian function, the solution to Eq. (4.55) is:

$$a(\tau) = \int_{-\infty}^{\tau} W(t) dt \propto \operatorname{erf}\left(\frac{\tau}{\sqrt{2}\tau_W}\right). \quad (4.56)$$

Thus, in the absence of recombination, a single excited state population model predicts that the excited state population would reach 97.5% of its maximum value roughly $2.77\tau_W$ after it rises 2.5% above its initial value. Introducing a decay channel (i.e., replacing $W(t)$ with $W(t) - a(t)/\tau_a$ in Eq. (4.55)) reduces the rise time even further. From Fig. 4.43, we can see that the longest rise time predicted by the Keldysh simulation would correspond to roughly $2.77 \times 40 = 110$ fs, and the volume averaged result predicts a rise time of 63 fs. Both of these options are far lower than our observed rise time of 250 fs, indicating that a single

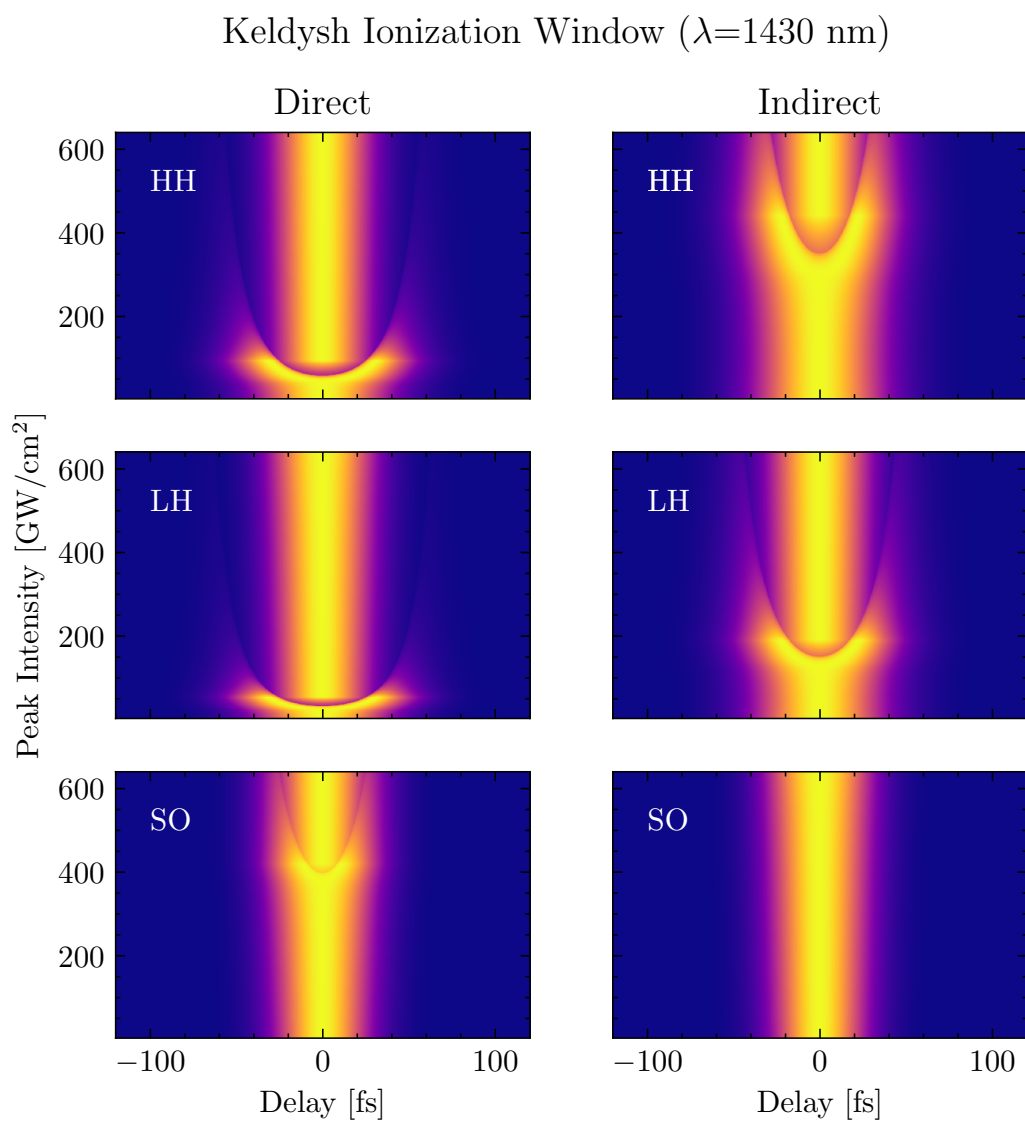


Figure 4.42: Initial state- and channel-resolved Keldysh excitation rate. The rate has been normalized for each intensity to showcase the intensity dependence of the excitation duration. Brighter colors correspond to a higher excitation rate.

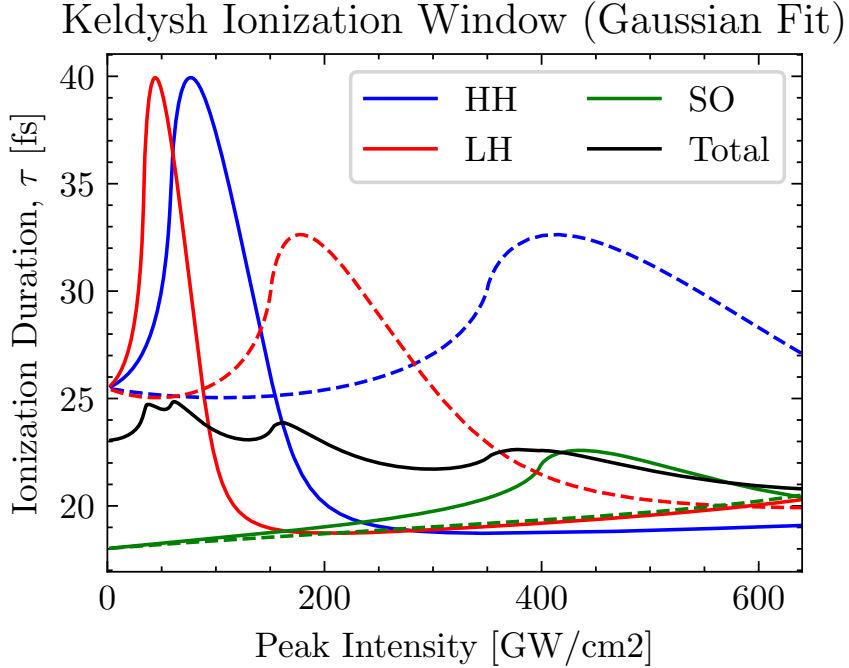


Figure 4.43: Initial band- and channel-resolved Keldysh excitation rate for $\lambda=1430$ nm. Solid (dashed) lines are direct (indirect) transitions. The total excitation rate includes all bands and transitions.

excited state is insufficient to explain the observed dynamics.

Next, consider a cascaded two-state model with decay pathways for each excited state (g.s. $\xrightarrow{W} a \xrightarrow{\tau_a} b \xrightarrow{\tau_b}$ g.s.):

$$\begin{aligned} a'_i(t) &= W(t) - \frac{a_i(t)}{\tau_{a,i}}, \\ b'_i(t) &= \frac{a_i(t)}{\tau_{a,i}} - \frac{b_i(t)}{\tau_{b,i}}, \end{aligned} \tag{4.57}$$

where the subscript $i = e, h$ refers to the electron or hole contribution. Here, the laser populates the initial state a , which decays to state b , which in turn decays to the ground state. The lifetimes of states a and b are τ_a and τ_b , respectively. At this point, we have not specified the physical meaning of either state, nor their decay mechanisms. The solution to

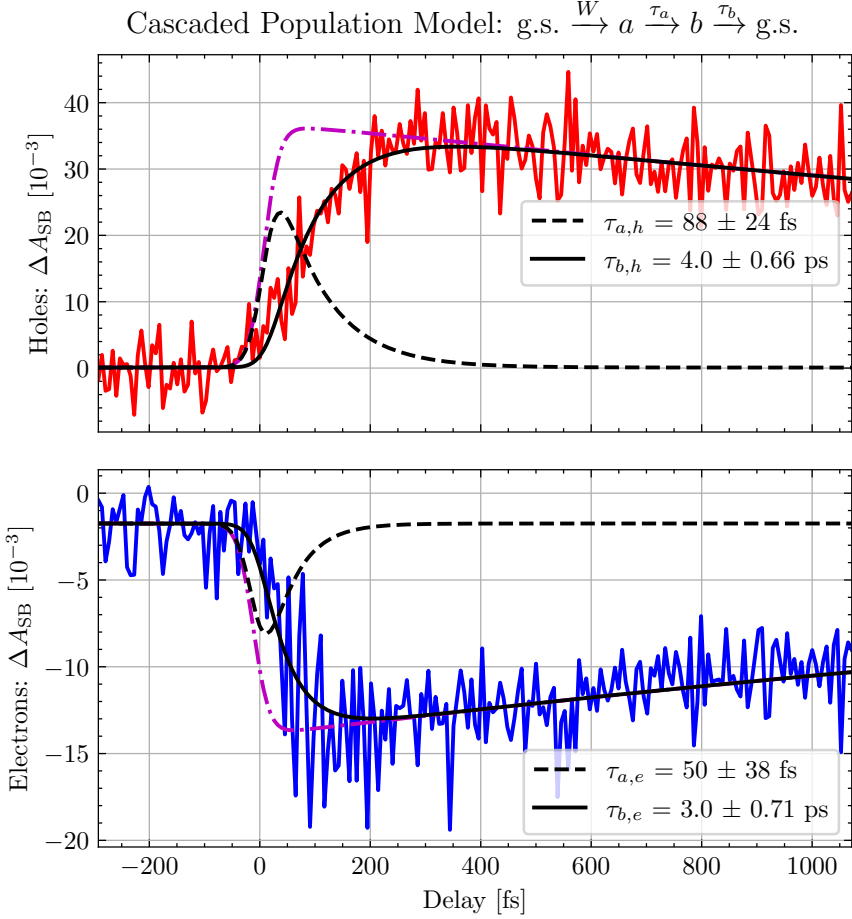


Figure 4.44: State $b(\tau)$ of Eq. (4.58) (solid black line) is fit to the integrated state blocking signal $\Delta A_{\text{SB}}(\tau)$ for holes (red) and electrons (blue). The dashed line shows state $a(\tau)$, and the magenta dashdot line shows the total excited population $a(\tau) + b(\tau)$. Lifetimes τ_a and τ_b are extracted from the fit.

this system of differential equations is:

$$\begin{aligned}
 a_i(\tau) &= e^{-\tau/\tau_{a,i}} \int_{-\infty}^{\tau} e^{t/\tau_{a,i}} W(t) dt, \\
 b_i(\tau) &= \left(\frac{\tau_{b,i}}{\tau_{b,i} - \tau_{a,i}} \right) e^{-\tau \left(\frac{1}{\tau_{a,i}} + \frac{1}{\tau_{b,i}} \right)} \left[\left(e^{\tau/\tau_{a,i}} - e^{\tau/\tau_{b,i}} \right) \int_{-\infty}^{\tau} e^{t/\tau_{a,i}} W(t) dt \right. \\
 &\quad \left. + e^{\tau/\tau_{a,i}} \int_{-\infty}^{\tau} \left(e^{t/\tau_{b,i}} - e^{t/\tau_{a,i}} \right) W(t) dt \right].
 \end{aligned} \tag{4.58}$$

State $a(\tau)$ experiences an immediate population increase in response to the laser excitation rate $W(\tau)$, followed by a decay. State $b(\tau)$, which is populated only by the decay of state $a(\tau)$, has a delayed rise time followed by a decay to the ground state. The latter

behavior matches our observation, so we fit $b(\tau)$ to the state blocking signals shown in Fig. 4.41. For the excitation rate $W(\tau)$, we use the total (including all channels and transitions) volume-averaged Keldysh rate for a pulse energy of $2.85 \mu\text{J}$. The results are shown in Fig. 4.44. For the holes, we see the initial state a has a lifetime $\tau_{a,h} = 88 \pm 24 \text{ fs}$ and the secondary state b has a lifetime of $\tau_{b,h} = 4.0 \pm 0.66 \text{ ps}$. For the electrons, the initial state has a slightly shorter lifetime of $\tau_{a,e} = 50 \pm 38 \text{ fs}$ followed by a secondary state lifetime of $\tau_{b,e} = 3.0 \pm 0.71 \text{ ps}$.

4.5.5 Discussion of Carrier Dynamics

We now turn to the physical interpretation of states a and b , starting with the holes. The valence band has a relatively simple band structure consisting of the heavy hole (HH), light hole (LH) and split-off (SO) bands. Band structure calculations in the literature indicate that the SO band has mostly $4s$ orbital character, while the HH and LH bands are primarily $4p$ [16]. As a reminder, the ΔA_{SB} hole signal originates from linear XUV-induced core-to-VB electronic transitions. Due to the dipole selection rules, the transition $3d \rightarrow 4s$ is forbidden, while $3d \rightarrow 4p$ is allowed. Thus, we would expect reduced detection sensitivity to holes in the SO band, while retaining visibility of hole populations in the HH and LH bands. We therefore associate the initial state a with the SO band, and b with the HH and/or LH bands. Our observations implies that the excitation rate from the HH and LH bands is significantly overestimated by the Keldysh simulation, which may follow from the $4p$ orbital character of these bands and the mostly $4s$ character of the Γ & L valleys in the CB [50]. Consequently, most excitation occurs from the lower-lying SO band.

Our measured time constants for the holes are in good agreement with the literature. In a similar experiment [16], Zürich reports a SO \rightarrow HH lifetime of $140 \pm 10 \text{ fs}$ and an electron-LH recombination lifetime of $1080 \pm 90 \text{ fs}$. Since we are using significantly different laser conditions, we would expect to be ionizing from a different part of the SO band, and to a different part of the CB, which can explain the different intravalley scattering time constant. Our electron-hole recombination time is significantly longer at $\tau_{b,h} = 4.0 \pm 0.66 \text{ ps}$, but this is not surprising since this timescale is strongly affected by grain boundary effects, which will be sample-dependent. The intravalley process SO \rightarrow LH is mediated by optical phonons, which later decay anharmonically to two acoustic phonons [50]. We will come back to the model shortly, but first we will discuss the electron component of the state blocking signal.

Germanium's conduction band has a rich structure (see Fig. 4.11), but our Keldysh simulation only considers excitation pathways to the two lowest lying CB valleys: a direct transition to the Γ valley, and an indirect transition to the L valley; excitation to the higher-lying X valley is not considered. We consider the orbital character of these bands when assigning them to our nominal states a and b . It is reported that the L and Γ valleys are mainly $4s$, and the X valley is mostly $4p$ [16, 50]. Therefore, we conclude that state a

represents a linear combination of Γ and L valley population densities, and likewise state b is the X valley population density. Due to the aggressive frequency filtering, we lack the spectral resolution to differentiate between Γ and L bands. Therefore, the measured lifetime $\tau_{a,e} = 50 \pm 38$ fs corresponds to the weighted average of inverse optical phonon scattering rates of $\Gamma \rightarrow X$ and $L \rightarrow X$. These timescales are consistent with the experimentally reported value by Kaplan [50]. According to calculations by Bailey & Stanton, the 50 fs timescale suggests that the initial electron energy is ~ 0.5 eV above the band minimum [163].

We now turn our attention to the physical origin of the longer timescale $\tau_{b,e} = 3.0 \pm 0.71$ ps. There are many physical processes that can cause such an observation, including the reduction of the excited electron population density via electron-hole recombination, population transfer into unobservable state, or diffusion of the excited electrons outside of the detection region. Diffusion can play an important role in reflectivity measurements where the detection volume is defined by the area of the XUV beam (diameter ~ 50 μm) and the skin depth (~ 10 nm). Since diffusion involves the slow process of mass transport, the largest contribution comes from electrons moving away from the surface rather than parallel to the surface. In contrast, our absorption measurement samples the entire thickness of the sample, so we are only sensitive to diffusion in the transverse direction. Therefore, we would expect the diffusion contribution to be three orders of magnitude smaller in a transmission geometry. Kaplan predicts a 10 ps lifetime for diffusion processes in their reflectivity experiment, suggesting that this effect is completely negligible in our transmission geometry.

Zürch observed a 1140 ± 50 fs electron signal decay lifetime and speculated that it was due to a trap-assisted electron-hole recombination process, which is expected to be dominant in defect-rich samples. On the other hand, Kaplan reported a 3.2 ± 0.2 ps electron signal lifetime, but assigned it to a $X \rightarrow L$ population transfer mediated by optical phonons. This assignment was bolstered by their observation that the central energy of the state blocking signal shifted by ~ 10 meV over a ~ 5 ps timescale. Unfortunately, our experiment has neither the temporal extent nor the spectral resolution to make this observation, but (as will be discussed below) we see evidence of this phonon population in the band shift component of our experimental data. Consequently, we assign our electron decay signal to the intervalley scattering process $X \rightarrow L$ with a lifetime of $\tau_{b,e} = 3.0 \pm 0.71$ ps, which is in perfect agreement with the previously reported figure.

4.5.6 Including Phonons

Now that we have a physical picture of the electron dynamics, we can revisit the assumptions that lead to Eqs. (4.57) and (4.58). The analysis suggests that optical phonons are created when the holes scatter from state SO to HH/LH (corresponding to $a_h \rightarrow b_h$), when electrons

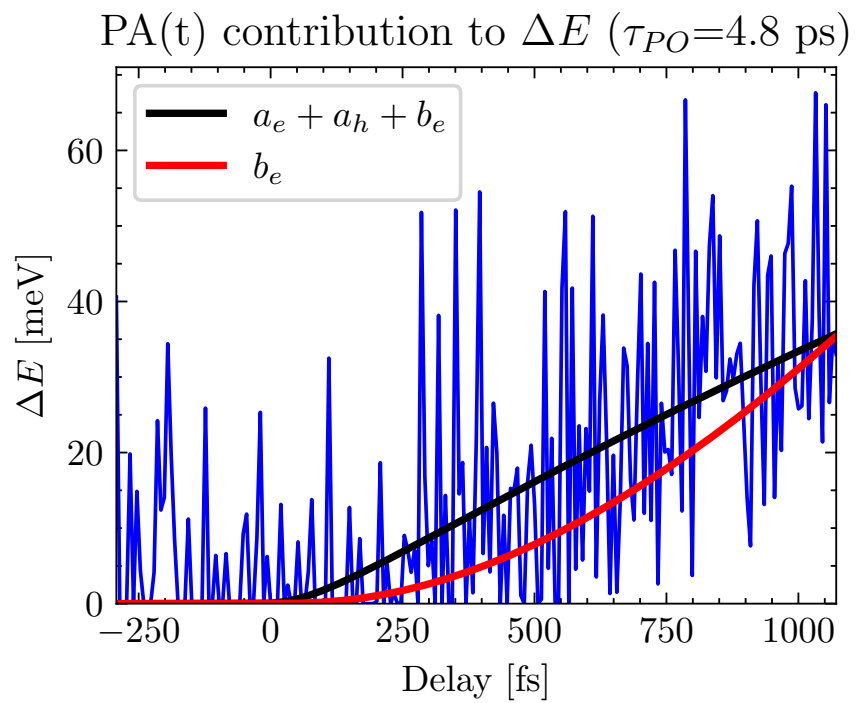


Figure 4.45: Comparison of the extracted band shift ΔE from Fig. 4.41 (blue) to the predicted acoustic phonon population density $PA(t)$ of Eq. (4.59). The black curve is $PA(t)$ when a_e , a_h and b_e are included as source terms in Eq. (4.59); the red curve is $PA(t)$ when b_e is the only source term. $PA(t)$ is plotted in arbitrary units.

scatter via $\Gamma \rightarrow X$ & $L \rightarrow X$ (both corresponding to $a_e \rightarrow b_e$), and also $X \rightarrow L$ (decay of b_e). It is reported that optical phonons in germanium decay anharmonically into two acoustic phonons which distort the bandgap [50]. We now add these populations to the model:

$$\begin{aligned} a'_i(t) &= W(t) - \frac{a_i(t)}{\tau_{a,i}}, \\ b'_i(t) &= \frac{a_i(t)}{\tau_{a,i}} - \frac{b_i(t)}{\tau_{b,i}}, \\ PO'(t) &= \left(\frac{a_e(t)}{\tau_{a,e}} + \frac{a_h(t)}{\tau_{a,h}} \right) + \frac{b_e(t)}{\tau_{b,e}} - \frac{PO(t)}{\tau_{PO}}, \\ PA'(t) &= 2 \frac{PO(t)}{\tau_{PO}} - \frac{PA(t)}{\tau_{PA}}, \end{aligned} \quad (4.59)$$

where the subscript $i = e, h$ again refers to the electron or hole contribution and PO (PA) is the optical (acoustic) phonon population density with lifetime τ_{PO} (τ_{PA}). We omit the analytical solution for $PA(t)$ and $PO(t)$, as the expressions are quite messy and not particularly illuminating.

The analytical solution of $PA(t)$ is shown in Fig. 4.45. In this figure, we compare the time evolution of $PA(t)$ to that of the extracted band shift, $\Delta E(t)$. We set $\tau_{PA} = \infty$ and use the electronic lifetimes $\tau_{a,e}$, $\tau_{a,h}$ and $\tau_{b,e}$ from the ΔA_{SB} signal fit (see Fig. 4.44). For the optical phonon lifetime, we use the literature value of $\tau_{PO} = 4.8$ ps [50]. In black, we show the solution of $PA(t)$ from Eq. (4.59), which has three source terms. We can see that when states a_e , a_h and b_e contribute to PA , the acoustic population density rises at $\tau \sim 100$ fs, which corresponds to the lifetimes of the shortest lived states (a_i). Removing the contribution of the a_i states (red curve) delays the rise of the PA to about $\tau \sim 250$ fs, which is shortly after state b_e reaches maximum population. Note that the acoustic phonon population density is plotted in arbitrary units, as the data is too noisy to be fit. Unfortunately, the data is too noisy to draw any conclusions about which model best describes the acoustic phonon population.

4.6 Summary

In this chapter, we developed experimental techniques for transient absorption in condensed matter systems using ultrafast MIR (1430 nm) wavelengths, an experimental first. These techniques were then applied to study electron and phonon dynamics in germanium thin films. In our experiment, the MIR wavelength induced electron dynamics via a mixture of tunnel ionization ($\gamma < 1$) and single-photon excitation. Our simulations suggest that most excitation is nonlinear, with $\gamma \leq 1$ suggesting that the dominant excitation pathway is tunneling. This is notably different from previous work in germanium that reported $\simeq 90\%$

single-photon ionization and $\gamma > 4$. Expressions were derived to relate the detection sensitivity to the relative MIR & XUV beam sizes and to account for misalignment of the two beams. The MIR intensity within the sample was simulated using a combination of diffraction and interference techniques. The linear & nonlinear electronic excitation of germanium was simulated using a nonlinear Keldysh model. The measured signal was spectrally decomposed into state blocking and band shift components using an existing numerical technique. A simple electronic population density model was fit to the state blocking data, and from this we deduced information about the MIR-induced electron and phonon dynamics. Holes were observed to be created in the split-off (SO) bands and scattered via optical phonons to the heavy hole (HH) and light hole (LH) bands within 88 ± 24 fs before undergoing recombination on a 4.0 ± 0.66 ps timescale. Additionally, we observe a suppressed excitation rate from the higher lying HH and LH valence bands when compared to the Keldysh prediction. This difference is attributed to low transition matrix elements between the states, which is not included in the Keldysh model. Electrons were excited to both the Γ and L bands, and scattered to the X valley within 50 ± 38 fs, before scattering back to the L valley within 3.0 ± 0.71 ps. The population model was modified to include the creation of optical phonons and anharmonic decay into acoustic phonons. The time evolution of the acoustic phonon population density compares favorably to the observed time evolution of the band shift component, which is suggestive of an acoustic phonon-mediated band gap renormalization process. Looking forward, future efforts should be focused on creating an XUV continuum using MIR light sources, which would mitigate most of the systematic sources of noise in our experiment. Additionally, picosecond delay stages should be implemented to directly study phonon dynamics, which make significant contributions to the measured ΔA signal.

Chapter 5

CONCLUSIONS

In this thesis, we laid the groundwork for performing attosecond transient absorption spectroscopy (ATAS) measurements in the condensed phase using mid-infrared (MIR) lasers. We designed, built and tested an attosecond transient absorption beamline (TABLE) and a two-dimensional XUV spectrometer. The vacuum system was designed to accept different detector endstations, much like a user facility. The pump arm of the TABLE was designed to be outside the vacuum system so that nonlinear optics or other systems can be inserted into the beam path, which broadens the potential phase space of future studies. A high pressure cell (HPC) was designed and demonstrated to be nearly two orders of magnitude brighter than existing XUV sources in the DiMauro lab. This technical achievement partially counteracts the low quantum efficiency and difficult phase matching conditions of HHG at longer wavelengths. Finally, this equipment was demonstrated in a prototypical ATAS experiment in a technologically important indirect bandgap semiconductor (germanium) using a $\lambda = 1430$ nm wavelength ultrafast excitation pulse. With a Keldysh parameter on the order of 1, the ionization channel is closer to the tunneling regime compared to previous reports in the literature. We observed electron and phonon dynamics in germanium that are consistent with what is reported in the literature. Our limited energy resolution, which is an artifact of our harmonic comb and detector nonlinearities, prevented us from resolving the energy dependence of the dynamics on the femtosecond timescale.

Future efforts should concentrate on making an XUV continuum and exciting the sample with longer wavelengths. An isolated attosecond pulse (IAP) would increase both spectral and temporal resolution. Increasing the pump wavelength would further reduce the Keldysh parameter γ , changing the nature of the initial ionization. For example, a below-bandgap 2 μm excitation would result in $\gamma \simeq 0.25$ while simultaneously suppressing single-photon ionization.

Appendix A

GUIDELINES FOR USING THE TABLE

A.1 TABLE / OMRON Pump-down Procedure

Special thanks to Andrew Piper for coding and wiring the OMRON safety system. Below is an operational guideline to pump the system down to UHV using the OMRON system. Please see Andrew Piper's OMRON manual for additional details on the microcontroller system.

This procedure assumes that the chambers are initially at atmospheric pressure, the rough pumps are turned on, and the solenoid shutoff valves on the roughing line are closed.

1. Seal and isolate all chambers. Close the manual valves between each turbo pump and the solenoid shutoff valves. Reattach any blow-off flanges (KF25 blanks) that may have come off from the previous venting cycle.
2. (Optional) As a test, ensure the OMRON's safety system is engaged by attempting to open one of the pneumatic gate valves via the control panel. **Caution: operating a gate valve between two chambers with a pressure differential can cause catastrophic system failure. Only perform this step after you have verified that all chambers are at atmospheric pressure.** If the gate valve opens while both chambers are above the upper setpoint, then the OMRON safety system is disabled. If the OMRON fails this test, check the status of the override switch.
3. Retract the metal filters from the beam path to protect them from potential pressure surges.
4. Initiate the pump-down sequence by pressing the OK button on the OMRON. This will open all solenoid valves simultaneously with a loud *thunk*.
5. Slowly open the manual valves while monitoring the gas load on the rough pumps. Use the two remote pressure monitoring systems (Raspberry Pis) to monitor the inlet pressure for each blower system. As a rule of thumb, try to keep the inlet pressure

below \sim 100 Torr during this step. **Warning: quickly opening the manual valves at atmosphere will result in pump oil being expelled into the rough pump's exhaust line. Continuing to run in this condition can lead to the overheating and eventual seizure of the rough pumps [65].**

6. Once the manual valves are fully open on all chambers, you can turn each blower system ON to accelerate the remaining pump-down procedure.
7. Power on the turbo power supplies and switch the turbos to ON. After a few seconds, the magnetically levitated turbos will start levitating with a soft *thunk*.
8. Each turbo will automatically start spinning when its chamber reaches the upper set point (\sim 200 mTorr). The turbos will take a few minutes to reach their final speed.
9. Wait for the system to pump down. It typically takes 15-45 minutes for the entire system to reach 10^{-6} Torr.
10. The pneumatic gate valves for adjacent chambers will be enabled when both chambers are below their lower setpoint pressure (about 5×10^{-6} Torr). Once all chambers are below their lower setpoints, the OMRON considers the system is to be fully pumped down.

Experiments can be performed in this state. When running the gas valve in the target chamber, it is advised to turn on the secondary blower to reduce the chamber pressure.

When experiments are not being performed in the apparatus, the system should be left in an idle UHV state with the blowers off, the chambers armed, and the gate valves separating the chambers closed. To arm the chambers press ESC + [chamber number] on the OMRON interface. The OMRON's display will update to show which chambers are armed (G: generation & differential pump chambers, M: mirror chamber, T: target chamber, S: photon spectrometer chamber).

A.2 TABLe / OMRON Venting Procedure

The OMRON system was designed with the ability to vent any single chamber or combination of chambers while keeping the rest of the system at UHV. This is not always possible, now that the mirror, target & spectrometer chambers share a single blower system and exhaust line. Any chambers that share a common exhaust line must be vented simultaneously or else you risk putting unnecessary mechanical stress on the remaining powered turbopumps. For example, the mirror, target & spectrometer chambers share a common exhaust line, and attempting to vent the one chamber while keeping the other turbos running will cause a turbopump error.

The following venting procedure assumes an initial condition of all chambers pumped down to UHV with the turbos running:

1. Turn off all gas sources. If the HPC is installed, follow the HPC shutdown procedure.
2. Turn off the blowers.
3. Block the laser into the interferometer.
4. Close the pneumatic gate valves separating the chambers.
5. Disarm the chambers by pressing ESC + [chamber number].
6. Verify the OMRON's safety system is not disabled by checking the bypass switch.
7. Enable the venting valves by switching ON the vent & purge controls on the control panel. Note: the chambers will not vent without this step.
8. Remove the KF clamps on the blow-off valves.
9. Start the OMRON venting script by pressing ALT + [chamber number] on the OMRON.
10. The user can now walk away from the system. It will take a few hours to vent.

Once initiated, the venting script will immediately stop the turbopumps' motors, open the solenoid venting valves after 30 seconds, close the roughing line's solenoid valves after 30 minutes, and close the solenoid venting valves after about 5 hours. The preceding timeline was chosen following the manufacturer's recommendation, and to avoid closing the roughing line's valves before the turbos had completely stopped spinning.

A.3 The High Pressure Cell (HPC)

A.3.1 Introduction

This section will discuss the initial setup and day-to-day operational details of the HPC. For the HHG & pressure performance of the HPC, see Section [3.2.4](#).

Figure [A.1](#) is a picture of the exterior of the generation chamber, showing the ancillary vacuum hardware associated with the HPC. A small oil-lubricated RV pump (not shown) provides differential pumping to the interior of the HPC. An inline Baratron diaphragm pressure sensor (effective range: 1 – 760 Torr) tracks the interior pressure of the edge-welded bellows. A manual gate valve is used to isolate the HPC from the RV pump when the additional pumping is not needed. Right angle KF fittings were used to route the HPC's vacuum line above the pump arm of the interferometer. The optics associated with the interferometer can be seen below this hardware on the optical table.

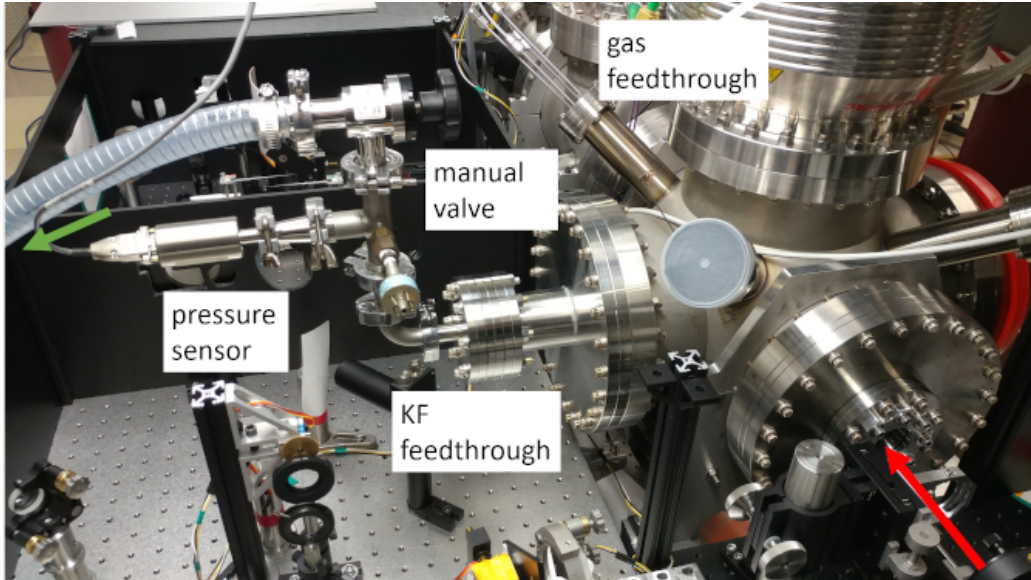


Figure A.1: Exterior view of the generation chamber with the HPC installed showing the ancillary vacuum hardware. Red arrow indicates input laser path; green arrow points towards the HPC's RV pump.

A.3.2 Initial Installation and Alignment

First, a note about laser safety. As with all initial alignment procedures, the lowest possible laser power should be used to minimize both accidental laser drilling of the HPC components and the danger posed by stray light and back reflections. The surface most likely to cause laser scatter is the front face of the outer pipe, which is roughened stainless steel located about 3/8" before the focus. The material's roughness and the negative radius of curvature of the incoming light make it unlikely that incident light will coherently focus to a point upon reflection. However, it is possible that the sidewall of the outer pipe's aperture could act as a focusing mirror. Additionally, the hose clamp or mounting bracket could coherently reflect light towards the user. The user is advised to strictly follow all laser safety protocols during this alignment procedure. Whenever possible, direct observation of the laser beam on the surfaces of the HPC should be avoided, instead a remote sensor (webcam) should be used to view the interior of the generation chamber.

The initial installation of the HPC can be time consuming and tedious, but once installed it will retain its alignment indefinitely (weeks or months). As with a free expansion gas jet, fine adjustments to the pointing should be done on a daily basis. However, these adjustments will usually take less than 5 minutes.

Optically, the HPC cell consists of four pinhole apertures (diametrically opposed pinholes on both the inner and outer pipes) with the laser focus near the center of the inner pipe.

The optical transmission of the HPC is therefore very sensitive to the relative alignment of these components, as well as the pointing of the laser into the HPC. To simplify the alignment, the two innermost holes are laser drilled *in-situ* after the outer pipe's apertures have been aligned. To maintain the relative alignment of the inner & outer apertures, the user should refrain from adjusting the inner pipe after the initial alignment is completed. Therefore, daily alignment of the HPC consists of moving all four apertures together via the in-vacuum motorized XYZ stages.

The first step of the HPC installation is installing the rough vacuum feedthrough flange. The TABLE's generation chamber uses a custom flange (a 4.5" CF blank with a KF16 half nipple welded to the air-side and a KF16 bulkhead groove & tapped holes machined into the vacuum side). To accommodate the length of the in-vacuum bellows, we use a custom 10" CF to 4.5" CF reducing nipple (OAL = 4.25"), which acts as a spacer between the feedthrough flange and the KF16 flange on the HPC. Although it was absent from the original design, a spacer 4.5" CF flange (thickness = 0.68") between the feedthrough and the reducing full nipple is used to relax the compression in the bellows and allow for a larger range of motion. For convenience, the user should install the edge-welded bellows to the bulkhead flange before installing the flange on the chamber.

The supporting bracket for the HPC was designed to be interchangeable with the free gas nozzle's bracket. See Fig. A.2 for details. This design allows the user to change the gas source type (HPC, LPC, or free expansion jet) without disturbing the alignment of the XYZ stage to the optical axis. For completeness, we will assume that the XYZ stage has been misaligned or removed from the chamber. First, the user should align the laser to the interferometer so that the laser path in the generation chamber can be used as a reference. Then, the stage should be positioned in the chamber so that the focus is roughly in the center of the stage's motion. Next, the stage's k-direction should made parallel to the optic axis. This can be done by tracking the position of the laser on a card mounted to the stage while moving the stage upstream and downstream of the focus. After clamping the stage to the breadboard, check that the alignment is still true before continuing to the next step.

Now that the XYZ stage is aligned to the laser, we will install the outer pipe of the HPC and align its apertures to the laser. We do so by maximizing the light transmission through the apertures. This is best done in two steps: first, coarse alignment is done visually at low power (insufficiently intense to laser drill the pipe), followed by fine adjustments using a power meter at moderate intensities (above the noise floor of the power meter). Note that drilling out the outer pipe's apertures will lessen the alignment requirements at the expense of the HPC's differential pumping performance. Given the chamber's small internal dimensions, it is not practical to place a power meter in the generation chamber after the focus during the alignment procedure. Rather, it is preferable to divert the beam out of the vacuum system using the linear actuator & silver mirror assembly located approximately 85

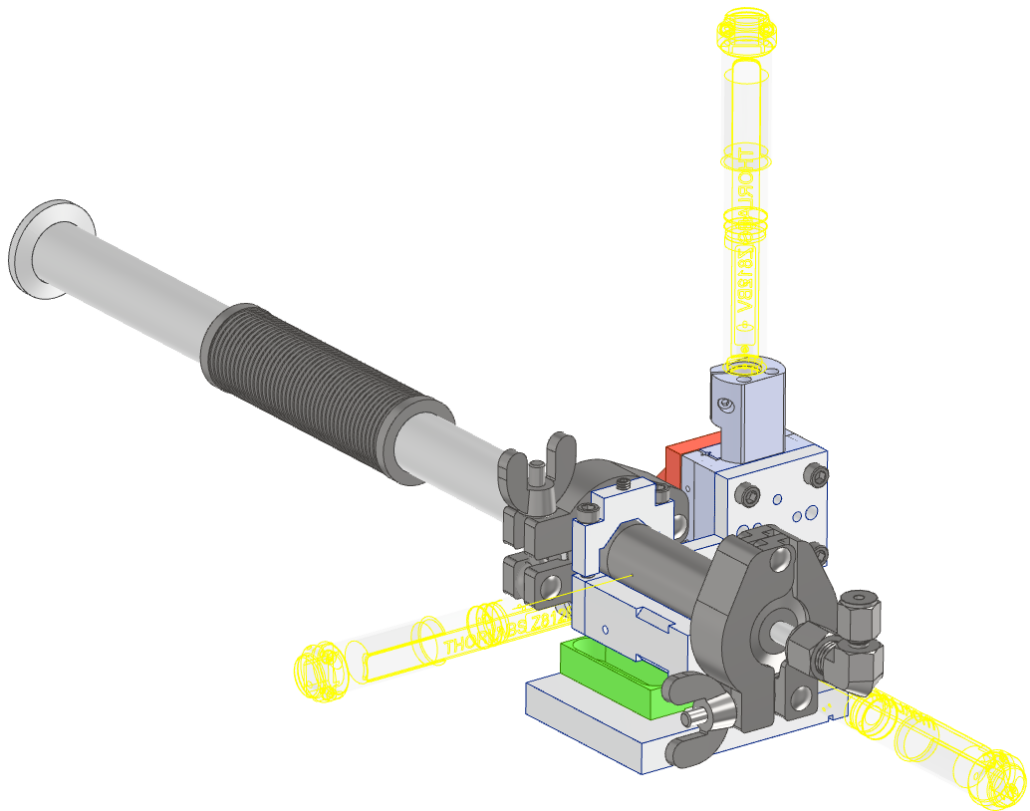


Figure A.2: The HPC with bracket installed on the XYZ translation stage, configured for the generation chamber. The hose clamp and gas supply tube are omitted from this drawing for clarity.

cm downstream of the focus.³² When inserted, the linear actuator intersects the beam path and redirects the beam out of the vacuum system through a window onto the upper deck of the optical table. Note that for most generation focusing conditions, the large beam size at the diverting mirror makes this beam path lossy. To accurately calculate the transmission through the HPC, it is necessary to measure the power immediately after the HPC in the generation chamber.

For the coarse alignment, the input beam intensity should be reduced using an upstream iris, to the point that it is barely visible near the focus. Since a tightened KF connection prevents rotation of the components, the alignment of the outer pipe is done prior to making any KF connections. However, the KF clamps should be fitted on either end of the pipe to ensure that there is enough room to make the connections without disturbing the alignment once finished. The outer pipe should be placed in its cradle, with the aluminum & hose clamps made snug around the pipe but not taut.³³ Transmission should be optimized by iteratively tuning the following parameters: (1) rotation of the pipe in the cradle, (2) height of the cradle using the vertical motor, and (3) horizontal (transverse) position of the assembly using both the horizontal motor and the position of the pipe in the cradle. For fine adjustment, the iris should be adjusted so that the power meter reads about 20–30 mW when measured after the linear actuator.³⁴ The clamps should be tightened so that movement of the pipe is possible, but difficult. The area around the power meter should be covered to prevent air currents from affecting the measurement. The transmitted power should be optimized using the same procedure as before.

Once the outer pipe is aligned, tighten all connections and connect the bellows to the outer pipe. Check that the alignment has not been changed by torquing these connections. Verify that the unattenuated laser beam can pass through the outer pipe without interference, as shown in Fig. A.3.

Next we install the inner pipe. First, attach the gas delivery feedthrough flange onto the HPC assembly without the inner pipe. Being mindful to not disturb the alignment of the outer pipe, check that the gas delivery tubing does not interfere with the laser path. Remove the gas delivery feedthrough flange, cut the inner pipe to length (OAL = 1.75”), and make the Swagelok connection between the inner pipe and the KF feedthrough. Make sure the inner pipe is normal to the flange’s sealing surface, otherwise the laser will skim the sidewall of the inner pipe rather than go through the center. If this happens, the laser-gas interaction length will be reduced and the HHG performance of the system will suffer. Install the gas delivery assembly onto the HPC assembly by tightening the KF clamp.

³²Special thanks to Eric Moore for designing and installing this optomechanical component.

³³The HPC’s XYZ assembly and bracket were designed for the TABLE generation chamber. If it is being installed elsewhere, the user should verify that the height is correct. When installed correctly, the bottom of the Z-motor range should correspond to the HPC lowered completely out of the way of the laser; the top of the range should correspond to the laser going through the center of the HPC, with about 1 mm to spare.

³⁴This power is appropriate for a 1 kHz repetition rate and a generation focal length of 30 or 40 cm.

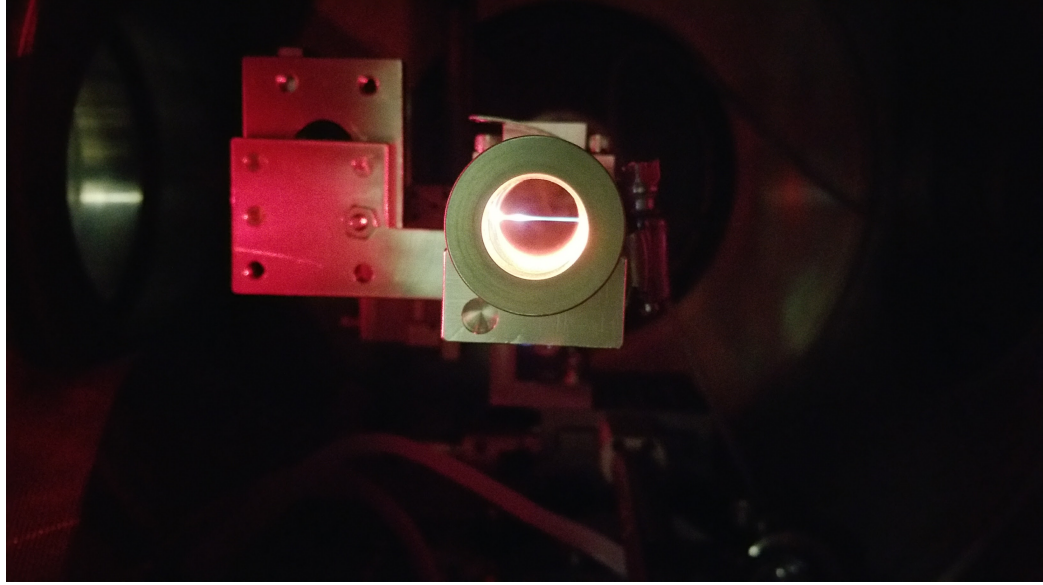


Figure A.3: Laser filament in the aligned outer pipe of the HPC. The inner pipe is not yet installed. Alignment of the outer pipe is done at very low intensities; after alignment the power was increased to create a filament for illustrative purposes only. This picture was taken in the target chamber during the initial testing of the HPC. The geometry of this chamber requires that the orientation of the mounting bracket is reversed compared to what is shown in Fig. A.2.

Laser drilling the inner pipe will sputter a significant amount of metal onto the inner surfaces of the chamber. It is therefore important to protect the optics from the resulting metal plume. Since the active drilling surface is on the upstream face of the pipe, most of the material will go upstream. Therefore, the laser window needs to be swapped out for a "sacrificial" window prior to drilling.³⁵ Out of an abundance of caution, close the gate valve to the mirror chamber, retract the linear actuator & silver mirror from the beam path, and block the generation chamber's vacuum aperture with a card.

Laser drilling should be done with the appropriate safety precautions: wearing laser goggles, notifying coworkers of your activity, and posting signs on the entrances to the lab to reduce unnecessary foot traffic. The user can cover up the chamber's flanges and set up a webcam to remotely monitor the laser drilling status to minimize the risk of inadvertent laser exposure.

At this point, the actual process of laser drilling is quite simple. There is no way to control the exact positioning of the inner pipe relative to the outer pipe, so there are no

³⁵Using a window with different optical properties (i.e., thickness or material), or no window at all, will change the pointing and effective focal length of the beam. It has been suggested that the laser window could be protected by placing a thin sheet of transparent plastic between the window and the HPC, but this method has not been tested.

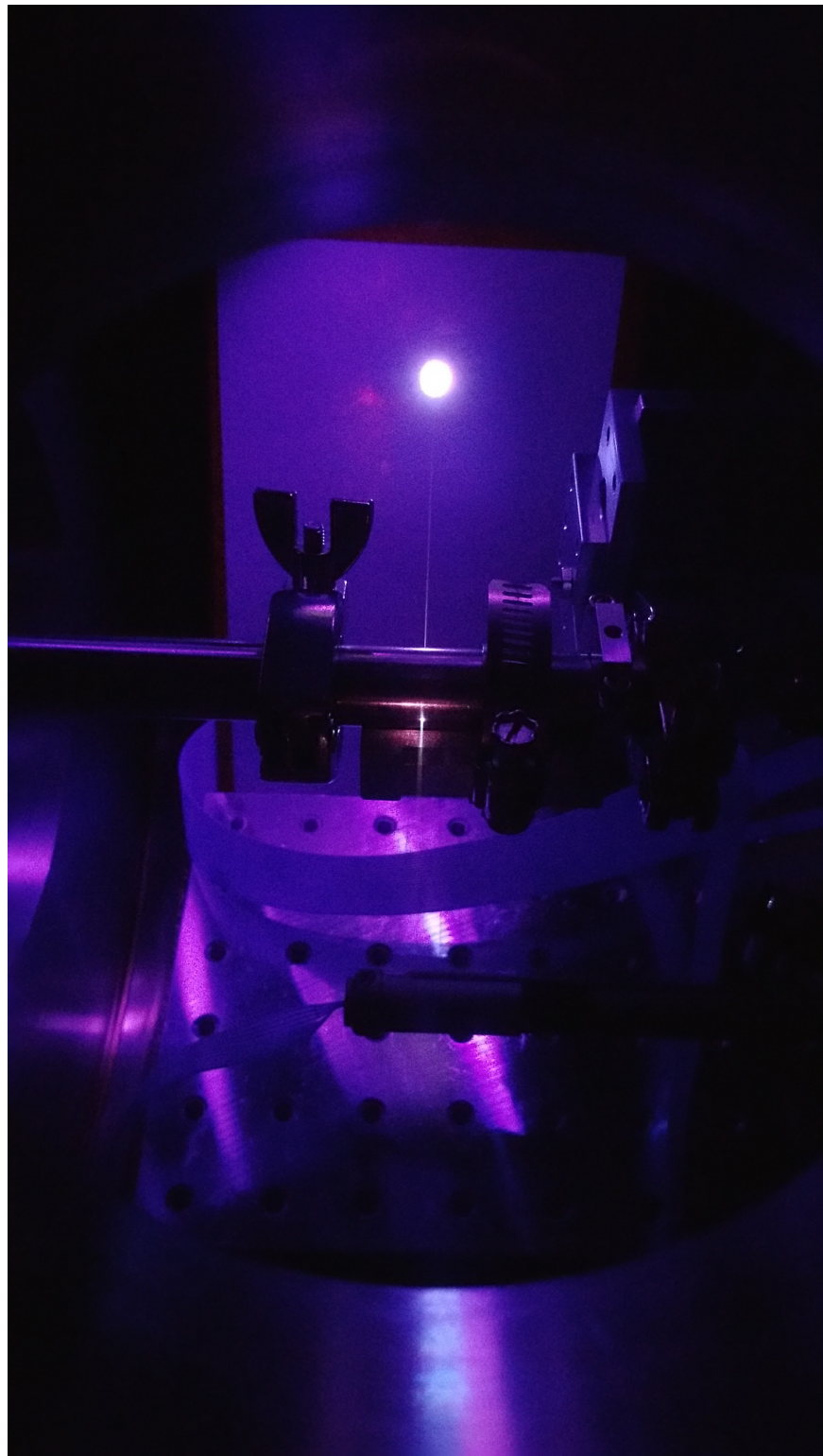


Figure A.4: Laser drilling the inner pipe. A card blocks the laser after exiting the HPC. The HPC was pressurized with Ar gas to enhance the filament for illustrative purposes.

adjustments to make. Rather, the design relies on the mechanical alignment of the inner pipe relative to the outer pipe, which is ultimately set by the gas feedthrough weld, the Swagelok / KF fittings. On the other hand, a used inner pipe cannot be reinstalled to the HPC once it is removed, since alignment is effectively impossible. To laser drill the pipe, simply let the unattenuated beam into the chamber and wait a few minutes until the laser emerges from the exit of the HPC. See Fig. A.4.

If you are planning on scanning the k-direction of the HPC during an experiment, you should do so now while you are set up for laser drilling. Similarly, if you are using a chromatic focusing scheme and are planning on changing wavelengths during your experiment (which will change the effective focal length), you should step through the full range of wavelengths while drilling. Doing so will open up the apertures slightly, resulting in additional metal deposition on the sacrificial laser window and reduced HPC pressure performance.

After laser drilling is complete, reinstall the laser window and verify the HPC has retained its alignment.

A.3.3 Alignment with the HPC Installed

Once lowered out of the beam path, the HPC does not affect the daily pointing procedure. However, there are some extra considerations that need to be made if the HPC is installed. The small apertures of the HPC and the non-linear nature of HHG demand high accuracy in the pointing into the cell, so small corrections to the positioning of the HPC have to be made after the daily pointing procedure is completed.

Pointing into the Interferometer

If the interferometer is already aligned, the presence of the HPC does not really complicate the daily procedure of the beamline. In this case, the user should block the laser into the generation chamber and align the pointing into the interferometer using the pump arm, via the standard procedure.³⁶ Since harmonic generation is extremely sensitive to pointing, the user may have to make small tweaks to the transverse position of the HPC after a nominal alignment of the interferometer. This can be achieved by setting a fast camera exposure (< 0.5 s) and optimizing HHG yield with respect to the HPC vertical & horizontal position (take 10 - 25 μm steps). In our experience, the optimal HPC position is typically within 50 μm of the previous day's position.

The HPC's apertures may no longer be circular if the HPC has been subjected to accidental laser drilling or significant laser drift. Non-circular apertures may result in a complex spatial profile of the harmonics, which can make the optimization of the harmonic yield difficult.

³⁶Failure to block the laser prior to changing the pointing may result in laser-drilling the HPC.

Aligning the Interferometer

If the interferometer needs to be realigned, then the HPC must be lowered out of the way of the laser path. Unless major changes were made to the interferometer, the angle of the HPC's apertures should remain aligned to the k-vector of the generation arm. In this case, the optimal position of the HPC can be found by maximizing the transmitted power of an attenuated laser through the HPC, as described in the latter part of Section A.3.2. If major modifications were made to the interferometer, the user should consider aligning the HPC from scratch.

A.3.4 Using the HPC

The extra vacuum pump adds complications to the TABLe operating procedures described in Appendices A.1 and A.2. Before pumping the TABLe down from atmosphere, ensure the HPC's manual valve (see Fig. A.1) is closed.

Increase the backing pressure until the internal bellows pressure reaches \sim 20 Torr, or until the generation chamber reaches \sim 3 mTorr (whichever happens first). Then, turn on the HPC's RV pump and slowly open the external manual valve. The pressure inside the system should drop. This order of operations ensures the net gas flow direction will be into the RV pump rather than the generation chamber, minimizing the chance of oil contamination in the main TABLe apparatus. Once the HPC's vacuum pump is running, the user can continue increasing the backing pressure until the operating pressure is reached.

Note that the pressure differential between the inside of the HPC's bellows and the generation chamber cannot exceed 120 Torr without risking damage to the HPC's bellows. The shutdown procedure follows the same steps, but in reverse. Lower the backing pressure to the HPC until the generation chamber pressure is $\sim 5 \times 10^{-4}$ Torr, then close the manual valve to the HPC's RV pump. Once the valve is closed, shut off the gas completely and turn off the RV pump. The TABLe system is now ready to be vented (Appendix A.2), or left idle.

BIBLIOGRAPHY

- [1] Sven Grundmann, Daniel Trabert, Kilian Fehre, Nico Strenger, Andreas Pier, Leon Kaiser, Max Kircher, Miriam Weller, Sebastian Eckart, Lothar Ph. H. Schmidt, Florian Trinter, Till Jahnke, Markus S. Schöffler, and Reinhard Dörner. Zeptosecond birth time delay in molecular photoionization. *Science*, 370(6514):339–341, October 2020.
- [2] Ferenc Krausz and Mark I. Stockman. Attosecond metrology: From electron capture to future signal processing. *Nature Photon*, 8(3):205–213, March 2014.
- [3] Linda Young, Kiyoshi Ueda, Markus Gühr, Philip H Bucksbaum, Marc Simon, Shaul Mukamel, Nina Rohringer, Kevin C Prince, Claudio Masciovecchio, Michael Meyer, Artem Rudenko, Daniel Rolles, Christoph Bostedt, Matthias Fuchs, David A Reis, Robin Santra, Henry Kapteyn, Margaret Murnane, Heide Ibrahim, François Légaré, Marc Vrakking, Marcus Isinger, David Kroon, Mathieu Gisselbrecht, Anne L’Huillier, Hans Jakob Wörner, and Stephen R Leone. Roadmap of ultrafast x-ray atomic and molecular physics. *J. Phys. B: At. Mol. Opt. Phys.*, 51(3):032003, February 2018.
- [4] Alan Mak, Georgii Shamuilov, Peter Salén, David Dunning, János Hebling, Yuichiro Kida, Ryota Kinjo, Brian W J McNeil, Takashi Tanaka, Neil Thompson, Zoltán Tibai, György Tóth, and Vitaliy Goryashko. Attosecond single-cycle undulator light: A review. *Rep. Prog. Phys.*, 82(2):025901, February 2019.
- [5] Stephen Bradley Schoun. *Attosecond High-Harmonic Spectroscopy of Atoms and Molecules Using Mid-Infrared Sources*. Ph.D. thesis, The Ohio State University, Columbus, OH, 2015.
- [6] S. Eich, A. Stange, A. V. Carr, J. Urbancic, T. Popmintchev, M. Wiesenmayer, K. Jansen, A. Ruffing, S. Jakobs, T. Rohwer, S. Hellmann, C. Chen, P. Matyba, L. Kipp, K. Rossnagel, M. Bauer, M. M. Murnane, H. C. Kapteyn, S. Mathias, and M. Aeschlimann. Time- and angle-resolved photoemission spectroscopy with

optimized high-harmonic pulses using frequency-doubled Ti:Sapphire lasers. *Journal of Electron Spectroscopy and Related Phenomena*, 195:231–236, August 2014.

- [7] Eric Gullikson. CXRO X-Ray Interactions With Matter. http://henke.lbl.gov/optical_constants/.
- [8] Edson R. Peck and Donald J. Fisher. Dispersion of Argon. *J. Opt. Soc. Am., JOSA*, 54(11):1362–1364, November 1964.
- [9] Charles R. Mansfield and Edson R. Peck. Dispersion of Helium. *J. Opt. Soc. Am., JOSA*, 59(2):199–204, February 1969.
- [10] Enrico Nichelatti. Complex refractive index of a slab from reflectance and transmittance: Analytical solution. *J. Opt. A: Pure Appl. Opt.*, 4(4):400–403, July 2002.
- [11] B. L. Henke, E. M. Gullikson, and J. C. Davis. X-Ray Interactions: Photoabsorption, Scattering, Transmission, and Reflection at $E = 50\text{--}30,000 \text{ eV}$, $Z = 1\text{--}92$. *Atomic Data and Nuclear Data Tables*, 54(2):181–342, July 1993.
- [12] Malcolm R. Howells. Mirrors for Synchrotron-Radiation Beamlines. In A. S. Schlachter and F. J. Wuilleumier, editors, *New Directions in Research with Third-Generation Soft X-Ray Synchrotron Radiation Sources*, NATO ASI Series, pages 359–385. Springer Netherlands, Dordrecht, 1994.
- [13] Richard Pfisterer and Steve Johnston. FRED Optical Engineering Software. Photon Engineering.
- [14] Antoine Camper, Amélie Ferré, Nan Lin, Emmanouil Skantzakis, David Staedter, Elizabeth English, Bastian Manschwetus, Frédéric Burgy, Stéphane Petit, Dominique Descamps, Thierry Auguste, Olivier Gobert, Bertrand Carré, Pascal Salières, Yann Mairesse, and Thierry Ruchon. Transverse Electromagnetic Mode Conversion for High-Harmonic Self-Probing Spectroscopy. *Photonics*, 2(1):184–199, March 2015.
- [15] NSM Archive - Physical Properties of Semiconductors. <http://www.ioffe.ru/SVA/NSM/Semicond/index.html>.
- [16] Michael Zürch, Hung-Tzu Chang, Lauren J. Borja, Peter M. Kraus, Scott K. Cushing, Andrey Gandman, Christopher J. Kaplan, Myoung Hwan Oh, James S. Prell, David Prendergast, Chaitanya D. Pemmaraju, Daniel M. Neumark, and Stephen R. Leone. Direct and simultaneous observation of ultrafast electron and hole dynamics in germanium. *Nat Commun*, 8(1):15734, August 2017.

- [17] Zenghu Chang, Paul B. Corkum, and Stephen R. Leone. Attosecond optics and technology: Progress to date and future prospects [Invited]. *J. Opt. Soc. Am. B*, 33(6):1081, June 2016.
- [18] T. Carette, J. M. Dahlström, L. Argenti, and E. Lindroth. Multiconfigurational Hartree-Fock close-coupling ansatz: Application to the argon photoionization cross section and delays. *Phys. Rev. A*, 87(2):023420, February 2013.
- [19] David R Miller. Free Jet Sources (Chap 2). In Giacinto Scoles, editor, *Atomic and Molecular Beam Methods*, volume 1, pages 14–82. Oxford University Press, 1988.
- [20] M. Hentschel, R. Kienberger, Ch. Spielmann, G. A. Reider, N. Milosevic, T. Brabec, P. Corkum, U. Heinzmann, M. Drescher, and F. Krausz. Attosecond metrology. *Nature*, 414(6863):509–513, November 2001.
- [21] Ferenc Krausz. From femtochemistry to attophysics. *Phys. World*, 14(9):41–46, September 2001.
- [22] M. Ossiander, F. Siegrist, V. Shirvanyan, R. Pazourek, A. Sommer, T. Latka, A. Guggenmos, S. Nagele, J. Feist, J. Burgdörfer, R. Kienberger, and M. Schultze. Attosecond correlation dynamics. *Nature Phys*, 13(3):280–285, March 2017.
- [23] Franz X. Kärtner, Erich P. Ippen, and Steven T. Cundiff. Femtosecond Laser Development. In Jun Ye and Steven T. Cundiff, editors, *Femtosecond Optical Frequency Comb: Principle, Operation, and Applications*, pages 54–77. Kluwer Academic Publishers, Boston, 2005.
- [24] Zenghu Chang. *Fundamentals of Attosecond Optics*. CRC Press, Boca Raton, 2011.
- [25] A Picón, L Plaja, and J Biegert. Attosecond x-ray transient absorption in condensed-matter: A core-state-resolved Bloch model. *New J. Phys.*, 21(4):043029, April 2019.
- [26] Jie Li, Xiaoming Ren, Yanchun Yin, Kun Zhao, Andrew Chew, Yan Cheng, Eric Cunningham, Yang Wang, Shuyuan Hu, Yi Wu, Michael Chini, and Zenghu Chang. 53-attosecond X-ray pulses reach the carbon K-edge. *Nat Commun*, 8(1):186, December 2017.
- [27] R. W. Schoenlein. Generation of Femtosecond Pulses of Synchrotron Radiation. *Science*, 287(5461):2237–2240, March 2000.
- [28] Y. Ding, Z. Huang, D. Ratner, P. Bucksbaum, and H. Merdji. Generation of attosecond x-ray pulses with a multicycle two-color enhanced self-amplified spontaneous emission scheme. *Phys. Rev. ST Accel. Beams*, 12(6):060703, June 2009.

- [29] L.V. Keldysh. Ionization in the Field of a Strong Electromagnetic Wave. *SOVIET PHYSICS JETP*, 20:1307–1314, May 1965.
- [30] K. J. Schafer, Baorui Yang, L. F. DiMauro, and K. C. Kulander. Above threshold ionization beyond the high harmonic cutoff. *Phys. Rev. Lett.*, 70(11):1599–1602, March 1993.
- [31] P. B. Corkum. Plasma perspective on strong field multiphoton ionization. *Phys. Rev. Lett.*, 71(13):1994–1997, September 1993.
- [32] M V Ammosov, N B Delone, and V P Krainov. Tunnel ionization of complex atoms and of atomic ions in an alternating electromagnetic field. *Sov. Phys. JTEP*, 64(6):1191–1194, 1986.
- [33] Yu Hang Lai, Junliang Xu, Urszula B. Szafruga, Bradford K. Talbert, Xiaowei Gong, Kaikai Zhang, Harald Fuest, Matthias F. Kling, Cosmin I. Blaga, Pierre Agostini, and Louis F. DiMauro. Experimental investigation of strong-field-ionization theories for laser fields from visible to midinfrared frequencies. *Phys. Rev. A*, 96(6):063417, December 2017.
- [34] A M Perelomov, V S Popov, and M V Terent’ev. Ionization of Atoms in an Alternating Electric Field. *Soviet Phys. JETP*, 23:924, 1966.
- [35] X M Tong and C D Lin. Empirical formula for static field ionization rates of atoms and molecules by lasers in the barrier-suppression regime. *J. Phys. B: At. Mol. Opt. Phys.*, 38(15):2593–2600, August 2005.
- [36] J. Tate, T. Auguste, H. G. Muller, P. Salières, P. Agostini, and L. F. DiMauro. Scaling of Wave-Packet Dynamics in an Intense Midinfrared Field. *Phys. Rev. Lett.*, 98(1):013901, January 2007.
- [37] A. D. Shiner, C. Trallero-Herrero, N. Kajumba, H.-C. Bandulet, D. Comtois, F. Légaré, M. Giguère, J-C. Kieffer, P. B. Corkum, and D. M. Villeneuve. Wavelength Scaling of High Harmonic Generation Efficiency. *Phys. Rev. Lett.*, 103(7):073902, August 2009.
- [38] P. Colosimo, G. Doumy, C. I. Blaga, J. Wheeler, C. Hauri, F. Catoire, J. Tate, R. Chirla, A. M. March, G. G. Paulus, H. G. Muller, P. Agostini, and L. F. DiMauro. Scaling strong-field interactions towards the classical limit. *Nature Phys*, 4(5):386–389, May 2008.
- [39] Jan Rothhardt, Manuel Krebs, Steffen Hädrich, Stefan Demmler, Jens Limpert, and Andreas Tünnermann. Absorption-limited and phase-matched high harmonic generation in the tight focusing regime. *New J. Phys.*, 16(3):033022, March 2014.

- [40] M. Lewenstein, Ph. Balcou, M. Yu. Ivanov, Anne L’Huillier, and P. B. Corkum. Theory of high-harmonic generation by low-frequency laser fields. *Phys. Rev. A*, 49(3):2117–2132, March 1994.
- [41] Philippe Balcou, Pascal Salières, Anne L’Huillier, and Maciej Lewenstein. Generalized phase-matching conditions for high harmonics: The role of field-gradient forces. *Phys. Rev. A*, 55(4):3204–3210, April 1997.
- [42] Pascal Salières, Anne L’Huillier, and Maciej Lewenstein. Coherence Control of High-Order Harmonics. *Phys. Rev. Lett.*, 74(19):3776–3779, May 1995.
- [43] S. Kazamias, S. Daboussi, O. Guilbaud, K. Cassou, D. Ros, B. Cros, and G. Maynard. Pressure-induced phase matching in high-order harmonic generation. *Phys. Rev. A*, 83(6):063405, June 2011.
- [44] Philippe Balcou, Anne S. Dederichs, Mette B. Gaarde, and Anne L’Huillier. Quantum-path analysis and phase matching of high-order harmonic generation and high-order frequency mixing processes in strong laser fields. *J. Phys. B: At. Mol. Opt. Phys.*, 32(12):2973–2989, January 1999.
- [45] S. Kazamias, F. Weihe, D. Douillet, C. Valentin, T. Planchon, S. Sebban, G. Grillon, F. Augé, D. Hulin, and Ph. Balcou. High order harmonic generation optimization with an apertured laser beam. *Eur. Phys. J. D*, 21(3):353–359, December 2002.
- [46] J. Pupeikis, P.-A. Chevreuil, N. Bigler, L. Gallmann, C. R. Phillips, and U. Keller. Water window soft x-ray source enabled by a 25 W few-cycle 2.2 Mm OPCPA at 100 kHz. *Optica, OPTICA*, 7(2):168–171, February 2020.
- [47] E. Constant, D. Garzella, P. Breger, E. Mével, Ch. Dorrer, C. Le Blanc, F. Salin, and P. Agostini. Optimizing High Harmonic Generation in Absorbing Gases: Model and Experiment. *Phys. Rev. Lett.*, 82(8):1668–1671, February 1999.
- [48] E.J. Takahashi, Y. Nabekawa, H. Mashiko, H. Hasegawa, A. Suda, and K. Midorikawa. Generation of Strong Optical Field in Soft X-Ray Region by Using High-Order Harmonics. *IEEE J. Select. Topics Quantum Electron.*, 10(6):1315–1328, November 2004.
- [49] Krupa Ramasesha, Stephen R. Leone, and Daniel M. Neumark. Real-Time Probing of Electron Dynamics Using Attosecond Time-Resolved Spectroscopy. *Annu. Rev. Phys. Chem.*, 67(1):41–63, May 2016.
- [50] Christopher J. Kaplan, Peter M. Kraus, Andrew D. Ross, Michael Zürch, Scott K. Cushing, Marieke F. Jager, Hung-Tzu Chang, Eric M. Gullikson, Daniel M. Neumark, and Stephen R. Leone. Femtosecond tracking of carrier relaxation in germanium with extreme ultraviolet transient reflectivity. *Phys. Rev. B*, 97(20):205202, May 2018.

- [51] Brett M. Marsh, Bethany R. Lamoureux, and Stephen R. Leone. Ultrafast time-resolved extreme ultraviolet (XUV) photoelectron spectroscopy of hole transfer in a Zn/n-GaP Schottky junction. *Structural Dynamics*, 5(5):054502, September 2018.
- [52] Scott K. Cushing, Ilana J. Porter, Bethany R. de Roulet, Angela Lee, Brett M. Marsh, Szilard Szoke, Mihai E. Vaida, and Stephen R. Leone. Layer-resolved ultrafast extreme ultraviolet measurement of hole transport in a Ni-TiO₂-Si photoanode. *Sci. Adv.*, 6(14):eaay6650, April 2020.
- [53] Anthony Cirri, Jakub Husek, Somnath Biswas, and L. Robert Baker. Achieving Surface Sensitivity in Ultrafast XUV Spectroscopy: M2,3-Edge Reflection–Absorption of Transition Metal Oxides. *J. Phys. Chem. C*, 121(29):15861–15869, July 2017.
- [54] Stephen J. Hageman. *Complex Attosecond Transient Absorption Spectroscopy*. PhD thesis, The Ohio State University, Columbus, OH, 2020.
- [55] Antoine Camper, Hyunwook Park, Stephen J. Hageman, Greg Smith, Thierry Auguste, Pierre Agostini, and Louis F. DiMauro. High relative-phase precision beam duplicator for mid-infrared femtosecond pulses. *Opt. Lett., OL*, 44(22):5465–5468, November 2019.
- [56] A. Camper, T. Ruchon, D. Gauthier, O. Gobert, P. Salières, B. Carré, and T. Auguste. High-harmonic phase spectroscopy using a binary diffractive optical element. *Phys. Rev. A*, 89(4):043843, April 2014.
- [57] Antoine Camper, Amélie Ferré, Valérie Blanchet, Frédéric Burgy, Dominique Descamps, Stéphane Petit, Thierry Ruchon, and Yann Mairesse. Combined high-harmonic interferometries for vectorial spectroscopy. *Opt. Lett., OL*, 40(22):5387–5390, November 2015.
- [58] Joseph W. Goodman. *Introduction to Fourier Optics*. McGraw-Hill Series in Electrical and Computer Engineering. McGraw-Hill, New York, 2nd ed edition, 1996.
- [59] Nicolas Passilly, François Treussart, Rolland Hierle, Renaud de Saint Denis, Kamel Aït-Ameur, and Jean-François Roch. Simple interferometric technique for generation of a radially polarized light beam. *J. Opt. Soc. Am. A*, 22(5):984, May 2005.
- [60] Gleb Vdovin, Fred van Goor, and Guyskk. LightPipes for Python. Flexible Optical.
- [61] Donna Strickland and Gerard Mourou. Compression of amplified chirped optical pulses. *Optics Communications*, 56(3):219–221, December 1985.

- [62] S. Zahedpour, J. K. Wahlstrand, and H. M. Milchberg. Measurement of the non-linear refractive index of air constituents at mid-infrared wavelengths. *Opt. Lett.*, 40(24):5794, December 2015.
- [63] Razvan Cristian Chirla. *Attosecond Pulse Generation and Characterization*. Ph.D. thesis, The Ohio State University, Columbus, OH, 2011.
- [64] Timothy Gorman. *Attosecond Probing of Electron Dynamics in Atoms and Molecules Using Tunable Mid-Infrared Drivers*. Ph.D. thesis, The Ohio State University, Columbus, OH, 2018.
- [65] Dietrich Kiesewetter. *Dynamics of Near-Threshold Attosecond Electron Wavepackets in Strong Laser Fields*. Ph.D. thesis, The Ohio State University, Columbus, OH, 2019.
- [66] D.J. Kane and R. Trebino. Characterization of arbitrary femtosecond pulses using frequency-resolved optical gating. *IEEE J. Quantum Electron.*, 29(2):571–579, Feb./1993.
- [67] Jean-Claude Diels and Wolfgang Rudolph. *Ultrashort Laser Pulse Phenomena: Fundamentals, Techniques, and Applications on a Femtosecond Time Scale*. Optics and Photonics. Elsevier / Academic Press, Amsterdam; Boston, 2nd ed edition, 2006.
- [68] I. H. Malitson. Interspecimen Comparison of the Refractive Index of Fused Silica. *J. Opt. Soc. Am.*, 55(10):1205, October 1965.
- [69] Masahiko Daimon and Akira Masumura. High-accuracy measurements of the refractive index and its temperature coefficient of calcium fluoride in a wide wavelength range from 138 to 2326 nm. *Appl. Opt.*, 41(25):5275, September 2002.
- [70] Alejandro D. Farinas and Evan D. Green. Optical beam steering and sampling apparatus and method, May 2009.
- [71] Joseph Ladislas Wiza. Microchannel plate detectors. *Nuclear Instruments and Methods*, 162(1):587–601, June 1979.
- [72] Zhou Wang. *Mid-Infrared Strong-Field Laser Interactions with Nanoclusters and Semiconductors*. Ph.D. thesis, The Ohio State University, Columbus, OH, 2018.
- [73] Andrew Piper. *Andrew Piper's Dissertation (in Progress)*. PhD thesis, The Ohio State University, 2022.
- [74] Qi Zhang, Kun Zhao, Jie Li, Michael Chini, Yan Cheng, Yi Wu, Eric Cunningham, and Zenghu Chang. Suppression of driving laser in high harmonic generation with a microchannel plate. *Opt. Lett.*, 39(12):3670, June 2014.

- [75] Sierra O'Bryan. *High Resolution XUV Spectrometer: An Overview*. Master's Thesis, The Ohio State University, Columbus, OH, May 2015.
- [76] L. Drescher, O. Kornilov, T. Witting, G. Reitsma, N. Monserud, A. Rouzée, J. Mikosch, M. J. J. Vrakking, and B. Schütte. Extreme-ultraviolet refractive optics. *Nature*, 564(7734):91, December 2018.
- [77] Andrew Zangwill. *Modern Electrodynamics*. Cambridge University Press, Cambridge, 2013.
- [78] David T. Attwood. *Soft X-Rays and Extreme Ultraviolet Radiation: Principles and Applications*. Cambridge University Press, Cambridge ; New York, 2000.
- [79] A. Sentenac and J. Daillant. Statistical Aspects of Wave Scattering at Rough Surfaces. In Jean Daillant and Alain Gibaud, editors, *X-Ray and Neutron Reflectivity: Principles and Applications*, Lecture Notes in Physics, pages 59–84. Springer Berlin Heidelberg, Berlin, Heidelberg, 2009.
- [80] A. Gibaud and G. Vignaud. Specular Reflectivity from Smooth and Rough Surfaces. In Jean Daillant and Alain Gibaud, editors, *X-Ray and Neutron Reflectivity: Principles and Applications*, Lecture Notes in Physics, pages 85–131. Springer Berlin Heidelberg, Berlin, Heidelberg, 2009.
- [81] Krassimir N. Stoev and Kenji Sakurai. Review on grazing incidence X-ray spectrometry and reflectometry. *Spectrochimica Acta Part B: Atomic Spectroscopy*, 54(1):41–82, January 1999.
- [82] C. Bourassin-Bouchet, M. M. Mang, F. Delmotte, P. Chavel, and S. de Rossi. How to focus an attosecond pulse. *Opt. Express, OE*, 21(2):2506–2520, January 2013.
- [83] H. Noda, T. Namioka, and M. Seya. Geometric theory of the grating. *J. Opt. Soc. Am.*, 64(8):1031, August 1974.
- [84] L. Poletto, F. Frassetto, F. Calegari, S. Anumula, A. Trabattoni, and M. Nisoli. Microfocusing of attosecond pulses by grazing-incidence toroidal mirrors. *Opt. Express, OE*, 21(11):13040–13051, June 2013.
- [85] Jacques Arnaud. Representation of Gaussian beams by complex rays. *Appl. Opt., AO*, 24(4):538–543, February 1985.
- [86] Paul Kirkpatrick and A. V. Baez. Formation of Optical Images by X-Rays. *J. Opt. Soc. Am.*, 38(9):766, September 1948.

- [87] Hiroto Motoyama, Takahiro Saito, and Hidekazu Mimura. Error analysis of ellipsoidal mirrors for soft X-ray focusing by wave-optical simulation. *Jpn. J. Appl. Phys.*, 53(2):022503, February 2014.
- [88] J. Peatross, J. L. Chaloupka, and D. D. Meyerhofer. High-order harmonic generation with an annular laser beam. *Opt. Lett., OL*, 19(13):942–944, July 1994.
- [89] Joseph Ladislas Wiza. Microchannel plate detectors. *Nuclear Instruments and Methods*, 162(1-3):587–601, June 1979.
- [90] G.W. Fraser. X- and γ -ray imaging using microchannel plates. *Nuclear Instruments and Methods in Physics Research*, 221(1):115–130, March 1984.
- [91] S. L. Sorensen, T. Åberg, J. Tulkki, E. Rachlew-Källne, G. Sundström, and M. Kirm. Argon 3s autoionization resonances. *Phys. Rev. A*, 50(2):1218–1230, August 1994.
- [92] Jonathan Mooney and Patanjali Kambhampati. Get the Basics Right: Jacobian Conversion of Wavelength and Energy Scales for Quantitative Analysis of Emission Spectra. *J. Phys. Chem. Lett.*, 4(19):3316–3318, October 2013.
- [93] Karl Jousten, editor. *Handbook of Vacuum Technology*. Wiley-VCH Verlag GmbH & Co. KGaA, Weinheim, second, completely revised and updated edition edition, 2016.
- [94] M. H. Hablanian. *High-Vacuum Technology: A Practical Guide*. Number 111 in Mechanical Engineering. Marcel Dekker, New York, 2nd ed., rev. and expanded edition, 1997.
- [95] G. M. Fryer and Richard Maling Barrer. A theory of gas flow through capillary tubes. *Proceedings of the Royal Society of London. Series A. Mathematical and Physical Sciences*, 293(1434):329–341, August 1966.
- [96] David C. Venerus. Laminar capillary flow of compressible viscous fluids. *J. Fluid Mech.*, 555:59, May 2006.
- [97] Lev Davidovič Landau, Evgenij M. Lifšic, and Lev Davidovich Landau. *Fluid Mechanics*. Number by L. D. Landau and E. M. Lifshitz ; Vol. 6 in Course of Theoretical Physics. Elsevier/Butterworth Heinemann, Amsterdam [u.a], 2. engl. ed., rev., reprint. with corr edition, 2011.
- [98] Virendra N. Mahajan. Uniform versus Gaussian beams: A comparison of the effects of diffraction, obscuration, and aberrations. *J. Opt. Soc. Am. A*, 3(4):470, April 1986.
- [99] Tenio Popmintchev, Ming-Chang Chen, Oren Cohen, Michael E. Grisham, Jorge J. Rocca, Margaret M. Murnane, and Henry C. Kapteyn. Extended phase matching

- of high harmonics driven by mid-infrared light. *Opt. Lett., OL*, 33(18):2128–2130, September 2008.
- [100] Tenio Popmintchev, Ming-Chang Chen, Alon Bahabad, Michael Gerrity, Pavel Sidorenko, Oren Cohen, Ivan P. Christov, Margaret M. Murnane, and Henry C. Kapteyn. Phase matching of high harmonic generation in the soft and hard X-ray regions of the spectrum. *PNAS*, 106(26):10516–10521, June 2009.
 - [101] U. Even. The Even-Lavie valve as a source for high intensity supersonic beam. *EPJ Techn Instrum*, 2(1):17, December 2015.
 - [102] C. Altucci, T. Starczewski, E. Mevel, C.-G. Wahlström, B. Carré, and A. L’Huillier. Influence of atomic density in high-order harmonic generation. *J. Opt. Soc. Am. B*, 13(1):148, January 1996.
 - [103] Wolfgang Christen. Stationary flow conditions in pulsed supersonic beams. *The Journal of Chemical Physics*, 139(15):154202, October 2013.
 - [104] Daniel Irimia, Rob Kortekaas, and Maurice H. M. Janssen. In situ characterization of a cold and short pulsed molecular beam by femtosecond ion imaging. *Phys. Chem. Chem. Phys.*, 11(20):3958, 2009.
 - [105] Congsen Meng and Maurice H. M. Janssen. Measurement of the density profile of pure and seeded molecular beams by femtosecond ion imaging. *Review of Scientific Instruments*, 86(2):023110, February 2015.
 - [106] Daniel Irimia, Dimitar Dobrikov, Rob Kortekaas, Han Voet, Daan A. van den Ende, Wilhelm A. Groen, and Maurice H. M. Janssen. A short pulse (7 microsecond FWHM) and high repetition rate (dc-5kHz) cantilever piezovalve for pulsed atomic and molecular beams. *Review of Scientific Instruments*, 80(11):113303, November 2009.
 - [107] A. E. Siegman. How to (Maybe) Measure Laser Beam Quality. In *DPSS (Diode Pumped Solid State) Lasers: Applications and Issues*, page MQ1, Washington, D.C., 1998. OSA.
 - [108] Anthony E. Siegman. New developments in laser resonators. In Dale A. Holmes, editor, *OE/LASE ’90, 14-19 Jan., Los Angeles, CA*, page 2, Los Angeles, CA, June 1990.
 - [109] Anthony E. Siegman. Defining, measuring, and optimizing laser beam quality. In Anup Bhowmik, editor, *OE/LASE’93: Optics, Electro-Optics, & Laser Applications in Science& Engineering*, pages 2–12, Los Angeles, CA, February 1993.

- [110] Andreia A. Almeida, Armando V. F. Zuffi, Paulo S. F. de Matos, Nilson D. Vieira, and Ricardo E. Samad. Harmonics Beams Characterization Using the Knife-Edge Technique. In *High-Brightness Sources and Light-Driven Interactions*, page ET4A.1, Long Beach, California, 2016. OSA.
- [111] Marcos A. de Araújo, Rubens Silva, Emerson de Lima, Daniel P. Pereira, and Paulo C. de Oliveira. Measurement of Gaussian laser beam radius using the knife-edge technique: Improvement on data analysis. *Appl. Opt.*, 48(2):393, January 2009.
- [112] J. W. G. Tisch, R. A. Smith, J. E. Muffett, M. Ciarrocca, J. P. Marangos, and M. H. R. Hutchinson. Angularly resolved high-order harmonic generation in helium. *Phys. Rev. A*, 49(1):R28–R31, January 1994.
- [113] Annelise R. Beck, Daniel M. Neumark, and Stephen R. Leone. Probing ultrafast dynamics with attosecond transient absorption. *Chemical Physics Letters*, 624:119–130, March 2015.
- [114] Stephen R. Leone, C. William McCurdy, Joachim Burgdörfer, Lorenz S. Cederbaum, Zenghu Chang, Nirit Dudovich, Johannes Feist, Chris H. Greene, Misha Ivanov, Reinhard Kienberger, Ursula Keller, Matthias F. Kling, Zhi-Heng Loh, Thomas Pfeifer, Adrian N. Pfeiffer, Robin Santra, Kenneth Schafer, Albert Stolow, Uwe Thumm, and Marc J. J. Vrakking. What will it take to observe processes in 'real time'? *Nature Photon*, 8(3):162–166, March 2014.
- [115] Romain Geneaux, Hugo J. B. Marroux, Alexander Guggenmos, Daniel M. Neumark, and Stephen R. Leone. Transient absorption spectroscopy using high harmonic generation: A review of ultrafast X-ray dynamics in molecules and solids. *Phil. Trans. R. Soc. A*, 377(2145):20170463, May 2019.
- [116] Eleftherios Goulielmakis, Zhi-Heng Loh, Adrian Wirth, Robin Santra, Nina Rohringer, Vladislav S. Yakovlev, Sergey Zherebtsov, Thomas Pfeifer, Abdallah M. Azzeer, Matthias F. Kling, Stephen R. Leone, and Ferenc Krausz. Real-time observation of valence electron motion. *Nature*, 466(7307):739–743, August 2010.
- [117] He Wang, Michael Chini, Shouyuan Chen, Chang-Hua Zhang, Feng He, Yan Cheng, Yi Wu, Uwe Thumm, and Zenghu Chang. Attosecond Time-Resolved Autoionization of Argon. *Phys. Rev. Lett.*, 105(14):143002, October 2010.
- [118] Wei Cao, Erika R Warrick, Daniel M Neumark, and Stephen R Leone. Attosecond transient absorption of argon atoms in the vacuum ultraviolet region: Line energy shifts versus coherent population transfer. *New J. Phys.*, 18(1):013041, January 2016.

- [119] Andrew Chew, Nicolas Douguet, Coleman Cariker, Jie Li, Eva Lindroth, Xiaoming Ren, Yanchun Yin, Luca Argenti, Wendell T. Hill, and Zenghu Chang. Attosecond transient absorption spectrum of argon at the L 2 , 3 edge. *Phys. Rev. A*, 97(3):031407, March 2018.
- [120] Shaohao Chen, M. Justine Bell, Annelise R. Beck, Hiroki Mashiko, Mengxi Wu, Adrian N. Pfeiffer, Mette B. Gaarde, Daniel M. Neumark, Stephen R. Leone, and Kenneth J. Schafer. Light-induced states in attosecond transient absorption spectra of laser-dressed helium. *Phys. Rev. A*, 86(6):063408, December 2012.
- [121] M. Justine Bell, Annelise R. Beck, Hiroki Mashiko, Daniel M. Neumark, and Stephen R. Leone. Intensity dependence of light-induced states in transient absorption of laser-dressed helium measured with isolated attosecond pulses. *Journal of Modern Optics*, 60(17):1506–1516, October 2013.
- [122] Ming-Fu Lin, Adrian N. Pfeiffer, Daniel M. Neumark, Stephen R. Leone, and Oliver Gessner. Strong-field induced XUV transmission and multiplet splitting in $4\ d^{-1}\ 6\ p$ core-excited Xe studied by femtosecond XUV transient absorption spectroscopy. *The Journal of Chemical Physics*, 137(24):244305, December 2012.
- [123] Birgitta Bernhardt, Annelise R. Beck, Xuan Li, Erika R. Warrick, M. Justine Bell, Daniel J. Haxton, C. William McCurdy, Daniel M. Neumark, and Stephen R. Leone. High-spectral-resolution attosecond absorption spectroscopy of autoionization in xenon. *Phys. Rev. A*, 89(2):023408, February 2014.
- [124] Xuan Li, Birgitta Bernhardt, Annelise R. Beck, Erika R. Warrick, Adrian N. Pfeiffer, M. Justine Bell, Daniel J. Haxton, C. William McCurdy, Daniel M. Neumark, and Stephen R. Leone. Investigation of coupling mechanisms in attosecond transient absorption of autoionizing states: Comparison of theory and experiment in xenon. *J. Phys. B: At. Mol. Opt. Phys.*, 48(12):125601, June 2015.
- [125] Annelise R. Beck, Birgitta Bernhardt, Erika R. Warrick, Mengxi Wu, Shaohao Chen, Mette B. Gaarde, Kenneth J. Schafer, Daniel M. Neumark, and Stephen R. Leone. Attosecond transient absorption probing of electronic superpositions of bound states in neon: Detection of quantum beats. *New J. Phys.*, 16(11):113016, November 2014.
- [126] Erik R. Hosler and Stephen R. Leone. Characterization of vibrational wave packets by core-level high-harmonic transient absorption spectroscopy. *Phys. Rev. A*, 88(2):023420, August 2013.
- [127] Andrew R. Attar, Lorena Pitocco, and Stephen R. Leone. Core-to-valence spectroscopic detection of the CH₂Br radical and element-specific femtosecond photodissociation dynamics of CH₂IBr. *J. Chem. Phys.*, 141(16):164308, October 2014.

- [128] Erika R. Warrick, Wei Cao, Daniel M. Neumark, and Stephen R. Leone. Probing the Dynamics of Rydberg and Valence States of Molecular Nitrogen with Attosecond Transient Absorption Spectroscopy. *J. Phys. Chem. A*, 120(19):3165–3174, May 2016.
- [129] Michael P. Ziemkiewicz, Camila Bacellar, Katrin R. Siefermann, Stephen R. Leone, Daniel M. Neumark, and Oliver Gessner. Femtosecond time-resolved XUV + UV photoelectron imaging of pure helium nanodroplets. *J. Chem. Phys.*, 141(17):174306, November 2014.
- [130] Ilana J. Porter, Scott K. Cushing, Lucas M. Carneiro, Angela Lee, Justin C. Ondry, Jakob C. Dahl, Hung-Tzu Chang, A. Paul Alivisatos, and Stephen R. Leone. Photoexcited Small Polaron Formation in Goethite (α -FeOOH) Nanorods Probed by Transient Extreme Ultraviolet Spectroscopy. *J. Phys. Chem. Lett.*, 9(14):4120–4124, July 2018.
- [131] M. Schultze, K. Ramasesha, C. D. Pemmaraju, S. A. Sato, D. Whitmore, A. Gandman, J. S. Prell, L. J. Borja, D. Prendergast, K. Yabana, D. M. Neumark, and S. R. Leone. Attosecond band-gap dynamics in silicon. *Science*, 346(6215):1348–1352, December 2014.
- [132] Scott K. Cushing, Angela Lee, Ilana J. Porter, Lucas M. Carneiro, Hung-Tzu Chang, Michael Zürch, and Stephen R. Leone. Differentiating Photoexcited Carrier and Phonon Dynamics in the Δ , L , and Γ Valleys of Si(100) with Transient Extreme Ultraviolet Spectroscopy. *J. Phys. Chem. C*, 123(6):3343–3352, February 2019.
- [133] Michael Zürch, Hung-Tzu Chang, Peter M. Kraus, Scott K. Cushing, Lauren J. Borja, Andrey Gandman, Christopher J. Kaplan, Myoung Hwan Oh, James S. Prell, David Prendergast, Chaitanya D. Pemmaraju, Daniel M. Neumark, and Stephen R. Leone. Ultrafast carrier thermalization and trapping in silicon-germanium alloy probed by extreme ultraviolet transient absorption spectroscopy. *Structural Dynamics*, 4(4):044029, July 2017.
- [134] Josh Vura-Weis, Chang-Ming Jiang, Chong Liu, Hanwei Gao, J. Matthew Lucas, Frank M. F. de Groot, Peidong Yang, A. Paul Alivisatos, and Stephen R. Leone. Femtosecond M_{2,3}-Edge Spectroscopy of Transition-Metal Oxides: Photoinduced Oxidation State Change in α -Fe₂O₃. *J. Phys. Chem. Lett.*, 4(21):3667–3671, November 2013.
- [135] Chang-Ming Jiang, L. Robert Baker, J. Matthew Lucas, Josh Vura-Weis, A. Paul Alivisatos, and Stephen R. Leone. Characterization of Photo-Induced Charge Transfer and Hot Carrier Relaxation Pathways in Spinel Cobalt Oxide (Co₃O₄). *J. Phys. Chem. C*, 118(39):22774–22784, October 2014.

- [136] Mihai E. Vaida and Stephen R. Leone. Femtosecond Extreme Ultraviolet Photoemission Spectroscopy: Observation of Ultrafast Charge Transfer at the n-TiO₂/p-Si(100) Interface with Controlled TiO₂ Oxygen Vacancies. *J. Phys. Chem. C*, 120(5):2769–2776, February 2016.
- [137] Ming-Fu Lin, Max A. Verkamp, Joshua Leveillee, Elizabeth S. Ryland, Kristin Benke, Kaili Zhang, Clemens Weninger, Xiaozhe Shen, Renkai Li, David Fritz, Uwe Bergmann, Xijie Wang, André Schleife, and Josh Vura-Weis. Carrier-Specific Femtosecond XUV Transient Absorption of PbI₂ Reveals Ultrafast Nonradiative Recombination. *J. Phys. Chem. C*, 121(50):27886–27893, December 2017.
- [138] M. Volkov, S. A. Sato, F. Schlaepfer, L. Kasmi, N. Hartmann, M. Lucchini, L. Gallmann, A. Rubio, and U. Keller. Attosecond screening dynamics mediated by electron localization in transition metals. *Nat. Phys.*, pages 1–5, August 2019.
- [139] Romain Géneaux, Christopher J. Kaplan, Lun Yue, Andrew D. Ross, Jens E. Bækhøj, Peter M. Kraus, Hung-Tzu Chang, Alexander Guggenmos, Mi-Ying Huang, Michael Zürch, Kenneth J. Schafer, Daniel M. Neumark, Mette B. Gaarde, and Stephen R. Leone. Attosecond Time-Domain Measurement of Core-Level-Exciton Decay in Magnesium Oxide. *Phys. Rev. Lett.*, 124(20):207401, May 2020.
- [140] Timothy Nathan Nunley, Nalin S. Fernando, Nuwanjula Samarasingha, Jaime M. Moya, Cayla M. Nelson, Amber A. Medina, and Stefan Zollner. Optical constants of germanium and thermally grown germanium dioxide from 0.5 to 6.6 eV via a multisample ellipsometry investigation. *Journal of Vacuum Science & Technology B, Nanotechnology and Microelectronics: Materials, Processing, Measurement, and Phenomena*, 34(6):061205, November 2016.
- [141] Marieke F. Jager, Christian Ott, Christopher J. Kaplan, Peter M. Kraus, Daniel M. Neumark, and Stephen R. Leone. Attosecond transient absorption instrumentation for thin film materials: Phase transitions, heat dissipation, signal stabilization, timing correction, and rapid sample rotation. *Review of Scientific Instruments*, 89(1):013109, January 2018.
- [142] Yi-Hsin Chiu, Nicholas G. Minutillo, Robert E.A. Williams, Greg J. Smith, David W. McComb, John A. Carlin, Ezekiel Johnston-Halperin, and Fengyuan Yang. Photoluminescence evolution in GaAs/AlGaAs core/shell nanowires grown by MOCVD: Effects of core growth temperature and substrate orientation. *Journal of Crystal Growth*, 429:1–5, November 2015.
- [143] E. G. Gamaly, A. V. Rode, B. Luther-Davies, and V. T. Tikhonchuk. Ablation of

- solids by femtosecond lasers: Ablation mechanism and ablation thresholds for metals and dielectrics. *Physics of Plasmas*, 9(3):949–957, February 2002.
- [144] Drake R. Austin, Kyle R. P. Kafka, Yu Hang Lai, Zhou Wang, Cosmin I. Blaga, and Enam A. Chowdhury. Femtosecond laser damage of germanium from near- to mid-infrared wavelengths. *Opt. Lett., OL*, 43(15):3702–3705, August 2018.
 - [145] Drake R Austin. *Semiconductor Surface Modification Using Mid-Infrared, Femtosecond Laser Pulses*. Ph.D. thesis, The Ohio State University, Columbus, OH, 2017.
 - [146] P. Stampfli and K.H. Bennemann. Theory for the laser-induced instability of the diamond structure of Si, Ge and C. *Progress in Surface Science*, 35(1-4):161–164, January 1990.
 - [147] Olga Sergaeva, Vitaly Gruzdev, Drake Austin, and Enam Chowdhury. Ultrafast excitation of conduction-band electrons by high-intensity ultrashort laser pulses in band-gap solids: Vinogradov equation versus Drude model. *J. Opt. Soc. Am. B*, 35(11):2895, November 2018.
 - [148] S V Popruzhenko. Keldysh theory of strong field ionization: History, applications, difficulties and perspectives. *J. Phys. B: At. Mol. Opt. Phys.*, 47(20):204001, October 2014.
 - [149] Vitaly Gruzdev and Olga Sergaeva. Ultrafast modification of band structure of wide-band-gap solids by ultrashort pulses of laser-driven electron oscillations. *Phys. Rev. B*, 98(11):115202, September 2018.
 - [150] V. E. Gruzdev, V. L. Komolov, and S. G. Przhibel'skiĭ. Ionization of nanoparticles by supershort moderate-intensity laser pulses. *J. Opt. Technol.*, 81(5):256, May 2014.
 - [151] Kaikai Zhang. *Atomic and Molecular Dynamics in Intense Mid-Infrared Fields*. Ph.D. thesis, The Ohio State University, Columbus, OH, 2015.
 - [152] N. S. Shcheblanov, M. E. Povarnitsyn, P. N. Terekhin, S. Guizard, and A. Couairon. Nonlinear photoionization of transparent solids: A nonperturbative theory obeying selection rules. *Phys. Rev. A*, 96(6):063410, December 2017.
 - [153] Kevin Luke, Yoshitomo Okawachi, Michael R. E. Lamont, Alexander L. Gaeta, and Michal Lipson. Broadband mid-infrared frequency comb generation in a Si₃N₄ microresonator. *Opt. Lett.*, 40(21):4823, November 2015.
 - [154] Steven Byrnes. Tmm: Simulate light propagation in multilayer thin and/or thick films using the fresnel equations and transfer matrix method., February 2017.

- [155] Steven J. Byrnes. Multilayer optical calculations. *arXiv:1603.02720 [physics]*, November 2019.
- [156] Bertil Nistad and Johannes Skaar. Causality and electromagnetic properties of active media. *Phys. Rev. E*, 78(3):036603, September 2008.
- [157] B. Harbecke. Coherent and incoherent reflection and transmission of multilayer structures. *Appl. Phys. B*, 39(3):165–170, March 1986.
- [158] Koji Ohta and Hatsuo Ishida. Matrix formalism for calculation of electric field intensity of light in stratified multilayered films. *Appl. Opt.*, 29(13):1952, May 1990.
- [159] Charalambos C. Katsidis and Dimitrios I. Siapkas. General transfer-matrix method for optical multilayer systems with coherent, partially coherent, and incoherent interference. *Appl. Opt.*, 41(19):3978, July 2002.
- [160] Atef Shalabney and Ibrahim Abdulhalim. Electromagnetic fields distribution in multilayer thin film structures and the origin of sensitivity enhancement in surface plasmon resonance sensors. *Sensors and Actuators A: Physical*, 159(1):24–32, April 2010.
- [161] L. Viña, S. Logothetidis, and M. Cardona. Temperature dependence of the dielectric function of germanium. *Phys. Rev. B*, 30(4):1979–1991, August 1984.
- [162] Ming-Fu Lin, Max A. Verkamp, Elizabeth S. Ryland, Kaili Zhang, and Josh Vura-Weis. Impact of spatial chirp on high-harmonic extreme ultraviolet absorption spectroscopy of thin films. *J. Opt. Soc. Am. B*, 33(9):1986, September 2016.
- [163] D. W. Bailey and C. J. Stanton. Calculations of femtosecond differential optical transmission in germanium. *Journal of Applied Physics*, 77(5):2107–2115, March 1995.